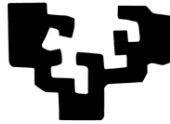EUSKAL HERRIKO UNIBERTSITATEA – UNIVERSIDAD DEL PAIS VASCO

MATERIALEN FISIKA SAILA – DEPARTAMENTO DE FÍSICA DE MATERIALES

eman ta zabal zazu

Universidad
del País Vasco

Euskal Herriko
Unibertsitatea

Electronic and Self-healing Properties of Polymer-Inorganic Hybrids Enabled by Vapor Phase Infiltration

Oksana Yurkevich

PhD thesis

Supervised by Prof. Mato Knez

2022

This PhD thesis has been performed at

CIC nanoGUNE

Nanomaterials group

Donostia – San Sebastián, Spain

Resumen

Permitir la autoreparación de los materiales es de vital importancia para ahorrar recursos y energía en numerosas aplicaciones emergentes. Si bien las estrategias para la autoreparación de polímeros están avanzando, los mecanismos para materiales inorgánicos semiconductores son escasos debido a la falta de agentes de cicatrización adecuados. En esta tesis demostramos el desarrollado de un concepto para la autoreparación con óxidos metálicos. Este concepto consiste en el crecimiento de nanopartículas (óxidos metálicos) dentro polímeros halogenados, mayoritariamente, y su posterior migración impulsada por la entropía a sitios con defectos inducidos externamente, lo que conduce a la reparación del defecto. Aquí demostramos que el conjunto de materiales de autoreparación se ha ampliado para incluir semiconductores, lo que aumenta la fiabilidad y la sostenibilidad de los materiales funcionales mediante el uso de óxidos metálicos. Además, demostramos que las propiedades eléctricas de los óxidos conductores pueden restaurarse parcialmente tras la autoreparación. Tales propiedades son de gran interés para un posterior desarrollo de electrodos flexibles y transparentes.

La reorganización de nanopartículas (NP) impulsada por la entropía, como se describe en este trabajo, sugiere una vía alternativa, prometedora y segura para permitir la autoreparación de los óxidos metálicos. Como primer paso, se necesita un sistema con NP de óxido metálico (MeO), bien disperso dentro de una matriz preferiblemente polimérica. Esto se puede obtener por infiltración en fase de vapor (VPI) de un polímero con materiales inorgánicos. Mediante esta estrategia se consigue un material híbrido o nanocompuesto con un recubrimiento de película delgada inorgánica del mismo u otro MeO, según la configuración del proceso. Esta matriz polimérica con NP dispersas en ella, puede servir como depósito de agentes para curar defectos en la película de MeO. Tras la formación del defecto, los efectos químicos y físicos en el sistema impulsarán la aglomeración y, finalmente, cerrarán el defecto de esta manera consiguiendo la autoreparación del polímero.

A diferencia de la química húmeda, el método VPI propuesto se basa en el procesos de arriba-hacia-abajo (procesos top-down) modificando una fina capa de la superficie del substrato, sin afectar la

totalidad del sustrato polimérico. Una migración de NP sólidas en lugar de líquidas aumenta la seguridad del sistema. Además, el método permite la autoreparación de películas delgadas semiconductoras en lugar de crear una mezcla de semiconductores y polímeros autoreparables como se describió en otros trabajos. Este enfoque ofrece una posible solución para mejorar la confiabilidad de los materiales en la electrónica flexible y otras aplicaciones, como las barreras de permeación.

Para formar un defecto de manera controlable se ha utilizado un haz de iones enfocado (FIB) (Figura 1a). Mediante el FIB se grabó una pequeña sección del recubrimiento InxOy, exponiendo el material híbrido subyacente al medio ambiente (Figura 1b). Como era de esperar, los mapas de rayos X de dispersión de energía (EDX) mostraron mayores intensidades de las señales de carbono y cloro del ParyleneC expuesto y menores intensidades de las señales de indio y oxígeno en el área con patrón FIB (Figura 1c). Después de utilizar el FIB sobre la fina película de óxido metálico, el nanocompuesto (ParyleneC/In$_x$O$_y$) se expuso al aire durante cinco minutos el híbrido. Las imágenes SEM muestran una especie de esfera que cubre completamente el área expuesta (Figura 1d). Los mapas EDX de esa región confirman que la neoformación esférica consiste en indio y oxígeno (Figura 1e). Además, se encontró una señal de cloro, aunque más baja que la de la superficie circundante. Es importante destacar que el escaneo EDX de la característica recién formada no muestra la presencia de carbono. Obviamente, al encontrarse con el aire, el defecto sanó lentamente por la migración del material inorgánico atrapado.
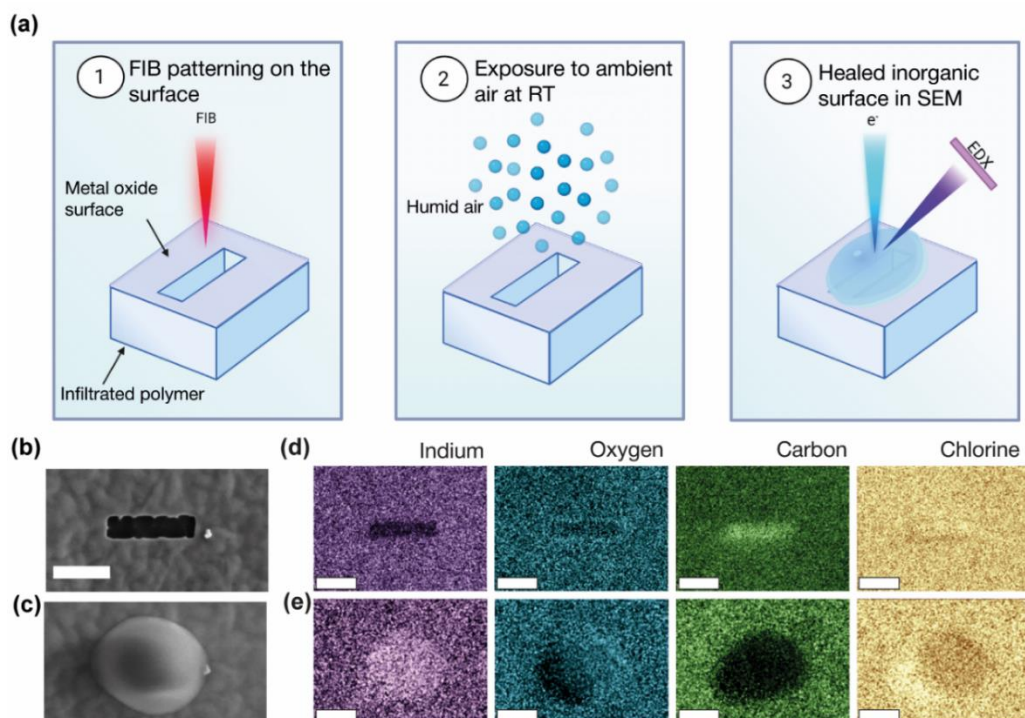
Figura 1. Curación de las películas delgadas de óxido metálico. (a) Esquema del procedimiento experimental para la investigación de autocuración. Imágenes SEM de la superficie grabada con FIB de la muestra híbrida ParyleneC/In$_x$O$_y$ (b) antes y (d) después de la exposición al aire. Mapas EDX codificados por colores de In, O, C, ad Cl (c) antes y (e) después de la exposición al aire. Barra de escala en imágenes (b-e): 1 µm.

Se repitió el mismo procedimiento de grabado con FIB seguido de la exposición al aire del híbrido de PVC/ZnO, el cual resultó en la reparación de los defectos inducidos (Figura 2). La aglomeración de las NP en la interfaz híbrida/aire del patrón grabado con FIB ya era evidente después de cinco minutos de exposición al aire y continuó hasta el cierre completo de la ruptura.
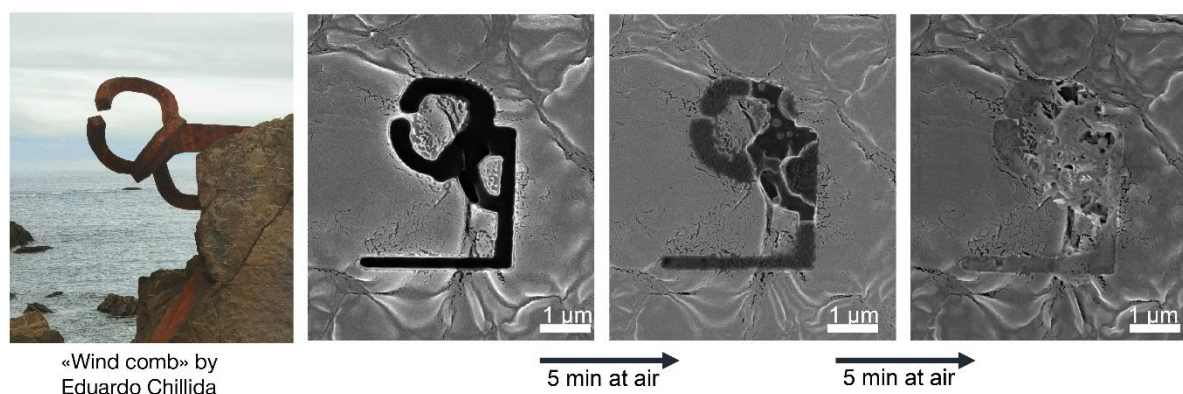

«Wind comb» by
Eduardo Chillida

5 min at air   5 min at air

Figura 2. Aurorepración de un patrón grabado selectivamente con FIB en la superficie de PVC/ZnO a lo largo del tiempo. La imagen de la izquierda es una foto de la escultura "Peine de viento", creada por Eduardo Chillida.

Para verificar si se puede restaurar la conductividad de un microdefecto reparado, fabricamos un híbrido a base de óxido de indio y estaño (ITO) y grabamos con FIB una tira rectangular para obtener un área conductora de 190 µm de largo y 35 µm de ancho (Figura 3a) con una resistencia eléctrica de 4,5 kOhm (Figura 3b). Medimos la resistencia mientras cortamos la tira en dos mitades por FIB, lo que hizo que la resistencia subiera hacia valores de GOhm. La sección de la tira abrió el circuito y condujo a la acumulación de diferentes potenciales en las dos mitades separadas. Las cargas opuestas en las dos sondas y las mitades de la franja dieron como resultado la atracción o repulsión del haz de electrones, lo que da como resultado las diferencias de contraste observadas en la micrografía (Figura 3(2)). El grabado y las medidas se realizaron en alto vacío dentro de la cámara de nuestro microscopio electrónico donde no se observó autoreparación. Al inundar la cámara con aire, la resistencia inicialmente se redujo a la mitad y después de mantenerse estable durante 8 segundos en el aire, se produjo una caída rápida de casi 5 órdenes de magnitud a 46 kOhm en 1 segundo (Figura

3c). El examen posterior del área con patrón de FIB mostró la reparación de la película delgada de ITO y la formación de algunos puentes entre las dos partes separadas de la tira conductora (Figura 3(3)). Por lo tanto, el proceso de curación no solo cerró la brecha en el material, sino que también restauró la funcionalidad electrónica.
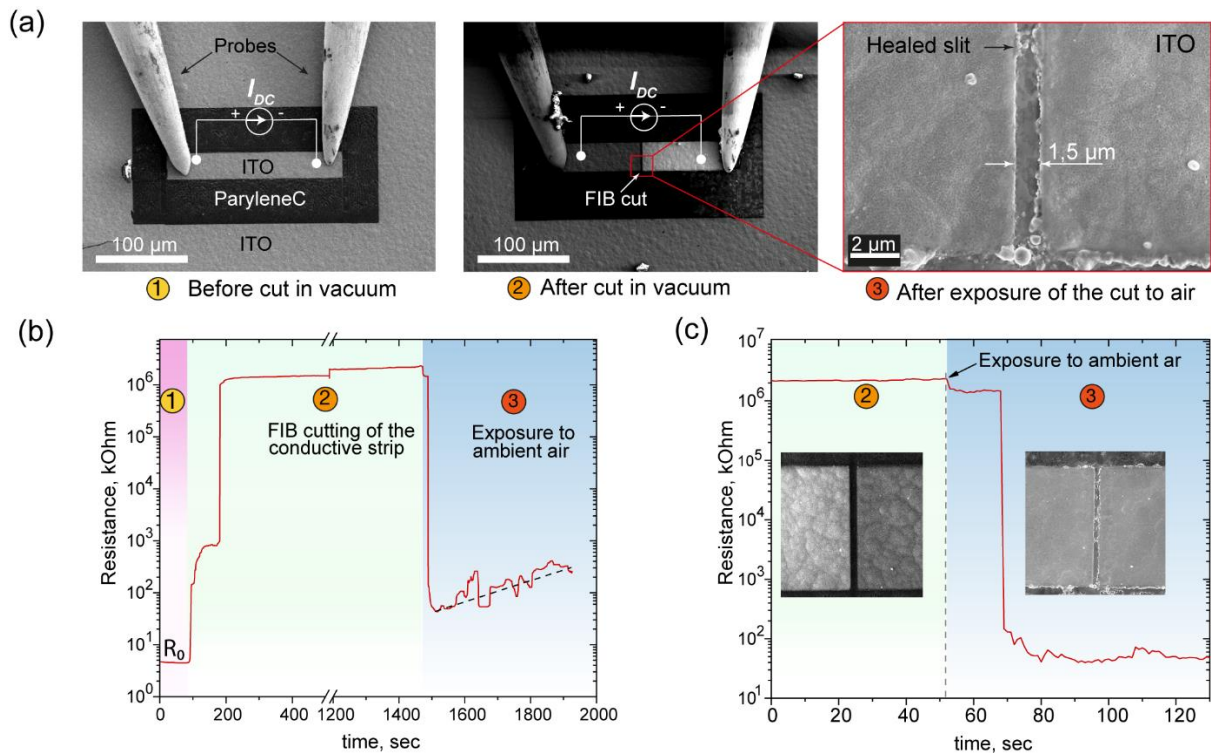

Figura 3. Restauración de la conductividad eléctrica (a) Imágenes SEM del área grabada con FIB en la superficie de ParyleneC/ITO y dos sondas colocadas en una franja conductora: (1) Antes de cortar en dos mitades; (2) después de cortar la tira en dos mitades; (3) Después de la exposición del corte al aire. (b) Evolución de la resistencia de la tira conductora de ITO durante las etapas 1-3 de corte y exposición al aire. (c) Sección límite ampliada de las etapas 2 y 3 en (b), que revela la evolución de la resistencia de la franja conductora de ITO en las etapas 2-3 durante la exposición al aire. Los recuadros muestran imágenes SEM de la franja seccionada antes y después de la autoformación de los contactos electrónicos.

La capacidad de autoreparación de los sistemas de polímero/MeO obtenidos puede explicarse mediante interacciones entrópicas. Las fuerzas de atracción de agotamiento entre las NP y las superficies del sustrato son de naturaleza entrópica y conducen a una segregación superficial de las NP. Estas fuerzas son causadas por la interacción de volumen excluido y surgen en una mezcla atérmica de NP y polímeros. En particular, el sistema gana entropía conformacional si las NP migran a la superficie y, en consecuencia, las cadenas de polímero no tienen que adherir las NP dentro del polímero. Este concepto se puede aplicar a nuestro sistema de polímeros híbridos/MeO. La VPI se

realizó a temperaturas elevadas, lo que condujo a la expansión del polímero y, en consecuencia, a un aumento de su volumen libre, haciéndolo accesible para la sorción de moléculas pequeñas. Después del proceso de infiltración, el sistema se enfrió a temperatura ambiente y, en consecuencia, el volumen del polímero se comprimió nuevamente. Sin embargo, el polímero ya estaba infiltrado con partículas de MeO, lo que provoca un aumento en la presión osmótica. Sin embargo, la difusión inmediata de las NP hacia la superficie estaba limitada debido a la capa protectora de MeO que actuaba como una barrera de difusión. Una vez que se alteró la integridad de la superficie a través del defecto inducido por la FIB, las NP de óxido metálico se difunden hacia la interfaz aire-sólido recién formada.

El presente trabajo demuestra una metodología para la autoreparación de recubrimientos de óxidos metálicos. Esto se hizo sin el uso de agentes curativos líquidos y reactivos, sino mediante el crecimiento de NP de óxido de metal bien dispersas dentro de polímeros clorados y permitiendo su difusión y agregación. Los defectos inducidos artificialmente en los recubrimientos quedaron sellados después de la exposición del sistema al aire. Es probable que esta autoreparación sea impulsada por un efecto entrópico, que surge en el sistema híbrido de óxido de metal/polímero e impulsa la migración de NP a los sitios dañados y las microfisuras. Además, nuestros estudios revelan que la presencia de haluros metálicos, como cloruros, es de crucial importancia para mejorar la movilidad de las nanopartículas de MeO dentro de la matriz polimérica huésped y, por lo tanto, la capacidad del sistema para autorepararse en general.

Nuestra metodología puede respaldar la longevidad de los materiales conductores transparentes actuales (óxido de zinc indio, óxido de estaño indio) ya que las grietas que ocurren al doblarse podrían recuperarse hasta cierto punto. Por lo tanto, este descubrimiento muestra un antes y un después en el desarrollo de más materiales inorgánicos de autoreparación mediante la infiltración de óxidos metálicos alternativos en polímeros halogenados o, así como, en el crecimiento de partículas de MeO halogenadas dentro de una variedad más amplia de polímeros no halogenados. En consecuencia, este desarrollo podría beneficiar a numerosas áreas tecnológicas: electrónica flexible, sensores portátiles, energía fotovoltaica, pantallas y energía al mejorar potencialmente la durabilidad y longevidad de los materiales.

Abstract

Enabling self-healing of materials is crucially important for saving resources and energy in numerous emerging applications. A plethora of recently published research works is dedicated to the development of strategies which allow for self-healing of materials, especially of those with certain technological importance. Given that most of the approaches are based on chemical processes, the vast majority of these works focus on the self-healing of organic materials, specifically polymers. At the same time, there is a growing demand for adapting such functionality to inorganic materials due to their importance in most developed electronics, including flexible electronics. The few existent examples of self-healing of inorganic materials rely on the incorporation of liquid healing agents, such as liquid metals or liquid precursors, into the devices. However, the development is in its infancy and further progress remains very challenging, mainly because of a lack of feasible healing agents and suitable ways to supply them to the damaged site.

In this thesis we have developed a concept for the self-healing of metal oxides, which is the most challenging type of material in this research area. This concept consists of growing metal oxide nanoparticles inside the bulk of halogenated polymers via vapor phase infiltration and their subsequent entropy-driven migration to externally induced defect sites, which eventually leads to the recovery of the defect. The hybrid material, i.e., the polymer matrix with dispersed NPs, can serve as a reservoir with healing agents for the repair of a cracked MeO film. The self-healing of inorganic materials and structures was realized also without liquid agents by making use of the mobility of inorganic NPs within polymers, as the spatial distribution of NPs can be tuned by means of harnessing both enthalpy and entropy.

Herein we present an expansion of the pool of self-healing materials to semiconductors such as indium, zinc, indium tin and zinc indium oxides, thereby allowing to increase the reliability and sustainability of future functional materials. We revealed that not only the morphology, but also the electrical properties of ITO can be largely restored upon healing. Such properties are of immediate interest for the further development of transparent flexible electrodes.

Table of Contents

Contents

Emerging hybrid materials

1.1 Hybrid materials

Nature is an immense source of inspiration for scientists, either as library of mysteries which need to be unraveled or a blueprint for mimicking its creations. Materials in nature were adjusted throughout millions of years to fulfil specific tasks, resulting in enormous variations in shapes, structures, and compositions. One of the classes of materials that emerged during the evolution of living creatures is hybrid materials. Those are multicomponent composites that consist of organic and inorganic fractions, blended at the submicrometric or nanometric scale. [1] As a result, their properties are described not only as sum of the properties of the constituents, but their synergy often boosts the properties or even leads to new functionalities. The origin of these properties comes from the physics and chemistry at the organic-inorganic interfaces and for that reason hybrids are divided into two classes based on the quality of the material interaction at the interfaces. Class I includes trapped or encapsulated materials with weak interactions between organic and inorganic moieties, such as Van-der-Waals, hydrogen bonding, or electrostatic interactions. Class II hybrid materials show "strong" chemical interaction between counterparts, such as covalent or ionocovalent bonds. [1]

Often, hybrid organic-inorganic materials outperform the conventional ones and consequently, they may be a response to challenges of modern technologies. For example, materials used in regular electronic devices must fulfil multiple requirements that are prerequisites for the reliable and efficient use of modern gadgets. While inorganic materials are advanced and have a broad use, the use in flexible electronics is largely impeded by their incompatible mechanical properties. Materials are needed which are robust to mechanical stress and suppress crack evolution, while they are also flexible and able to withstand multiple bending events. [2] Therefore, the development of hybrid electronic materials is a key solution for advances in the field of flexible electronics.

1.1.1 Vapor phase approach for fabricating functional hybrid materials

There is a plethora of approaches for fabricating organic-inorganic hybrid materials, and a majority of hybrid materials are synthesized using liquid chemical methods. [3]–[7] However, vapor phase

methods stand out as rapidly developing processing pathways, bringing benefits in the processing conditions and quality of the materials.[8] Within such solvent-free synthesis methods, vapor phase infiltration (VPI)[9], [10] and molecular layer deposition (MLD) [11] stand out. Both of them take their origin from atomic layer deposition (ALD). [12]–[14] In analogy to ALD, these methods rely on temporally separated gas phase reactions; in other words, chemical reactants, or precursors, are never present in the reactor simultaneously. Such a separation of the processing steps allows good control over the reaction paths, helping to avoid undesired side reactions in the gas phase and overgrowth.

MLD allows the synthesis thin organic films with excellent control over the thickness and conformality of the grown layers. To make hybrid materials by MLD, one has to complement organic layers with ALD-grown inorganic ones. The merged ALD and MLD layers constitute the hybrid organic-inorganic material whose properties depend on the concentration and nature of the organic and inorganic counterparts. The best-known family of such materials is called "metalcone", defined as metal alkoxide polymeric films. Metalcones already include alucones, [15] zincones, [16] zircones, [17] hafnicones, [18] titanicones, [19] vanadicones, [19] and indicones, [20] the properties of which aim to merge the original functionalities of the metal oxide with the mechanical flexibility of the organic part.

Vapor phase infiltration stands out from the ALD and MLD methods as it is a top-down and not a bottom-up approach. This technique emerged after the pioneering work of the Knez group in 2009, where the authors reported a drastic improvement in the mechanical properties of spider silk upon modification by VPI, which was originally called multiple pulsed infiltration (MPI). [21] Over the last decade, the number of research groups developing VPI processes constantly increased. Since the hybrid material is not a simple sum of its constituents but a novel material with own functionalities, many material combinations need to be tested. The variety of studied substrates includes biological objects such as spider silk, [21] collagen [22] and chitin, [23] fabrics like cellulose [24] or polyethylene terephthalate (PET), [25], [26] and different synthetic polymers such as polymethyl methacrylate (PMMA), [27], [28] polypropylene (PP), [29] PET, [26] polyethylene naphtalate (PEN), [30] Kevlar, [31] nylon 6, [29] Pellethane, [29] polytetrafluoroethylene (PTFE), [32] polydimethylsiloxane (PDMS), [27] Kapton, [27] SU-8, [33] polyurethane (PU), [34] polyimide, [34] and polyaniline(PA). [35]

Application of the gas-phase precursors to the soft substrates with prolonged exposure times leads to the precursors' sorption into the polymer and their subsequent diffusion inside the substrate. There, precursors can be physically trapped or they can chemically react with the available functional groups of the polymer host. The diffusion of the precursor into the polymeric substrate and its chemical reaction inside the bulk are critical points, distinguishing a VPI process from ALD. VPI results in a thin film coating on the surface of the substrate, together with the formation of an organic-inorganic hybrid layer (Figure 1.1). Such a layer can obtain utterly novel functionalities like triboelectricity [27] or superlinear conductivity; [36] besides, it can enhance the mechanical properties of the polymer. [24], [29], [32], [37], [38]
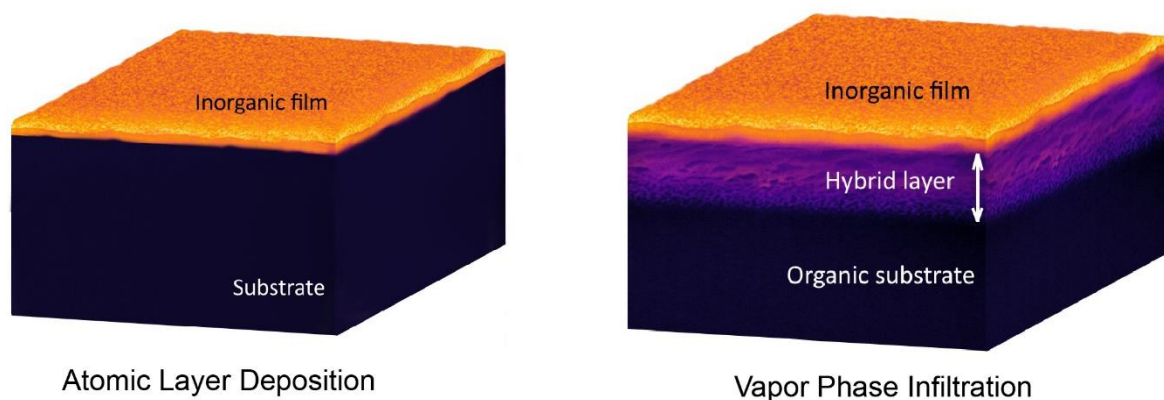
Figure 1.1 Comparison of the structures obtained after ALD and VPI processing.

1.1.2 Gas-phase deposited hybrids for electronic applications

One of the recent and very quickly expanding fields which can significantly benefit from hybrid materials, is electronics. Organic-inorganic hybrids promise a merger of the properties of conventional silicon-based semiconductor devices with the ability to be bent, stretched, or compressed without significantly compromising the functionalities. Such synergistic properties are vital for the development of wearable and foldable electronics, biomedical sensors for digital medicine, organic light-emitting diodes, low-power energy sources, or non-volatile memory applications. The great controllability of the gas-phase deposition processes allows for precise tuning of the electronic and mechanical properties of the hybrid. Many factors such as the dielectric constant, band gap, mobility, carrier concentration, etc., can be adapted by tuning the ratio of the organic to inorganic parts in the final composition. The easy scalability of the vapor-phase deposition techniques towards industrial scale, the purity of the formed structures, and the true chemical interaction between the organic and inorganic constituents make gas phase methods highly attractive for the development and integration of novel hybrid materials into devices. However, it is a young and growing field and for some applications only proofs-of-concept have been shown. Moreover, there are no or very few reports on hybrid materials with certain properties such as piezoelectric, pyroelectric, ferroelastic, superconducting, or ion-conducting which are synthesized by gas-phase methods. Taking into consideration all the benefits which hybrid materials can bring into the field of flexible electronics, there is a high demand for active research to fill this gap.

Gas-phase methods helped to achieve a significant progress in dielectric materials. One of the key challenges in the development of novel organic thin-film transistors (OTFT) is the need for a high-performance dielectric layer, as it has a direct impact on the TFT´s characteristics such as carrier mobility (μ), operation voltage, and power consumption. It is beneficial to keep the capacitance density as high as possible in order to achieve a low power consumption in OTFTs. This can be

achieved by increasing the dielectric constant (k-value) of the dielectric layer or by reducing its thickness. Hybrid organic-inorganic films are promising gate dielectrics for low-voltage operating organic thin-film transistors. Namely, by changing the amount and ratio of the organic and inorganic components, it becomes possible to tune the dielectric constant and dielectric strength (leakage resistance). Besides, the mechanical properties of the hybrids make them very attractive for flexible electronics.

There are already some successful examples of hybrid materials as dielectrics. Due to the well-known dielectric properties of zirconium oxide, Zr-based hybrids have proven their suitability for applications in OTFT. Zircones belong to the group of metalcone hybrids and form after reactions of zirconium tetra-t-butoxide with an organic diol. The group of S. George demonstrated the use of zircone as dielectric layer in pentacene-based OTFTs. [17] The hybrid films had leakage currents two orders of magnitude better that those of pure ALD-grown ZrO_2. At the same time the carbon constituents lowered the dielectric constant from ~16 for the ZrO_2 film to ~ 6.7 for the zircone film. Another example is based on aluminum oxide. Having a dielectric constant of about ~ 9.0 alumina is also a potentially good candidate for a use in OTFTs. Cheng et al. studied hybrids of self-assembled MLD-deposited octenyl-trichlorosilane layers and Al_2O_3 linkers, deposited from trimethyl aluminum (TMA) and H_2O by ALD. [39] Changing the number of MLD and ALD layers allowed to tune the band gap and the dielectric constant from ~7.00 to 6.09 eV and ~9.0 to 4.5, respectively.

Conductive and flexible films are crucial for many emerging applications, including displays, wearable devices, personal medical devices, photovoltaics, etc. Numerous research groups are investing their efforts into achieving highly conductive hybrid organic-inorganic materials, which at the same time maintain their mechanical flexibility.

Zinc oxide is among the most promising substitutes for the conductive and transparent In_2O_3. However, the intrinsic brittleness of inorganic oxides hampers their use in flexible applications. The group of S. George investigated a zincone hybrid, which is closely related to a ZnO film and, therefore, may combine the conductivity of ZnO with the flexibility of an organic layer.[40] They employed DEZ, hydroquinone (HQ) and water to perform MLD:ALD films. The reaction between DEZ and HQ generates a molecular chain in the form of $(-Zn-O\text{-phenylene-}O-)_n$, which is an electrical conductor. Measurements of a pure ZnO ALD film showed a conductivity of ~14 S m^{-1}, while the ALD:MLD alloy showed ~170 S m^{-1}, demonstrating a considerable enhancement of the conductivity in the hybrid alloy of more than one order of magnitude (Figure 1.2). The authors explained the conductivity enhancement with a higher electron mobility, which is caused by the electron coupling of the delocalized π-electrons from the conjugated phenylene rings in HQ and the neighboring ZnO clusters. At the same time the ZnO layer can provide a high density of charge carriers caused by oxygen vacancies in the ZnO layer. The conductivity values of the zincone:ZnO alloys outperformed that of inorganic zinc oxide and are largely comparable with high temperature-deposited ZnO or Al-doped ZnO. The origin of the enhanced conductivity of the 2:2 alloy, compared to the 1:1 alloy, was not clearly stated, but the values reached 170 S cm^{-1} and 116 S cm^{-1},

respectively. Moreover, optical measurements proved high transparency of the hybrids in the visible range. Such zincone:ZnO alloys are promising candidates to replace indium tin oxide (ITO) in displays and photovoltaic devices.
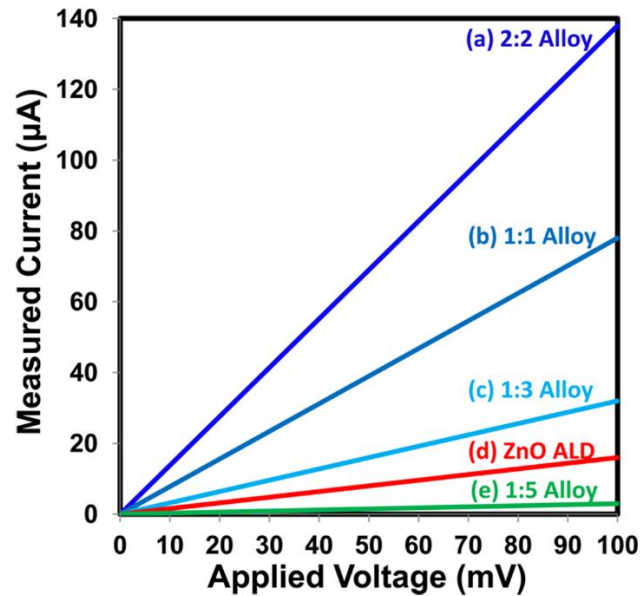

Figure 1.2 Measured current versus applied voltage for ZnO ALD film and various alloy films. Image taken with permission from the Ref [40].

Triboelectric nanogenerators (TENG) can also benefit from hybrid materials. The working principle of TENG devices is based on converting mechanical energy into electrical energy, which can be achieved by building an interface between two materials with different electronic affinity. TENGs opt for a broad application range, including wearable electronics, charging batteries, activators of chemical reactions, etc. However, to generate electricity, TENGs require friction between the triboelectric materials which causes wear. Therefore, modification of not only the surface, but also the bulk of the materials promises much better functionality and durability. Yanhao Yu et al. applied VPI of Al_2O_3 into various polymers, including PDMS, polyimide, and PMMA. [27] As a result of the infiltration, the Al_2O_3 moieties penetrated these polymers by at least 3 μm depth. The electron-attaining capability of such doped polymers was significantly reduced due to the strong repulsion of electrons by Al_2O_3. The combination of infiltrated and pristine polymers allowed to create high-performance TENG devices. But unlike a pure surface modification, which is commonly applied to tune TENG performance, the infiltration process allowed to overcome wearing of the surfaces of the triboelectric devices, as VPI doping changed the properties of the bulk of the polymer. The strategy appears as promising top-down approach to tune the efficiency of polymeric electronic devices.

1.2 Self-healing materials

Materials are susceptible to constant mechanical or electrical stress, ruptures, or cracks throughout the operational time. For centuries, researchers focused their efforts on improving the materials' hardness, toughness, and strength to prevent possible damage and increase their lifetime. However, this strategy can extend the operational lifetime only to a certain extent. The understanding that resources are limited, and that the ecology suffers from single-use devices, forces us to find solutions for the longevity of materials even under demanding conditions. [41] Substitution of standard materials with self-healing materials (SHM) that allow multiple healing events can potentially make the lifetime of a device infinite (Figure 1.3). [42] This approach is beneficial for sustainable technologies, even if the functional properties of the SHM do not outperform the conventional material or materials with enhanced damage prevention.
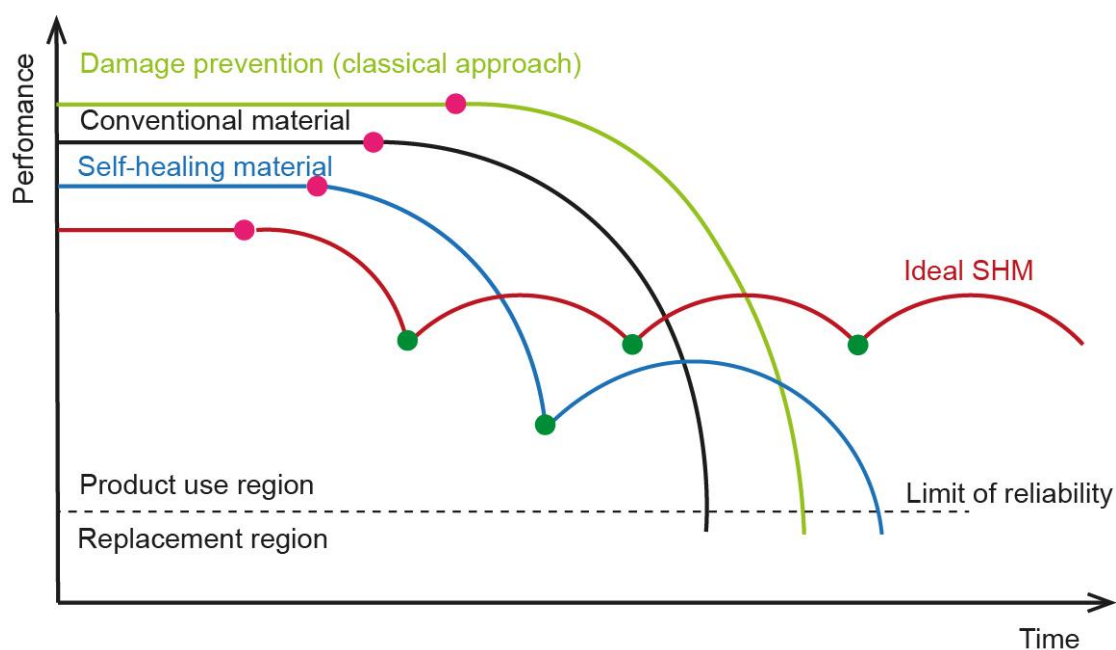
Figure 1.3 Concept of the performance degradation of materials with different design: black: conventional material; green – damage prevention; blue – SHM, red – ideal SHM. The image is adapted from Ref. [42]

A self-healing material is a material that can partially or fully restore its initial functionality or structure. Like hybrid materials, SHM are also inspired by nature. The idea behind is to mimic the recovery and healing capabilities of our natural bodies. Not only human skin or bones can regenerate, but healing also happens on the molecular level. Damage to the DNA is an ordinary incident that can lead to DNA mutation, uncontrollable growth, or death of cells, but pro-inflammatory cytokines act to withstand the decay. [43] Repair of microscopic damage in plants occurs via a cascade of chemical reactions initiated by oligopeptides and oligosaccharides. [44]

Interestingly, self-healing in nature is present outside "living tissues" as well. For example, byssal threads of marine mussels can self-heal via protein-coordination bonds. [45] Even though the exact mechanisms and chemistries in these processes are not yet fully understood, researchers impart this idea of developing SHM to recover from structural damage and restore materials functionality.

Self-healing materials are typically divided into intrinsic and extrinsic materials. Intrinsic materials possess healing as an inherent functionality, which can be activated by external stimuli or triggered by damage. Such materials can serve as healing matrixes for the other materials dispersed in them. The second group requires additional healing agents, for example, encapsulating them in micro-capsules or vascular networks. SHM can also be grouped into autonomic and non-autonomic SHM. Considering practical applications in soft devices, ideally self-healing materials should possess fully autonomic healing functionality that doesn't require additional inspection of the device, treatment with solutions, charge injections, annealing, or light stimuli. In such manner, safer materials with a longer service time can be developed, offering an elegant solution toward sustainability. Non-autonomic materials require an external trigger to initiate the healing process. The controversy of this classification arises from the type and accessibility of the external trigger. Many of them, such as UV light, humidity, or heat, can be applied under real-usage conditions. For example, heat can be applied as trigger if the material is exposed to sunlight during its operation. Therefore, it is also legitimate to call materials autonomic if they can heal in their real operating conditions. [42]

Self-healing materials were under investigation since the middle of the 20th century with the main focus on cement-based materials. [46] Even though it requires human inspection and an external heat stimulus, this approach enables the prevention of crack formation and propagation in concrete, not only extending the lifetime of the constructions, but also preventing possible catastrophic failures. Recently, the first works related to electronic materials, appeared (Figure 1.4). In 2007, Williams et al. discovered organometallic-metal composites that exhibit self-healing properties and conductivities of the order of 10^{-3}S cm^{-1} for electronics applications in high-risk usage conditions. [47] Later, in 2016, an intrinsically stretchable and healable semiconducting polymer was demonstrated. [48] However, during these years the main progress was achieved for polymers or polymer-based composites. [49]–[53]
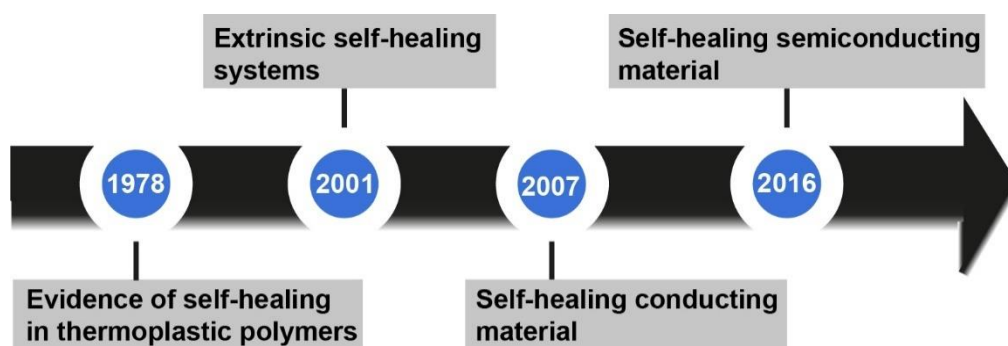

Figure 1.4 Timeline of the development of self-healing materials for electronic applications. Image adapted from Ref [46].

1.2.1 Approaches for self-healing materials

There are various approaches for creating self-healing materials. Those can be roughly classified into three categories: physical, chemical, and physico-chemical approaches (Figure 1.5). Physical approaches are commonly based on diffusion processes, [54] shape-memory effects, [55] phase-separated morphologies, [52], [56] exploitation of paramagnetic nanoparticles, [57] or entropic interactions within the nanocomposite. [58] Chemical approaches use the functional chain ends of the polymer to facilitate covalent [59], [60] or free-radical rebonding, [61] or introduce supramolecular dynamic bonds [62], [63] through ionic interactions[64] or metal-ligand coordination. [65] A combination of physical and chemical approaches usually involves entrapping of healing agents inside capsules or vascular fluid systems, which can fill up a defect and trigger chemical reactions of these reactive agents. [66]
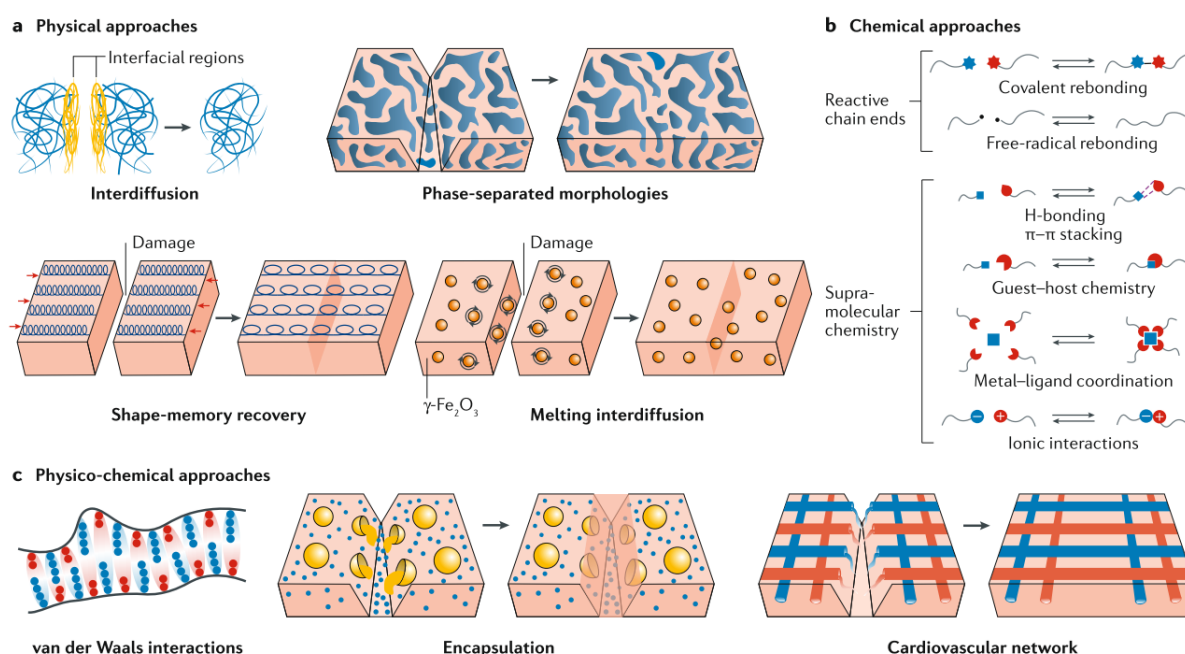
Figure 1.5 Self-healing mechanisms: (a) Physical processes including interdiffusion, phase-separated morphologies, shape-memory recovery, melting interdiffusion; (b) chemical processes; (c) combined physical and chemical processes. Image taken with permission from Ref [50].

While self-healing approaches for polymers are robust, the healing strategies for inorganic materials, or more specifically, semiconducting materials, are scarce, as discussed in the following.

1.2.2 Self-healing of inorganic materials: metals, metal oxides, ceramics

Most of the works on self-healing materials are devoted to polymers and polymer-based composites. The success of that research direction comes from the mobility of the polymer chains even at low

temperatures, ease of functionalization and modification of polymers, and the large volume of mobile molecules rather than mobile atoms. [42] However, examples and strategies for inducing self-healing functionality into inorganic materials exist as well.

Concrete and ceramics have been under active research in order to improve the performance, reliability, and longevity of these industrially important materials. In general, healing happens through mass transport. However, ceramics are generally very stable at elevated temperatures, meaning that they have high activation energies for diffusion. Researchers have developed two healing mechanisms for ceramic materials: oxidization and precipitation. [67]

For the implementation of oxidation-induced healing, ceramics are blended with carbide or nitride particles. These particles can oxidize upon additional energy supply, either in the form of heat or electricity. Various composite ceramics were developed based on SiC particles, for example Al_2O_3/SiC, [68] SiC/spinel, [69] PyC/SiC, [70] SiC–BN, [71] ZrO_2/SiC. [72] Besides, non-oxide ceramics also exhibited oxidation-induced self-healing. The so-called MAX phases are ceramic materials with high toughness, ductility, and metal-like electrical properties. They consist of alternating layers of MX (where M is a transition metal and X is carbon or nitrogen) and pure metals from the group A. Farle et al. compared and discussed more than 75 MAX phases with different compositions, such as Ti_2AlC, Ti_3AlC_2, V_2AlC, V_3AlC, Nb_2AlC, Zr_2AlC, Zr_2AlN, Ti_2SnC, Ti_3SnC_2, Nb_2SnC, Zr_2SnC, Ti_2InC, Nb_2InC, Zr_2InC, Zr_2InN, Ti_3SiC_2, which potentially can self-heal. [73] However, the required temperatures and time needed to heal a crack can be considered a disadvantage. For example, the healing of a 10 μm-wide crack on the surface of Ti_2AlC required annealing in air at 1200°C for 20 hours, [74] while that of a 4 μm-wide crack in Cr_2AlC took 5 hours at 1200°C. [75]

Precipitation-induced healing is a less developed area of research. Gu et al. demonstrated that notches in Nb_2O_5 pellets can be mended with $AgNbO_3$ upon adding Ag_2O into the damaged zone with consequent annealing at 950°C for 12 hours. [76] Another interesting mechanism for ceramics healing is a phase transition. Here, as different crystalline phases occupy different volumes and can lead to volume expansion, mending of the defect can occur. Phase transition of an eutectic alloy from $ZrO_{2,mkl}$ to $ZrO_{2,tetr}$ healed cracks in ZrO_2/Al_2O_3 composite, confirming the approach. [77]

Ceramic materials require high temperatures and prolonged timing to recover the defects. The challenge of self-healing functionality in inorganic materials originates from their rigidity and lack of liquid repairing agents. However, there are few successful examples of inorganic SHM where damage recovery goes through the release of the liquid agent stored in the microcapsules of microchannels. Few of the studies rely on the use of liquid metals (LM), such as a Ga-In-Sn alloy, [78] Ga-In nanoparticles, [79] eutectic Ga-In (EGaIn), [80], [81] or an EGaIn composite embedded in an elastomer. [82] These systems can restore their electrical functionality after damage and the healing happens within a second without additional energy sources. [82] Yet, the systems based on LM microcapsules or microfluidics have their drawbacks: a limited number of self-healing events, use of rare and expensive Ga, and poor material choice as it is limited to Ga-In alloys. Besides LM, microchannels can store liquid precursors. Liu et al. developed a polymeric delivery system filled

with liquid $TiCl_4$, a precursor that is reactive on air. [83] Upon breaking the integrity of a protective alumina oxide diffusional barrier, $TiCl_4$ was released and reacted with water vapor to titania. The main drawback is the safety risk associated with a hazardous HCl by-product, forming upon the reaction of $TiCl_4$ and H_2O.

1.2.3 Self-healing of semiconducting materials

The development of self-healing semiconducting materials is not straightforward. [46], [84] The challenge arises from the contrast in the nature of inorganic and the otherwise typically soft self-healing materials. Semiconductors are normally rigid and have some level of crystallinity, while self-healing is characteristic of soft materials with a high chain mobility. Therefore, consideration of hybrid materials that combine the desired properties for developing self-healing concepts for semiconductors is highly promising. There are just few examples in the literature which describe self-healing of semiconducting materials relying on organic semiconductors or on hybrid materials.

Recently, a healable organic semiconducting material was developed. [48] Organic semiconductors are of technological importance for the organic field-effect transistor (OFET) fabrication. Healing of the organic semiconductor was based on the polymer 2,6-pyridine dicarboxamide, with a flexible backbone and two amide groups, that undergo hydrogen bonding. [48] This bonding is the origin of the self-healing functionality, which was demonstrated for nanocracks not exceeding 100 nm in their lateral size. Besides, healing required an additional treatment with chloroform or temperature. However, the authors noted that an annealing step of 150°C for 30 minutes negatively affected the stretchability of the polymer. This drawback can negatively affect the use of the material for its main prevised application area as a part of OFET in stretchable electronic devices and wearable electronics.

An alternative approach for the development of flexible semiconducting materials relies on blends of semiconducting nanowires or nanofibers with elastomers. [85], [86] Recently, a self-healing system using such components was demonstrated and implemented into multifunctional FET. [87] The material was a blend of poly(urea-urethane) (PUU) and semiconducting carbon nanotubes (CNT). PUU possesses reversible hydrogen and disulfide bonds, allowing entirely autonomous recovery of a polymer, which also resulted in the healing of dispersed CNTs in the polymer and recovery of semiconducting FET channels. A complete healing of the material happened within 24 hours, while the conductivity regained within the first ten minutes after the damage. The fabricated OFET devices could withstand 500 stretching cycles at 25% strain without a notable decrease in their performance. The OFET device was applied as a skin sensor monitoring physiological parameters.

The authors of the review [46] see the development strategy of semiconducting SHM going in two different directions. The first direction relies on blends of semiconducting and self-healing polymers, which would allow obtaining stretchable semiconductors. Such works were demonstrated for PDMS [88] and styrene-ethylene-butylene-styrene (SEBS) [89], [90] polymers mixed with

conjugated semiconducting polymers. The second direction includes mixing of nanostructured inorganic semiconductors with self-healing polymers, similar to the work with CNTs and PUU blends. [87] Besides CNTs, also other nanostructured materials can be considered: various nanostructured carbon materials, Si whiskers, and Ag or Au nanorods.

This thesis focuses on exploring another way of inducting self-healing functionality – entropy.

1.2.4 Ordering through entropy

It has been extensively discussed that the properties of materials change upon transition from a macroscale to a nanoscale. [91] The surface area of a sphere is proportional to the square of its radius r, while its volume is proportional to r^3. The fraction of atoms at the surface scales with the surface area divided by volume, i.e., with the inverse radius of the sphere (r^{-1}). The same scaling law applies to other properties of a material, such as phase transition temperatures. Small clusters of materials start behaving more molecule-like rather than solid-state like. [91] When intensive properties of materials change and the phases are no longer well-defined, the rule of Gibbs phases also loses its applicability. [92] Therefore, the behavior of a nanosized system is distinct from the micro and macro-sized systems and is guided by the interfaces of nanosized objects. At the nanoscale, surfaces start to act not only as a framework, but they show a complex enthalpic and entropic interplay, [93] which is reflected in the Gibbs free energy (Eq.1).

$$\Delta G = \Delta H - T \Delta S \qquad \text{(Eq. 1)}$$

where G is free energy, H is enthalpy, S is entropy, and T is its temperature of the system. A change of the Gibbs free energy predicts the direction of the chemical reaction or phase transition, and the system tends to spontaneously get into a state with a minimum of free energy.

Tailoring the interfaces of nanosized objects, for example, nanoparticles (NPs), allows their organization in a specific way, and many research works are devoted to the self-assembly of the NPs. [94], [95] It has been demonstrated that NPs organization is almost exclusively driven by entropy interactions in some self-assembly systems. [96]–[99]

Ordering of such systems guided by entropy may seem counterintuitive, as the concept of entropy is in the common opinion described as a measure of disorder, chaos, and decay or progress towards those states. [100] Indeed, entropy is used to describe spontaneous irreversible changes in physicochemical systems. The second law of thermodynamics describes the direction of the energy exchange of bodies with different temperatures. Accordingly, without external energy supply heat always flows from the hotter object towards the colder. Rudolf Clausius concluded in 1854 that there should be a quantity that describes irreversible changes in isolated systems and named this quantity entropy, after the Greek word "transformation", to highlight the analogy in nature of entropy and energy. [101] He also defined that the entropy of the universe strives towards a

maximum. [101] The third law of thermodynamics, derived by Max Planck, shows a microscopic interpretation of the entropy reflected by the equation (2). [102]

$$S = k_B \ln W \qquad \text{(Eq. 2)}$$

This equation defines entropy as a mathematical product of the logarithm of the number of accessible states of the system (W) and Boltzmann's constant (k_B). Herewith the second law of thermodynamics can be rephrased to a spontaneous irreversible change in an isolated system going towards an increase of the number of states of the system. In classical statistical physics the number of states can be understood as the accessible volume in phase-space. It leads to the statement that isolated systems can spontaneously change only towards a (much) larger occupied volume in space. Frenkel commented on the word "much" by calculating that an increase of entropy by 0.1% for one liter (equal to one Joule per Kelvin) of water in ambient conditions would result in the surge of the number of states of the system by the stunning factor of $10^{10^{22,5}}$. [103]

Therefore, an increase in entropy corresponds to the growth of the number of accessible states. For some systems, this brings a visibly enhanced order.[103] Lars Onsager did the very first work on the spontaneous ordering of a system induced by entropy.[104] He analyzed the entropy for a fluid of thin, hard rods. His model predicts the transition from an orientationally disordered to a nematic (orientally ordered) phase of thin rods (Figure 1.6a). In Onsager's theory the number of states is determined through translational and orientational degrees of freedom of hard rods. Indeed, he found that a phase transition towards the nematic phase correlates with a decrease in the orientational entropy. However, there is a contribution of the translational entropy associated with the excluded volume. For a disordered system of the rods the excluded volume is large (or, in other words, the accessible volume is small), which decreases the translational entropy. In this way the ordering of the rods increases the translational entropy which results in the gain of the total entropy of the system, despite the simultaneous decrease in orientational entropy. Another famous example of ordering phase transition is the freezing of hard spheres (Figure 1.6b), which was first proven via Monte-Carlo calculations by Alder and Wainwright [96] and by Wood and Jacobson. [105] Initially, the scientific community met the theoretical evidence with great skepticism; however, it became widely accepted after 1957 and later experimentally proven. [106]

These theoretical works pushed the research on design of new interfacial assemblies by employing the knowledge of entropy forward. The entropy input can be divided by its nature: shape, rotational, vibrational, orientational, and conformational entropy. [93] The shape entropy guides the assembly of particles solely by steric factors. Some works showed that the entropic effect of shape is distinct from others[99], [107], [108] when the system reaches a moderate density. [109] Rotational and vibrational entropy is linked to the number of accessible states that particles can reach by rotational and vibrational modes and can be observed, for example, in Janus-particles. [110], [111]

Conformational entropy is associated with the conformational number of a molecule and therefore has a particularly pronounced impact on long-chain molecules including proteins, [112] RNA,

[113] and polymers. [114] It becomes critically important for blends of NPs and polymers. For NP-polymer interactions, conformational entropy brings the largest input for the NP assemblies and guides the distribution and agglomeration thereof.
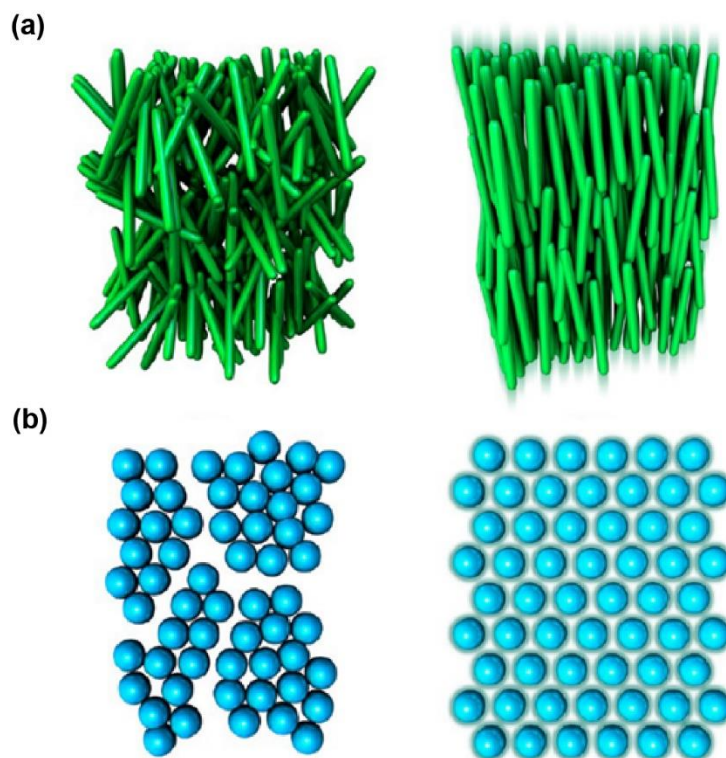

Figure 1.6 (a) Isotropically oriented thin hard rods and their transition towards a nematic phase. (b) Fluid of hard spheres and its freezing. The entropy increases from left to right. Figure is taken with permission from the Ref [93].

1.2.5 Bulk Aggregation and Surface Segregation of Nanoparticles

Already in 1954 Sho Asakura and Fumio Oosawa showed that a mixture of suspended particles and globular polymers separates into two fluid phases due to attractive interaction. [115] Later, the colloidal de-mixing was explained with depletion interactions. [116] Typically, particles blended with polymers tend to agglomerate into clusters guided by depletion attraction forces. Such a depletion attraction force arises from the excluded volumes and attracts particles to each other or towards the walls (Figure 1.7). Depletion attraction forces can be suppressed by roughening the surfaces of NPs or by polymer grafting. [117]

Conformational entropy is not only responsible for the bulk aggregation of NPs within the polymer but also for the surface segregation of NPs. [119] Surface segregation is usually observed when the concentration of NPs is low. In this case depletion attraction forces between NPs are also low and, consequently, NPs do not agglomerate into clusters. This facilitates their easier migration within

13

the polymer. [119] It was reported that depletion attraction can be overcome in the presence of interfaces. [120], [121] There is a first-order phase transition when NPs are expelled from the polymer towards the surface. In other words, interfaces induce an "entropic push" or depletion attraction between NP and a wall leading to a formation of a layer of NP near the walls, surfaces, or interfaces (Figure 1.8). [122] By tuning the concentration of the NPs, the depletion attraction can be controlled and the system can achieve surface segregation, bulk aggregation, or a mixture of those states. [119]
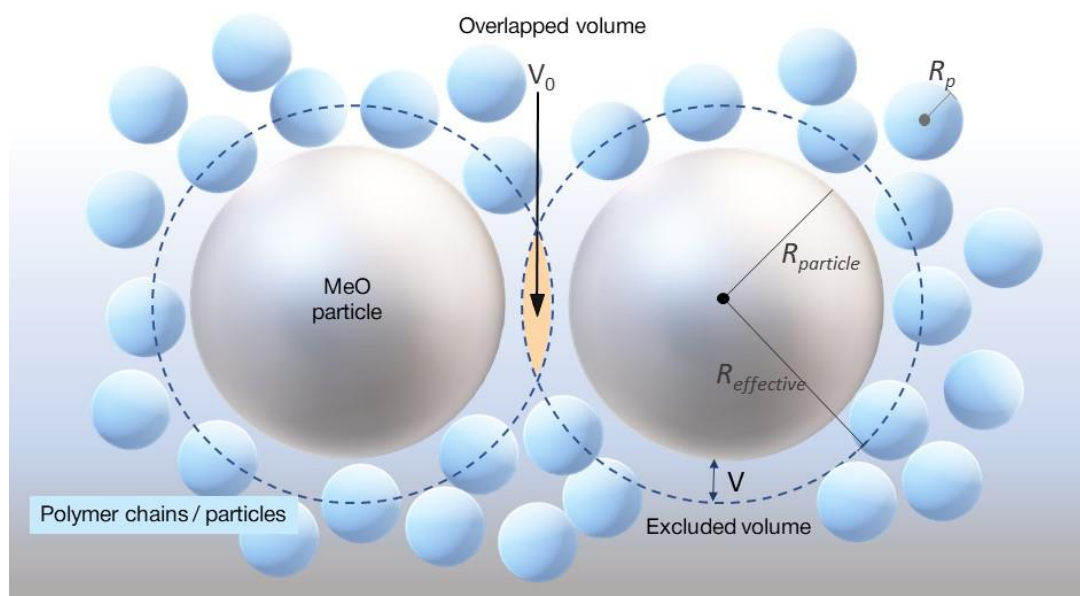
Figure 1.7 Schematic of the attraction between MeO particles (grey spheres) in a polymer solution (indicated by light blue spheres) originating from the excluded volume between the particles themselves and the osmotic pressure induced by the surrounding polymer chains/particles. Image taken with permission from the Ref. [118]
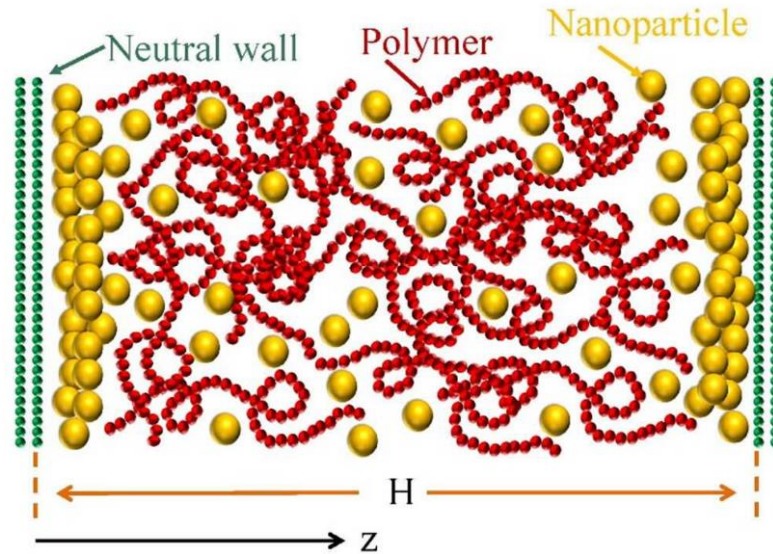
Figure 1.8 Schematic of a thin polymer layer, blended with spherical NPs and a layer of NPs formed at the interfaces. Figure taken with permission from [119].

1.2.6 Entropic interactions for self-healing materials

Damage to a material may lead to the formation of new interfaces, and a migration and aggregation of NPs at this interface can serve for healing of the structure. [123] Thus, entropy can be employed to build structurally complex systems, capable of self-healing. Introducing appropriate enthalpic interactions between NPs and polymeric media can enhance this self-healing effect. [123] Gupta et al. synthesized an auto-responsive hybrid composite based on PMMA, filled with core-shell CdSe/ZnS NPs. [58] The NPs were coated with poly(ethylene oxide) (PEO) which is not miscible with PMMA and therefore the enthalpic interactions between the NPs and the PMMA matrix were fully eliminated. This resulted in a homogeneous distribution of the NPs throughout the polymer. Upon annealing in vacuum at 170°C for 20 hours, the protective thin silicon oxide layer cracked, forming new PMMA/air interfaces (Figure 1.9a). A strong fluorescence in the cracks proved that CdSe/ZnS NPs agglomerated at the cracks (Figure 1.9b). This behavior was facilitated by the absence of interactions between the NPs and the PMMA matrix, and the lower surface energy of PEO compared to PMMA. However, the decisive factor was the entropic penalty inflicted on the PMMA molecular chains by the NPs. At least two times larger fluorescence intensities in the cracks were observed for 5.2 nm-sized NPs, coated with PEO. [58] This shows that particles which are larger than the gyration radius of the polymer impose higher entropic penalties. Tailoring the entropic and enthalpic interactions opens a refined approach towards self-healing of materials.
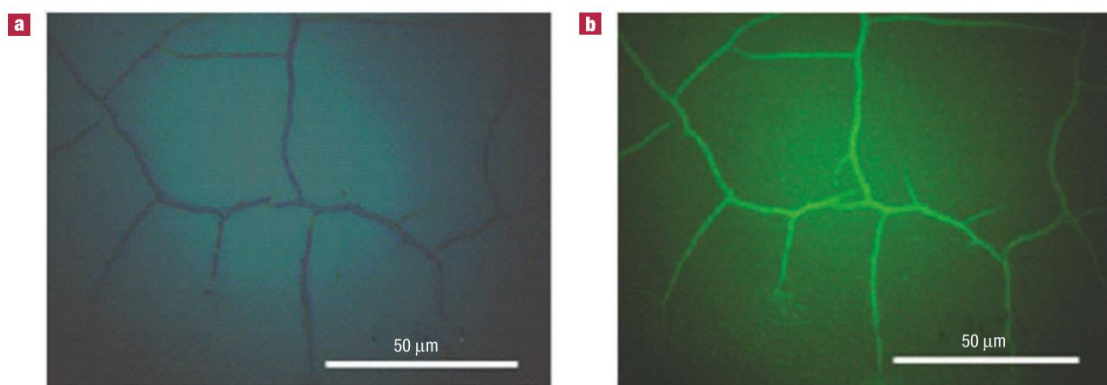
Figure 1.9 Fluorescence microscopy of cracks on the surface of a SiO_x layer on a structure consisting of 3.8-nm-sized CdSe/ZnS particles, coated with PEO and dispersed in a PMMA matrix; (a) Bright-field image (b) Fluorescence image of the same area. Figure taken with permission from Ref [58].

1.3 Objective and structure of the thesis

This thesis aims to develop flexible, transparent, and conductive materials utilizing VPI. To achieve this goal, new hybrid organic-inorganic materials combinations were developed, expanding the list of known VPI processed materials with ParyleneC-based hybrids. The low-temperature infiltration process extends the applicability of the process to more temperature-sensitive polymers.

Since flexible electronic devices are susceptible to tearing, stretching, and puncturing, advances in the development of self-healing transparent conductive oxide (TCO) materials are imperative. The controlled fabrication and investigation of the blends of polymers and metal oxides (MeO) led to the discovery of a new self-healing functionality of the resulting hybrids. This works aims to investigate and gain an understanding of the effect of the NPs´ surface segregation which leads to the self-healing of the metal oxide coatings.

Chapter 2 overviews the main experimental methods used to fabricate and investigate the hybrid materials.

Chapter 3 describes the development of a ParyleneC/In_xO_y hybrid. Approaches for the low-temperature gas-phase deposition of indium oxide are discussed. This work shows that the choice of the oxygen-containing precursor impacts the growth per cycle (GPC) and crystallinity of the resulting films. The structural, optical, and electrical properties of the ParyleneC/In_xO_y hybrid are studied and the applicability of the hybrid structures as flexible electrodes is evaluated.

Chapter 4 focuses on the synthesis and properties of ParyleneC/ZnO hybrids. The infiltration characteristics, structural properties, and the chemical composition of the hybrid are analyzed. The possible mechanism of the precursor reactions with the polymer is discussed based on results of

density functional theory (DFT) calculations. The sizes and the distribution of the NPs within the polymer are studied as it is an indicator of stock material needed for the self-healing process.

Chapter 5 evidences the self-healing mechanisms within the hybrid ParyleneC/MeO structures. Healing is observed for different types of defects and various polymeric substrates. The mechanism of healing is discussed, revealing the necessity of halogen groups that prevent the interaction between the polymeric matrixes and the dispersed metal oxide NPs.

The prospects of this work and the main conclusions of this research are discussed in Summary and outlook chapter.

<div style="text-align: right; font-size: 3em; color: crimson;">2</div>

Experimental techniques and methods

2.1 Vapor Phase Infiltration

2.1.1 VPI fundamentals

Vapor phase infiltration is a chemical process that evolved from the ALD method. ALD became widely applied due to outstanding conformality, a low number of defects, and precise thickness control of the films. The growth of the film starts on functional groups available on the surfaces of materials. However, if applied to polymeric substrates, ALD leads to the subsurface growth of inorganic material, not excluding the formation of a film on the surface. [124] In this case, the interfaces become poorly defined and might even lose the adhesion between the polymer and inorganic thin film. [125] Infiltration, which at first was perceived as a side reaction, appeared to be beneficial for many structures and applications, including imparting diffusional barrier properties, [126] enhancing mechanical toughness, [21] improving etching resistance of lithography resists, [127] altering optical properties, [128] and enhancing the conductivity.[129] This method was introduced first by the group of Knez in 2009. [21] Since this time, it became widely applied and known under different names – vapor phase infiltration, [130] sequential infiltration synthesis (SIS), [131] multiple pulsed infiltration (MPI), [35] sequential vapor infiltration (SVI), [26] or atomic layer infiltration. [126] All these methods are based on the same processes that rely on reactions between gas-phase reactants and the substrate. Therefore, it has been proposed to unify different nomenclatures under the name VPI [130] or even ALD. [124] To promote infiltration into the soft substrates, an exposure step is added to a typical ALD cycle (Figure 2.1). This additional time ensures a diffusion of a precursor molecule into the polymer bulk. ALD and VPI are both based on the same types of sequential chemical reactions, which makes most ALD chemicals applicable for VPI processes. Exceptions may apply for temporally unstable precursors, i.e., molecules which self-decompose within the time period needed for the diffusion (exposure time).
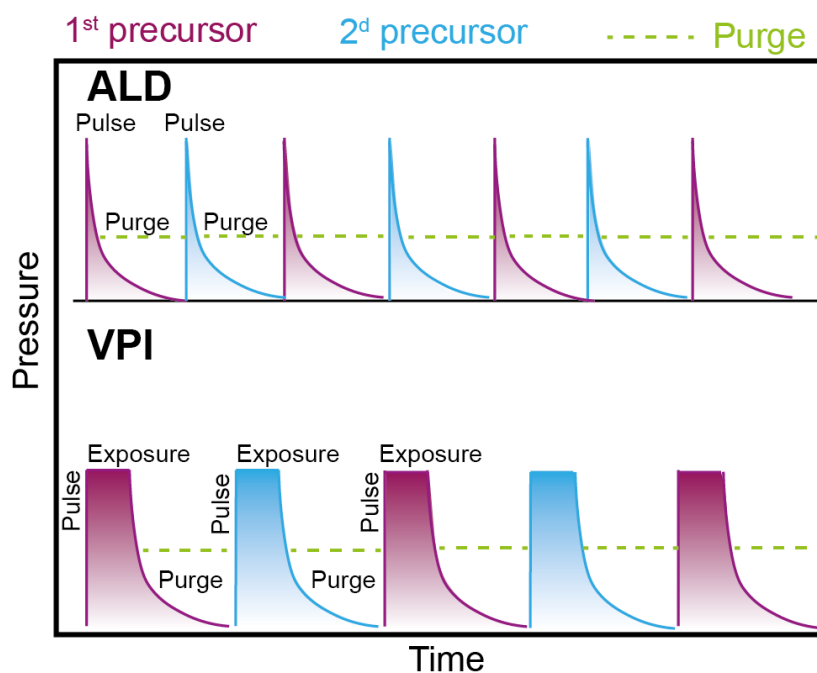
Figure 2.1 Schematic of typical pressure profiles for ALD and VPI processes. The pink, blue and green lines represent the partial pressure of the 1st and 2nd precursors and a carrier/purge gas, respectively. The gas flow is usually kept constant even during the exposure step unless the reactor is hermetically sealed between the pulse and purge sequences. The image is adapted from Ref. [10]

During VPI a polymeric substrate is subjected to sequential pulses of two or more distinct vaporized precursor molecules. The precursors alternately infiltrate the substrate and undergo chemical reactions. The first precursor typically binds to the functional groups on the surface and in the bulk of the substrate, while the second precursor reacts with the first bound precursor, both on the surface and in the bulk. An idealized schematic is shown in Figure 2.2. As a first step, a vaporized metal-organic precursor is pulsed into the reactor. Owing to the free volume of the polymer, the precursor molecules can in-diffuse and chemisorb onto reactive functional sites of the polymer. Even in the case of an inert polymer, the subsurface growth can occur, as the precursor can be physically trapped or physisorbed. [132] After purging, the same procedure is repeated with a second precursor, in our example water, which reacts with the absorbed first precursor forming the corresponding metal oxide in the bulk and on the surface of the polymer. Those two exposure-purge sequences for the two precursors demark one VPI cycle and can be repeated multiple times, thereby adding an increment of inorganic material to the substrate with each cycle. Eventually, an organic-inorganic hybrid material with a MeO coating is obtained, as shown in step 5 of Figure 2.2. Once the coating becomes defect-free and sufficiently thick, it will act as a permeation barrier for the precursors and prevent further infiltration. Continued processing will only add to the outer ALD coating. The fact that VPI is a solution-free process makes it valuable for the post-processing of previously prepared structures or devices. [8]
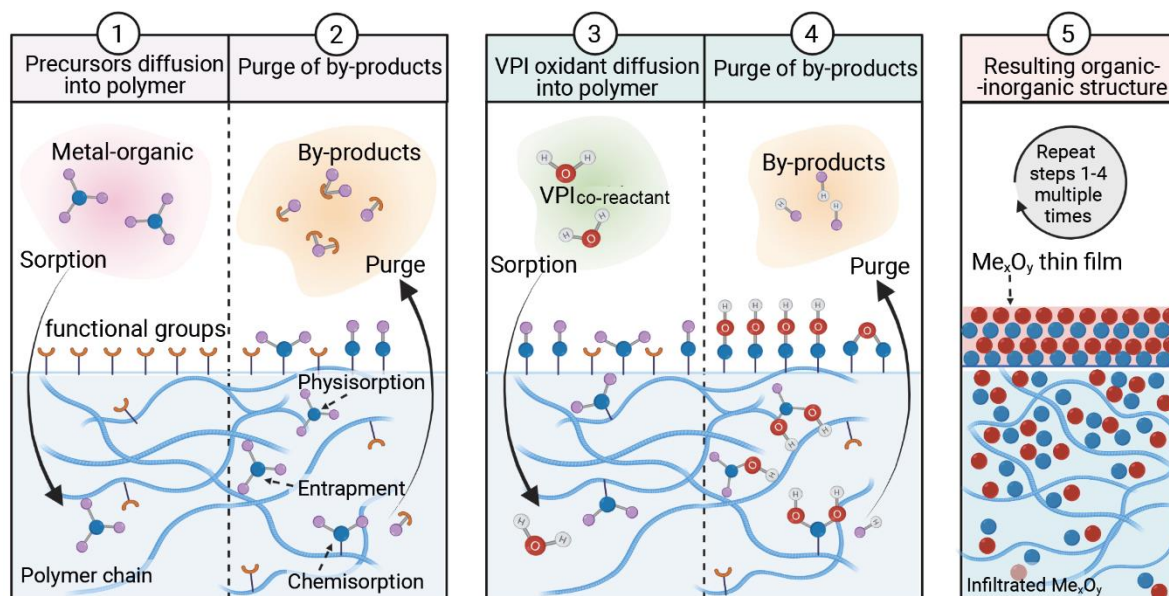
Figure 2.2 Schematic of the organic-inorganic hybrid material fabrication by VPI. Steps 1 to 2 and 3 to 4 indicate the individual exposure and purge steps of the two precursors in one VPI cycle and the sorption, binding, and reaction events during those steps. Step 5 is a schematic of the resulting polymeric hybrid material with a thin film coating and a blended inorganic subsurface. Image taken with permission from the Ref. [118]

There are several factors that affect the infiltration process, including but not restricted to, penetrant size and shape, free volume of the polymer, and precursor-polymer reactivity. A small size of the reactant is preferable to accelerate its diffusion into the polymer. The processing temperature also has a direct impact on the specific volume of the polymer. Heating of the polymer leads to a decrease in its mass density and an increase in the polymer chain volume and the free volume. The free volume of a polymer gains an enhancement upon exceeding its glass transition temperature and therefore facilitates the infiltration of a polymer. Upon cooling of the polymer after the VPI process, the polymer chains "freeze", leaving it in a non-equilibrium state with a fixed free volume. [10] Such kind of "kinetically trapped" free volume depends on the prior processing conditions of the polymer and can be employed for tuning the infiltration process. Interestingly, chemical reactions of a polymer with a precursor might prevent infiltration into the polymer depth due to quick absorption of the precursor and subsequent steric hindrance. In contrast, engineering of a precursor-polymer system with only weak interactions is a route to overcome the diffusion-limited infiltration profiles. [133]

2.1.2 Materials and VPI conditions

We applied VPI to infiltrate the polymers ParyleneC and polyvinyl chloride (PVC) (Figure 2.3 a, b) with zinc, indium oxides and nickel oxides, as well as indium zinc oxide (IZO) and indium tin oxide

(ITO). Besides, several polymers were tested for the self-healing functionality, including PP, PU, PDMS, natural rubber, acrylonitrile butadiene styrene (ABS), PTFE, polystyrene (PS), PET, and PA-6.
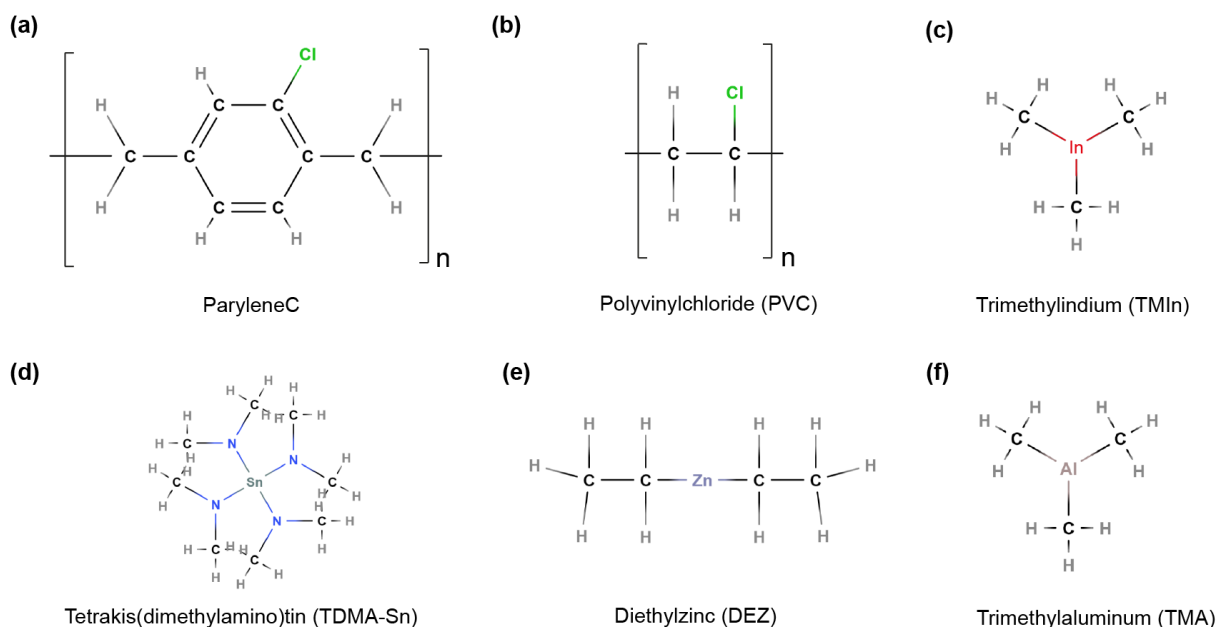

Figure 2.3 Chemical structures of (a) ParyleneC, (b) polyvinylchloride (PVC), (c) trimethylindium (TMIn), (d) Tetrakis(dimethylamino)tin(IV) (TDMA-Sn), (e) diethylzinc (DEZ), and (f) trimethylaluminum (TMA). Image taken with permission from the Ref. [118]

Materials. Free-standing plasma-deposited ParyleneC sheets with a thickness of 30-40 µm were purchased from Plasma Parylene Systems GmbH. PVC substrates with a thickness of 250 µm were purchased from Goodfellow. TMIn with a purity of 98% was purchased from STREM (Figure 2.3 c). Three oxygen-containing precursors were tested, namely purified water (Millipore, 18.2 MΩcm), a 30% aqueous solution of hydrogen peroxide (abcr GmbH) and ozone.

VPI processes. Infiltration was performed in an ALD reactor (Savannah S100; Cambridge Nanotech Inc.). This reactor has a controllable vacuum valve placed between the reactor and the pump which allows for obtaining VPI conditions. The manifold for the precursor supply was heated to 100°C. A continuous flow of nitrogen of 20 standard cubic centimeters per minute (sccm) was supplied through the manifold lines to the reactor during the entire VPI process to prevent backflow of the precursor into the manifold. After VPI, the heating was switched off until the reactor reached 80°C and was maintained at this temperature under a constant flow of nitrogen.

In_xO_y infiltration. Indium oxide infiltration was performed by VPI of TMIn and one of the oxygen-containing precursors: 30% hydrogen peroxide in an aqueous solution, ozone, or water. First, TMIn was pulsed for 0.4 s into the ALD reactor, and the vapor was kept inside the chamber for additional 30 seconds to allow the precursors to infiltrate the polymer. The exposure step was followed by 60

seconds of purging with N_2 gas to remove any unreacted precursor and by-products. The same steps were repeated for H_2O, H_2O_2, or ozone which demarked one infiltration cycle. The temperature was varied from 100 to 210°C. The exposure time was varied from 1 second to 50 seconds. The total number of VPI cycles was 150.

Thermally oxidized silicon substrates were placed into the reaction chamber together with ParyleneC. They served as reference samples for X-ray reflectivity (XRR) and X-Ray diffraction (XRD) studies.

ITO infiltration. The VPI of ITO was performed using TMIn, H_2O_2 and TDMA-Sn as precursors at 200°C (Figure 2.3 d). After every 15th cycle of TMIn/H_2O_2 with the pulse/exposure/purge sequence of 0.4/30/60 sec, one doping cycle of TDMA-Sn/H_2O_2 was performed with the same timing completing a so-called supercycle. In total, the process consisted of 25 supercycles.

ZnO infiltration. The VPI of ZnO was performed with DEZ and 30 % H_2O_2 or H_2O as precursors in the temperature range of 100-210°C (Figure 2.3 e). The pulse/exposure/purge sequence was 0.4/30/60 sec for both precursors. The N_2 gas was kept constant at the level of 20 sccm. The number of cycles was 100, if not stated otherwise.

IZO infiltration. The VPI of IZO was performed using TMIn, DEZ an H_2O_2 at 210°C. After every 9th cycle of TMIn/H_2O_2 one doping cycle of DEZ/H_2O_2 was performed, completing 20 supercycles in total.

Ni_xO_y infiltration. The VPI of nickel oxide (Ni_xO_y) was performed using nickelocene ($NiCp_2$) and ozone (O_3) at 220°C. was sublimed in a bubbler, with nitrogen gas assisting this process. The bubbler was kept at a temperature of 60°C. The pulse/exposure/purge sequence was 5/30/40 sec for $NiCp_2$ and 1/1/20 seconds for ozone to eliminate the impact of ozone on a polymer substrate.

Cl-doped ZnO infiltration. Halogen-doped ZnO infiltration into PDMS and PA-6 was performed by adding a 0.4 sec pulse of $SOCl_2$ after each 7th cycle of DEZ/H_2O, completing 15 supercycles in total.

Al_2O_3 deposition. In this work, alumina was used to create a diffusional barrier and to produce nanolaminates instead of hybrids. For depositing a thin A_2O_3 layer, 100 cycles of TMA/H_2O_2 were applied to ParyleneC at 210°C with the pulse/exposure/purge sequence being 0.2/1/30 sec for both precursors (Figure 2.3 f).

2.2 X-ray Diffraction and Reflectivity

X-ray diffraction (XRD) allows the identification of the crystallinity of a material, its phase composition, quantification of the size of crystallites, etc. An x-ray beam illuminates a specimen and electrons in the material scatter the electromagnetic radiation. Most of the waves undergo

destructive interference, however, a constructive component appears when the X-rays meet the criteria of Bragg's law (Equation 3):

$$n\lambda = 2\text{dsin}\theta \hspace{4cm} \text{(Eq. 3)}$$

Here, θ is the incidence angle of X-rays, d is the lattice spacing, and λ is the beam wavelength. Upon irradiation of a crystal with X-rays, a diffraction pattern consisting of several reflexes is detected. Those reflexes are converted into a model of the electron density of the crystal via Fourier transformation.

X-ray reflectivity (XRR) is surface-sensitive technique that can be realized with a similar setup as XRD. It is a reflectometric method, which analyses the X-ray wave reflected from a crystal at an angle equal to an incident angle. The analysis of the reflected X-rays allows estimation of the thickness, density and roughness of thin layers.

In our work, XRD and XRR studies were performed in the PANalytical X'Pert Pro diffractometer using Cu Kα radiation with the wavelength of λ=1.54 Å. XRR was performed only on the reference samples, i.e., coated Si substrates, due to their lower roughness and well-defined interfaces. The GPC values were calculated from the ratio of the measured film thickness on the Si substrates to the total number of applied VPI cycles for each sample. XRD was measured from both hybrid organic-inorganic and reference samples obtained on Si substrates. The obtained spectra were compared with theoretically calculated powder spectra in the database materialscience.com.

2.3 Electron Microscopy

Electron microscopy is one of the most applicable investigation and visualization techniques for VPI-modified polymers. Infiltrated polymers have a modified layer whose depth varies depending on the type of polymeric substrate, precursors, and process conditions. In many cases the infiltration depth does not exceed 200 nm, which is the limit of the resolution of the optical microscopy as it is directly proportional to the photon wavelength in the visible region (Figure 2.4). Electron microscopy probes a specimen with electrons instead of photons that procure the resolution enhancement. Typical energies of the electrons in an electron microscope lie in the range of 1-30 keV for scanning electron microscopy (SEM) and 60-300 keV for (scanning) transmission electron microscopy ((S)TEM), which allows resolutions better than 1 nm in SEM and better than 50 pm in (S)TEM. SEM and TEM techniques possess high spatial resolution, which is necessary for a precise morphological characterization.

Another advantage of electron microscopy techniques is the interaction of electrons with atoms, which provides additional spectroscopic information from the specimen. For example, electron microscopy gives means for *in-situ* chemical characterization of the sample, such as energy-dispersive X-ray spectroscopy (EDX), Auger electron spectroscopy (AES), or electron energy loss spectroscopy (EELS), aiming at the investigation of the chemical composition of the sample, chemical bonding,
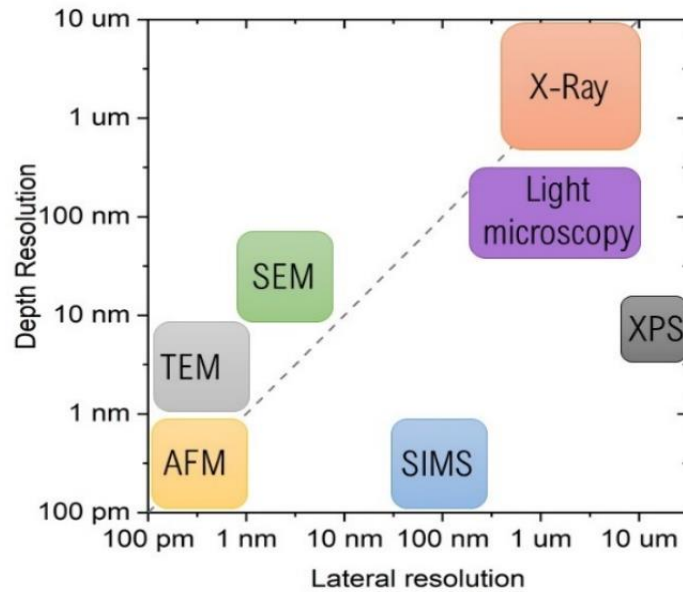
Figure 2.4 Comparison of the typical spatial resolution of different imaging and spectroscopy techniques: AFM, TEM, SEM, SIMS, X-Ray, XPS, and light microscopy.

and the valence state with a high spatial resolution. Information about the chemical composition can also be extracted from the backscattered electrons and electrons scattered at high angles (HAADF STEM). Application of various (S)TEM imaging techniques allows to study the structure down to the atomic level, visualize nanocrystals and clusters inaccessible with other methods, determine their crystal structure and orientation, and precisely measure their size. [134] This thesis employs all the methods indicated in Figure 2.4, except atomic force microscopy.

2.3.1 Scanning electron microscopy

SEM, like optical microscopy, is designed to examine material surfaces. In SEM, an electron beam is focused by condenser lenses to a spot with a diameter of 0.4-5 nm that scans a specimen surface line by line. At each specific surface spot, electrons are emitted from the specimen, which are collected by detectors. The interactions of a primary electron beam with the specimen can be divided into elastic and inelastic interactions.

Inelastic scattering occurs through a variety of interactions between the incident electron beam and electrons of the specimen. These interactions can also lead to the ionization of the specimen, exciting an electron. As a result of the relaxation of excited specimen electrons, the generation of secondary electrons (SE) occurs (Figure 2.5 a). SE do not carry information about the elemental composition. Instead, SE possess high spatial resolution and, therefore, are ideal for investigating topography changes and are used for imaging in high magnification.

Elastic scattering of an incident electron beam occurs on the atomic nucleus or by outer shell electrons of a specific energy. A primary electron loses negligible energy during a collision with a

specimen, but it undergoes a directional change in a wide angle. These electrons are called backscattered electrons (BSE) since the scattering angle is more than 90° (Figure 2.5 b). Since the BSE signal originates from collisions with the atomic nucleus, its intensity strongly depends on the mass of the nucleus. Therefore, it is very utile to represent the mass contrast of the specimen surface. However, the BSE signal arises from the greater depth of a sample and, therefore, its spatial resolution deteriorates.
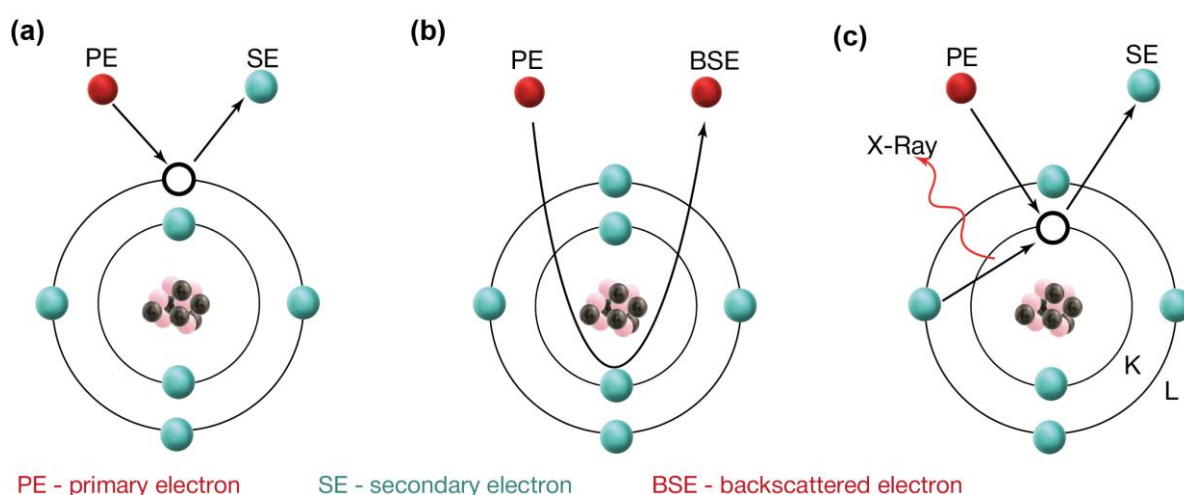

Figure 2.5 Schematic image of emission mechanisms of (a) secondary electrons, (b) backscattered electrons, and (c) characteristic X-ray irradiation from specimen atoms.

In this thesis, a Dualbeam FEI Helios 450s microscope (Thermofisher, USA) (Figure 2.6 a) was used as a multifunctional nano laboratory for morphology investigations, surface modification and patterning, three-dimensional characterization by cross-sectioning, mechanical and electrical testing, and thin sample preparation for the TEM measurements. The Helios 450s is equipped with electron and focused ion beam (FIB) columns, a micromanipulator, an energy-dispersed X-ray (EDX) detector, and a gas injection system for precursors. The electron gun is located perpendicular to the sample stage, while the ion gun is tilted at 38° to the surface and 52° to the electron gun. SEM measurements were performed at different accelerating voltages from 1 up to 5 keV, depending on the conductivity of a specific sample, to decrease the impact of an incident electronic beam on a specimen. Since the interaction of the incident electron beam can damage the chemical structure of a specimen and a high electron dose has the potential to recrystallize amorphous materials, the current of electrons typically didn't exceed 50 pA during imaging.

2.3.2 Energy-dispersive X-ray Spectroscopy

The interaction of electrons with atoms provides additional spectroscopic information from the specimen allowing in-situ chemical characterization of the sample with EDX. Each atom possesses
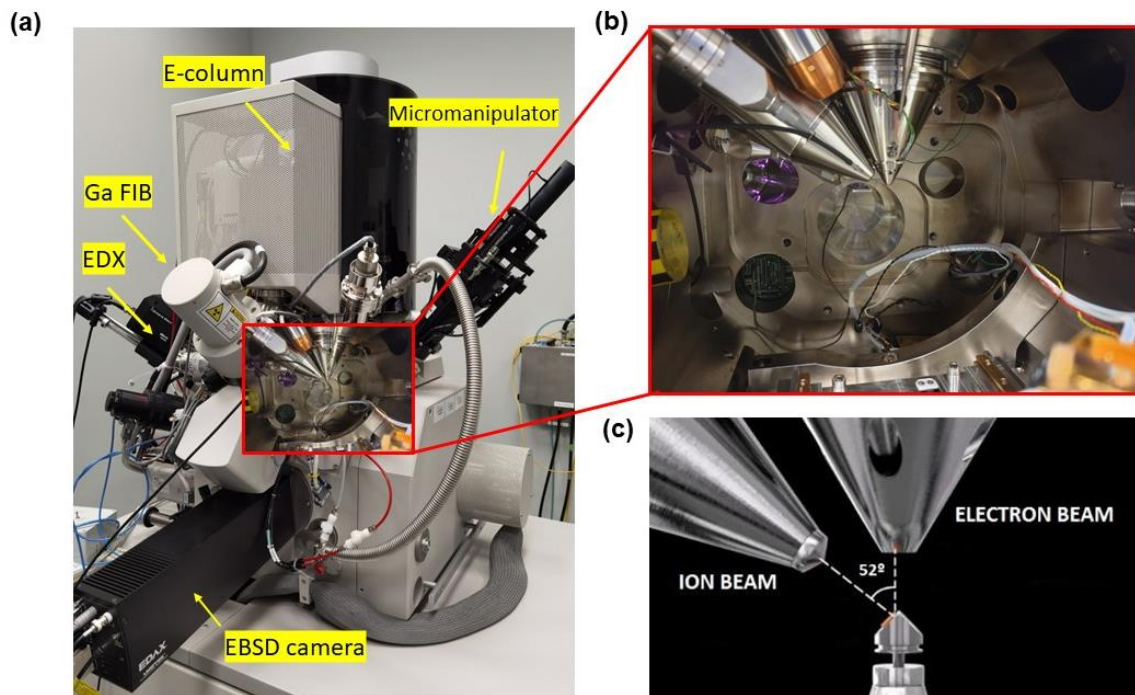
Figure 2.6 FEI Helios 450s microscope (a) Photo of the microscope; (b) photo of the chamber with electron and ion guns; (c) schematic image of the electron and ion guns position in relation to each other and a sample.

electrons at discrete energy levels. Primary (e-beam) electrons can excite and expel the electron from an inner shell, leaving an electron hole behind (Figure 2.5 c). An electron from a higher valence shell fills this hole at the same time generating an X-Ray photon, which is collected by an energy-dispersive spectrometer. The energy of the emitted X-Rays is characteristic of the difference in energy between the two shells and of the atomic structure of the emitting element and therefore allows for the precise identification of the chemical composition of the specimen.

The EDAX Octane Pro detector, installed in the FEI Helios 450s, allows the quantitative measurement of the chemical composition, element depth profiles, and element mapping of the investigated samples. For investigating In, Zn, and Sn-based hybrids the SEM was operated at the beam energy of 10 keV to reach the trade-off between the possibility of exciting the characteristic X-rays and avoiding beam-induced damage or charging artifacts. In TEM, the EDX measurements were performed in STEM using an EDAX SDD detector.

2.3.3 Focused Ion Beam Sample preparation

A focused ion beam (FIB) allows surface imaging, just like SEM. Besides imaging, the FIB also allows *in-situ* thin film deposition and sputtering of a specimen. During ion sputtering, accelerated and

focused ions bombard the surface and precisely remove the upper layers of the material. Furthermore, the FIB can be used to section the specimen for cross-sectional analyses. Examination of a cross-section of an infiltrated sample is the method-of-choice to visualize the hybrid organic-inorganic structure and measure the infiltration depth. To make a sample cross-section the stage should be turned perpendicular to the ion beam, which in our case required a stage tilt of 52° (Figure 2.6 b, c). However, cutting required a specific preparation to eliminate the radiational damage:

First, we applied a conductive carbon layer to increase the contrast between the MeO film and subsequent layers (Figure 2.7 a, b). Non-conductive specimen require an additional conductive layer to diminish the charging effect during FIB preparation. For that, 10-20 nm of a 50%/50% Pt-Au layer was magnetron-sputtered onto the specimen surface.
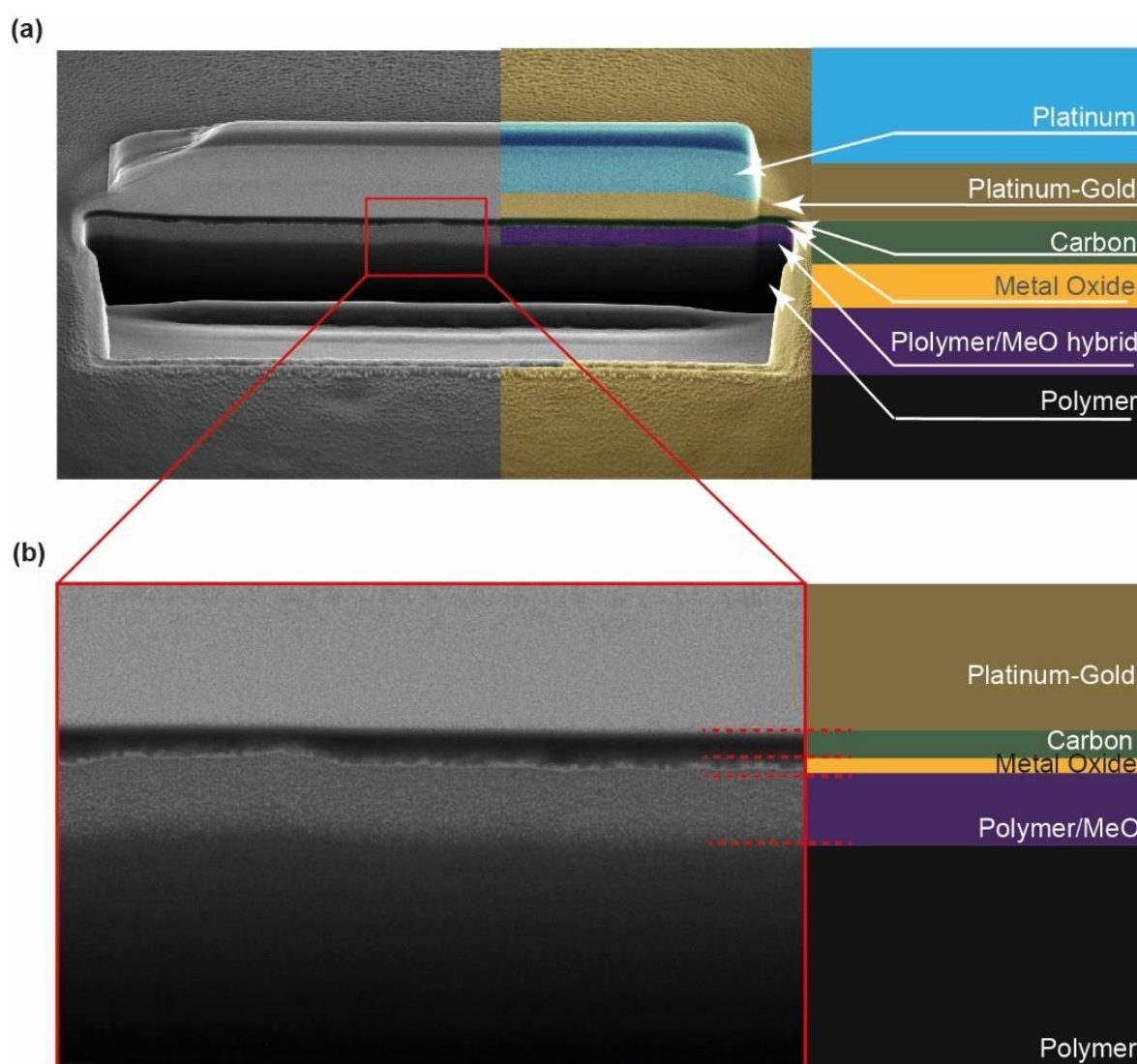
Figure 2.7 (a) Typical FIB cross-section of a polymer/MeO hybrid with a designation of the different layers. (b) Magnified image of the section highlighted with a red square in (a).

Second, a protective platinum layer was locally deposited with electron and ion beams to preserve the specimen surface from FIB-sputtering. This Pt layer is deposited inside the SEM/FIB chamber directly in the area of interest. For that, a precursor gas trimethyl(methylcyclopentadienyl) platinum(IV) ($MeCpPtMe_3$) is injected into the SEM/FIB chamber. Then, the surface is scanned with electron or ion beams, causing the precursor to decompose, thus forming the film selectively in the irradiated area. The ion current should be optimized to not etch the sample surface simultaneously with the precursor decomposition. After the formation of the protection layers, the FIB bulks out the volume of material, forming a cross-section with an ion voltage of 30 kV, and a current of 1-2.5 nA. On a typical cross-section presented in this thesis, there are Pt, Pt-Au (optional), C, MeO, polymer MeO, and polymer layers, as shown in Figure 2.7 a. Normally, the thin MeO film is separated with from a polymer/MeO hybrid with a pronounced border. In contrast, the hybrid organic-inorganic part decreases gradually and does not form a sharp interface.

FIB allows precise etching, making a lamella fabrication for TEM investigations possible. As a first step, the Pt layer with dimensions of about 15µm (X) x 1.5µm (Y) x 200nm (Z) is deposited using the $MeCpPtMe_3$ precursor and an electron beam. The accelerating voltage of electrons is typically 5 kV at currents of 1.4 nA. This layer protects the sample surface from the following Pt deposition by ions. In the second step, the stage is tilted to 52° to be perpendicular to the ion beam and a thicker Pt layer with dimensions of 15µm (X) x 1.5µm (Y) x 1.5 µm (Z) is deposited with the ion beam (Figure 2.8 a). The ion current varies between 93 pA - 0.28 nA at an acceleration voltage of 30 kV to have a decent Pt deposition rate but not damage the surface. Next, higher ion currents of 1-2.5 nA are used to perform staircase bulk-out etching (Figure 2.8 b). The typical etch depth is 6-8 µm to facilitate the following lamella extraction. The stage is placed back to a tilt of 0° to make a U-cut to free the lateral sides of the lamella. After that, the OmniProbe is inserted into the SEM chamber and placed in a contact with the Pt layer (Figure 2.8 c). After conjugation of OmniProbe and lamella with a Pt deposition, the lift-out process can be performed. Then, the OmniProbe Copper 3-Post Lift-Out Grid is positioned in the eucentric position of the chamber. The OmniProbe with the sample is inserted and placed in a contact with the grid (Figure 2.8 d). The sample is connected to the grid by ion deposition and cut from the OmniProbe. The stage is again tilted between 50-54° degrees to thin down the specimen from both lateral sides with an ion current of 0.46 – 1.0 nA and a beam energy of 30 keV until the thickness of the lamella reaches less than 100 nm thickness (Figure 2.8 e). The final cleaning of the lamella is performed with smaller ion beam energies of 2-5 keV and currents of 28-46 pA (Figure 2.8 f). A typical indication of an appropriate thickness for TEM investigations is the "shining" of the lamella in SEM, meaning that electrons can pass through it (Figure 2.8 f).
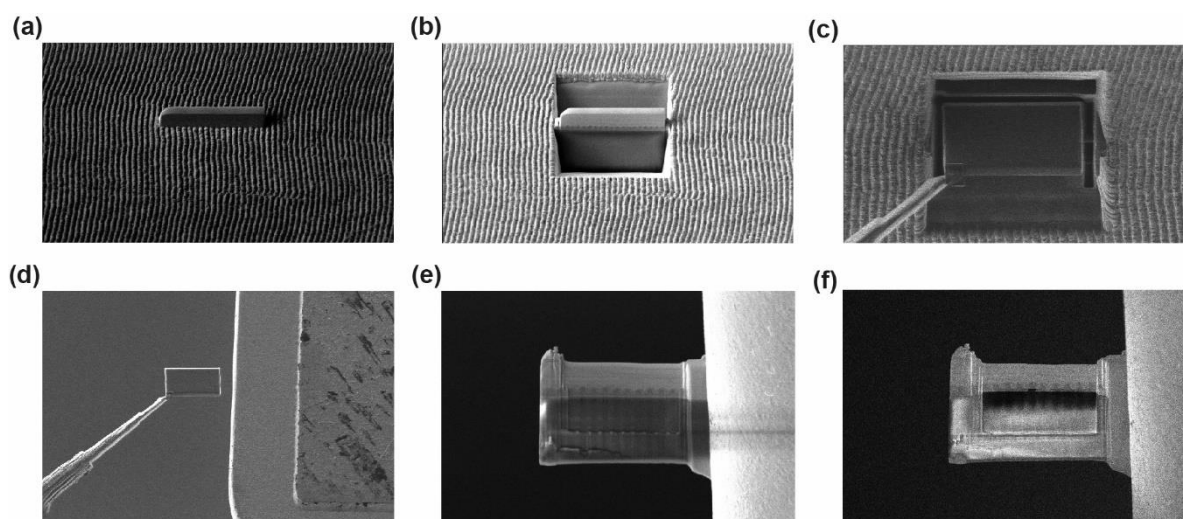
(a) **(b)** **(c)**

(d) **(e)** **(f)**

Figure 2.8 Steps of lamella preparation with a FIB: (a) Ion deposition of a Pt layer; (b) bulk-out sputtering of material; (c) U-shape cut and lift-out process with OmniProbe; (d) mounting of lamella on Omnigrid; (e) thinning, and (f) thinned and cleaned lamella.

2.3.4 Healing experiments

Apart from lamella fabrication and cross-sectioning, FIB served for etching patterns on the sample surfaces for the healing experiments. By sputter-etching the inorganic film from the surface (a few tens of nanometers), the hybrid organic-inorganic material beneath was exposed to ambient conditions. In other words, defects were produced in a controllable manner by FIB. The ion current varied between 40 pA and 0.4 nA, and the accelerating voltage was 30 keV.

To exclude possible radiation impact on a sample, we conducted additional experiments without the involvement of the ion beam etching. For that, we used the OmniProbe micromanipulator inside the SEM vacuum chamber to mechanically scratch the surface in a tractable way.

2.3.5 Transmission Electron Microscopy

When the thickness of a specimen is sufficiently low (typically less than 100 nm), high-energy electrons can transmit through it. On their trajectory within the sample, these electrons interact with the electron densities and nuclei of the material bulk. They get collected by a detector behind the specimen, i.e., by a CCD camera in TEM mode or angular/circular diodes in dark/bright field STEM modes. The accelerating voltages for TEM are higher than for SEM and are typically 80-300 keV as the electrons need sufficient energy to pass through the specimen. The lateral resolution of the TEM is less than 1 Angstrom and allows for examination of the material´s crystalline structure. In this thesis, TEM measurements were performed with a Titan 60-300 (Thermo Fisher Scientific, USA), equipped with an objective lens aberration corrector (Cs-corrector, CEOS), operated at the

accelerating voltage of 300 kV. The images were taken in standard bright field TEM or high-resolution TEM (HRTEM) modes, while STEM was used for chemical profiling or mapping. The TEM images were processed and quantified using the Gatan Digital micrograph software.

2.4 X-Ray Photoelectron Spectroscopy

X-ray Photoelectron Spectroscopy (XPS) is an electron spectroscopy technique that allows the investigation of the elemental and chemical state of an outer 5-10 nm of a solid specimen. XPS evolved from the photoelectric effect formulated by Hertz on the emission of electrons when electromagnetic radiation hits a material. It causes the emission of the electrons in random directions, however typically only electrons that escape from the sample into the vacuum can be detected. Other electrons must travel through the medium of the sample, where they undergo inelastic collisions, recombination, excitation of the sample, or trapping, which significantly lowers the number of escaping photoelectrons. Electron scattering within a material makes XPS a surface technique, with the exponential drop of the electron signal moving from the surface into the bulk of the material. Measuring the energy of the emitted electrons ($E_{kinetic}$) with a hemispherical electron detector allows calculating the binding energy ($E_{binding}$) of the electrons in the sample using the following Equation 4:

$$E_{binding} = E_{photon} - E_{kinetic} - \Phi_{sp} \qquad \text{(Eq. 4)}$$

where Φ_{sp} is the work function of the spectrometer, and E_{photon} is the energy of an incident photon. Since the chemical environment of an atom affects the electron binding energies, XPS allows analyzing the chemical surrounding of an atom of interest. Each element produces few characteristic peaks, that resemble the electronic configuration of the atom. The peak intensity depends on the element concentration in the studied volume; however, the relative sensitivity factor of each element has to be considered. Combined with a sputtering system, XPS becomes a powerful tool for investigating the changes in the chemical state of a specimen with depth as spectra can be recorded after each etching step.

XPS has been measured by Dr. Iva Šarić Janković and Prof. Mladen Petravić in the department of Physics at the University of Rijeka, Croatia. The spectra shown in Figure 5.19 were measured by Dr. Maxim Ilyin and Dr. Celia Rogero at the Materials Physics Center (CFM) of the Spanish national research council (CSIC) in San Sebastian, Spain. The chemical composition of the hybrid samples in this thesis was studied by XPS with a SPECS instrument equipped with a source of monochromatic Al Kα X-rays (E_{photon}=1486.7 eV). To study the state of chemical elements in the bulk of the hybrid, the surface material was removed by sputtering with a low-energy argon ion beam of 2 keV and a current of 10 µA. Since the conductivity of the hybrid is expected to alter with the etching depth, electron beam flooding was employed to neutralize possible charge accumulation. The pass energy was 50 eV for all survey scans and was reduced to 10 eV for the high-resolution

scans. The analysis of the XPS spectra was performed with the Casa XPS software. Binding energy correction was done with respect to the C 1s peak, positioned at a binding energy of 284.8 eV related to the organic carbon originating from the polymeric substrates. The spectra were fitted with sets of Gaussian-Lorentzian functions with Shirley background subtraction.

2.5 Secondary Ion Mass Spectrometry

Secondary Ion Mass Spectrometry (SIMS) is a method of determination of the chemical composition of a solid material via the detection of the secondary ions. Those ions are emitted from the sample surface when it is irradiated with the primary ion beam. Primary ions hit a sample, breaking the bonds between atoms, and setting them in motion. These atoms have enough kinetic energy to bring this impulse further, causing a cascade collision reaction. Freed atoms and molecular fragments are generated within the first 2-3 monolayers of a solid. Although most of the removed particles and molecular fragments from the sample are neutral, a percentage of these is positively or negatively charged. The relation of their mass to their charge M/Z is detected, and the positive or negative mass-spectra of the secondary ions can be plotted. O^- primary ions are used when an increased sensitivity towards the positive ions is desired. Cs^+ primary ions enhance the output of the negative secondary ions. Using the primary source with a large mass number facilitates the detection of the secondary ions of larger mass, which makes it especially useful for investigating organic samples. SIMS allows the determination of the chemical composition with outstanding elemental detection limits ranging from parts per million to parts per billion.

SIMS has been measured by Dr. Robert Peter and Prof. Mladen Petravić in the department of Physics at the University of Rijeka, Croatia. In-depth profiling of oxygen, indium, carbon, and chlorine in the ParyleneC/InxOy hybrid was done with a quadrupole-type SIMS instrument (Hiden SIMS Workstation) using a beam of Cs^+ primary ions of 5 kV and 20 nA and collecting O^-, InO^-, C^-, and Cl^- secondary ions.

2.6 Resistance measurements

2.6.1 Van der Pauw resistance measurements

The sheet resistance of the samples was measured using the Van der Pauw method. [135] It evolved from the four point-probe method, which is one of the most commonly used methods to measure resistance in semiconductor research. Instead of placing the four contacts in one line, the Van der Pauw method applies to specimens with arbitrary shapes and is suitable for the arbitrary placing of the four probes labeled A, B, C, and D (Figure 2.9 a). [135] The theory behind assumes that contacts

are ideal point contacts of infinitely small sizes that are placed onto a semi-infinite volume of an isotropic material of a uniform temperature.

(a)   **(b)**
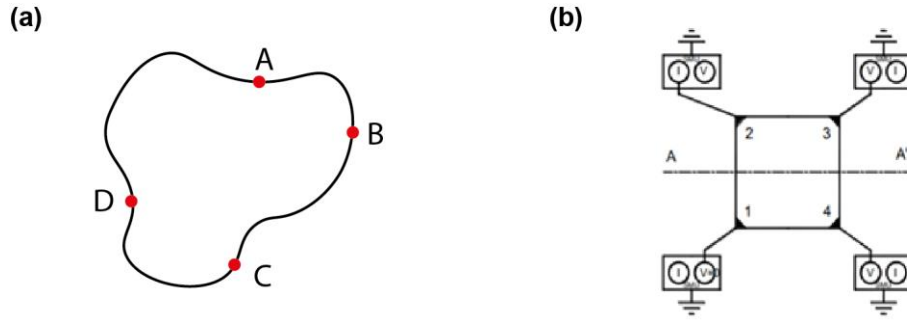

Figure 2.9 (a) Samples of arbitrary shape with four small contacts at arbitrary places for the measurement of the specific resistance by the Van der Pauw method. (b) Set-up for a Van der Pauw measurement for a square shaped sample. An SMU is connected at each contact. The image is taken with permission from the Ref. [136].

Van der Pauw's method gives the following equation for a flat sample of arbitrary shape:

$$exp\left(\frac{-\pi d R_{AB,CD}}{(\rho_x \rho_y)^{1/2}}\right) + exp\left(\frac{-\pi d R_{BC,AD}}{(\rho_x \rho_y)^{1/2}}\right) = 1 \qquad \text{(Eq. 5)}$$

where d is the thickness of the film and $(\rho_x \rho_y)^{1/2}$ is the specific resistance of the material, which is written in the following as ρ. The resistance $R_{AB,CD}$ is defined as the potential difference V_D-V_C between the contacts D and C per current through the contacts A and B. The resistance $R_{BC,DA}$ is defined in analogy. [135] Newton's iterative method for the solution of non-linear equations is effective in solving this equation for ρ:

$$f(\rho) = exp\left(\frac{-\pi d R_{AB,CD}}{\rho}\right) + exp\left(\frac{-\pi d R_{BC,DA}}{\rho}\right) - 1 = 0 \qquad \text{(Eq. 6)}$$

If we define ρ_0 as the initial approximation for the equation (6), the following approximations are found by the iteration

$$\rho_{n+1} = \rho_n - f(\rho_n)/f'(\rho_n)$$

Setting α for $exp\left(-\pi d R_{AB,CD}/\rho_n\right)$ and β for $exp\left(-\pi d R_{BC,DA}/\rho_n\right)$ we can find $(\rho_x \rho_y)^{1/2}$:

$$\rho_{n+1} = \rho_n - \frac{\rho_n^2(\alpha+\beta+1)}{\pi d(\alpha R_{AB,CD}+\beta R_{BC,DA})} \qquad \text{(Eq.7)}$$

W. Price extended the Van der Pauw method for a flat anisotropic material with one of the principal axes out of the plane of the sample so that there is no current flow in the direction perpendicular to

the sample. [137] He showed that for a rectangular shape with four electrodes placed on the sample corners the ratio $(\rho_x/\rho_y)^{1/2}$ can be calculated:

$$(\rho_x/\rho_y)^{1/2} = -\frac{b}{a\pi} \ln\{tanh[\pi d R_{BC,DA}/16(\rho_x\rho_y)^{1/2}]\} \qquad \text{(Eq. 8)}$$

, where a and b are the length of the rectangle, and their ratio equals 1 in the case of a square sample. The schematic setup is depicted in Figure 2.9 b. By solving equations (7) and (8) it becomes easy to find the individual values of the principal resistivities for a square shaped sample:

$$\rho_x = (\rho_x\rho_y)^{1/2} \times (\rho_x/\rho_y)^{1/2}$$

$$\rho_y = (\rho_x\rho_y)^{1/2} \div (\rho_x/\rho_y)^{1/2} \qquad \text{(Eq. 9)}$$

However, in the case of a thin (d<<a) isotropic sample of a square shaped sample, the equation for the specific resistance can be simplified to

$$\rho = \frac{U}{I}\frac{\pi}{ln2}d = dR_{\square} \qquad \text{(Eq. 10)}$$

Where $R_{\square}$ is the sheet resistance. In contrast to the specific resistance, it doesn't require the knowledge of the thickness of the conducting film on a dielectric substrate, which makes it a method of choice for the measurement of hybrid materials with a gradual density.

In our study, the sheet resistance of the hybrid materials was measured using the Van der Pauw method with a Keithley 4200-SCS characterization system. The samples were square shaped with dimensions of 1 x 1 cm and silver contacts (Leitsilber 200 conductive paint) were applied to the corners of the squares (Figure 2.10). The measurements were performed in ambient air at room temperature. The values of the $R_{\square}$ were found upon solving the Equations 8 and 9.

Figure 2.10 Photo of the Van der Pauw measurement setup.

Measurements of persistent photoconductivity (PPC) were conducted in the same setup. Irradiation was performed with a UV diode lamp with a main wavelength of 365 nm in ambient conditions.

2.6.2 Multiple bending tests

To study the changes in electrical properties upon mechanical damage, Van der Pauw measurements were repeated after multiple mechanical bending of a sample. Bending of ParyleneC/In$_x$O$_y$, ParyleneC/IZO, and ParyleneC/Al$_2$O$_3$/IZO was performed with a home-built bending device with a bending radius of 5.5 mm (Figure 2.11). The samples were square shaped with sizes of 1x1 cm and had contacts at the corners applied with silver paste. They were glued onto a rubber rotary stage with adhesive tape. The stage had an optical sensor used as a counter which recorded the number of rotations. This number and, therefore, the number of bending events was controlled by a script via Bluetooth. After a defined number of bending events, Van der Pauw measurements were conducted without detaching the sample from the rotary stage to not induce additional mechanical damage. All bending experiments and measurements were performed in air.
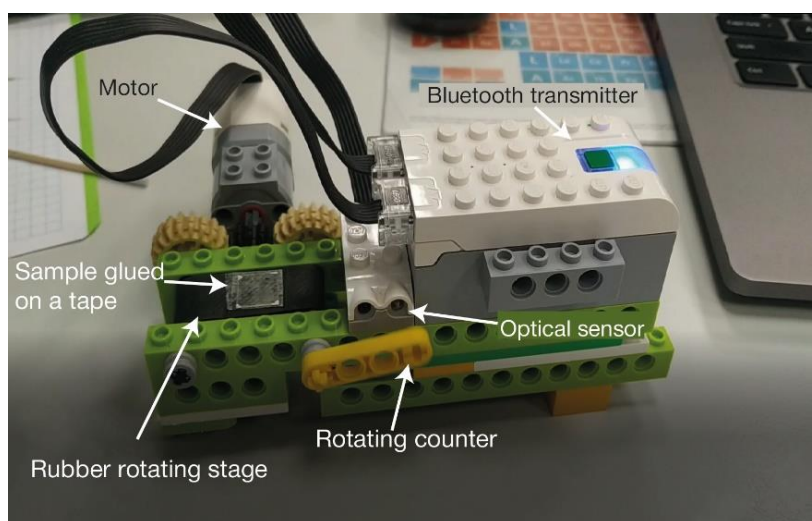
Figure 2.11 Home-built continuous bending tool.

2.6.3 Two-probe resistance measurements of a micro-sized stripe

Resistance measurements of a micro-sized stripe were performed inside the FEI 600 microscope chamber (Figure 2.12). A FIB at an accelerating voltage of 30 kV and a current of 6.5 nA was used to sputter-etch a 70 nm-thick ITO thin film from the surface of the hybrid, leaving behind a 190x35 μm sized conductive stripe, isolated with dielectric ParyleneC. Two Kleindiek Nanotechnik microprobes were placed at the two ends of the ITO stripe. A Keithley 2612A was used to apply a current of 10 μA and measure the resulting voltage. The probes were placed directly on the surface

of the ITO without the deposition of additional contacts. While measuring the resistance, the ITO stripe was cut into two halves by the FIB. The change in resistance was measured during venting of the chamber, i.e., exposure of the sample to ambient air.
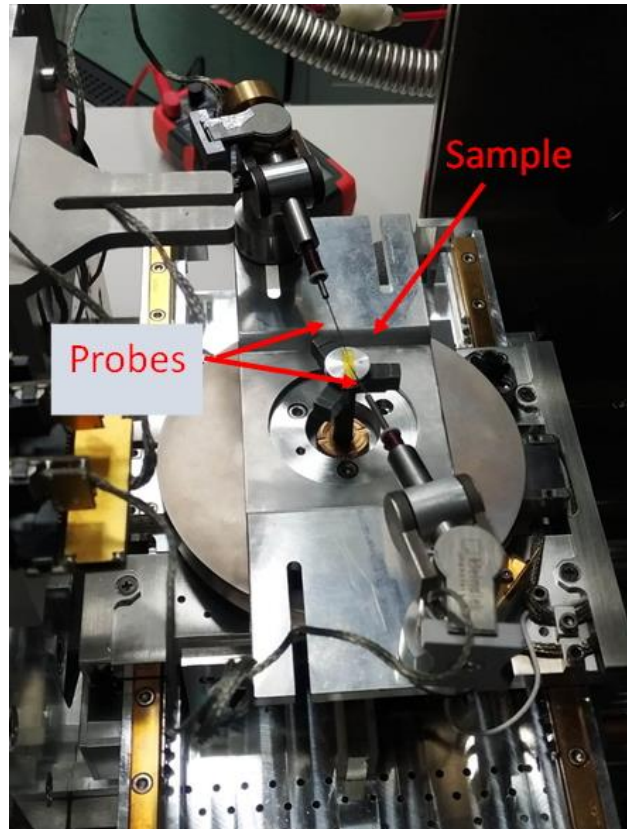
Figure 2.12 Photo of the experimental setup for the electrical resistance measurements inside the microscope chamber of a FEI 600 electron microscope. Image taken with permission from the Ref. [118]

2.7 Ultraviolet-Visible Spectroscopy

In this thesis, Ultraviolet-Visible Spectroscopy (UV-VIS) refers to absorption spectroscopy. UV-VIS spectroscopy is an important technique to determine the band gap of semiconductors. The absorption coefficient α and the photon energy hν are related through:

$$(\alpha h\nu)^{1/\gamma} = A(h\nu - E_g)$$
(Eq. 11)

where h is the Planck constant, ν is the photon frequency, E_g is the bandgap, and A is a proportional coefficient. The factor γ reflects the nature of the electron transition and is equal to ½ or 2 for direct

and indirect transition band gaps. [138] The factor γ was taken ½ as for direct allowed transitions when applied to indium oxide-based samples. [139]

The optical absorbance of the ParyleneC/MeO hybrids from 200 to 700 nm was measured with a NanoDrop 2000c spectrometer from Thermo Scientific. The binding energy values were extracted from the corresponding Tauc plots.

2.8 Attenuated total reflection Fourier-transform infrared spectroscopy

Infrared (IR) spectroscopy is a non-destructive method to probe molecular vibrations. For the analysis of the fundamental vibrations and associated rotational-vibrational structures, mid-infrared spectroscopy in the range from 4000 to 400 cm^{-1} is applied. Functional groups have characteristic absorption bands, thus measured absorption bands can be assigned to those. Typically, vibrations are infrared active if there is a change in the dipole moment, meaning that symmetric vibrations are not detectable with infrared spectroscopy. Detection of all asymmetric vibrations allows the investigation of almost all chemical groups in a sample and makes IR spectroscopy a powerful tool especially for investigating organic samples. These include vibrations along chemical bonds or stretching vibrations (ν) and vibrations associated with changes in bond angles – bending vibrations (δ – in plane, and π – out of plane).

The development of the IR technique led to the Fourier transformation infrared spectroscopy (FTIR), the main advantage of which is the enhanced measurement rates. It is achieved by simultaneous measurements of all IR frequencies. In FTIR spectroscopy, the IR beam is split into two using a Michelson interferometer. One of the beams is conducted towards a fixed mirror, and another propagates towards a moving mirror. The beams undergo a different path so that they, when recombined, interfere. The recorded interferogram represents the light output as a function of the actual mirror position. Fourier transformation of the obtained interferogram provides a spectrum of light absorption plotted versus the infrared frequency.

To study only the near-surface area of material of interest, the attenuated total reflectance (ATR) technique can be applied. ATR relies on the total internal reflection of light inside an ATR crystal, resulting in an evanescent wave atop the crystal. The evanescent wave penetrates the media to the depth in the order of magnitude of the wavelength of the incident beam, which is typically between 0.5 and 2 µm. The evanescent wave is attenuated in the characteristic regions of molecular vibration of the sample it experiences and then exits the crystal towards the IR detector. The crystals for the evanescence wave propagation are made from materials with a higher reflective index than that of the sample, such as germanium, silicon, or diamond.

Attenuated total reflection Fourier-transform infrared spectroscopy (ATR-FTIR) was measured with a PerkinElmer Frontier spectrometer. Every spectrum consists of 30 averaged scans from 4000 to 530 cm^{-1} with the resolution of 4 cm^{-1} at least three times for each sample.

2.9 Density functional theory calculations

DFT calculations were performed by our collaborators Arbresha Muriqi and Michael Nolan from the Tyndal National Institute, Cork, Ireland. The reaction thermodynamics of the VPI reactions were computed with DFT using the Vienna Ab initio Simulation Package (VASP) version 5.4. [140] The model for the polymer is a supercell composed of two Parylene C chains, each with a total of six rings. As precursors for the VPI process vaporized H_2O_2 and TMIn for the TMIn-based VPI system and H_2O_2 and DEZ for the DEZ-based VPI system were used.

The exchange−correlation functional is approximated by the Perdew−Burke−Ernzerhof general gradient approximation functional. [141] The valence electrons are described using the projector augmented wave potentials and the valence electronic configurations of the atoms used in these calculations are In: s^2p^1, Zn: $d^{10}p^2$, O: s^2p^4, Cl: s^2p^5, C:s^2p^2, and H:s^1. [142] The geometry was optimized by relaxing the ionic positions using an energy cut-off of 550 eV, with convergence in the energy of 1×10^{-4} eV and 2×10^{-2} eV/ Å in the forces. A Gamma-centered k-point sampling grid of $(3 \times 3 \times 1)$ is used. The computed equilibrium lattice parameters are a = 41.40 Å, b = 20 Å, c = 15 Å and $\alpha = \beta = \gamma = 90°$.

The energies were calculated for precursor incorporation and for further reactions of the precursors within the ParyleneC model using the following equation:

$$E_{int} = \sum E_P - \sum E_R \qquad \text{(Eq. 12)}$$

where E_P = energy of products and E_R = energy of reactants. E_{int} signifies an exothermic interaction and therefore stays for the favorable interactions. Within a class of similar reactions, those are more exothermic have more negative energies. To compute E_{int}, van der Waals interactions were also employed using the DFT-D3 parameterization. [143]

3

Indium oxide-based hybrid materials

Hybrid materials have the potential to outperform conventional material classes and therefore various routes for their synthesis are being explored. However, despite the enormous recent synthetic progress, the pool of successfully hybridized materials is still very limited, thereby lowering their practical applicability as the functionality of the materials relies on the choice of the organic and inorganic constituents and their interplay. Along with deepening the understanding of the physics and chemistry behind VPI, [10] a variety of hybrid material systems have been developed. The infiltrated inorganic compound of the fabricated hybrid systems is typically a metal oxide [144] such as Al_2O_3, [145] TiO_2, [128] ZnO, [35], [146] SnO_2, [147] WO_x, [148] VO_x, [149] Ga_2O_3, [133] or In_2O_3. [133]

The latter mentioned In_2O_3 is of paramount importance for the electronics industry, as it is the key component in materials used for transparent electrodes, especially in ITO or IZO. [150] Indium oxide (In_2O_3) is a well-known n-type semiconductor with high optical transparency and excellent chemical stability. It has, therefore, been applied in a number of optoelectronics applications, for example as TCOs in flat panel and touch screen displays [151] and in thin-film transistors, [152] solar panels [153] smart windows, [154] or biosensors. [155] Indium oxide films can be fabricated in numerous ways; however, ALD brings about benefits in terms of conformality and precision of the coating. [156] A key-limitation for TCOs is their brittleness. This drawback can potentially be tackled by formation of a hybrid structure, composed of indium oxide and a flexible polymer. Merging the conductivity of indium oxide with the flexibility of a polymer may result in an attractive solution for reliable electrodes in flexible electronics.

The first published works on In_2O_3 infiltration used a PMMA host matrix. [28], [133], [157] PMMA, having a low melting temperature, doesn't allow annealing of the system for enhancing the conductivity of In_2O_3 without being destroyed. Therefore, the resulting electrode after annealing will be inorganic indium oxide with poor mechanical flexibility. A hybrid material should reflect a synergy of both the organic and inorganic counterparts and therefore the choice of a polymeric substrate with higher thermal stability for infiltration with In_2O_3 may be a valid route towards flexible conductive hybrid fabrication.

ParyleneC is a polymer of the family poly(p-xylylene), however, with one hydrogen atom on each phenyl ring being substituted by chlorine. [158], [159] It is an exceptionally thermally stable polymer that can resist temperatures of up to 200°C in air and up to 500°C in vacuum. [160] Its physical characteristics made ParyleneC a suitable substrate for flexible electronics [158] due to its flexibility and pronounced moisture barrier properties, [161] while its low dielectric constant made it applicable as a gate dielectric in organic field-effect transistors, [162] organic thin-film transistors, [163] non-volatile memories [164] and biomedical sensors. [165] Still, ParyleneC acts as a passive substrate in all those cases and widening its application range by introducing new properties is desired. The most promising approach is hybridization with inorganics, as outlined before.

3.1 Low-temperature deposition of In_xO_y

For an ALD deposition of indium oxide, a selection of metal-organic precursors can be used. For VPI restrictions for the processing temperatures occur as most polymeric substrates have a low thermal tolerance. This limits the applicability of the precursor candidate indium chloride due to its high thermal budget. [166], [167] Another limiting factor is the size of the precursor molecules. The diffusion constant was shown to decrease exponentially with the increase of the diameter of spherical molecules, [168] therefore, a further crucial condition for VPI is to use the smallest possible precursor molecules. This condition eliminates most of the literature-reported precursors, such as cyclopentadienyl indium, [169] diethyl[1,1,1-trimethyl-N-(trimethylsilyl)silanaminato]-indium (INCA), [170], [171] (dimethylamino-kN)propyl-kC]dimethyl-Indium (DADI), [170] and tris(1-dimethylamino-2-methyl-2-propoxy)indium [172] from the precursor selection.

Trimethylindium (TMIn) is a metal-organic precursor which was successfully used in indium oxide ALD processes. [139], [156], [173], [174] The proposed reaction scheme for TMIn and H_2O was following [174]:

$$InOH^* + In(CH_3)_3 \rightarrow In-O-In(CH_3)_2^* + CH_4 \qquad (Eq. 13)$$

$$InCH_3^* + H_2O \rightarrow InOH^* + CH_4 \qquad (Eq. 14)$$
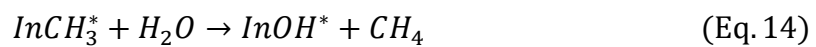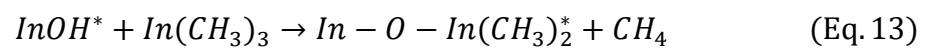
The ALD processing window is around 200-250°C for the TMIn/H_2O ALD process [173] and for processing temperatures below 200°C, ozone was applied. [139] Surprisingly, under SIS (aka VPI) processing conditions instead of ALD, meaning application to polymeric substrates with a significantly extended precursor residence time in the reaction chamber, the indium oxide grew inside the PMMA with water [28] or H_2O_2 [157] as counter precursors already at temperatures as low as 80°C. A possible explanation for the low-temperature growth is the overcoming of the slow reaction kinetics of In-$(CH_3)^*$ groups with an oxidant for prolonged exposure times during the VPI process. [133] Another possible explanation might be based on a slow autocatalytic decomposition of the precursor [175] and a resulting slow parasitic chemical vapor deposition (CVD) process. The small size of the TMIn molecule and its reactivity below 200°C promise good performance for infiltrating ParyleneC.

First, we evaluated the process performance with the three precursor combinations TMIn with H_2O, H_2O_2, or ozone. GPC was determined with indium oxide films grown at process temperatures below 210°C on oxidized Si wafers as reference substrates under the same process conditions as the polymeric substrates. The key difference between ALD and VPI is the extended exposure time, 30 seconds for the applied VPI process, which is required for the dissolution into and diffusion of the precursors inside the soft material, or for promoting a kinetically hindered chemical reaction. Interestingly, during each of the processes (TMIn/H_2O, TMIn/H_2O_2, or TMIn/O_3) indium oxide was grown on the silicon substrate even in the temperature range of 110-210°C (Figure 3.1 a). A high GPC of 0.9-1.5 Å/cycle was observed upon the use of hydrogen peroxide, but a thin film growth was also obtained with the less reactive water vapor, albeit of somewhat lower GPC (0.4-0.9 Å/cycle). Note that an ALD window was not observed in neither case, as seen by the absence of a flat region in the curves in Figure 3.1 a. An increase of the exposure time from 1 to 50 seconds in the TMIn/H_2O process led to an increase of the GPC from 0.25 to 0.75 Å/cycle at the deposition temperature of 170°C (Figure 3.1 b) and didn't significantly change upon further increase to 70 seconds. A few performed deposition processes with ozone as the oxygen-containing precursor resulted in the highest GPC among all processes (Figure 3.1 a).
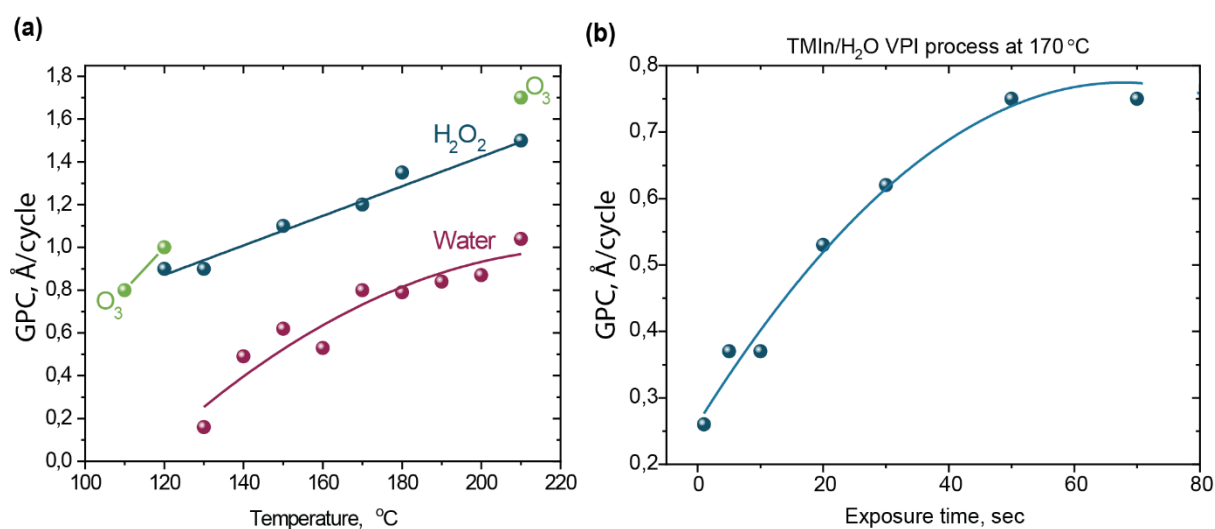
Figure 3.1 (a) GPC of indium oxide thin films on silicon substrates after applying the TMIn/H_2O or TMIn/H_2O_2 processes over the indicated temperature range. (b) GPC of indium oxide of the TMIn/H_2O VPI process performed at 170°C with varied exposure time.

The measured GPCs were higher than those reported in the literature. [156], [173], [176] Applying the TMIn/H_2O precursor combination, Salami et al. found that the binding of TMIn to the substrate is not saturative and that applying a double pulse of TMIn increased the GPC from 0.46Å to 0.55Å/cycle. [139] Also, an extremely high Langmuir exposure of H_2O (~2 Torr s) was needed for a saturative conversion of surface-adsorbed In-$(CH_3)^*$ to In-OH* groups. [173] Such exposure

is about 30 times higher than required for other ALD-grown metal oxides such as ZnO from DEZ/H_2O, HfO_2 from tetrakis(ethylmethylamido)hafnium (TEMAHf)/H_2O, or TiO_2 from titanium tetra-isopropoxide (TTIP)/H_2O in the very same reactor. [173] The group of S. George conducted in-situ FTIR studies of the In_2O_3 (TMIn/H_2O) and Al_2O_3 growth (TMA/H_2O). [174], [177] They found that the conversion of In-$(CH_3)^*$ groups to In-$(OH)^*$ groups requires much longer water exposures than that of Al-$(CH_3)^*$ to Al-$(OH)^*$. This indicates that the reaction kinetics of TMIn with H_2O is very slow. The factor limiting GPC and conformality of indium oxide films was attributed to low hydroxyl coverage at the surfaces at 252°C. [174] Promotion of the low-temperature growth of indium oxide may also result from the trapping of reactive oxygen species in the subsurface of the film. A recent study demonstrates that subsurface reservoirs with reactive oxygen species lower the nucleation temperature of the ALD synthesis. [178], [179] Although the authors described the effect for the ALD-growth of metal oxides on solid substrates, the same mechanism may be valid for the present VPI process, too.

Besides increasing the GPCs, the prolonged exposure times also reduced the onset temperature for crystal formation. We observed the first diffraction peaks of the cubic bcc indium oxide phase on the reference silicon substrates at temperatures of 170°C for water (Figure 3.2 a), 150°C for hydrogen peroxide (Figure 3.2 b), and 120°C for ozone (Figure 3.2 c), while earlier studies reported the formation of polycrystalline indium oxide above 200°C only and the ALD processes was performed with the highly reactive ozone. [156] The peaks at 2θ values of 38.5 and 56 degrees are artifacts stemming from silver contacts on the surface of the samples. In contrast to the ALD-deposited film, where only the strongest (222) peak was observed, [156] indium oxide films obtained at VPI conditions with 30 seconds of exposure time had also reflexes from other crystalline orientations (Figure 3.2). Our findings also show that the use of the more reactive hydrogen peroxide and ozone enhances the crystallinity of the films.

By analyzing different oxygen-containing precursors we concluded that the use of the highly reactive ozone or hydrogen peroxide promotes higher GPC and lower onset temperatures for crystallization. These findings are in line with the other metal oxide ALD processes mentioned above. For example, the growth of tin oxide from TDMA-Sn and hydrogen peroxide doubled compared to that after using TDMA-Sn and water. [180] Besides, use of H_2O_2 leads to the synthesis of ZnO with more interstitial oxygen and fewer oxygen vacancies than H_2O-ZnO. [181] It is known that hydrogen peroxide decomposes to form water and oxygen $2H_2O_2 \rightarrow 2H_2O + O_2$, or even to HO· radicals in the presence of catalysts. [182] Known catalysts include transition metals, for example Fe, which is the main constituent of the walls of the used stainless-steel reaction chamber. These radicals can enhance the nucleation and lower crystallization onset temperature.
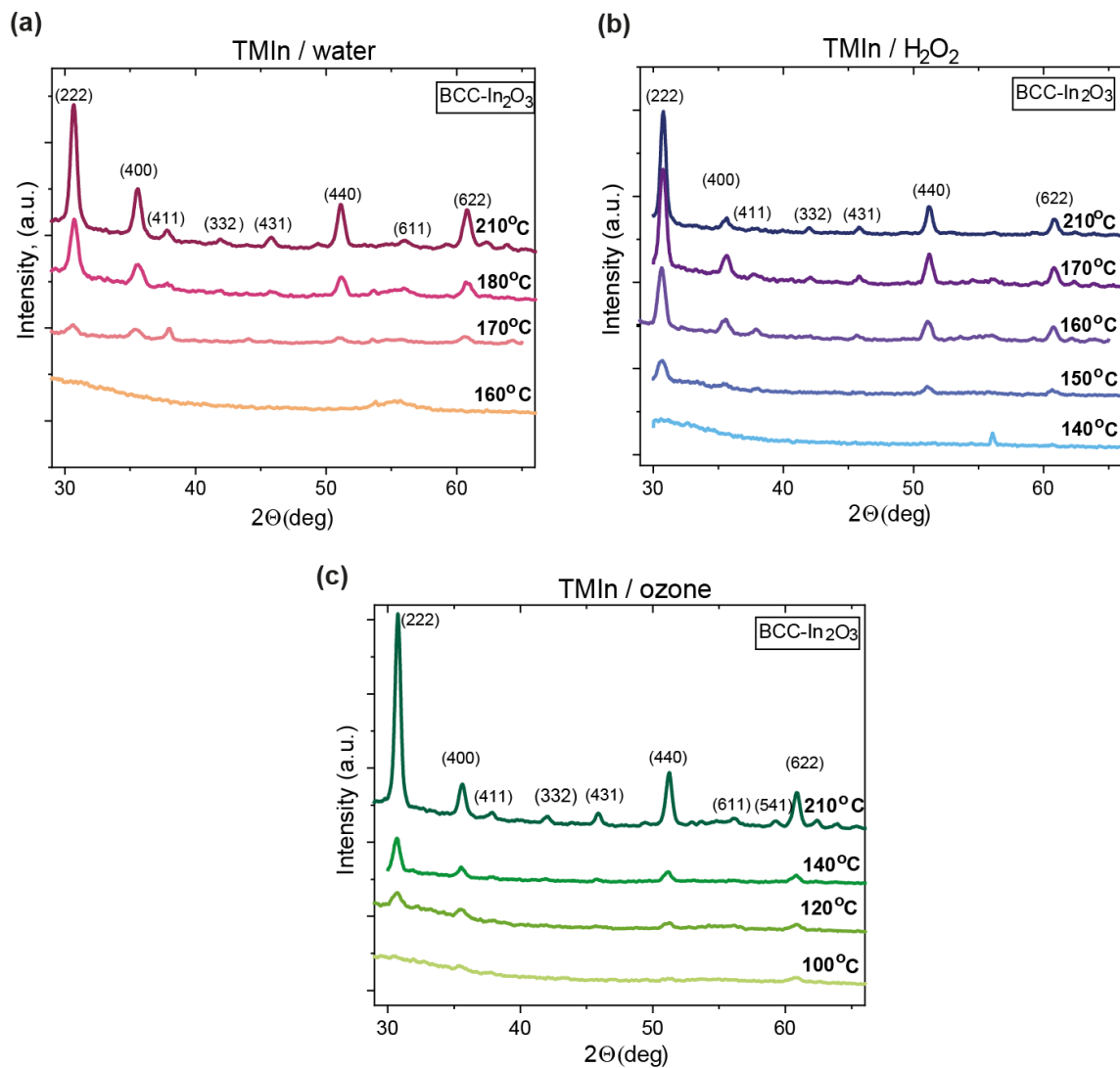
Figure 3.2 X-ray diffractograms of indium oxide films deposited on silicon oxide substrates at the indicated processing temperatures: (a) TMIn/ H_2O, (b) TMIn/H_2O_2 and (c) TMIn/ozone.

3.2 Indium oxide infiltration into ParyleneC

3.2.1 Chemical composition

When the conditions described in the previous section are applied to a polymeric substrate, the dissolution of the precursor into the polymer and its diffusion therein take place. The diffusivity of the precursor below the surface of a polymer depends on many factors, such as the size and shape of the precursor, free volume of the polymer, tortuosity of the cavities in the polymer, and the precursor-polymer reactivity. [10] The most direct way to study the infiltration is an investigation

of the cross-section of an infiltrated polymer. In our case the cross-sectional TEM micrographs confirmed the formation of inorganic NPs in the subsurface of ParyleneC after both TMIn/H_2O and TMIn/H_2O_2 processes (Figure 3.3 a, b). The darker areas in the micrographs correspond to the heavier chemical elements, i.e., indium. The infiltration depth upon applying the TMIn/H_2O_2 process was around 300 nm, which is twice the infiltration depth after the TMIn/H_2O process. The density of the inorganic NPs decreased gradually with the infiltration depth. However, a drastic change in the concentration of infiltrated indium oxide occurred at about half of the infiltration depth, namely at 60 nm and 150 nm for the TMIn/H_2O and TMIn/H_2O_2 samples, respectively, causing sudden contrast changes in the micrographs.
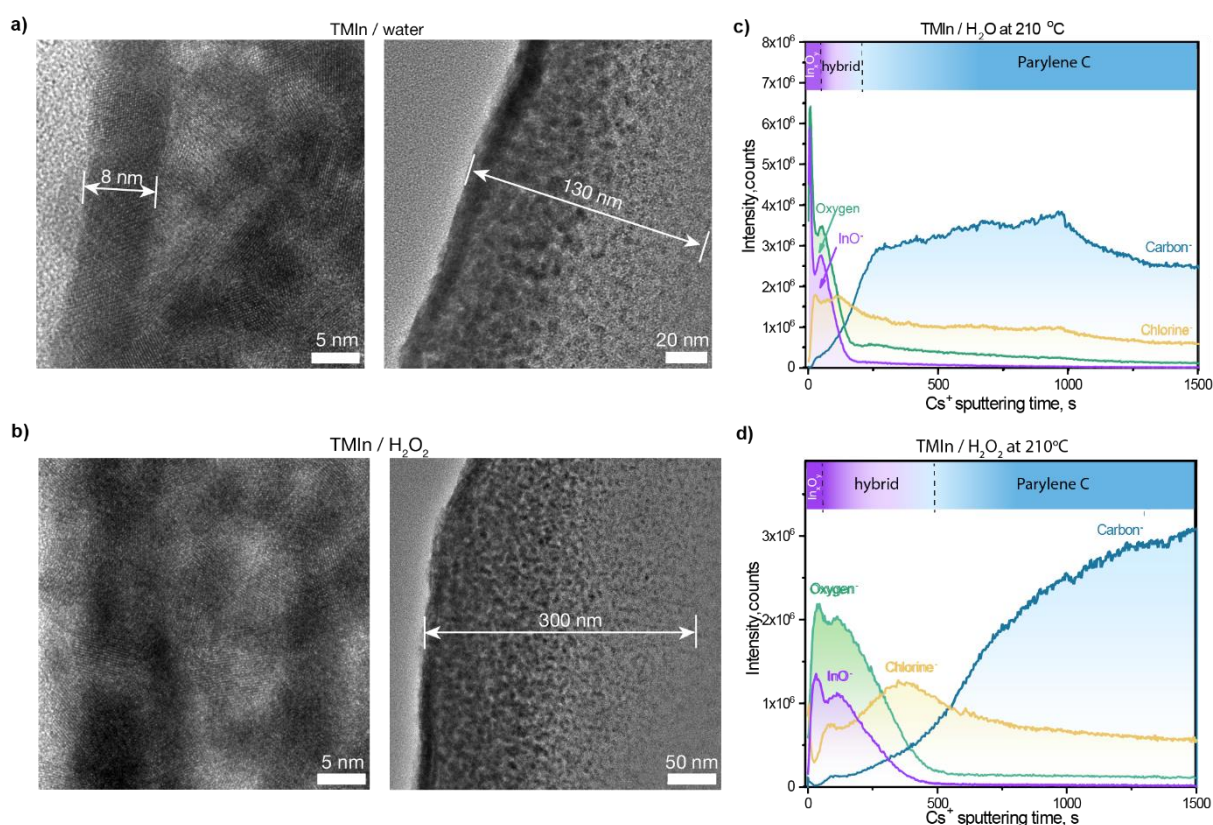
Figure 3.3 Bright-field TEM micrographs of cross-sectioned (a) TMIn/H_2O and (b) TMIn/H_2O_2 samples with different magnification. The respective sample surfaces are on the left-hand sides of the micrographs. SIMS depth profiles of the (c) TMIn/H_2O and (d) TMIn/H_2O_2 samples obtained after 150 cycles of VPI at 210°C.

The hybrid nature of the samples was proven by compositional depth profiles measured by SIMS. With progressing sputtering time, the initially intense signals of InO⁻ and O⁻ ions were continuously substituted by chlorine and carbon ion signals stemming from the polymer (Figure 3.3 c, d). The comparison of the SIMS data with the TEM micrographs indicates that the sharp and intense peaks of InO⁻ and O⁻ for the TMIn/H_2O sample (Figure 3.3 c) correspond to the thin

indium oxide film at the sample surface, visible as a dark line on the left-hand side of Figure 3.3 a. The hybrid material started underneath the inorganic film where InO^-, O^-, Cl^-, and C^- ion signals were simultaneously detected. For the $TMIn/H_2O_2$ sample, there was no pronounced indium oxide layer, but chlorine was present already at the very surface (Figure 3.3 b). As expected, the sputtering time needed for reaching the border of the hybrid layer of the $TMIn/H_2O_2$ sample was about twice that of the $TMIn/H_2O$ sample, as the infiltration upon the use of H_2O_2 precursor was considerably deeper. An increase in the chlorine signal at the hybrid/polymer interface was observed for both samples. Similar behavior of chlorine at a metal oxide/polymer interface was reported previously for aluminum oxide ALD coatings on ParyleneC [183] and was explained by the formation of metal chlorides at the polymer/metal-oxide interface. Indeed, an investigation of the chlorine signal by XPS revealed a significant presence of metal-bound chlorine alongside organic chlorine, originating from ParyleneC, for both $TMIn/H_2O_2$ and $TMIn/H_2O$ processes (see Figure 3.4 a, b, Figure 3.5 a, b).
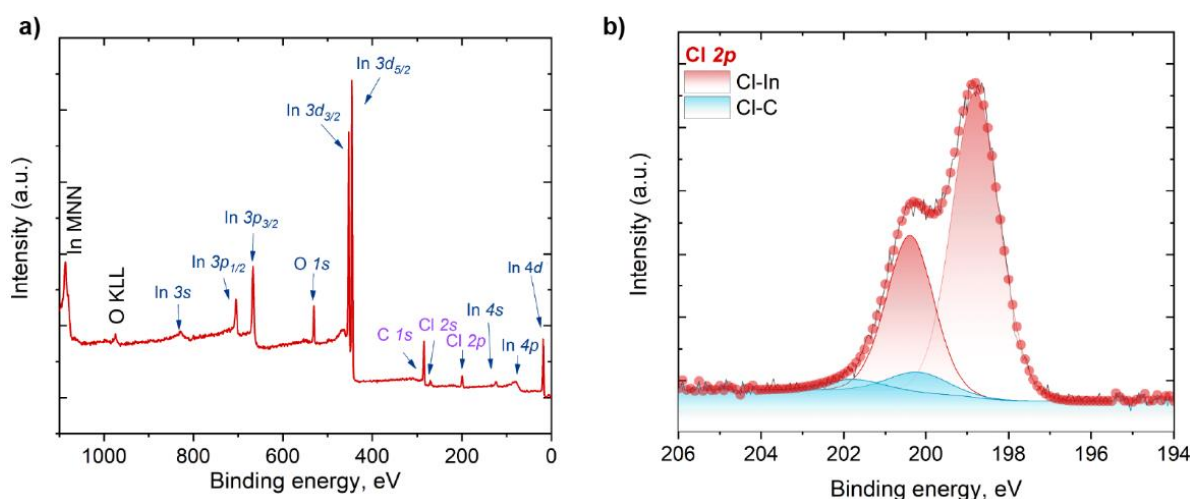
Figure 3.4 (a) XPS survey of the $TMIn/H_2O_2$ sample after 130 minutes of Ar+ sputtering; (b) XPS spectrum around Cl 2p core levels (full circles), deconvoluted into several contributions (shaded peaks).

The XPS survey spectrum of the $TMIn/H_2O_2$ sample in Figure 3.4a was obtained after 130 minutes of sputtering with an Ar^+ ions. The spectrum is dominated by signals of carbon, chlorine, indium, and oxygen which indicates the presence of a hybrid material. A deconvolution of the Cl 2p photoemission peak reveals chlorine in two different chemical states (Figure 3.4 b). The Cl $2p_{3/2}$ peak at the binding energy of 198.8 eV and the Cl $2p_{1/2}$ peak at 202.2 eV correspond to indium-bound chlorine.[184] Despite being originally bound to ParyleneC, more than 90% of the detected chlorine was bound to indium, even after 130 minutes of Ar^+ sputtering. The organic chlorine is found at higher binding energies: Cl $2p_{3/2}$ at 200.0 eV and Cl $2p_{1/2}$ at 201.6 eV. A similar observation was made from the $TMIn/H_2O$ sample. After 85 minutes of sputtering, XPS showed presence of

indium oxide together with carbon and chlorine (Figure 3.5 a). Again, indium-bound chlorine dominated the Cl 2p signal (Figure 3.5 b).
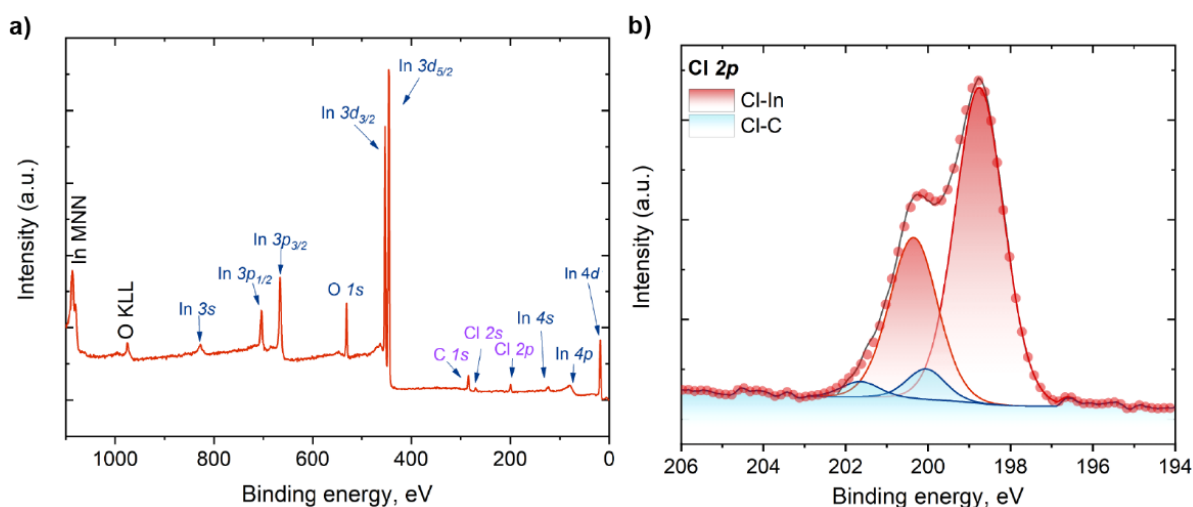

Figure 3.5 (a) XPS survey spectrum of the TMIn/H_2O sample after 85 minutes of Ar^+ sputtering; (b) XPS spectrum around Cl 2p core levels (full circles) deconvoluted into several contributions (shaded peaks). The sample was processed with by 150 VPI cycles at 210°C.

Processing temperatures affect the infiltration in different ways. Elevated temperatures during VPI can potentially augment the infiltration depth by increasing the mobility of the precursor and the free volume of a polymer. At the same time, higher temperatures lead to an enhanced mobility of the polymer chains which hampers the infiltration. [10] By reducing the infiltration temperature from 210°C to 150°C, the thickness of the indium-containing layer was halved, implying a significant decrease in the thickness of the hybrid layer (Figure 3.6 a). Importantly, it also lowered the admixture of chlorine in the inorganic indium oxide film (Figure 3.6 b). Consequently, the thicknesses of the hybrid and indium chloride layers can be tailored by adjusting the process temperature.

Despite the modification of the polymer, the thermal stability of ParyleneC remained largely unchanged. The derivative thermogravimetric analysis performed in a nitrogen flow showed just a slight change of the mass loss curve of the pristine substrate compared to a ParyleneC/In_xO_y hybrid obtained at an infiltration temperature of 180°C (Figure 3.7 a). The hybrid sample starts to degrade at 500°C, while the main decomposition peak of ParyleneC itself is higher by only four degrees Celsius (Figure 3.7 b, c), indicating only a minor impact of the VPI process on the thermal stability of the substrate.
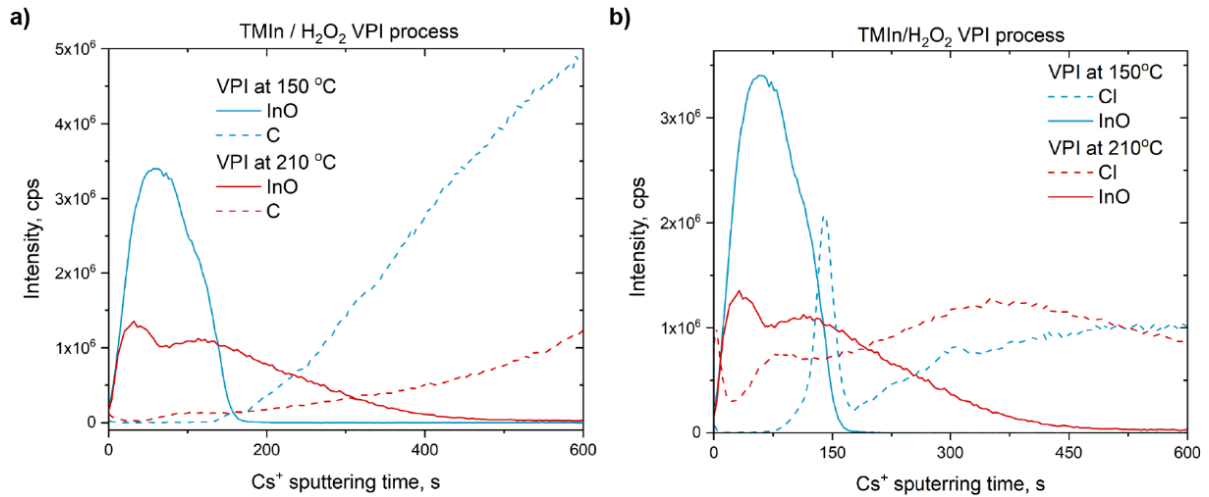
Figure 3.6 SIMS depth profiles of ParyleneC infiltrated with TMIn/H_2O_2 at 150°C and 210°C obtained by Cs$^+$ ion-bombardment and collection of (a) C$^-$ and InO$^-$ ions; (b) Cl$^-$ and InO$^-$ ions.
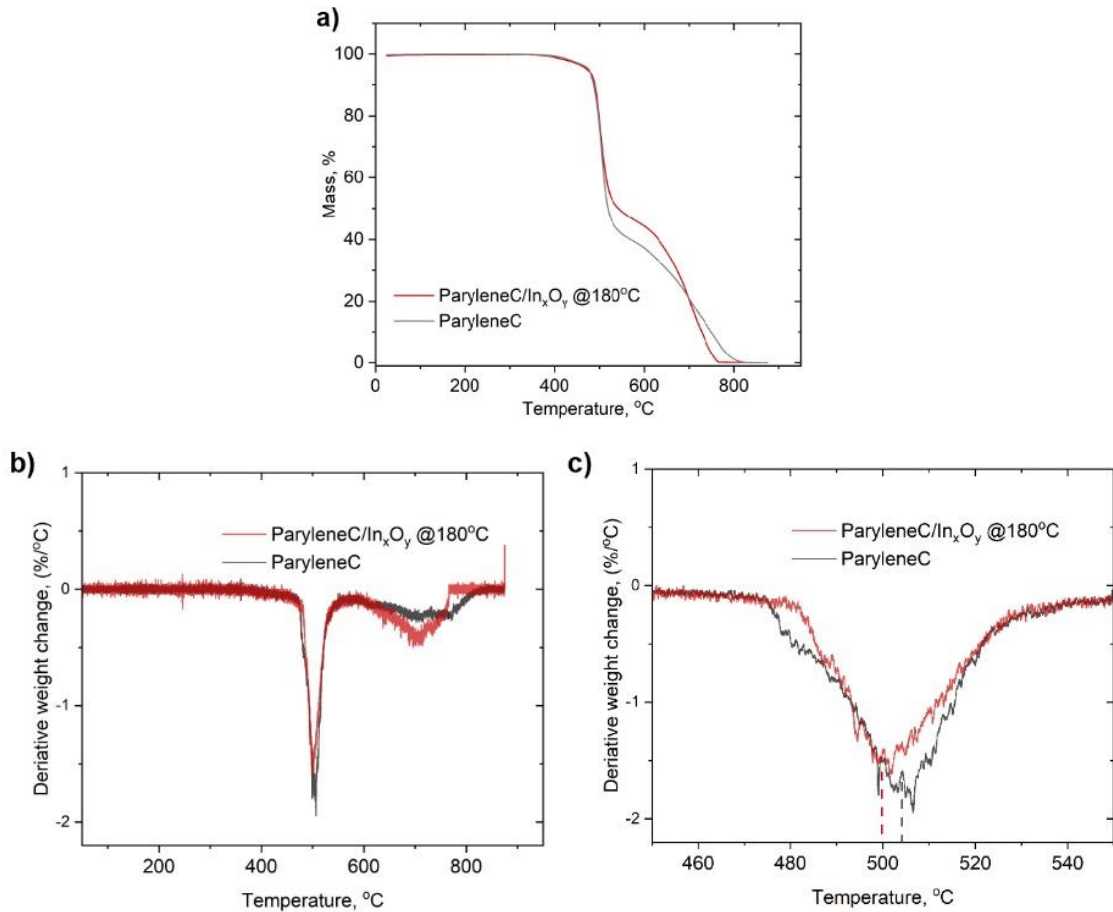

Figure 3.7 Comparison of (a) thermogravimetric analysis (TGA) and (b) derivative thermogravimetric analysis (DTA) of pristine ParyleneC and ParyleneC infiltrated with 150 cycles of TMIn/H_2O_2 at 180°C. (c) Magnification of the temperature region around 500°C from graph shown in (b). Image taken with permission from the Ref. [118]

The usage of ozone, that is the third type of oxygen-containing precursors, led to the degradation of the polymer and/or hybrid material (Figure 3.8 a). In some polymers ozone can degrade the polymeric chains, which is even more pronounced at elevated temperatures. [185] To verify any possible effect of ozone on the polymer, an extensive number of 700 VPI cycles with TMIn/O_3 was run, whereafter a thick indium oxide film formed which cracked and delaminated, as seen in the FIB cross-section (Figure 3.8a). Besides, voids were observed at the interface of the indium oxide film and the polymer. According to the SIMS data, this part is corresponding to indium oxychloride (Figure 3.8 b), without the admixture of carbon, unlike the TMIn/H_2O and TMIn/H_2O_2 samples. Most probably the TMIn/ozone VPI process led to an etching of the polymeric chains, while the chlorine remained incorporated into the deposited indium oxide film in the form of indium oxychloride. Given the polymer degradation and suppressed organic-inorganic hybrid formation, ozone is not a favorable choice as a VPI precursor for this specific polymer and will not be further discussed in this work.
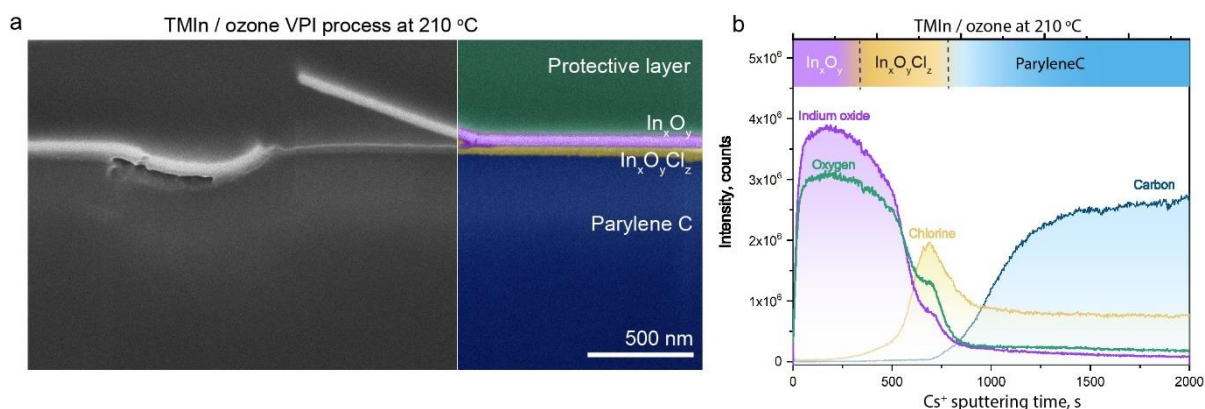
Figure 3.8 ParyleneC/In_xO_y obtained after 700 VPI cycles of TMIn/O_3 at 210°C (a) SEM image of a cross-section; (b) SIMS depth profile.

3.2.2 Structure and crystallinity

One of the main differences between the TMIn/H_2O and TMIn/H_2O_2 samples was the formation of the profound, 8 nm thick polycrystalline inorganic indium oxide film on the surface of the TMIn/H_2O sample (Figure 3.9 a), while the TMIn/H_2O_2 sample showed amorphous inorganic In_xO_y NPs (Figure 3.9 b) with chlorine admixture already at the surface (Figure 3.3 d). TEM micrographs and the reflexes in the reciprocal space obtained by Fast Fourier Transformation (FFT) showed that the In_xO_y NPs were polycrystalline in both samples (Figure 3.9 a, b). The interplanar distances matched those of cubic indium oxide and each lattice spacing was visualized as a virtual dark-field image (Figure 3.9 c, d). Overlaying them over the corresponding bright-field images highlights the distribution of the indium oxide nanocrystals within the bulk of the polymer (Figure 3.9 e, f).
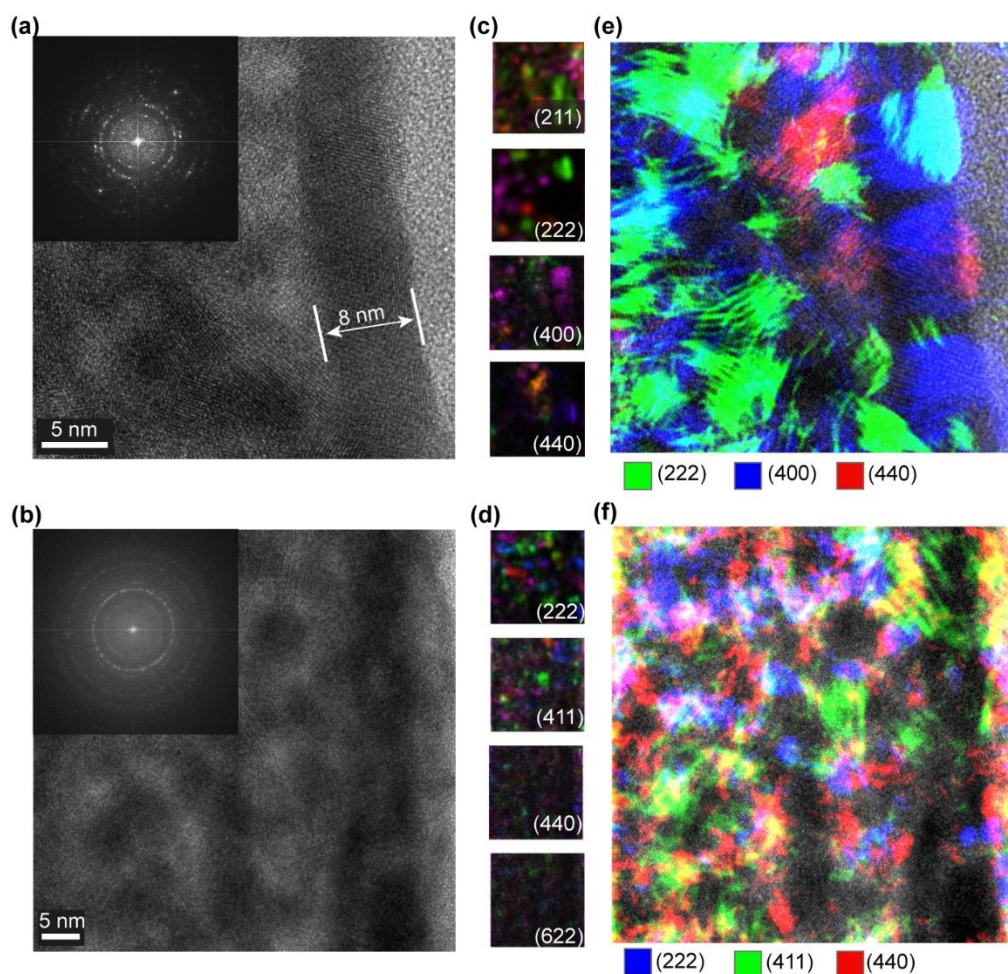
Figure 3.9 TEM bright-field micrographs and corresponding FFT images of indium oxide nanocrystals dispersed in ParyleneC after VPI: cross-sections of (a) TMIn/H_2O and (b) TMIn/H_2O_2 samples obtained after 150 VPI cycles at 210°C. Specific lattice spacings, calculated from the FFT images, are shown as virtual dark-field images for (c) TMIn/H_2O and (d) TMIn/H_2O_2 and correspond to cubic indium oxide. The colors are associated with various azimuthal positions of the reflections on the ring of the FFT image. (e) and (f) are false-colored virtual dark field images of TMIn/H_2O and TMIn/H_2O_2, respectively, overlayed over the bright-field TEM images in (a) and (b). The different lattice spacings are marked with different colors as indicated below the images.

X-ray diffraction of the samples obtained upon VPI at 210°C showed broad peaks with low intensity of cubic indium oxides at 30.4°, 35.4°, 50.9°, 60.5° (Figure 3.10). The TMIn/H_2O spectra showed more profound peaks than those of TMIn/H_2O_2. This is consistent with the observation of the formation of an 8 nm thick indium oxide film at the surface of the TMIn/H_2O sample, where the sizes of the crystallites reached 8 nm as well. The dispersed crystallites within the polymer had smaller diameters as their growth was restricted by the free accessible volume of the polymer. Therefore, despite the H_2O_2 lowering the onset temperatures for crystallization on silicon substrates

from 170 to 150°C (Figure 3.2 a, b), the XRD patterns of the hybrid samples appeared to be more distinguished when water was applied as precursor. Peaks marked with "X" stem from residues originating from the silver paste contacts applied for electrical measurements.
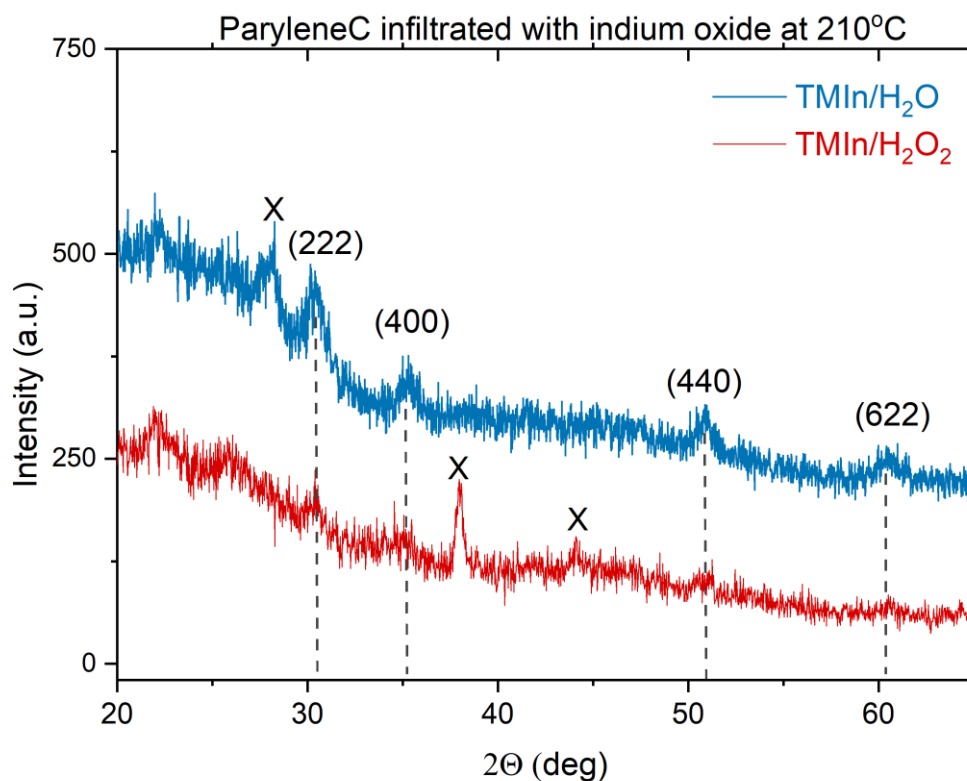

Figure 3.10 X-ray diffractograms of indium oxide infiltrated into ParyleneC at a processing temperature of 210°C after 150 cycles of TMIn/ H_2O and TMIn/H_2O_2.

The average crystal size can be directly measured from the virtual dark field images of the hybrids (Figure 3.9 c, f). It reached 2.9 nm in the TMIn/H_2O_2 and 2.7 nm in the TMIn/H_2O samples (Figure 3.11). This distribution was obtained after measuring the crystal size through the whole thickness of the hybrids (not all the corresponding images are shown here). The average diameter tends to decrease with the infiltration depth, most likely due to the gradual decrease in concentration of the precursors inside the substrate during the VPI process. The largest crystals didn't exceed 8.0 nm in diameter, which is equal to the film thickness on the surface of the TMIn/H_2O sample. Still, most of the crystals are less than 4 nm in size. The high number of the NPs with diameters less than 2 nm for the TMIn/H_2O_2 sample can be explained with higher infiltration depth and a more profound gradient of the indium oxide within the polymer. This profound hybrid layer with a lower NPs density favors a higher number of NPs with a small diameter. The small size of the crystallites is the cause for the samples to have low-intensity broad peaks in the corresponding XRD patterns (Figure 3.10). These polycrystalline NPs densely agglomerate in the near-surface bulk, and many of them are intimately interconnected, potentially forming electronic conduction paths.
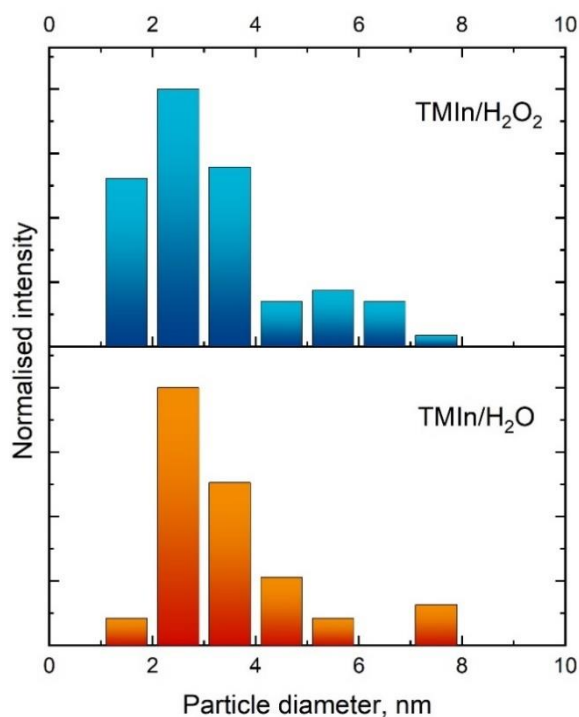
Figure 3.11 Distribution of the average diameters of infiltrated particles in the subsurface of the TMIn/H_2O_2 (blue) and TMIn/H_2O (red) samples.

3.3 Reaction kinetics of TMIn/H_2O_2 infiltration into ParyleneC

3.3.1 Density functional theory calculations of TMIn and H_2O_2 infiltration

We employed DFT calculations to investigate the possible chemical reactions during the infiltration process of ParyleneC with TMIn and H_2O_2. In the first step of our calculations, the TMIn molecule was placed between two ParyleneC chains and the structure was allowed to relax. Figure 3.12 a shows the model of the atomic structure of the ParyleneC chains infiltrated with TMIn. The calculated incorporation energy of -0.52 eV indicates infiltration of the precursor rather than formation of a bond between TMIn and the polymer, which is also clear from the atomic structure shown in Figure 3.12 a. Next, we investigated the interactions between infiltrated TMIn and H_2O_2 by examining the possible reactions when H_2O_2 molecules are added to the system. We found two possible reactions after the introduction of H_2O_2:

The first reaction involves the transfer of two H atoms from the polymer chain to the CH_3 ligands of TMIn to release two CH_4 molecules as by-products, while In-CH_3 binds to the aliphatic C atom

of the polymer chain from which the H atoms were transferred; this C-In distance is 2.12 Å. The remaining CH_3 ligand of TMIn can interact with another H_2O_2 molecule to release a new CH_3OH by-product and this reaction produces an OH group that binds indium forming C-In-OH species, with an In-O distance of 2.04 Å and an In-C distance of 2.12 Å. The calculated In-O bond in In-OH is shorter when compared to the calculated In-O bond in In_2O_3 in a previous study, which was found to be 2.11 Å. [186] InOH is the usual product that forms when TMIn is exposed to a co-reactant such as H_2O or H_2O_2, where the intercalated precursor is irreversibly converted to the oxide/hydroxide form. [157] The calculated energy for this reaction is -1.89 eV, giving a total energy gain of -2.41eV relative to the free precursors and ParyleneC. The optimized structure of the reaction product is presented in Figure 3.12 b.
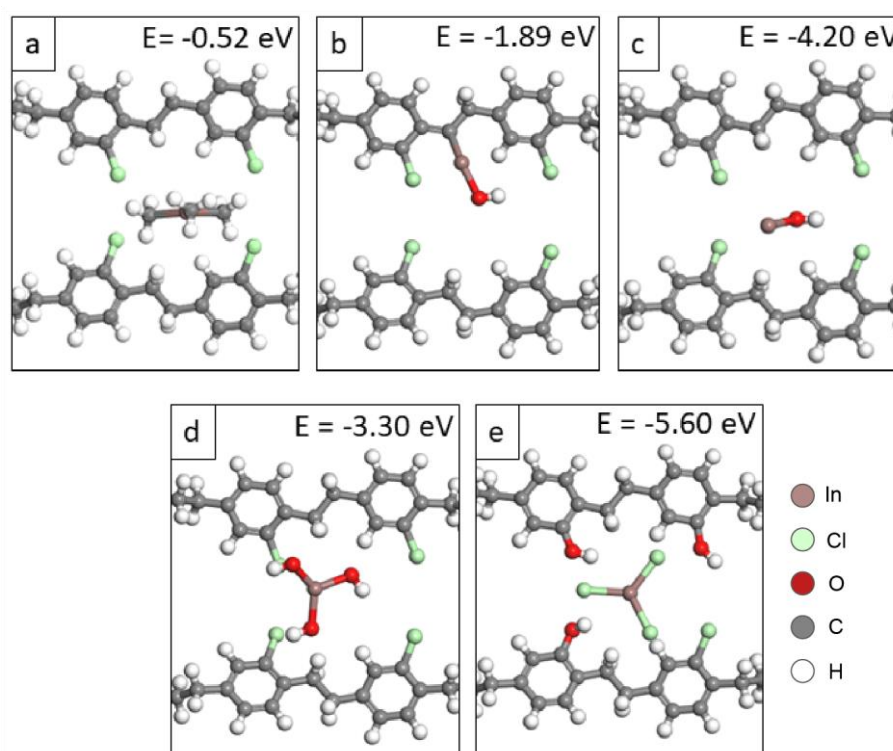
Figure 3.12 Optimized structures and energy gains of ParyleneC infiltrated with (a) TMIn, (b) TMIn and H_2O_2 with C-In-OH formation, (c) TMIn and H_2O_2 with In-OH formation, (d) TMIn and two H_2O_2 with $In(OH)_3$ formation, (e) TMIn and two H_2O_2 with $In(Cl)_3$ and phenol formation.

In the second reaction we consider the formation of ethane from two CH_3 ligands of TMIn and CH_3OH upon interaction with H_2O_2. This reaction produces a free OH group that binds to In to form In-OH, similar to the first reaction. In contrast to the first reaction, here the In-OH adduct remains infiltrated between the two ParyleneC chains, see Figure 3.12 c. The calculated energy for

this reaction is -4.1eV, giving a total reaction energy of -4.62eV. The calculations show that the second reaction is more favorable and therefore was used for modelling the second reaction.

We also analyzed the possible reactions when the concentration of H_2O_2 is increased. This is done by expanding the model system presented in Figure 3.12 c to include a second H_2O_2 molecule. We found that when a second H_2O_2 molecule is added to this system, two more reactions can occur. The first reaction favorably causes the formation of $In(OH)_3$ with a calculated energy of -3.31eV, see Figure 3.12 d. The second reaction causes the formation of $InCl_3$ and phenol species, as a result of the exchange of Cl atoms of ParyleneC with OH groups from $In(OH)_3$. The calculated energy for this reaction is -5.6eV, see Figure 3.12 e. Therefore, the DFT results show that with increased concentration of H_2O_2, the formation of $InCl_3$ species and phenol groups is the most favorable reaction, consistent with the experimental findings where In-Cl (Figure 3.4 b, Figure 3.5 b) species were observed by XPS. Furthermore, indium chloride itself can react with water vapor to indium oxide, as demonstrated by earlier ALD works. [167], [187]

3.3.2 Infrared absorption of infiltrated ParyleneC

Additional information on the chemical bonding was obtained by ATR-FTIR. The factor limiting the usability of ATR-FTIR for studying such hybrid systems is the relatively large analysis depth of the technique compared to the thickness of the hybrid layer. The signal of the unmodified bulk ParyleneC typically dominates the spectra, which is why untreated and infiltrated polymers show only minor differences. The notable bands of untreated ParyleneC are listed in Table 1 and compared to the bands of ParyleneC/In_xO_y hybrids.

Table 1. Assignment of the FTIR spectral bands of untreated and indium oxide-infiltrated ParyleneC.

Assignment	Measured wavenumber, cm^{-1}	Referenced wavenumber, cm^{-1}	Reference
C=O stretch	1715-1650	1730-1690	[188]
		1695	[189]
		1705	[190]
		1718, 1696, 1608	
Skeletal aromatic C-C vibrations	1607, 1557,	1607, 1557	[191]
		1608, 1555	[190]
	1514	1513	[192]
C-C ring stretching vibrations	1493	1496	[191]
CH$_2$ rocking vibrations	1451	1452	[191]

Assignment	Measured wavenumber, cm^{-1}	Referenced wavenumber, cm^{-1}	Reference
C-C deformation vibrations	1401	1403	[191]
In-plane deformation vibrations of C-H bonds in aromatic rings	1207, 1156, 1106, 1076	1200-1000	[191]
Cl bound to aromatic ring vibrations	1048, 875	1051, 877	[191]
		1045, 875	[190]
Two neighboring H atoms bonded to aromatic ring	823	827	[191]
Cl – bound to an aromatic ring	792, 630, 604	601	[194]
	<530	505	[195]

One of the features observed upon indium oxide infiltration was a broadening of the O-H stretching peak at 3550-3370 cm^{-1} that may originate from entrapped water molecules in the bulk of the polymer, likely sealed with the indium oxide film coating, and/or from the In(OH)$_3$ formed in the subsurface of the polymer (Figure 3.13). [196]
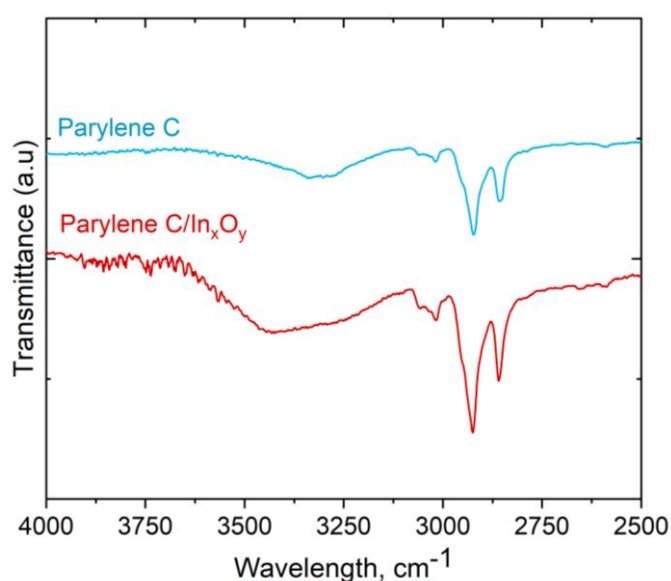
Figure 3.13 Comparison of FTIR spectra of pristine ParyleneC and ParyleneC infiltrated with In$_x$O$_y$ in the wavenumber range of 4000-2500 cm^{-1}.

In Figure 3.14 an average of 23 spectra of pristine substrates is compared with an average of spectra of 86 different TMIn/H$_2$O$_2$ VPI-processed samples. The standard deviation of each data set is also indicated in the graph, thereby allowing to visualize the dispersion between different spectra. The increased deviation of the peak shoulder at 1430 cm^{-1} from the average Figure 3.14 a indicates a change related to CH$_2$ rocking vibrations after infiltration. [191] A slight change at 1378 cm^{-1}

54

indicates an enhancement of the C-C deformation vibration band (Figure 3.14 a). The change in the peak shoulder at 1094 cm^{-1} relates to C-H deformations in aromatic ring vibrations which can be linked to the transfer of H atoms from the backbone to the TMIn molecule with a consequent binding of indium atoms to the polymer backbone (Figure 3.12 b, Figure 3.14 b). The evolution of the peak at 1076 cm^{-1} can be attributed to C-O stretching vibrations, as previously shown by DFT calculations. The peaks at 1047 and 874 cm^{-1} originate from vibrations of chlorine bound to an aromatic ring, which shifted to lower wavenumbers after infiltration. An additional peak evolved at 792 cm^{-1} indicating InCl₃ formation. This supports our earlier statement of the phenol formation after the substitution of Cl atoms of ParyleneC with OH groups from In(OH)₃. Overall, the FTIR measurements corroborated the DFT-calculated results, proving the formation of i) C-O bonds which were not present in the ParyleneC, and ii) indium chloride. Despite the partial deterioration of the ParyleneC, its thermal stability remained largely unaffected. The derivative thermogravimetric analysis showed a downshift of the of the main decomposition peak by only four degrees Celsius (Figure 3.7 c).
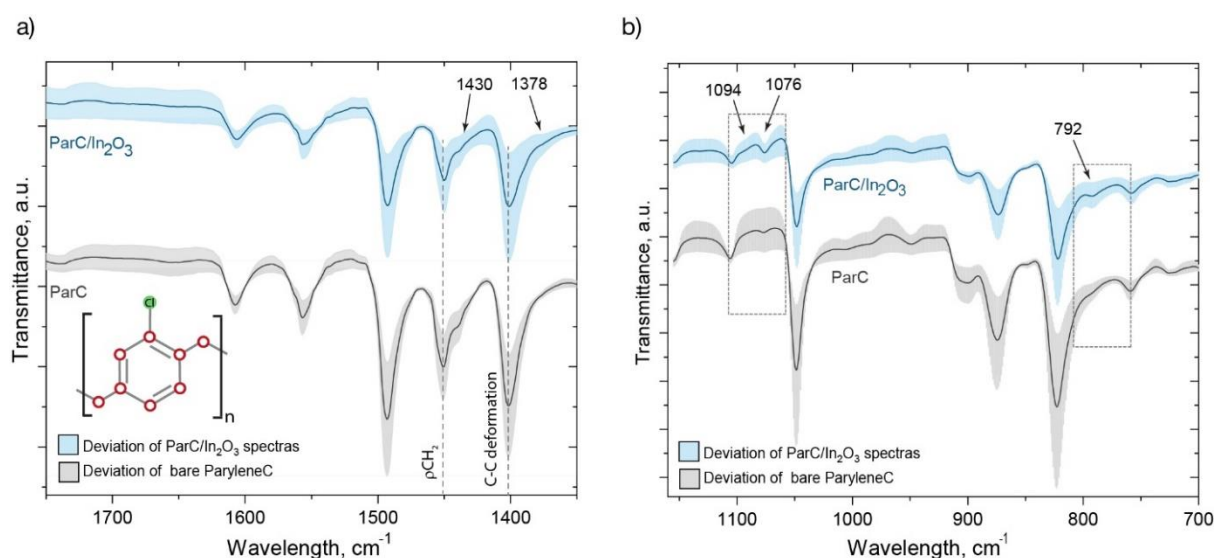

Figure 3.14 Aggregated ATR-FTIR spectra, including indicated deviations, of ParyleneC (gray) and ParyleneC/In$_x$O$_y$ (light blue) of following spectral regions: (a) 1750-1350 cm^{-1}; (b) 1150-700 cm^{-1}.

3.4 Electronic properties of the ParyleneC/In$_x$O$_y$ hybrids

3.4.1 Absorption spectroscopy and band gap evolution

The evaluation of the electronic functionality of the indium oxide-based hybrids is of importance for judging their application perspectives. The measurement of the conductivity of such hybrid systems is complicated as it requires knowledge of the thickness of the conducting layer as precisely

as possible. However, the studied systems have hybrid layers with density gradients which do not allow to precisely define which part of the layer still contributes to the conductivity and which not. Deeper sections of the infiltrated polymer with a low In_xO_y particle density are unlikely to provide the necessary continuous pathways for the electrons to conduct. We applied the Van der Pauw method for assessing the sheet resistance (Rs). The lowest values of the sheet resistance were obtained for the highest infiltration temperatures of 210°C for $TMIn/H_2O$ (Figure 3.15). However, the difference in the Rs between $TMIn/H_2O$ and $TMIn/H_2O_2$ samples was one order of magnitude in favor of the latter, despite the 8 nm thick inorganic In_xO_y capping layer on the $TMIn/H_2O$ sample. This difference even rose at low infiltration temperatures and reached more than five orders of magnitude for samples grown at 150°C. The sheet resistance value for $TMIn/H_2O$ at 150°C is not shown in Figure 3.15 as it was higher than 10^9 $\Omega/\square$ and consequently out of the measurement range. Importantly, the Rs values for $TMIn/H_2O_2$ increased only by a factor of about 3 from 9 k$\Omega/\square$ to 33 k$\Omega/\square$ after lowering the VPI processing temperature from 210°C to 135°C, respectively, and remain two orders of magnitude higher than those of the conventionally deposited In_2O_3 films (Rs=390$\Omega/\square$) upon annealing at 500°C. [197]
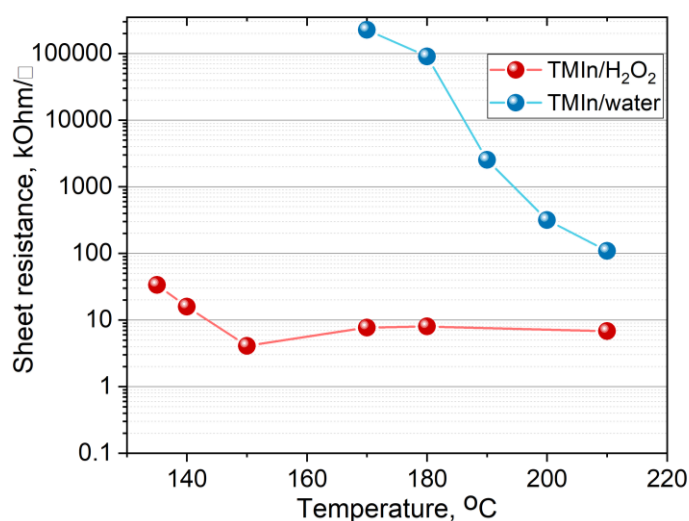

Figure 3.15 Comparison of the sheet resistance values of the ParyleneC/In_xO_y hybrids formed at different VPI process temperatures using 150 cycles of $TMIn/H_2O_2$ (red) or $TMIn/H_2O$ (blue).

The optical absorbance was measured to affirm the differences in the sheet resistance of the samples grown with the two different oxygen sources (Figure 3.16). The main contribution to the absorbance in the UV range comes from ParyleneC. The absorbance of the $TMIn/H_2O$ samples changed only marginally at low VPI process temperatures, rising from 0.4 to 1.0% at 550 nm (Figure 3.16 a), but at temperatures above 170°C the changes became pronounced. In contrast, the absorbance of the $TMIn/H_2O_2$ samples showed an obvious increase below 150°C and remained rather stable at process temperatures of 150-210°C, with the absorbance rising from 0.4 to 1.5% at 550 nm (Figure 3.16 b). The corresponding Tauc's plots (Figure 3.16 c, d) allowed extraction of the optical band gap values, [138] which are plotted in the insets of the graphs. For both processes we

observe a narrowing of the band gap with increasing process temperatures, which most likely originates from a higher concentration of charge carriers. [198] The overall decrease in the band gap occurred from 4.2 to 3.6 eV for both samples, in agreement with the reported direct band gap of indium oxide of 3.7 eV. [199] While at 210°C the optical band gaps are similar for both systems, hydrogen peroxide led to a narrower band gap at lower infiltration temperatures, which is consistent with the lower sheet resistance values. As the inorganic metal oxide film at the surface of the TMIn/H$_2$O$_2$ sample was not dense and contained chlorine (see Figure 3.9 b, f), we conclude that the hybrid ParyleneC/In$_x$O$_y$ also takes part in the electronic transport.
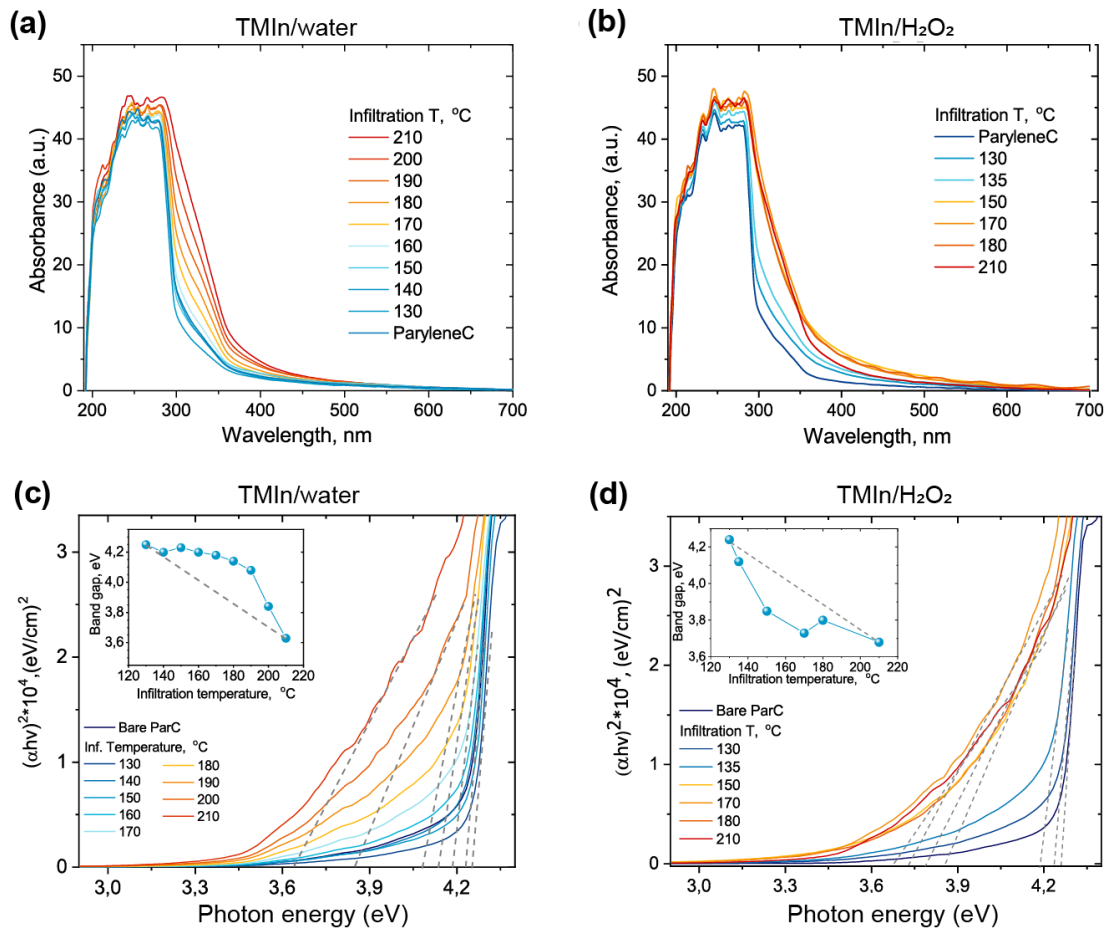

Figure 3.16 Optical absorbance spectra of (a) TMIn/H$_2$O and (b) TMIn/H$_2$O$_2$ samples obtained after 150 VPI cycles at different infiltration temperatures as indicated in the legends. Tauc's plots of (c) TMIn/H$_2$O and (d) TMIn/H$_2$O$_2$. The evolution of the band gap values with the VPI process temperatures was obtained from Tauc's plots and are shown in the insets of the corresponding figures.

The use of both water and hydrogen peroxide in the indium oxide VPI process led to a film growth and infiltration of ParyleneC. Hydrogen peroxide lowered the process temperatures required for

obtaining polycrystalline indium oxide. At the same time the size of the indium oxide crystallites, dispersed in the polymer, remained comparable. Despite the band gaps being similar for both systems, resistances of the samples had a difference of one order of magnitude at 210°C. This difference further increased with lowering the infiltration depth. These observations may be explained with the different reactivities of water and hydrogen peroxide. Indeed, hydrogen peroxide is more reactive by adding oxygen and HO· radicals to the system. From the observed enhanced GPC values from the reference $TMIn/H_2O_2$ ALD process silicon substrates it may be speculated that upon application to a polymer more infiltrated material and deeper infiltration depths will result. This will generate more hybrid conduction paths which enhance the conductivity. The effect becomes even more prominent at lower processing temperatures, as seen from the GPC values on Si substrates (Figure 3.1). As a result, the hydrogen peroxide precursor is beneficial for the indium oxide formation with higher conductivity.

3.4.2 Stoichiometry and oxygen vacancies

A further factor that affects the resistivity of a material is the level of doping. In the case of indium oxide, the common dopants that affect the resistivity are oxygen vacancies. [199], [200] They act as shallow donors having a strong influence on the carrier concentrations, thereby contributing to an n-type conductivity. [199], [201] The stoichiometry of the indium oxide grown in the ParyleneC can be determined from the XPS data since this specific polymer does not contain oxygen (Table 2). Similar to ALD-grown indium oxide films, which typically are oxygen deficient, [200], [202] VPI also led to the formation of nonstoichiometric In_xO_y already at the very surface of the samples (Figure 3.17 a). After 10 minutes of Ar^+ sputtering the In/O ratio reached the value of 1.2, twice as high as expected for stoichiometric indium oxide. The In/O ratio increased considerably with the Ar^+ ion sputtering time for the $TMIn/H_2O$ sample, which can be attributed to the appearance of indium chlorides (Figure 3.5 b). A quick rise of the oxygen deficiency after 300 minutes of Ar^+ ion sputtering for the $TMIn/H_2O$ sample was due to a sharp decrease of the oxygen content in the hybrid, while the drop in the indium concentration was not significant (Table 2). Similar behavior was observed for the $TMIn/H_2O_2$ sample, where traces of indium were detected much deeper in the bulk than oxygen, which went beyond the detection limit after 780 minutes of sputtering (Table 3).

Table 2. Chemical composition of the $TMIn/H_2O$ sample determined from the XPS survey spectra. The last column is the relative share of chlorine bound to indium amongst the total amount of chlorine.

Time Ar^+ sputtering, min.	C, at. %	O, at. %	In, at. %	Cl, at. %	$\frac{Cl_{In}}{Cl_{total}} \times 100\%$
0	32,4	33,8	33,8	0,0	0
10	7,7	42,8	49,5	0,0	0
25	7,2	42,0	50,9	0,0	0

55	8,7	41,2	50,1	0,0	0
85	27,2	28,8	37,7	6,3	86,7
100	44,4	17,9	28,9	8,8	92,5
130	50,9	15,6	25,6	8,0	87,6
300	64,1	5,3	19,8	10,8	75,1

Table 3. Chemical composition of the TMIn/H$_2$O$_2$ sample determined from XPS. The last column is the relative share of chlorine bound to metal amongst the total amount of chlorine. Missing values indicate missing high-resolution measurements.

Time Ar+ sputtering, min.	C, at. %	O, at. %	In, at. %	Cl, at. %	$\dfrac{Cl_{In}}{Cl_{total}} \times 100\%$
0	13,9	38,4	45,7	2,1	-
10	21,9	33,4	41,2	3,5	100
130	50,8	7,1	15,4	6,7	92,0
250	86,6	2,1	5,2	6,1	82,0
370	71,9	7,4	7,4	14,3	-
430	89,8	1,3	3,6	5,3	-
490	91,0	0,8	2,7	5,3	57,4
600	90,2	1,2	2,2	6,4	54,3
660	90,9	0,8	2,0	6,2	-
780	91,8	0	1,6	6,6	44,1
900	92,8	0	1,4	5,8	41,9

The photoemission peaks around the O 1s core levels of both samples attest the presence of oxygen vacancies (Figure 3.17 b, c). The data points were collected from three different positions of the samples, namely near the surface, at the onset of the hybrid, and in a bulk section of the hybrid. The deconvoluted O 1s peaks show contributions of at least three components. The main component at the BE of 530.2 eV is attributed to the metal-oxide bond (In-O). [203] The contribution of oxygen vacancies is related to the peak at 531.2 eV (O$_{vac}$), and that of hydroxide at 532.2 eV (O-H). [200] An additional low-intensity contribution at 533.5 eV after 10 minutes of Ar$^+$-etching of the TMIn/H$_2$O sample is assigned to metal carbonates (C-O-In) or chemisorbed H$_2$O. [204] As discussed before, the TMIn/H$_2$O process grew an 8 nm thick indium oxide film. Apparently, 10 minutes of Ar$^+$ sputtering did not completely remove the film since no chlorine signal was detectable yet (Table 2), which would be expected if the hybrid or bulk polymer had been reached. The appearance of C-O bonds indicates that chemical reactions of the TMIn/H$_2$O process at 210°C were not complete and that 7.7 at.% of carbon impurities remained in the film. These impurities could cause a higher sheet resistance than that of the H$_2$O$_2$ sample, as it was observed in Figure 3.15. In general, the indium oxide moieties were highly oxygen-deficient regardless of the choice of the oxygen-containing precursor. It can be only partially explained by the formation of metal-halogen bonds. The unusually high oxygen deficiency may be related to the convergence of oxygen vacancies

(Figure 3.17 b, c), metallic indium inclusions, or indium chloride formation (Figure 3.4 b, Figure 3.5 b).
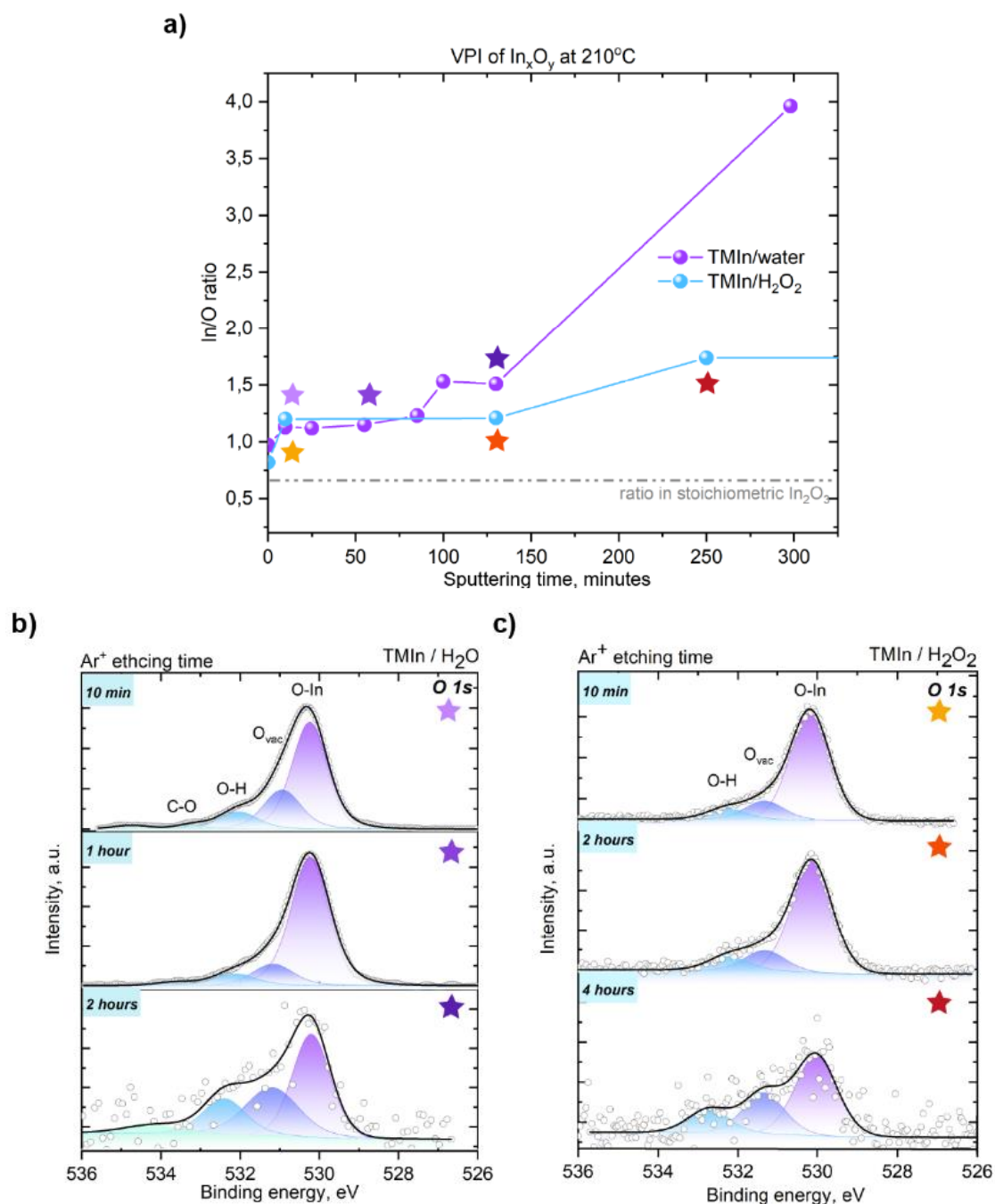

Figure 3.17 (a) Evolution of the In/O ratio *vs.* Ar$^+$ sputtering time, measured by XPS; evolution of the O 1s peak upon Ar$^+$ sputter-etching at three different depth positions of (b) TMIn/H$_2$O and (c) TMIn/H$_2$O$_2$. Stars of the same color in (a), (b) and (c) mark the data points obtained after the same sputtering time.

3.4.3 Resistance evolution with bending

Finally, the deterioration of the electronic functionality of the samples upon bending was tested with a homemade bending device (Figure 3.18 a). The TMIn/H$_2$O$_2$ sample was glued to a rubber band which rotated over the radius of 5.5 mm for a defined number of times (Figure 3.18 b). Surprisingly, the initial sheet resistance values dropped from 5.2 to 3.0 kOhm/□ after the first 100 bending events (Figure 3.18 a). Further bending by up to 7000 times caused no significant changes in the sheet resistance. Such behavior of the hybrid ParyleneC/In$_x$O$_y$ system can be explained by the redistribution of the MeO NPs due to the coexistence of compression and tension stresses during bending (see inset of Figure 3.18 a). Tension can lead to the rupture of a thin inorganic film and to the stretching of the hybrid and polymeric parts of the substrate. That leads to an increase of the free volume accessible for the migration of NPs and their subsequent agglomeration at the interfaces and ruptures. Such NP agglomeration can be explained by depletion attraction forces. [118] Thus, the bending can condense inorganic NPs near the surface layer of the hybrid, thereby forming new conductive pathways which will result in the observed decrease of the sheet resistance (Figure 3.18 a). The advantage of the developed organic-inorganic conductive hybrid is the absence of a well-defined inorganic film on the surface in case of low numbers of VPI cycles or, otherwise, the presence of a chemically surface-bound thin film, which makes the system less susceptible to cracking upon bending. In contrast, conventional ITO films show drastic changes upon bending over radii below 10 mm. [205], [206]
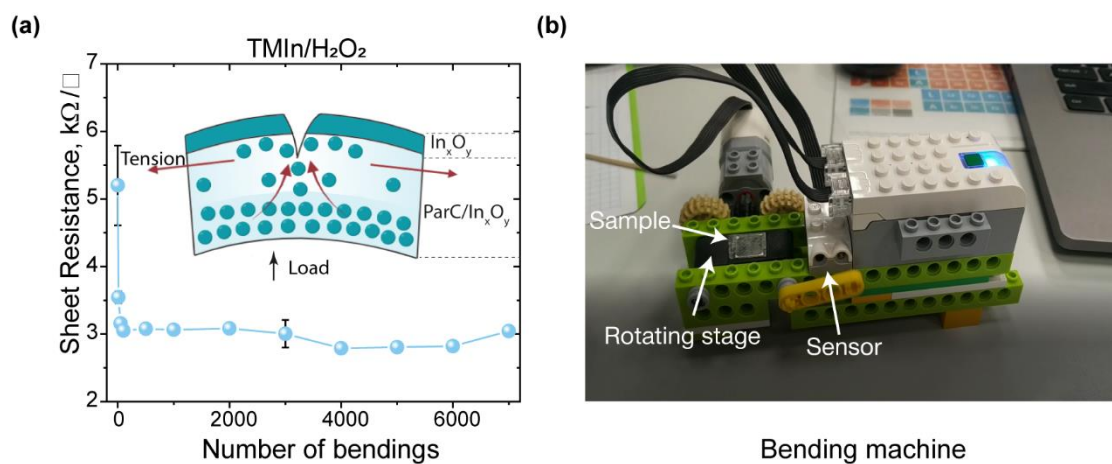

Figure 3.18 (a) Evolution of the sheet resistance of ParyleneC/In$_x$O$_y$ sample upon repetitive bending. The VPI was conducted with 150 cycles of TMIn/H$_2$O$_2$ at 210°C. Inset: Schematic of the mechanical stress that appears upon folding of the hybrid sample. (b) Home-built continuous bending tool.

We didn't observe any cracks on the surface of the bent samples with the optical microscope. To observe crack generation and propagation, we decided to apply more bending stress by minimizing

the bending radius. We examined the surfaces of the hybrid after a single time bending over a smaller radius of 1mm and compared it to a ParyleneC/Al_2O_3/In_xO_y nanolaminate which served as a reference sample. For the formation of the nanolaminate, a 10 nm thin alumina oxide layer was deposited by ALD to serve as a protective layer against a diffusion of precursors into the polymer. After that the Al_2O_3-coated ParyleneC and the pristine polymer were exposed to 150 alternating pulses of TMIn and H_2O_2 at 210°C. Upon bending of the samples, we observed the formation of cracks on the surface of the nanolaminate and the effect of charging in the SEM, which proved that the conducting paths were disrupted (Figure 3.19 a). Bending of the hybrid structure led to swelling of the film, albeit without the complete detachment of the indium oxide from the polymer (Figure 3.19 b). Possibly, the ParyleneC-In_xO_y hybrid prevents such crack formation. However, we cannot judge the contribution of the Al_2O_3 sublayer to the total brittleness of the structure.
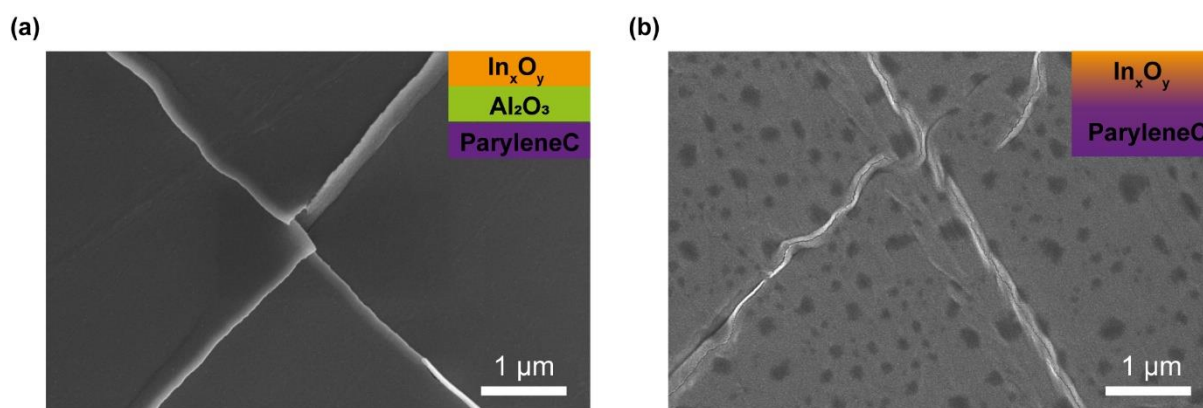

Figure 3.19 SEM image of the sample surfaces of (a) the ParyleneC/Al_2O_3/In_xO_y nanolaminate and (b) the ParyleneC/In_xO_y hybrid after bending over the radius of 1mm.

3.4.4 Persistent photoconductivity

Photoconductivity is an increase in the conductivity upon irradiation with light. When this change persists with time, that is, the conductivity has a slow decay over hours or even days without optical excitation, that phenomenon is called persistent photoconductivity (PPC). [207] Many semiconductors show PPC, including ZnO [208] and In_2O_3. [209] One of the common explanations for this phenomenon links PPC to defects that trap charge carriers. A prolonged stay of the charge carriers in such activation centers causes persistent enhancement of the conductivity. [210] The PPC of indium oxide is associated with the oxygen vacancies, their photoreduction, and oxidation. [211]

We investigated the effect of UV light by irradiating samples with a UV lamp with a central wavelength of 365 nm. The resistance measurements were conducted at ambient conditions using a two-probe setup with simultaneous irradiation (Figure 3.20). As discussed earlier in this chapter, the thickness of the layer that takes part in the electronic transport cannot be determined precisely

for the hybrids due to the variation of the density of the NPs along the sample depth. Therefore, we measured the change in the resistance and not resistivity. The resistance of the hybrids obtained at different temperatures decreased upon UV irradiation. The most significant changes were observed within the first few minutes of photoexcitation. The higher the initial values of the resistance were, the larger was the relative decrease in resistance (see inset in Figure 3.20). For the sample infiltrated at 210°C the resistance decreased by a factor of 1.8 from 203 Ohm to 115 Ohm, while for the sample infiltrated at 135°C the resistance decreased by a factor of 3.6 from 1411 Ohm to 385 Ohm. Without irradiation the reduced resistance of the hybrids remained. For example, for the sample infiltrated at 135°C, the resistance increased from 385 Ohm to 392 Ohm after 5 hours (Figure 3.20).
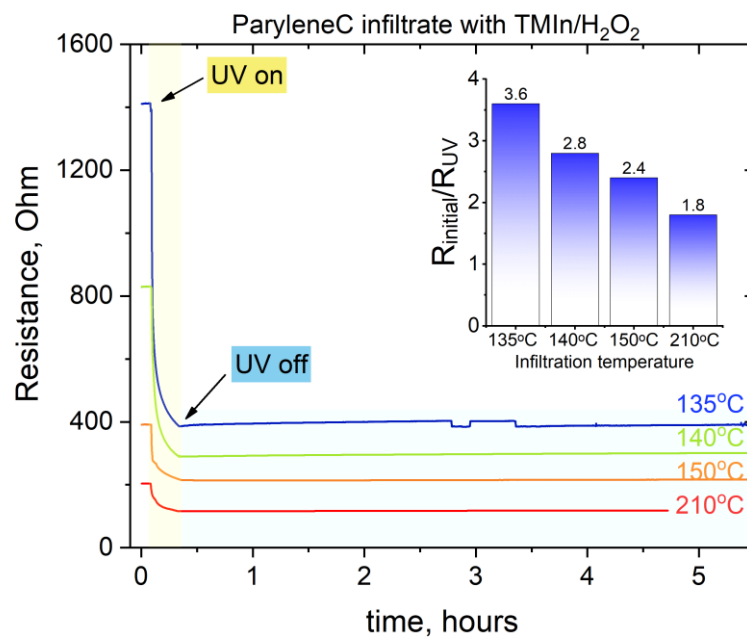

Figure 3.20 Evolution of resistance upon UV irradiation of ParyleneC infiltrated with 150 cycles of TMIn/H$_2$O$_2$ at different infiltration temperatures. The ratio of the values of the resistances before and after 15 minutes of UV irradiation is shown in the inset.

The sheet conductance after UV irradiation was measured in a 4-probe setup applying the Van der Pauw method. The measurements were repeated once per day during the first 5 days after UV-light irradiation and in longer time intervals thereafter as shown in Figure 3.21. Between the measurements the samples were stored in a dark place at room temperature in air while during the measurement they were still exposed to the laboratory light. For comparing samples obtained at different infiltration temperatures, the sheet conductance values were normalized to the conductance value just after the finalization of UV irradiation G(t=0) = 1 (Figure 3.21), where t is time, and G is the conductivity. The striking feature of the UV-induced conductivity of indium oxide is that the recombination of additional charge carriers is extremely slow. The photo-induced

conductivity can stay stable for days, and the rate of the conductivity decay of the samples produced at 210°C and 135°C remains comparable.
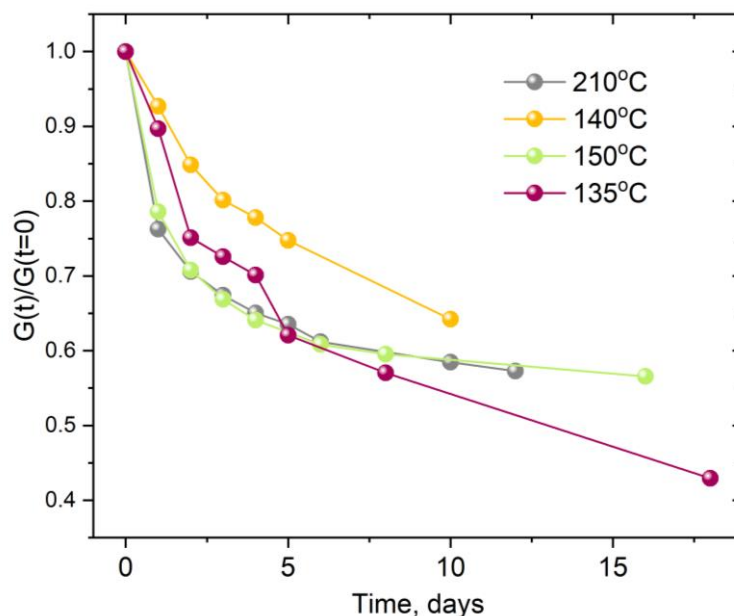

Figure 3.21 Time decay of the conductance of the ParyleneC/In$_x$O$_y$ hybrid obtained after 150 cycles of TMIn/H$_2$O$_2$ infiltration at different temperatures: 135°C, 140°C, 150°C, and 210°C.

The PPC of polycrystalline indium oxide was investigated earlier by Dixit et al. [209] It was shown that the photo-induced conductivity of an indium oxide film decreased to 0,4G(t=0) within the first 10 hours. [209] The recombination rate was reduced by placing the indium oxide sample into vacuum, and the conductivity dropped to only 0.7G(t=0). The authors further decreased the recombination rate by cooling the sample. In our work, such a conductivity drop for the UV-irradiated hybrids took place over more than 10 days. However, in the study of Dixit the resistance after irradiation decreased by two orders of magnitude, while it decreased by one order of magnitude in our work. The use of vacuum conditions in the study of Dixit could facilitate oxygen photoreduction reactions and lead to a larger PPC. [209] The proposed mechanism is the partial reduction of the indium oxide under UV irradiation in vacuum or inert gas conditions. This may lead to the creation of oxygen vacancies which act as dopants and enhance the conductivity. A range of various amorphous metal oxides with inherent persistent photoconductivity has been investigated, such as indium-gallium-zinc oxide, indium-strontium-zinc oxide, indium-strontium-oxide, indium-zinc-oxide. [212] Such materials can act in a similar way as the short-term and long-term memory of the brain, in this way mimicking the functionality of neurons. In the mentioned systems, indium is the component responsible for the PPC enhancement. Therefore, the development of the polymer-based indium oxide hybrids with persistent photoconductivity can open new horizons for the construction of the devices with a neuromorphic architecture.

3.5 Conclusions

We developed and studied a novel semiconductor-based flexible conductive hybrid, comprised of indium oxide NPs distributed inside the polymer ParyleneC. We showed that the use of hydrogen peroxide as the second precursor in a TMIn-based VPI process is beneficial over the use of water. The reactivity of H_2O_2 is responsible for the higher GPC of the TMIn/H_2O_2 VPI, deeper infiltration depths, and lower onset temperatures for the crystallite formation of indium oxide than the TMIn/H_2O process. The formed hybrids had sheet resistance values down to 3 kOhm/□ without an additional annealing step, despite the formation of indium chloride alongside with In_xO_y. The TMIn/H_2O_2 samples showed deeper infiltration and a narrower band gap, which led to values of sheet resistance being one order of magnitude lower than those of the TMIn/H_2O samples processed at 210°C. This difference increased to more than five orders of magnitude upon infiltration below 150°C. Interestingly, in contrast to TMIn/H_2O, the sheet resistance of TMIn/H_2O_2 was not considerably affected by the processing temperature with changes remaining within one order of magnitude. The bending tests proved that indium-based hybrid structures can withstand multiple bending events. Even the formation of additional conduction pathways is possible through rearrangement of inorganic NPs within the polymer matrix following the previously reported self-healing properties. Since ParyleneC is a dielectric and indium oxide a wide band gap semiconductor, the merged structures have application potential as flexible electrodes in, for example, wearable electronics, displays, solar cells, or medical sensors. In addition, being derived from ALD, the VPI process can be performed in an ALD reactor (minor adaptations may be required) and the sample fabrication can be upscaled to industrial sizes or quantities. Besides, such processes can be integrated into production lines, opening many perspectives for future applications of the described organic-inorganic hybrids.

4

Zinc oxide-based hybrid materials

Zinc oxide is a wide band-gap II-VI semiconductor that is prospective for numerous applications due to its high transparency to visible light, piezoelectric properties, tunable electronic conductivity, absorbance of ultraviolet light and the thus related antibacterial properties. The most discussed applications of ZnO include sensors for gases and chemicals, catalysts, solar cells, UV light-emitting diodes, and thin-film transistors. [213]–[216] Many doping strategies to enhance specific properties of ZnO are known and only ALD enabled the synthesis of ZnO films with 22 different dopants. [217] The most prominent examples, In-doped ZnO or Al-doped ZnO, are being considered as substitutes for ITO due to their low cost and considerable conductivity.

Among the variety of known ALD precursors for ZnO deposition, DEZ is by far the most common as it exothermically reacts with water even at room temperature (Equation 15):

$$Zn(C_2H_5)_2^* + H_2O(g) \rightarrow ZnO^* + 2C_2H_6(g) \qquad \text{(Eq. 15)}$$
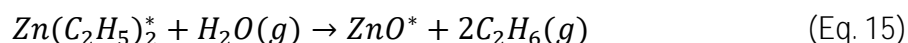
Due to the wide applicable temperature range and great performance, DEZ is the precursor of choice for the majority of ALD and VPI ZnO processes. Infiltration of DEZ has been applied to many polymer systems to manipulate their properties. For example, DEZ infiltration allowed tuning of mechanical properties of cellulose, [24] greatly enhanced the conductivity of polyaniline (PANI), [218] altered the porosity of polymers, [132] prevented dissolution of cis-polyisoprene in toluene, [219] and induced high photoluminescence in PMMA. [220] Other studies deepened the fundamental understanding of VPI, such as the effect of the solvent residues inside the SU-8 resist on infiltration, [33] or the mechanism of infiltration of nonreactive polymers such as poly(3-hexylthiophene). [221]

4.1 Zinc oxide infiltration into ParyleneC

4.1.1 Structure of ParyleneC/ZnO hybrid from DEZ/H$_2$O VPI

We performed VPI of ParyleneC with DEZ and water at a range of temperatures from 80 to 200ºC. DEZ has a wide reactivity window and a high vapor pressure at ambient pressures, which makes it attractive for applications to polymeric substrates. However, the best optically and electrically performing films are obtained at elevated processing temperatures of 90-200ºC, as known from ALD studies. [213] Heating of the whole system can further facilitate the VPI process since the available free volume of a polymer increases with the temperature. Upon post-investigation of the FIB cross-sections of ParyleneC/ZnO samples, we observed hybrid layers with different thicknesses (Figure 4.1).
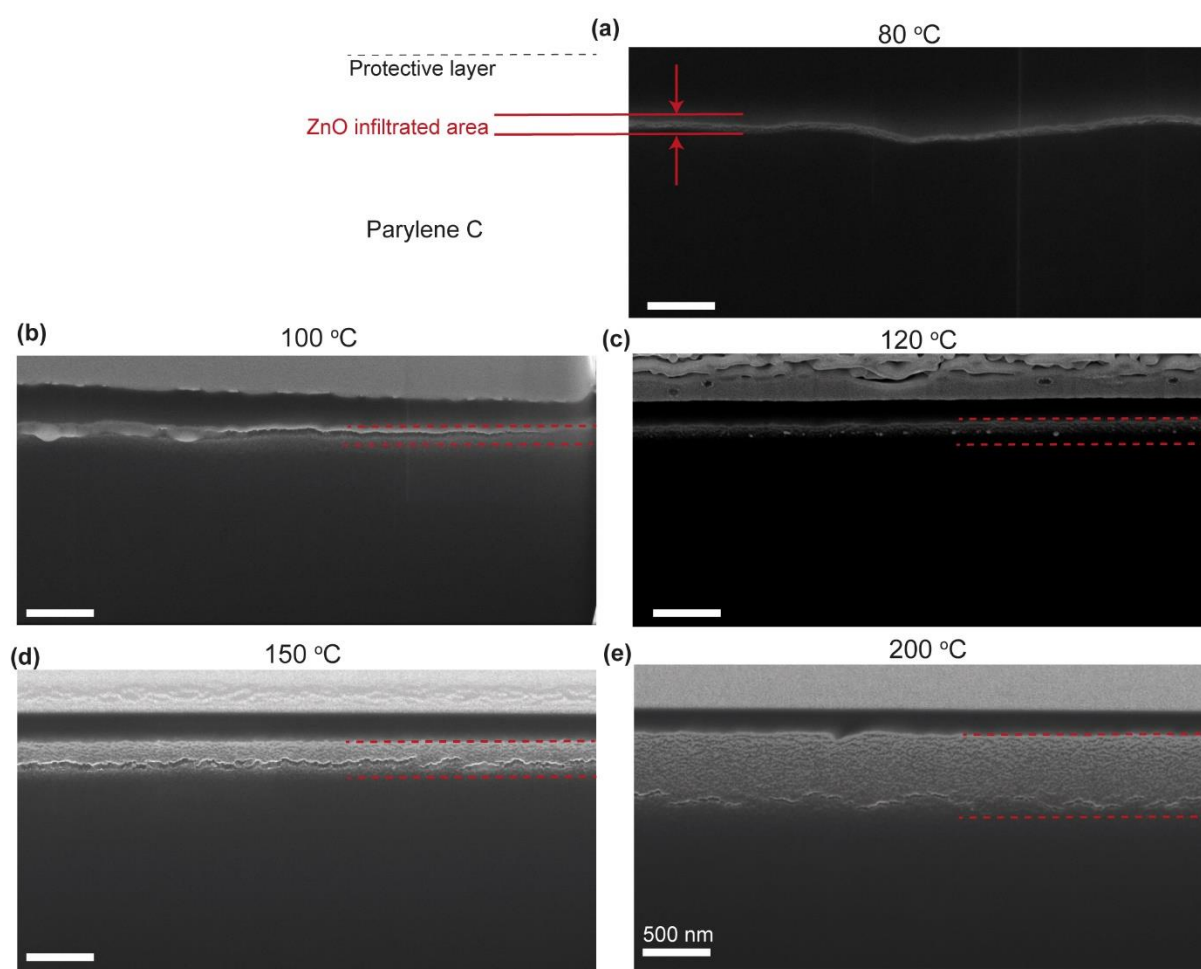

Figure 4.1 FIB cross-sections of the ParyleneC/ZnO hybrids infiltrated with 100 VPI cycles of DEZ/H$_2$O at different processing temperatures: (a) 80ºC; (b) 100ºC; (c) 120ºC; (d) 150ºC; (e) 200ºC. The scale bars in all images represent 500 nm.

Unexpectedly, the ParyleneC/hybrid interfaces partially degraded under the electron beam with an accelerating voltage of 5kV and a current of 50pA, as seen on the cross-sections in Figure 4.1 b, d, e. The formed hybrid layers delaminated from the polymer, inducing a crack which propagated on the ParyleneC/hybrid interface. The reason for this delamination might be ion etching which may occur during the preparation of the FIB cross-sections.

The high reactivity of DEZ resulted in higher infiltration depths than the indium oxide infiltration. The thickness of the hybrid reached 880 nm at 200°C, while it was only 300 nm for the comparable ParyleneC/In_xO_y hybrid processed at 210°C (Figure 4.2). The thickness of the hybrid didn't exceed 200 nm for infiltration temperatures lower than 120°C, followed by a markable increase of the infiltration depth with temperature. It is not likely that this increase is linked to overcoming the glass transition temperature (Tg) of the polymer, since the Tg of ParyleneC is only 90°C. [160] Neither is it caused by an enhanced GPC, as the GPC of the DEZ/H_2O ALD process is known to reach the maximum at 150°C and then decreases by 35% at 200°C. [222] Presumably, an incremented kinetic energy of DEZ and H_2O at high temperatures is the reason for the enhanced precursor diffusion and, consequently, higher infiltration depths.
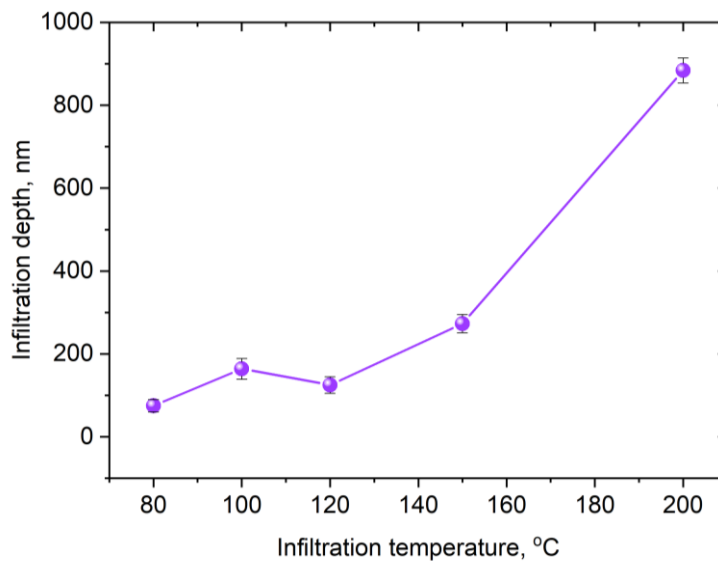

Figure 4.2 Evolution of the infiltration depth of ZnO into ParyleneC as a function of the processing temperature.

The SEM images of the surfaces of the ParyleneC/ZnO hybrids are shown in Figure 4.3 a, b, c, d. They are smooth, but polycrystalline as proven by XRD (Figure 4.4). The crystalline patterns show wurtzite-type zinc oxide. [181], [223] The signals from the most pronounced crystalline planes (100), (002), and (101) are seen for all infiltration temperatures, which is characteristic for the formation of disoriented nanocrystallites. In contrast, the formation of columnar structures with a preferential <002> ZnO orientation was observed upon the use of hydrogen peroxide as oxygen-containing precursor instead of water. [223]
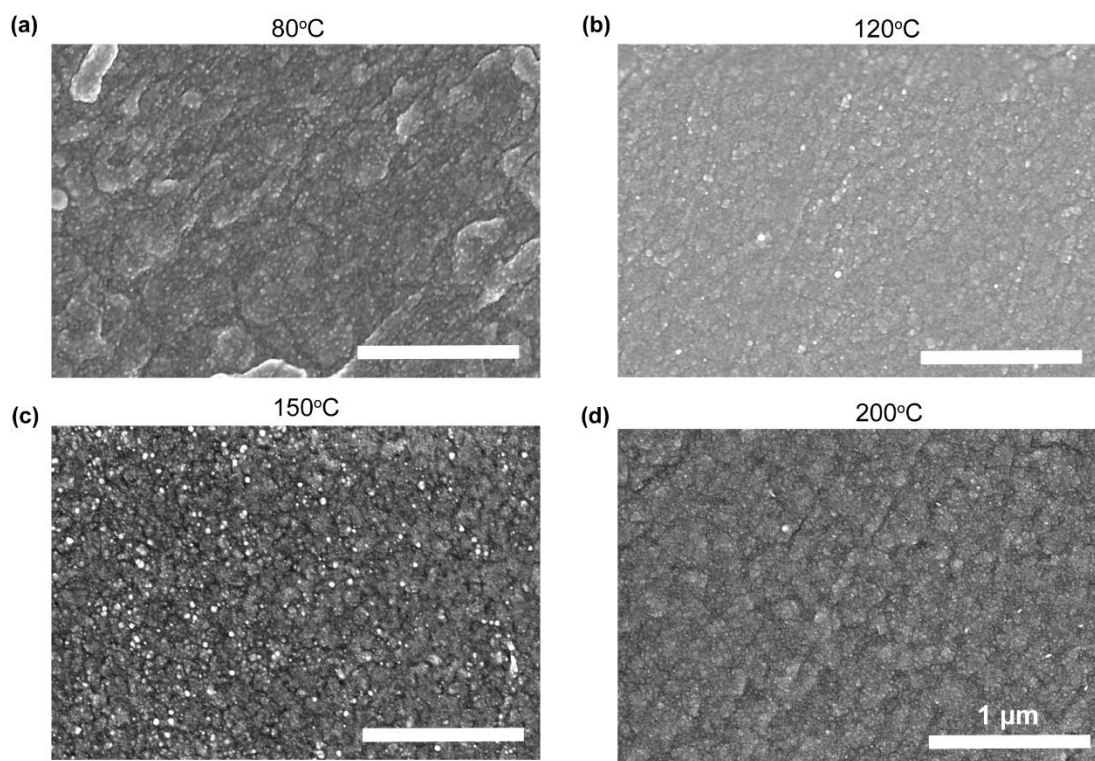
69

Figure 4.3 SEM top view micrographs of the ParyleneC/ZnO hybrids after 100 DEZ/H_2O cycles at various VPI processing temperatures: (a) 80°C, (b) 120°C, (c) 150°C and (d) 200°C. The scale bars in all images represent 1 µm.

The hybrids infiltrated at 200°C showed more intense diffraction peaks if compared to the those obtained at 100°C and 150°C (Figure 4.4). The Scherrer equation allows estimating the size of the crystallites from the XRD data (Equation 16). It describes the relation between the size of nanocrystallites and the broadening of a peak in a diffraction pattern.

$$d = \frac{K\lambda}{\beta cos\theta}$$
(Eq. 16)

In this equation d is the average size of the crystallites, K is a dimensionless shape factor, λ is the X-Ray wavelength, β is the line broadening (full width) at half of the maximum intensity (FWHM) in radians, and θ is the Bragg angle. The coefficient K can have different values and is 0.9 for spherical particles. The size of the ZnO crystallites in the ParyleneC/ZnO samples reached 10.0, 11.5, and 11.1 nm for the samples infiltrated at 100°C, 150°C, and 200°C, respectively.

Zinc oxide is a wide band-gap semiconductor transparent to visible light. It has a direct optical band gap of 3.2-3.4 eV, [214], [224], [225] which makes ZnO applicable in several photoelectronic applications. Unmodified ParyleneC is transparent in the visible region and starts to absorb near UV light with an abrupt increase in absorption when the wavelength becomes less than 300 nm (Figure 4.5 a). Upon ZnO infiltration, the absorbance of the hybrid in the near UV region drastically increases, and this behavior is more prominent at higher infiltration temperatures. At the
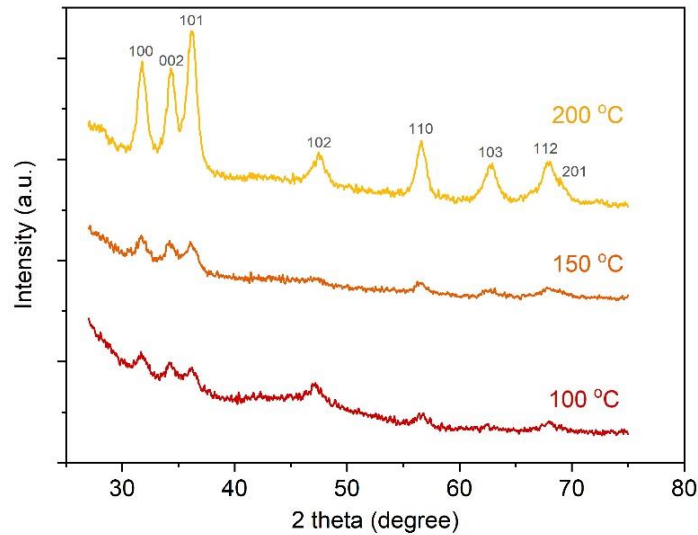
Figure 4.4 XRD patterns of the ParyleneC/ZnO hybrids after VPI of DEZ/H_2O at different infiltration temperatures: 100°C, 150°C, and 200°C.
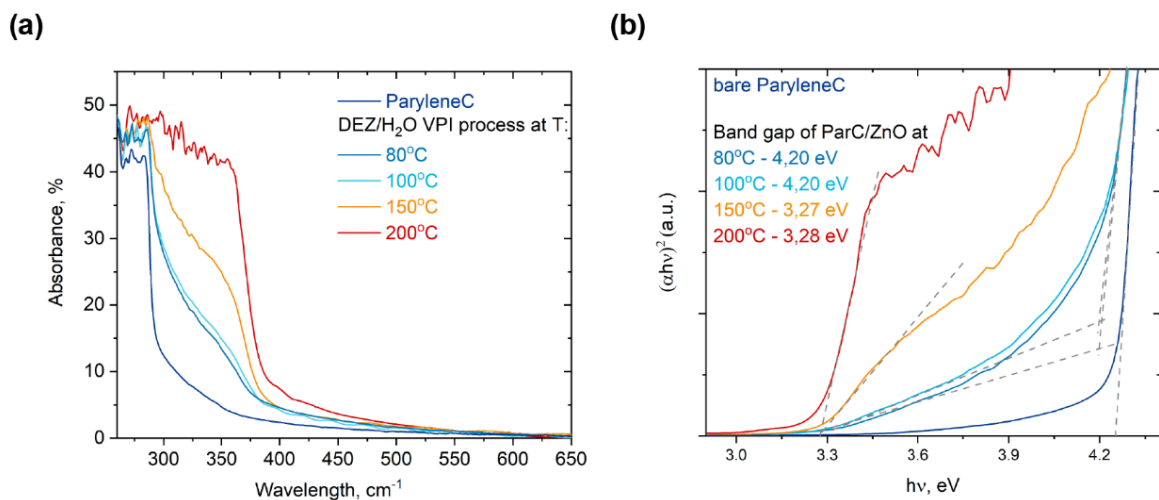

Figure 4.5 (a) Optical absorbance spectra of ParyleneC after infiltration with100 DEZ/H_2O cycles at different process temperatures as indicated in the legends. (b) Tauc's plots derived from absorbance spectra in Figure 4.5a.

same time, the transparency in the visible region remains. For example, at the wavelength of 550 nm, the absorption doesn't exceed 1.5 % (Figure 4.5 a). The direct band gaps of the hybrids were estimated from the Tauc's plot by extrapolating the fit of the linear region to α=0 or the baseline (Figure 4.5 b). [138] The direct band gap energy was 3.27 and 3.28 eV for the hybrids infiltrated with DEZ/H_2O at 150°C and 200°C, respectively. These values match the band gaps reported for the undoped ZnO while doping with chlorine can alter the band gap to higher energies. [224]

4.1.2 Structure of ParyleneC/ZnO hybrid from DEZ/H_2O_2 VPI

Hydrogen peroxide can substitute water as oxygen-containing ALD or VPI precursor in zinc oxide processes. For the indium oxide deposition with TMIn, hydrogen peroxide facilitates higher GPC, crystallinity, and polymer infiltration depths. However, the zinc oxide growth from DEZ and hydrogen peroxide does not always bring about benefits, especially for potential electronic applications. It was shown that the use of H_2O_2 led to lower GPC compared to a standard DEZ/H_2O process. [215] Besides, the oxygen-reach conditions of the DEZ/H_2O_2 process lowered the formation of oxygen vacancies (O_v). [223] The absence of O_v dopants led to an increase in ZnO resistivity and a decrease in carrier concentration and mobility. [223] Despite the mentioned drawbacks of the hydrogen peroxide use in ALD, the VPI process may perform differently and therefore the VPI of DEZ/H_2O_2 should be studied. Besides, for a growth of IZO, the H_2O_2 may prove beneficial for the indium oxide component.

The infiltration of ZnO with 100 DEZ/H_2O_2 cycles at 200°C and 30 seconds of exposure time resulted in an infiltration depth of 400 nm (Figure 4.6 a), which is about half as much as that of the DEZ/H_2O process (Figure 4.1e). Interestingly, the cross-sectional SEM image of the hybrid material shows a high density of inorganic moieties. The intense signal of the secondary electrons drops after 200 nm depth, indicating an alteration in the density of the inorganic moieties dispersed in the organic-inorganic layer. Apart from tuning the processing temperatures, a variation of the VPI exposure times allows adjusting the infiltration depth. An increase in exposure time from 30 to 50 seconds resulted in a 50% increase in the hybrid layer thickness, from 400 to 600 nm (Figure 4.6 b). In both cases, after 30 seconds and 50 seconds of exposure time, two distinct areas with different densities of infiltrated ZnO NPs were observed (Figure 4.6).
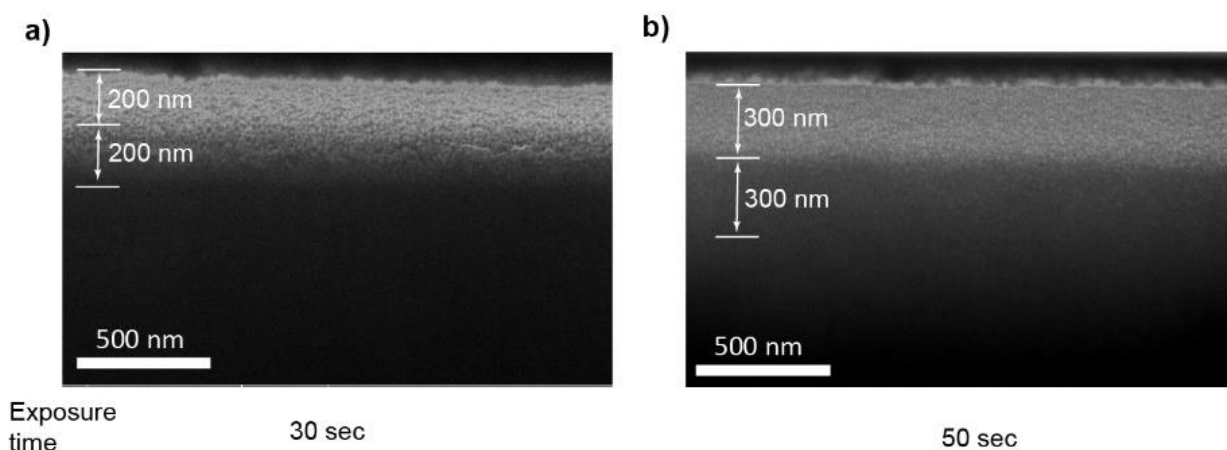

Figure 4.6 SEM micrographs of cross-sections of the ParyleneC/ZnO hybrids after 100 VPI cycles of DEZ/H_2O_2 at 210°C and different exposure times: (a) 30 and (b) 50 seconds.

Substitution of water with hydrogen peroxide also led to the wurtzite-type polycrystalline structure of zinc oxide (Figure 4.7). However, in this case the XRD peaks appeared to be less prominent. The most intense XRD peak after the DEZ/H_2O process arose from the (101) crystalline plane, while

in the case of hydrogen peroxide the highest intensity came from the crystalline plane (002). This is consistent with observations in previous works on ZnO deposition by ALD. [181], [214], [226] The crystalline orientations of ZnO are strongly influenced by the growth rates and, consequently, the reaction temperature. At a low deposition temperature of 100^oC the DEZ/H_2O ALD- grown zinc oxide has a preferential growth in the <002> orientation. The (002) plane has a low surface energy, which drives this thermodynamically favorable growth. [181] However, with increased deposition temperature the GPC also increases. The atoms do not have sufficient time to move and relax at sites of lower surface energy, and other crystalline planes - (100) and (101) - start dominating. Such a suppression of the plane (002) doesn't occur for DEZ/H_2O_2, as the GPC of this process remains lower than that of the DEZ/H_2O process.
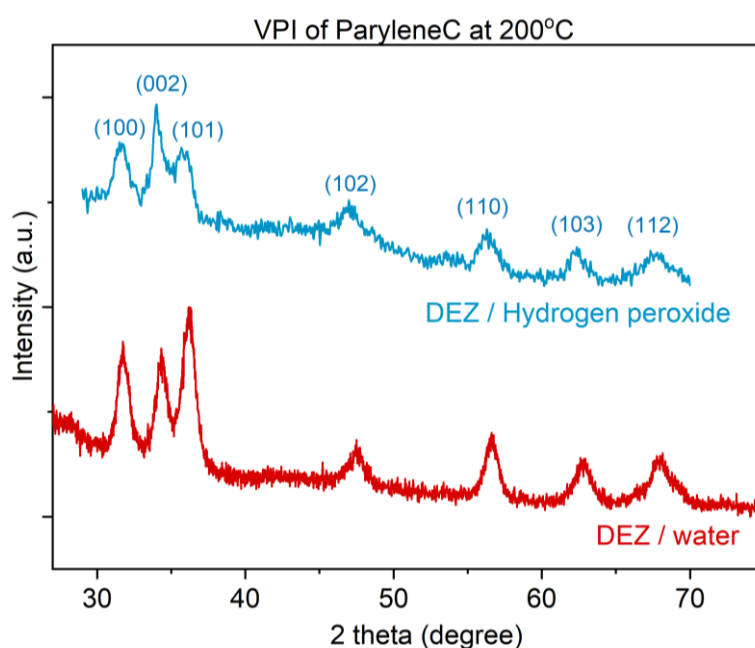

Figure 4.7 XRD patterns of ParyleneC/ZnO hybrids obtained after VPI with 100 cycles of DEZ/H_2O and DEZ/H_2O_2 at 200^oC.

Zinc oxide NPs grew inside the polymer in the confinement of polymer chains, which could induce additional stress and alter a local crystalline structure within the hybrid layer. Besides, even post-treatment of ZnO films with hydrogen peroxide is sufficient to turn ZnO partly into zinc peroxide, which was shown previously. [227] To evaluate the possibility of ZnO_2 formation within the hybrid material, we performed TEM investigations on a ParyleneC/ZnO lamella (Figure 4.8a). The hybrid material consists of inorganic nanocrystals with sizes of less than 5 nm that are dispersed within the polymeric matrix. FFT of the micrograph in Figure 4.8a gives an electron diffraction pattern in the reciprocal space (Figure 4.8 b). The measured interplane distances correspond to wurtzite-type zinc oxide (Table 4).
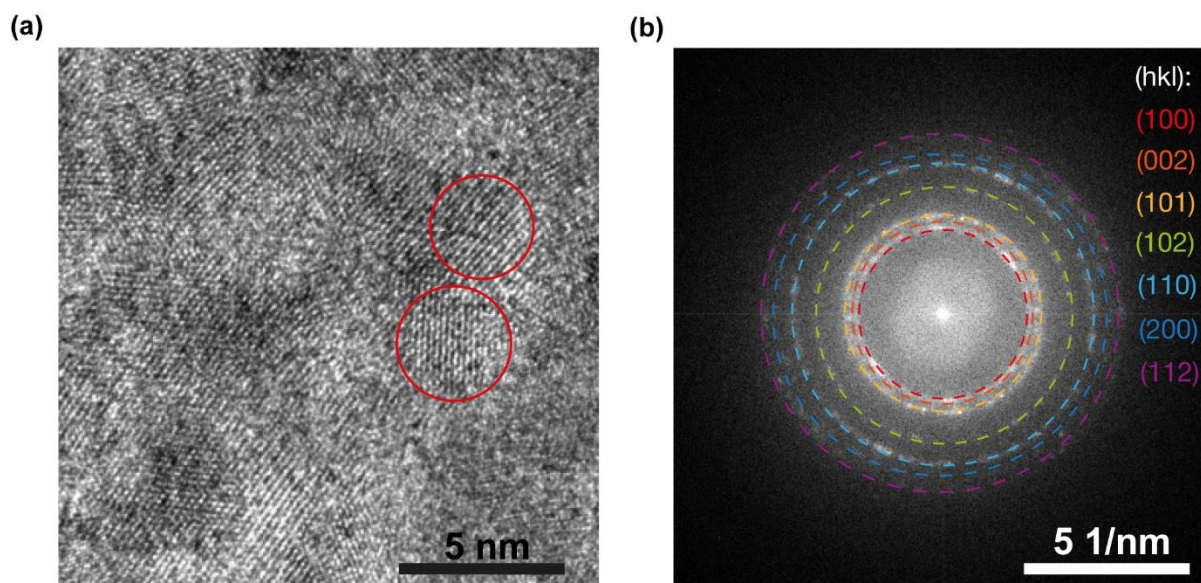
(a)

(b)

Figure 4.8 (a) TEM micrograph of inorganic clusters formed in ParyleneC after infiltration with 100 DEZ/H_2O_2 cycles at 210°C. The red circles mark two nanocrystals inside the polymer matrix (b) FFT image of the micrograph depicted in (a).

Table 4. Interplane spacings of ZnO measured from Figure 4.8(b), compared to the calculated X-ray diffraction pattern.

hkl	d_{hkl} (Å) measured	d_{hkl} (Å) calculated [228]
(100)	2.91	2.848
(002)	2.66	2.653
(101)	2.52	2.510
(102)	1.97	1.942
(110)	1.68	1.645
(200)	1.53	1.503
(112)	1.41	1.398

4.2 Chemical structure of the ParyleneC/ZnO hybrid system

The chemical characterization of the ParyleneC/ZnO obtained with the DEZ/H_2O_2 process, as measured by EDX (Figure 4.9 a) and XPS (Figure 4.9 b), proved the formation of the hybrid with simultaneous presence of carbon, chlorine, zinc, and oxygen. The EDX depth profiles indicated a

formation of the hybrid starting from the very surface down to a depth of about 450 nm. The ratio of Zn to O varied from 0.75 to 1.25 from the surface towards the hybrid/polymer interface. Interestingly, the hybrid layer showed a high atomic concentration of chlorine. While in the pristine polymer the concentration of chlorine should be around ~ 6 at.%, in the hybrid layer it reached even 15 at.% (Figure 4.9 a).
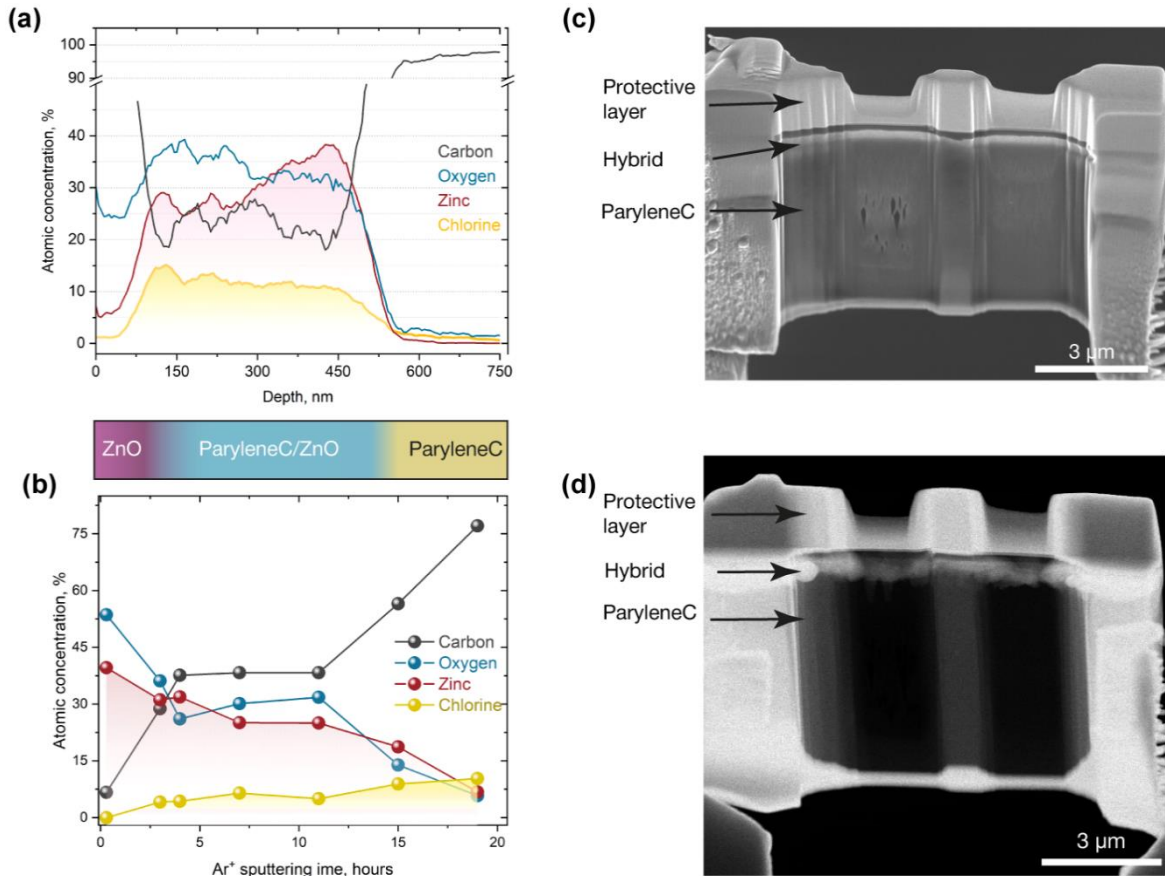

Figure 4.9 Chemical composition of the ParyleneC/ZnO hybrid after 100 VPI cycles of DEZ/H$_2$O$_2$ at 210°C: (a) EDX depth profile obtained during TEM measurements on cross-sectioned lamellas; (b) XPS atomic concentration depth profiles; (c) SEM image of a ParyleneC/ZnO lamella before exposure to air; (d) TEM micrograph of a ParyleneC/ZnO lamella after *ex-situ* transfer and thus exposure to air. Image taken with permission from the Ref. [118]

We prepared lamella with less than 100 nm thickness for the TEM investigations by FIB (Figure 4.9 c). Surprisingly, the lamella appeared to substantially change in the SEM-FIB chamber before exposure to air (Figure 4.9 c) and after the transport to the TEM chamber in ambient conditions (Figure 4.9 d). The lateral surface of the hybrid became overgrown (Figure 4.9 d). The possible explanations are the redistribution of the inorganic nanoclusters, initially dispersed within the restricted lamella volume, or chemical reactions. Such pronounced mobility of inorganic clusters

opens the pathway to the self-healing functionality of the ParyleneC/ZnO hybrid, which is discussed in further detail in Chapter 5. The EDX spectra shown in Figure 4.9 a reflect the chemical composition of the ParyleneC/ZnO hybrid that reacted with air upon sample handling. The observed newly grown part was confirmed to be an intermix of carbon, chlorine, zinc, and oxygen.

Unlike the EDX measurements, the XPS depth profiles were measured *in-vacuo*. Ar$^+$ ion etching steps and intermediate spectra collection were performed within the same vacuum chamber without exposure of a sample to air. A 10-minute Ar$^+$ ion etching step helped to clean the surface from the atmospheric contaminants. At this near-surface layer, a chlorine admixture was not yet detected, while the concentration of carbon reached 6.7 at.% (Figure 4.9 b). This carbon admixture can be related to impurities introduced by the VPI process or the hybrid material formation. Despite the usage of hydrogen peroxide as precursor, zinc oxide was oxygen-deficient with a Zn:O ratio of ~0.7:1. At the same time a concentration of 6.7 at.% of carbon was measured. With proceeding etching time, the ratio of Zn to O increased and reached 1.3 after 15 hours of sputtering. Within the analyzed hybrid thickness, the chlorine concentration varied from 4.1 at.% to 10.3 at.%, increasing from the surface towards the hybrid/polymer interface. The chlorine distribution is, however, not identical in the EDX and XPS measurements. In XPS, with the measurements having been performed in-vacuo, the amount of chlorine slowly increased from the surface towards the hybrid/polymer interface. In the EDX measurements, the chlorine amount is the highest in the hybrid area and decreased towards 3 at.% in the bulk of the polymer.

Similar to indium oxide, after VPI of ZnO the XPS spectrum showed chlorine in two different states, namely bound to carbon or to zinc (Figure 4.10 a). The appearance of the second Cl 2p doublet is evident from a comparison of the chlorine signals after 20 minutes and 3,5 hours of Ar$^+$ ion sputtering. The Cl 2p signal at 200,8 eV becomes wider and the shape changes, which points towards a coexistence of Cl-C and Cl-Zn bonds near the sample surface.

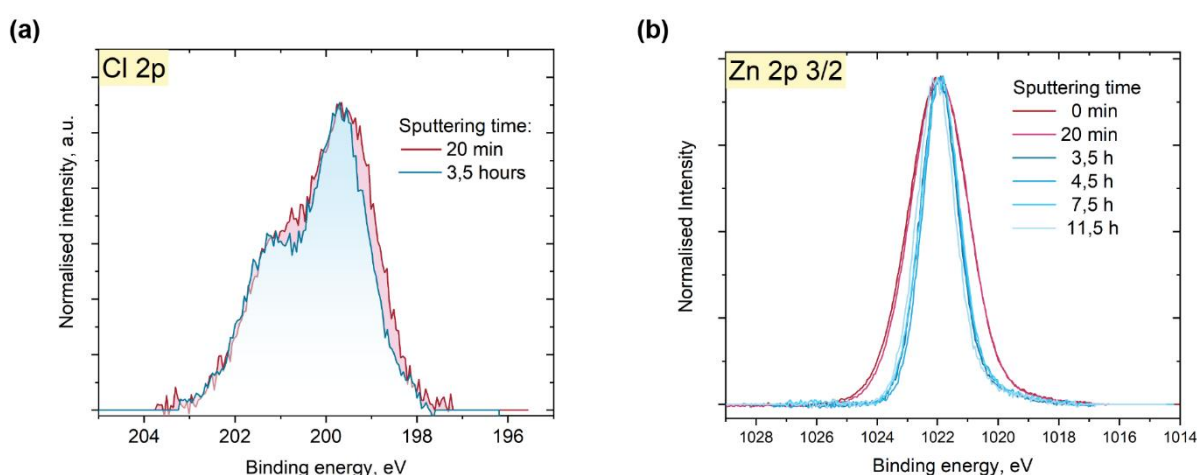Figure 4.10 XPS characterization of the ParyleneC/ZnO hybrid after 100 VPI cycles of DEZ/H$_2$O$_2$ at 210°C. Depth evolution of the (a) Cl 2p, and (b) Zn 2p 3/2 doublets with the indicated sputtering time. Image taken with permission from the Ref. [118]

However, in contrast to the Cl-In in the ParyleneC/In$_x$O$_y$ system (Figure 3.4 b and Figure 3.5 b) the amount of the Cl-Zn bonds is marginal and the main component is polymer-bound Cl. In the same manner the signal of Zn 2p 3/2 near the surface differs from that in the bulk (Figure 4.10 b). The peaks in the spectra collected from the surface and after 20 minutes of sputtering with Ar$^+$ ions are wider than the peaks collected after 3.5 hours of sputtering and more. The larger width indicates that the Zn near the sample surface is present in two different states, which is in line with the presence of the near-surface chlorine. Importantly, zinc oxide clusters are Cl-free in the bulk of the hybrids.

The oxygen signal in the XPS consists of three components, located at binding energies of 531.2, 532.0, and 533.3 eV (Figure 4.11). The peak position at the lower binding energy side of O1s corresponds to oxygen bound to Zn and stays intense throughout the whole measured thickness. The peak at 532.0 eV resembles the oxygen vacancies, and their amount decreases with the etching depth. [229] The component with the highest binding energy of 533.3 eV stems from O-H bonds, [227], [229] which has a moderately high intensity at the as grown surface and after 20 minutes of Ar$^+$ ion sputtering. The hydroxide species and oxygen vacancies may originate from the interaction of the sample surface with air and therefore are less intense in the bulk of the hybrid.
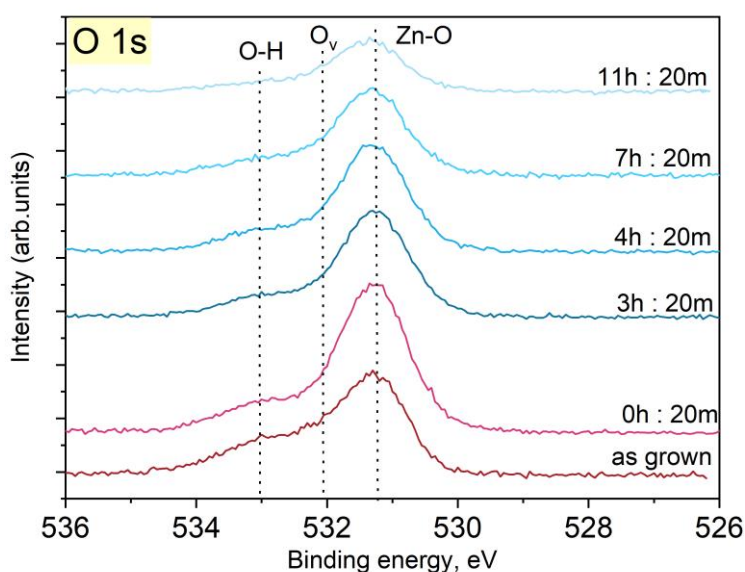

Figure 4.11. Depth evolution of the O 1s XPS peak of the ParyleneC/ZnO hybrid after 100 VPI cycles of DEZ/H$_2$O$_2$ at 210°C with the sputtering time.

4.3 Reaction kinetics of DEZ/H$_2$O$_2$ infiltration into ParyleneC

4.3.1 Infrared absorption of the ParyleneC/ZnO hybrid

Like the ParyleneC/In$_x$O$_y$ system, the analysis of the ParyleneC/ZnO hybrid by FTIR is complicated. VPI modifies only the near-surface layer, about 100-900 nm in dependance on the precursor choice and used temperature, while the remaining thickness of the polymer is unchanged. Therefore, the FTIR spectrum is dominated by the ParyleneC substrate. We aggregated 101 FTIR spectra for the zinc oxide-infiltrated polymer and compared it with 23 aggregated spectra of untreated ParyleneC. The standard deviation of each data set is shown in the graph with lighter colors: light blue for ParyleneC/ZnO and light gray for ParyleneC.

After infiltration of the polymer with ZnO, the shape of the peaks at 1607 and 1555 cm^{-1} changed. Besides, a new peak appeared at 1514 cm^{-1}, suggesting the augmentation of skeletal vibrations of aromatic C-C carbon (Figure 4.12). [191]–[193] The complex region of the C-O stretch and C-O-H vibrations for Parylene-C is located at 1421 cm^{-1}. The growth of zinc oxide in the polymer bulk increased the absorption in the 585-530 cm^{-1} region. [230] No new peaks in the region 900-800 cm^{-1} were observed, pointing towards an absence of ZnCl$_2$.
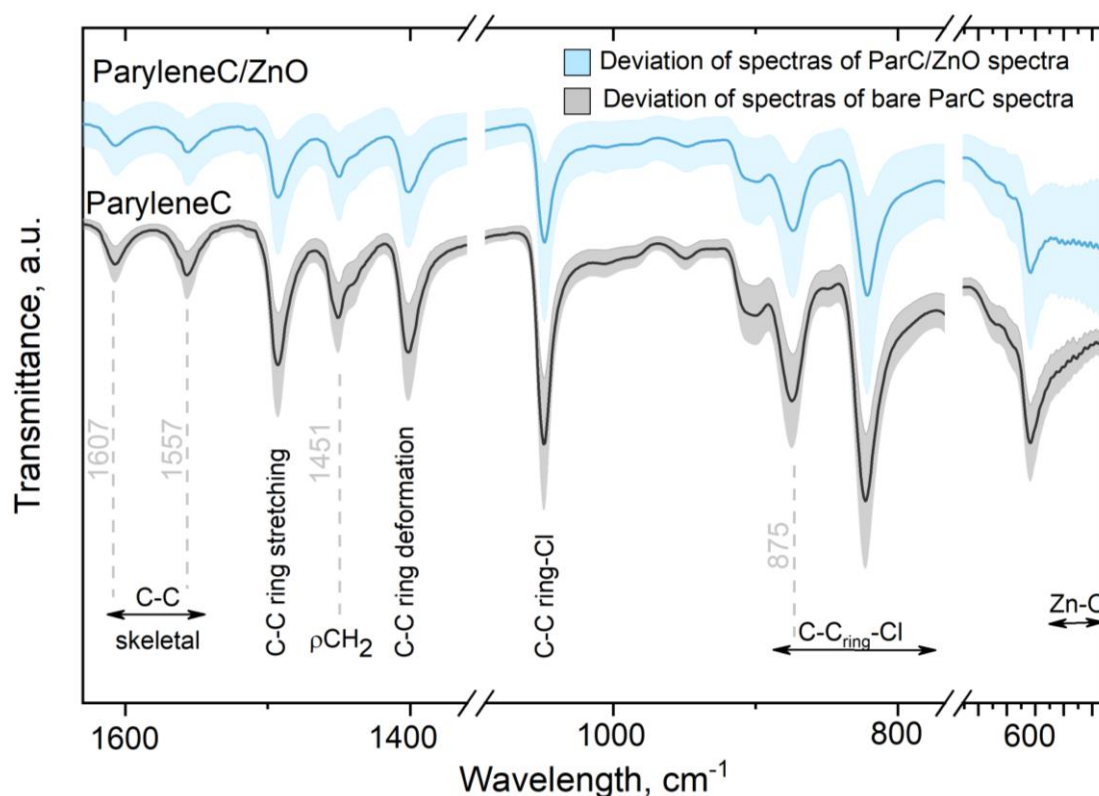

Figure 4.12 Aggregated ATR-FTIR spectra, including indicated deviations, of ParyleneC (gray) and ParyleneC/ZnO (light blue).

The thermal stability of ParyleneC was evaluated by TGA in a nitrogen flow. The thermal degradation of the ParyleneC/ZnO hybrid happened in the temperature range of 30-722°C, which is 88°C less than for the neat polymer (Figure 4.13 a). An infiltration of zinc oxide into ParyleneC lowered the onset of the material degradation by 2°C, as shown with DTA (Figure 4.13 b). The thermal degradation of the hybrid started at 504°C and progressed much slower that the untreated ParyleneC until 675°C. Beyond this temperature the hybrid degraded faster than ParyleneC. Alteration and improvement of the thermal stability of various polymers after VPI hybridization was also observed in earlier works. [31], [130], [231]
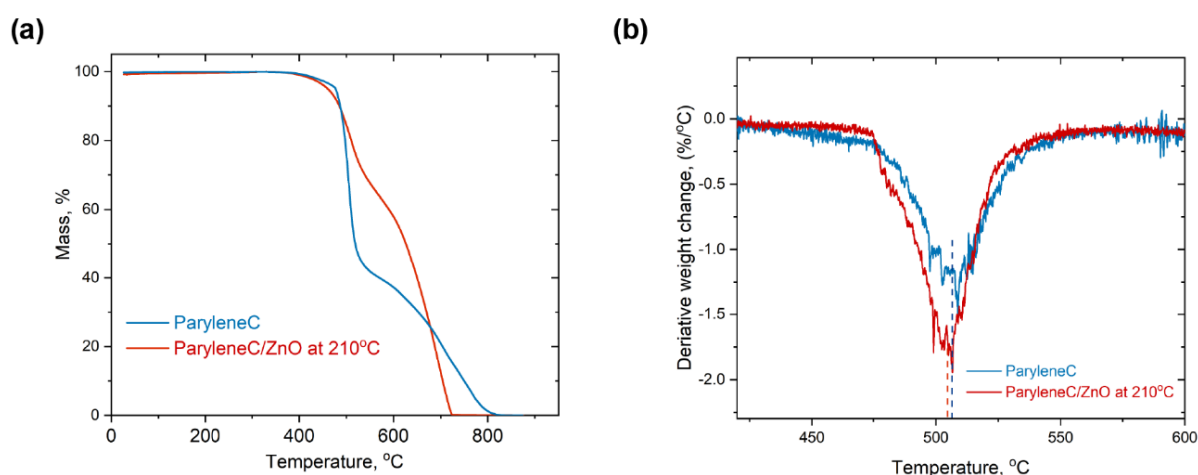

Figure 4.13 Comparison of (a) TGA and (b) DTA of pristine ParyleneC and ParyleneC infiltrated with 100 VPI cycles of DEZ/H$_2$O$_2$ at 210°C.

4.3.2 Density functional theory calculations of DEZ and H$_2$O$_2$ infiltration

To understand the growth mechanism of ZnO-infiltrated ParyleneC films, the system was modelled by DFT. Figure 4.14a shows the atomic structure of the applied model of ParyleneC chains infiltrated with DEZ. The calculated incorporation energy of -0.59eV shows that DEZ infiltration into the polymer is favorable and, like TMIn, that the precursor does not bind to the polymer. The energy gain upon infiltration of DEZ is higher than that upon infiltration of TMIn (-0.52eV); this is likely because DEZ, being a larger molecule than TMIn, has stronger vdW interactions with the polymer, which increases the interaction energy.

Next, we analyzed the possible reactions upon introduction of H$_2$O$_2$ and found that during the H$_2$O$_2$ pulse three reactions are possible. The first reaction involved the transfer of one H atom from the polymer chain to the CH$_3$CH$_2$ ligand of the DEZ molecule to form a new ethane molecule that is released as by-product, while the remaining Zn-CH$_2$CH$_3$ binds to the aliphatic C atom of the polymer chain from which the H atom is transferred. Upon interaction with H$_2$O$_2$, the remaining CH$_3$CH$_2$ ligand is released in form of CH$_3$CH$_2$OH and the remaining OH group from this

reaction binds to carbon-bound Zn to form C-Zn-OH with C-Zn and Zn-O distances of 1.97Å and 1.78 Å, respectively. The calculated energy for this reaction is -3.26 eV, which with the energy gain upon infiltration gives a total energy gain of -3.85eV. The resulting optimized structure is shown in Figure 4.14 b.

The second reaction involved the transfer of one Cl atom from the polymer ring to the CH_3CH_2 ligand of DEZ, releasing CH_3CH_2Cl, and CH_3CH_2OH and ZnOH that are formed after reacting with H_2O_2. The ZnOH adduct binds to the aromatic C atom from which the Cl atom was transferred, with a C-Zn distance 1.91 Å (Figure 4.14 c). The calculated energy gain for this reaction is -3.39 eV, which results in a total energy gain of -3.98eV. The elimination of CH_3CH_2 ligands from DEZ as ethane and the formation of Zn-OH was also observed in a previous study, where Kevlar was infiltrated with DEZ and H_2O. [31]

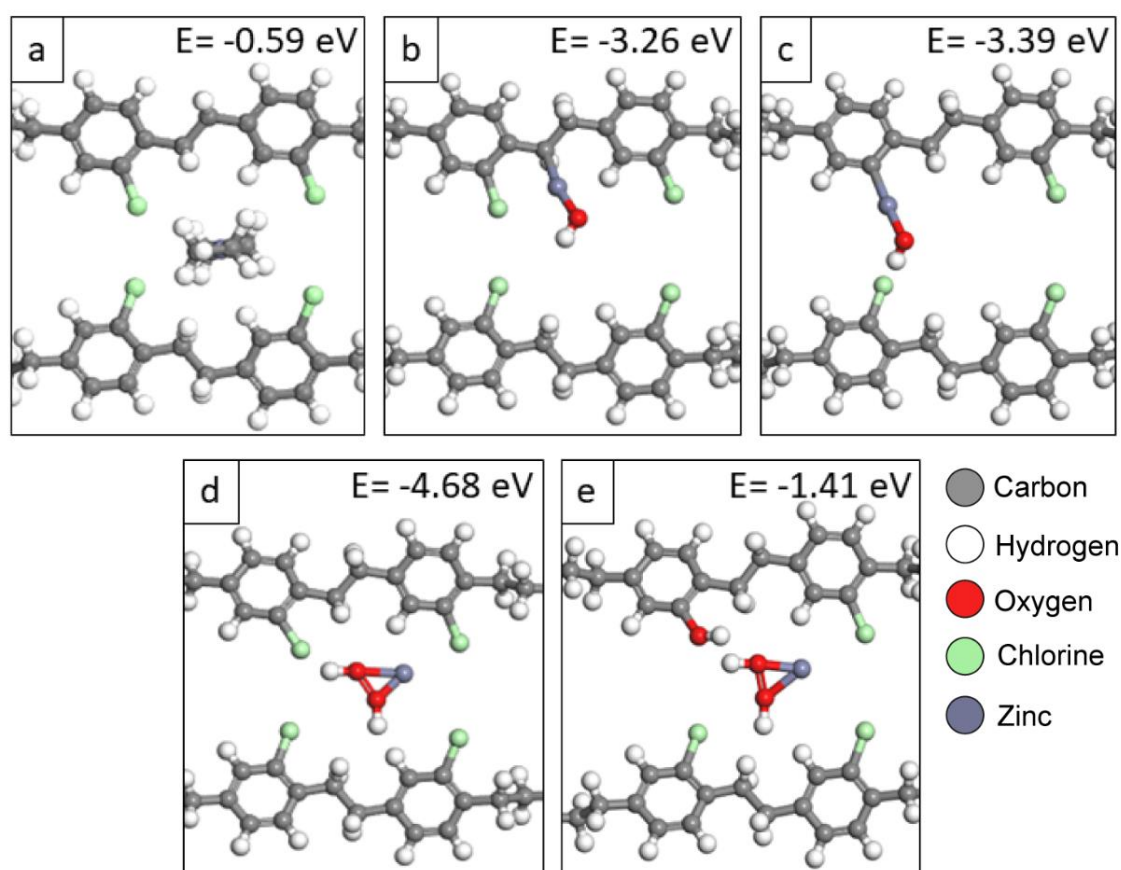Figure 4.14 Optimized structures of ParyleneC infiltrated with (a) DEZ, (b) DEZ and H_2O_2, resulting in C-Zn-OH formation, (c) DEZ and H_2O_2, resulting in ring-bound C-Zn-OH, (d) DEZ and H_2O_2, resulting in $Zn(OH)_2$ formation, and (e) DEZ and two H_2O_2, resulting in $Zn(OH)_2$ and phenol formation. Color assignment: grey – carbon, white – hydrogen, red – oxygen, green – chlorine, purple – zinc.

In the third reaction we considered the formation of the by-product butane from the two CH$_3$CH$_2$ ligands of DEZ and the formation of interstitial Zn(OH)$_2$ from the interactions with H$_2$O$_2$ as shown in Figure 4.14 d. The calculated energy gain for this reaction is -4.68 eV and the resulting total energy gain is -5.27 eV. The DFT calculations in this scenario indicate that Zn-O bonds are formed but not Zn-Cl bonds, which is consistent with the observation from XPS which indicates absence of Zn-Cl species in the hybrid. The calculations show that the formation of interstitial Zn(OH)$_2$ is very favorable.

Finally, we explored the possible reactions when a second H$_2$O$_2$ molecule is added to the system. To evaluate whether the formation of phenyl rings is favorable during this reaction, we considered the reaction product presented in Figure 4.14 c as reactant. We found that upon adding a second H$_2$O$_2$ molecule to the system it can dissociate to generate two OH groups, where one OH group replaces ZnOH in the hybrid to form a phenol ring and the other OH binds to ZnOH to form Zn(OH)$_2$ (Figure 4.14 e). The calculated energy gain of -3.84 eV indicates that the formation of Zn(OH)$_2$ and phenol is favorable.

4.4 Conclusions

ParyleneC/ZnO hybrids were obtained after VPI of DEZ/H$_2$O or DEZ/H$_2$O$_2$ in a wide range of processing temperatures. Both XRD and electron diffraction analyses showed that the hybrids contain ZnO with a polycrystalline wurtzite structure after being processed in the temperature range from 80 to 200°C. The infiltration depths reached 880 nm after VPI of DEZ/H$_2$O at 200°C with only 30 seconds of exposure time. Despite such a thick modified layer the hybrids remained optically transparent in the visible range. In contrast to the indium oxide-based hybrids, which were contained a large amount of chlorine bound to indium, after infiltration of DEZ/H$_2$O$_2$ only traces of zinc chloride were observed in the near-surface layer. The infiltration mechanism is a physical trapping of DEZ, followed by the growth of ZnO NPs within the polymer matrix. These zinc oxide NPs most likely are not chemically interacting with the polymer chains, which results from DFT calculations and is supported by FTIR and XPS measurements. The thermal resistance of the hybrid was improved when compared to pristine ParyleneC in the temperature region up to 675°C.

5

Entropy-driven self-healing of metal oxides assisted by polymer-inorganic hybrid materials

Results from this experimental chapter are published by Iurkevich et. al., Ref. [118]

5.1 Self-healing of inorganic materials

Among the most intriguing properties of many materials found in any life form is the ability to self-heal. The adaptation of such an ability into engineered materials is of paramount interest, not least in view of resource and energy efficiency since synthetic materials also suffer damage or fracture during their lifetime. The development of engineered self-healing materials has so far focused on soft matter. [50], [232] For a reliable operation of, for example, flexible electronics, the functional material should harness outstanding electrical properties together with robustness to mechanical stress. The combination of these two properties is typically found in inorganic materials such as metals and metal oxides, therefore inorganic materials which can self-recover are in high demand. [233] Examples of self-healing materials for applications in electronics and related fields are scarce. The few existing ones describe materials which can restore their crack-degraded conductivity, [234] including semiconducting polymers, [181] conductive polymer networks [90], [235] microchannels and microcapsules filled with Ga-based LM alloys, [41], [82] or metal-containing solutions, [83] and ionic hydrogels. [236], [237] Further progress remains challenging, primarily because of the lack of feasible healing agents and suitable ways to supply them to the damaged site. In theory, the most logical way to construct self-healing materials is by the entrapment of reactive precursors within the bulk material which react only upon exposure to air, for example at a damaged site. Unfortunately, this is a complex and potentially dangerous approach due to the reactivity of the applied chemicals. [83]

We aim to widen the pool of self-healing materials from soft matter and metals towards MeO, including the highly demanded TCOs. MeOs are typically very inert in ambient conditions. Healing cracks in MeOs by recrystallization would require considerable energy investment. If a device contains polymers, for example as a substrate in the case of flexible electronics, such an energy input will be incompatible with the thermal range of the polymers and is therefore not applicable. Self-healing of inorganic materials and structures could alternatively be realized by loading a polymeric substrate with inorganic NPs and enabling their mobility inside the substrate. The spatial distribution of NPs can be tuned by harnessing both enthalpy and entropy. [93], [238]–[240] In suitable material systems, the NPs can migrate to new damage-induced interfaces, agglomerating and thereby performing self-healing events. [58] However, a polymer coating on inorganic NPs was required in that work, which shielded the NPs and therefore affected their functional properties. [58]

An entropy-driven NP reorganization, as described in this work, is a promising and safe alternative pathway to allow healing of metal oxides. As a first step, a system with MeO nanoparticles, well-dispersed inside a preferably polymeric host matrix, is needed. This can be obtained by VPI of a polymer with inorganic materials. [9], [130], [241] The approach will yield a hybrid or nanocomposite polymer-inorganic material with an inorganic thin film coating of the same or another MeO, depending on the process setup. [146] This polymer matrix with dispersed NPs can then serve as a reservoir for agents for healing defects in the MeO film. Upon defect formation, synergistic chemical and physical effects in the system will drive agglomeration and eventually close the defect.

In contrast to wet chemistry, the proposed VPI method relies on top-down modification of a thin subsurface layer, which does not seriously affect the bulk of the polymeric substrate. A migration of solid NPs rather than liquids increases the safety of the system. Besides, the method allows self-healing of thin semiconducting films instead of creating a blend of semiconductors and self-healing polymers as it was described in other works. [46], [87] This approach offers a possible solution for enhancing the reliability of materials in flexible electronics and other applications such as permeation barriers.

5.2 Structure and composition of ParyleneC/MeO hybrids

We applied VPI to infiltrate the polymer ParyleneC with oxides of zinc, indium, or tin-doped indium. ParyleneC is well-known for its thermal stability and biocompatibility. [242] All mentioned metal oxides are individually of technological importance for a variety of optoelectronic applications [215] and the combination of indium and zinc oxides yields the TCO IZO, which is among the most efficient transparent electronic conductors and often substitutes tin ITO which dominates the flat-panel industry. [243], [244] After VPI, hybrid structures consisting of ParyleneC and indium oxide, zinc oxide or ITO particles, conformally coated with the corresponding metal oxide film, were obtained. The coatings therein served as test structures for investigating their ability to self-heal and the particles were the reservoirs for the healing process. The chemical properties of the ParyleneC/ZnO system have already been discussed in Chapter 4.

5.2.1 Properties of the ParyleneC/In$_x$O$_y$ hybrid system

The infiltration and the properties of ParyleneC infiltrated with In$_x$O$_y$ have been partly discussed in Chapter 3. As our experimental findings revealed that the use of hydrogen peroxide as oxygen-containing precursor is beneficial for the enhanced GPC and crystallinity of indium oxide, as well as the increased infiltration depth and resistance of the hybrids, for the investigation of the self-healing process we focused on ParyleneC infiltrated with TMIn/H$_2$O$_2$ at 210°C.

We undertook a systematic characterization of the chemical composition and morphology of the ParyleneC/In$_x$O$_y$ system. The EDX analyses were performed on FIB-prepared lamellae with *ex-situ* transfer to the TEM chamber, while XPS depth-profile was done *in-vacuo* by Ar$^+$ ion etching. Both EDX and XPS analyses confirmed the formation of the hybrid organic-inorganic material (Figure 5.1 a, b). The signals of indium, oxygen, chlorine, and carbon were observed down to a depth of 300 nm as measured by EDX (Figure 5.1 a). However, distinct indium oxide nanoparticles were only observed down to a depth of 150 nm using HRTEM (Figure 5.1 c). It was also noted that the concentration of the particles within the matrix decreased with the infiltration depth. In the bright-field TEM image of Figure 5.1 c, indium appears darker due to the combination of absorption/density and diffraction contrasts. Interestingly, the chlorine concentration at the hybrid/polymer interface was surprisingly high and reached 14.1±2.5 at. % (Figure 5.1 a, b), more than double of that found in pristine ParyleneC (~6 at.%). Despite the partial elimination of chlorine in the polymer subsurface, the thermal stability of the polymer remained almost unaltered as can be seen from the thermogravimetric analysis discussed in Chapter 3 (Figure 3.7).
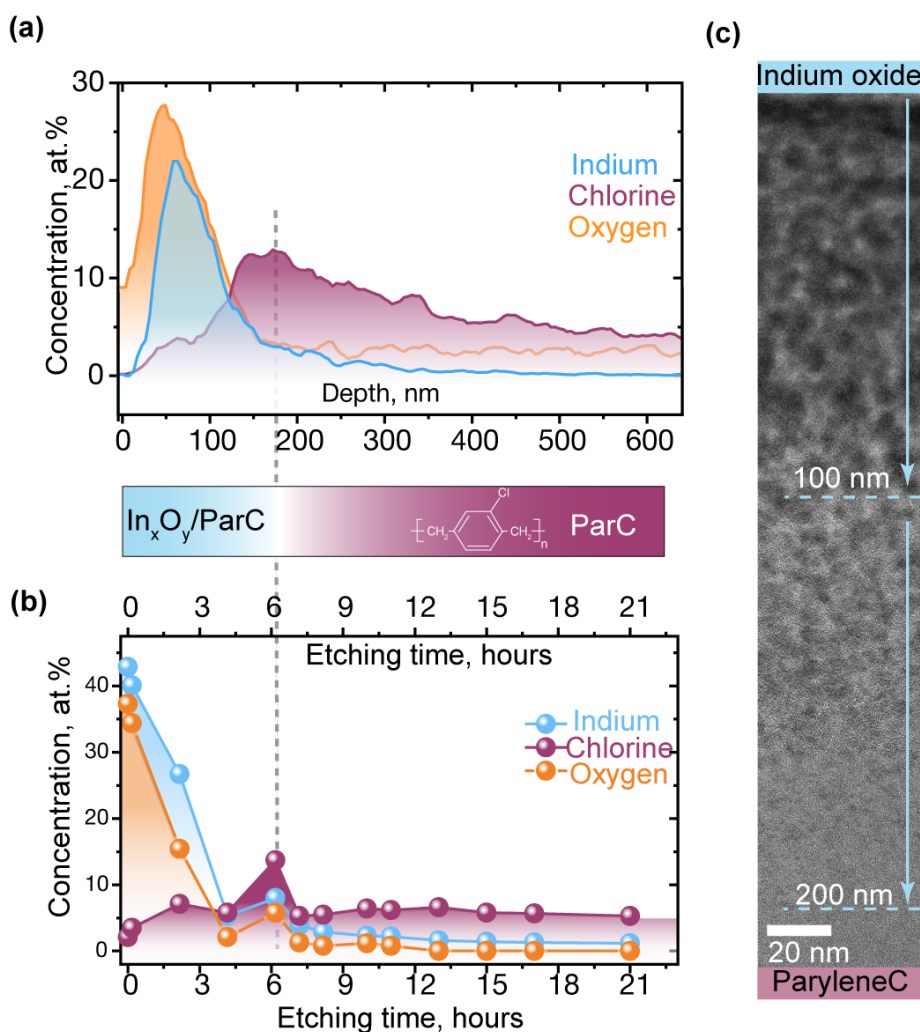
Figure 5.1 Chemical characterization of the ParyleneC/In$_x$O$_y$ hybrid after VPI processing. (a) EDX-derived atomic concentration depth profiles of In, Cl and O. (b) XPS-derived atomic concentration depth profiles of In, Cl and O. (c) Merged panorama image of the depth profile assembled from six HRTEM images.

To account for the excess chlorine in the hybrid, we applied depth profiling by etching and XPS to track the evolution of the chlorine 2p photoemission spectrum with its characteristic doublet shape. [184] It was recently shown that despite the high stability of the polymer, treatment with metalorganic vapors induces metal chloride formation. [183] For ParyleneC infiltrated with trimethyl indium (TMIn/H$_2$O$_2$), the Cl 2p signal was best fit with two doublet peaks, each showing the characteristic Cl 2p$_{3/2}$ - 2p$_{1/2}$ spin-orbit splitting of 1.6 eV for all infiltration depths (Figure 5.2 a, b), thereby confirming the presence of two different chemical states of chlorine. We attribute the Cl 2p$_{3/2}$ peak at 200 eV to chlorine bound to organic carbon, while the peak at lower binding energies corresponds to metal chlorides. [184] Surprisingly, most of the chlorine near the surface (92 at. %) was bound to indium and only 8 at. % to carbon. Apparently, the infiltration of TMIn/H$_2$O$_2$ not only led to the In$_x$O$_y$ formation inside the bulk of the polymer, but also to splitting of the C-Cl bond

and indium chloride formation. Thus, the obtained hybrid is not a simple sum of the constituent ParyleneC and In_xO_y, but also contains additional inorganic chlorides.
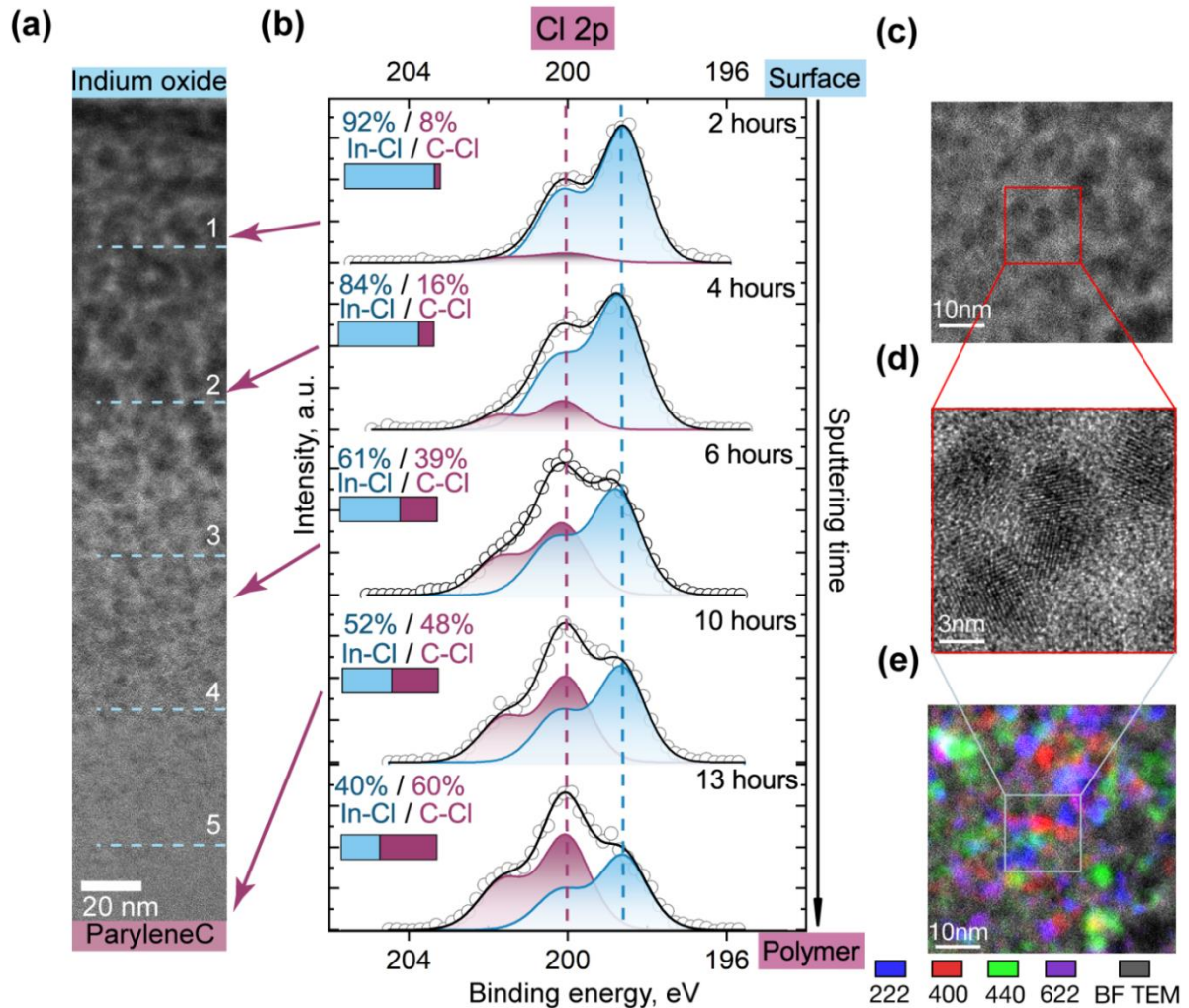

Figure 5.2 Chemical and structural characterization of the ParyleneC/In_xO_y hybrid after VPI processing. (a) Merged panorama image of the depth profile assembled from six HRTEM images with their boundaries marked with numbers 1 through 5, while the corresponding Fast Fourier Transformation images marked with the same numbers can be found at Figure 5.3 a. (b) Depth evolution of the XPS Cl 2p doublet vs sputtering time. The correlation of the spectra with the analyzed area is indicated with arrows between the images (a) and (b). The related etching depth can be roughly estimated from the comparison of the graph Figure 5.1(a) with (b). (c) TEM micrograph of inorganic clusters obtained in ParyleneC after VPI. (d) Magnified micrograph of the indicated section in Figure 5.2c. (e) False-colored virtual dark field image overlaid on the bright-field TEM image in Figure 5.2c. Distinct lattice spacings are marked with different colors as indicated below the image.

Despite the formation of indium chloride throughout the entire hybrid section, electron diffraction confirmed the presence of the cubic structure of indium oxide clusters at all infiltration depths

(Figure 5.3 a). The crystallinity of the NPs is clearly seen from the magnified HRTEM images (Figure 5.2 c and d). The indium oxide nanoparticles were confined in the ParyleneC matrix in a variety of crystal orientations as shown in the false-colored virtual dark field image overlayed on the corresponding bright-field TEM image in Figure 5.2 e. The average diameter of the crystallites dispersed in ParyleneC reached 2.7±0.9 nm (Figure 5.3 b).
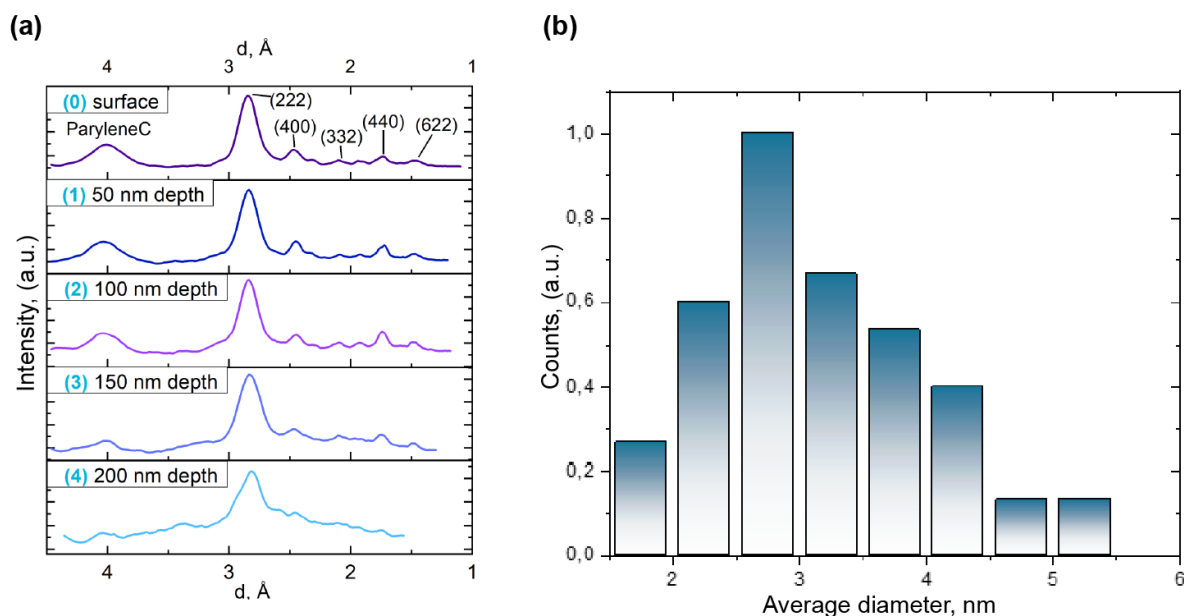

Figure 5.3 (a) Integrated radial intensity profiles obtained from HRTEM images through Fast Fourier transformation (FFT) of a ParyleneC/In_xO_y hybrid structure at different infiltration depths. The lattice spacing corresponds to cubic In_2O_3. (b) Normalized diameter distribution of indium oxide nanoparticles in the ParyleneC/In_xO_y hybrid.

5.3 Healing of morphological defects

To study the capability of the material system to heal defects we first generated a scratch in the coating of the ZnO-based hybrid (ParyleneC/ZnO) with a micromanipulator (Figure 5.4). While remaining in vacuum, no changes occurred at the scratched area. The morphological changes of the scratch were observed by SEM over time. The onset of healing of the damaged area was detected after 1 day of exposure of the sample to the atmosphere. Nano-sized neoformations appeared dispersed over the scratched surface as marked with the red arrows (Figure 5.4; 1 day of exposure to air). In subsequent SEM investigations the scratch was completely healed (Figure 5.4; 8 days of exposure to air). EDX analysis of the area showed the formation of inorganic zinc oxychloride, where the chloride originates from the halogenated polymer which was used as a substrate.
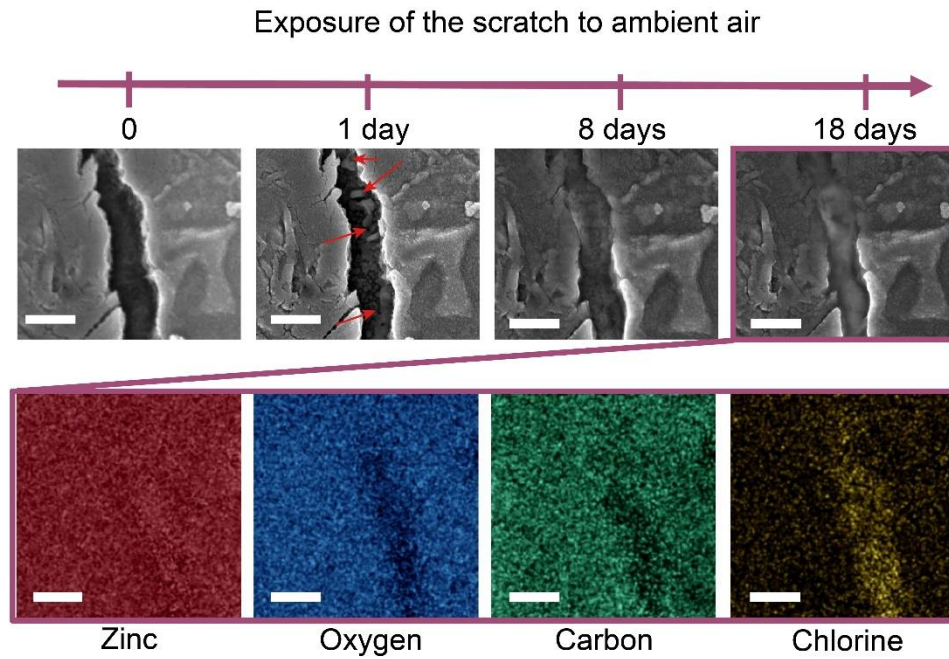
Exposure of the scratch to ambient air

Figure 5.4 Top row: Mechanically induced scratch on the surface of ParyleneC/ZnO and its healing over time. The scratch was produced in vacuum with a micromanipulator. Bottom row: EDX maps of the mended scratch after its exposure and storage in atmosphere at room temperature. Scale bar: 500 nm.

Interestingly, mechanical defects of smaller dimensions heal faster. For example, a 40 nm wide crack on the ParyleneC/ZnO surface, induced by mechanical treatment of the sample, started healing already after 5 minutes on air at ambient conditions (Figure 5.5). The reason behind the slow healing of the crack in Figure 5.4 may originate from the deep scratch, which damaged a significant part of the hybrid layer below the inorganic coating layer.
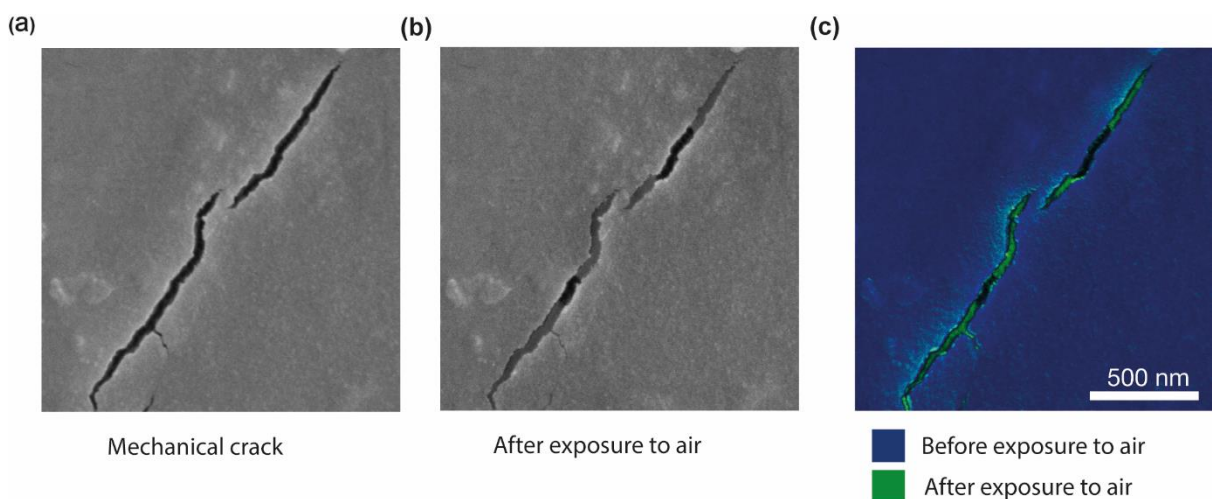

Figure 5.5 Mechanically induced crack on the surface of ParyleneC/ZnO (a) before exposure to air; (b) after 5-minute exposure to air. (c) Overlay of Figure 5.5 a and b, where the green color highlights the healed areas.

89

In further experiments a FIB was used for better control when forming the defect (Figure 5.6 a) and indium oxide (In_xO_y) was used instead of ZnO. A small section of the In_xO_y coating was etched away by FIB, exposing the underlying hybrid material to the environment (Figure 5.6 b). As expected, the EDX maps showed increased intensities of the carbon and chlorine signals from the exposed ParyleneC and decreased intensities of indium and oxygen signals in the FIB-patterned area (Figure 5.6 c). After FIB-sputtering of the metal oxide thin film, the hybrid ParyleneC/In_xO_y was exposed to air for five minutes. The SEM images show a spherical feature that completely covered the exposed area (Figure 5.6 d). The EDX maps of that region confirm that the spherical neoformation consists of indium and oxygen (Figure 5.6 e). A chlorine signal was also present in the grown feature, albeit lower than that of the surrounding surface. Importantly, the EDX scan of the newly formed feature doesn´t show presence of carbon. Obviously, upon encountering ambient air the defect healed slowly by migration of the entrapped inorganic material.
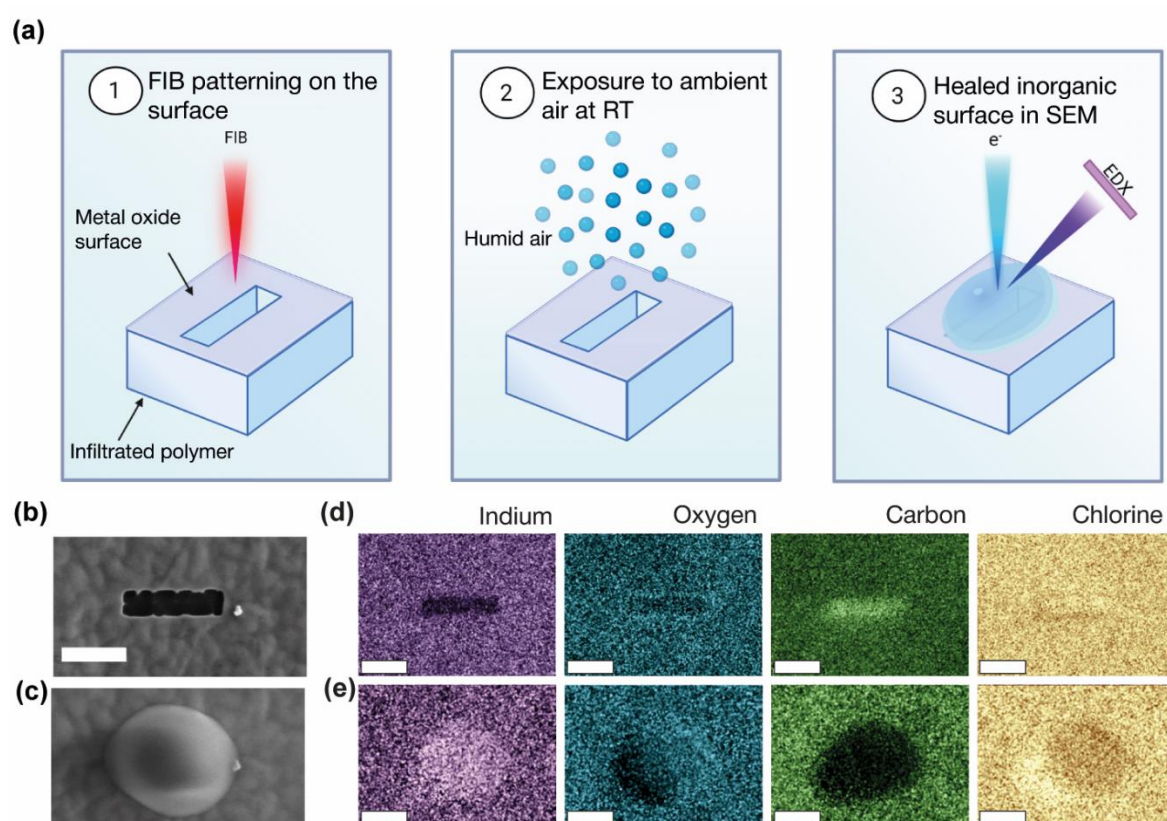
Figure 5.6 Healing of the metal oxide thin films. (a) Schematic of the experimental procedure for the self-healing investigation. SEM images of the FIB-etched surface of the ParyleneC/In_xO_y hybrid sample (b) before and (d) after exposure to air. Color-coded EDX maps of In, O, C, ad Cl (c) before and (e) after exposure to air. Scale bar in images (b-e): 1 μm

The same process of defect mending was observed for the ParyleneC/ZnO hybrid. A defect in the shape of letter "N" was written into the ZnO film by FIB (Figure 5.7 a), which upon exposure to air

healed within 5 minutes (Figure 5.7 b). A further interesting observation is that a depletion zone formed around the letter N where the oxygen and zinc signal intensities decreased and the carbon signal intensity increased, thereby indicating a lateral diffusion of the infiltrate towards the induced defect site (Figure 5.7 c). Such lateral mobility occurred within the area up to 1 μm distant from the defect. Like in healing processes in various life forms, where damaged tissue regenerates because blood serves as a reservoir and delivers the necessary building material to the injured site, the healing of the defects in our material systems implies that the hybrid structures, consisting of a polymer with dispersed metal oxide particles, are the reservoirs for the healing agent.
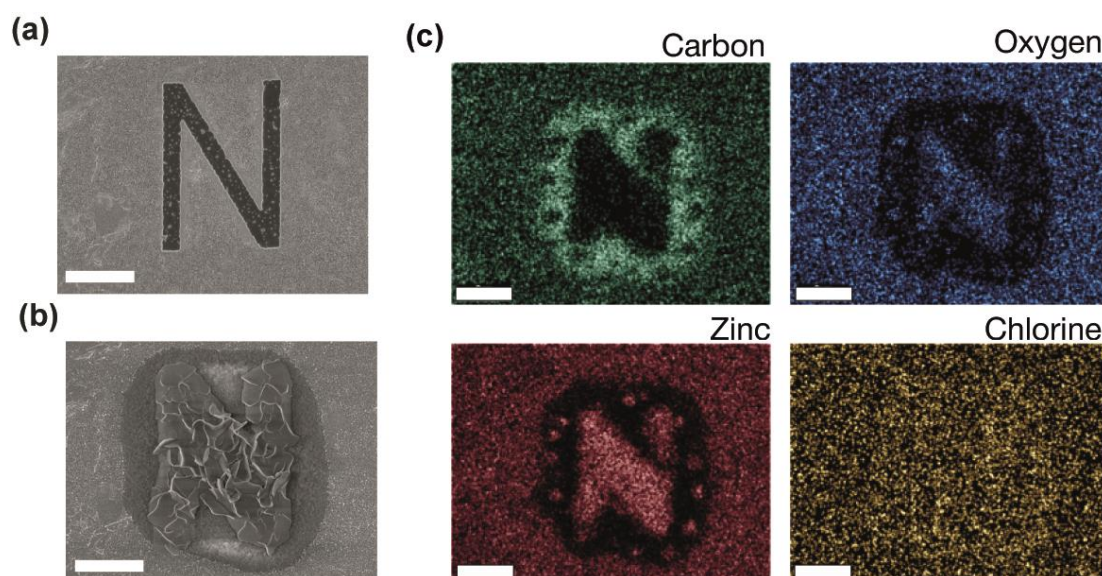
Figure 5.7 Healing of selectively FIB-etched patterns on the surface of ParyleneC/ZnO (a) before and (b) after exposure to air. (c) EDX maps of the mended ParyleneC/ZnO hybrid structure shown in (b). The scale bar in the images (a-c) is 2 μm.

A cross-sectional image of the neoformation on the surface of the ParyleneC/ZnO, previously etched with FIB, showed that the healed part is not dense and consists of fiber-like structures (Figure 5.8). EDX maps obtained from the healed ParyleneC/ZnO structure visualize the distribution of zinc, oxygen, and chlorine in the system (Figure 5.8). The intensity of the zinc signal in the healed part is exceeding the intensity of the Zn signal in the infiltrated part of the hybrid. Interestingly, there is an increased chlorine intensity at the boundary separating the infiltrated and non-infiltrated parts of ParyleneC.

Figure 5.8 STEM micrograph of the healed ParyleneC/ZnO structure and corresponding EDX maps of the zinc, oxygen, carbon, and chlorine elements.

An EDX point analysis was performed in three different areas to compare the chemical composition in the newly grown part (1), the near-surface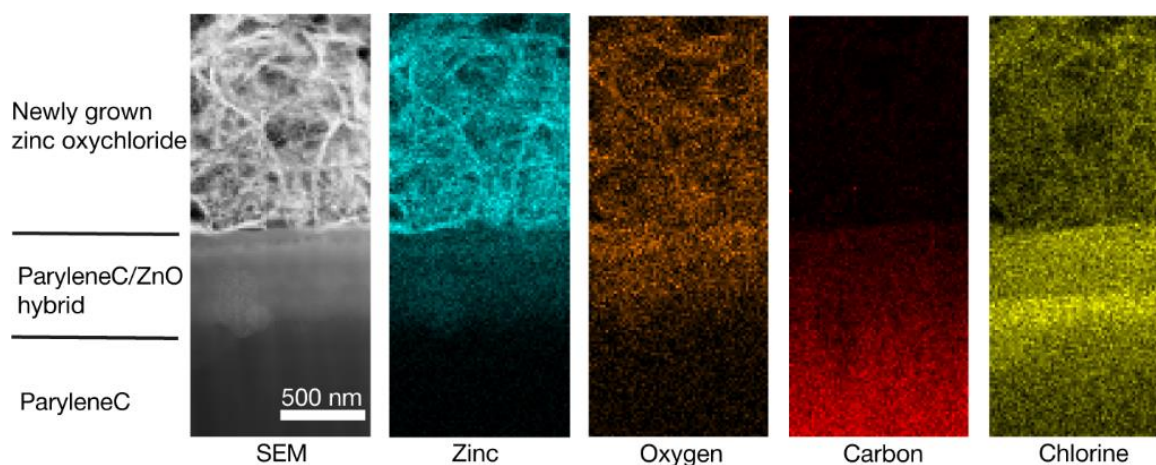 area of the ParyleneC/ZnO hybrid (2), and in the bulk of the ParyleneC/ZnO (3) (Figure 5.9). The results of the EDX analyses from those areas are summarized in the Table 5. Apparently, the neoformation is oxygen-deficient zinc oxide with 64.9 and 25.3 at. % of Zn and O, respectively, having a Zn:O ratio of ~ 2.5:1. The amount of Cl admixture reached 6.6 ±0.2 at %, while the concentration of C at the neoformation didn't exceed 3.3±0.2 at. % (Table 5). Assuming that zinc can be incorporated into the structure in the form of $ZnCl_2$, the overall Zn to O ratio remains highly oxygen deficient. The ParyleneC/ZnO hybrid near the surface is comprised of one third nearly stoichiometric ZnO and the polymer with an increased amount of chlorine of 11.8 at. %. The level of chlorine decreased in the bulk of the ParyleneC/ZnO hybrid, reaching 6.9 at. %, which is close to the Cl concentration in the pristine ParyleneC polymer.
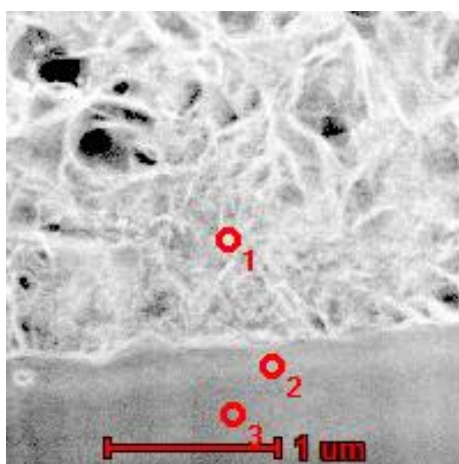

Figure 5.9 STEM micrograph of a healed ParyleneC/ZnO structure: (1) material grown after exposure to air; (2) near surface area of the ParyleneC/ZnO hybrid; (3) bulk of ParyleneC/ZnO.

Table 5. Atomic concentrations of the main components in ParyleneC/ZnO at the three different points depicted in Figure 5.9.

Point #	Element	Weight %	Atomic %	Uncertainty %
1	C(K)	0.8	3.3	0.2
	O(K)	8.2	25.3	0.4
	Cl(K)	4.7	6.6	0.2
	Zn(K)	86.2	64.9	1.0
2	C(K)	27.7	54.5	0.7
	O(K)	12.6	18.6	0.4
	Cl(K)	17.8	11.8	0.3
	Zn(K)	41.9	15.1	0.6
3	C(K)	49.5	73.9	0.8
3	O(K)	10.3	11.5	0.3
	Cl(K)	15.2	7.7	0.2
	Zn(K)	25.4	6.9	0.4

The effect of mass transport is also observable when a cross-section is exposed to air. In the case of a cross-section the ratio of the hybrid volume which can initiate healing of the surface coating is higher than that in the case of crack formation or etching due to the increased depth profile (Figure 5.10 a). After 10 minutes of exposure to air the surface became covered with flower-like neoformations (Figure 5.10 b). Interestingly, star-like structures were formed even on the specimen surface, while the sample was covered with the conductive carbon and Au-Pt layers prior to FIB-etching. Most likely this is caused by the redeposition of the sputtered hybrid material during FIB processing. The EDX chemical analysis showed that the newly formed nanoflowers and nanostars were composed of zinc, oxygen, and chlorine, but not carbon (Figure 5.10 c).
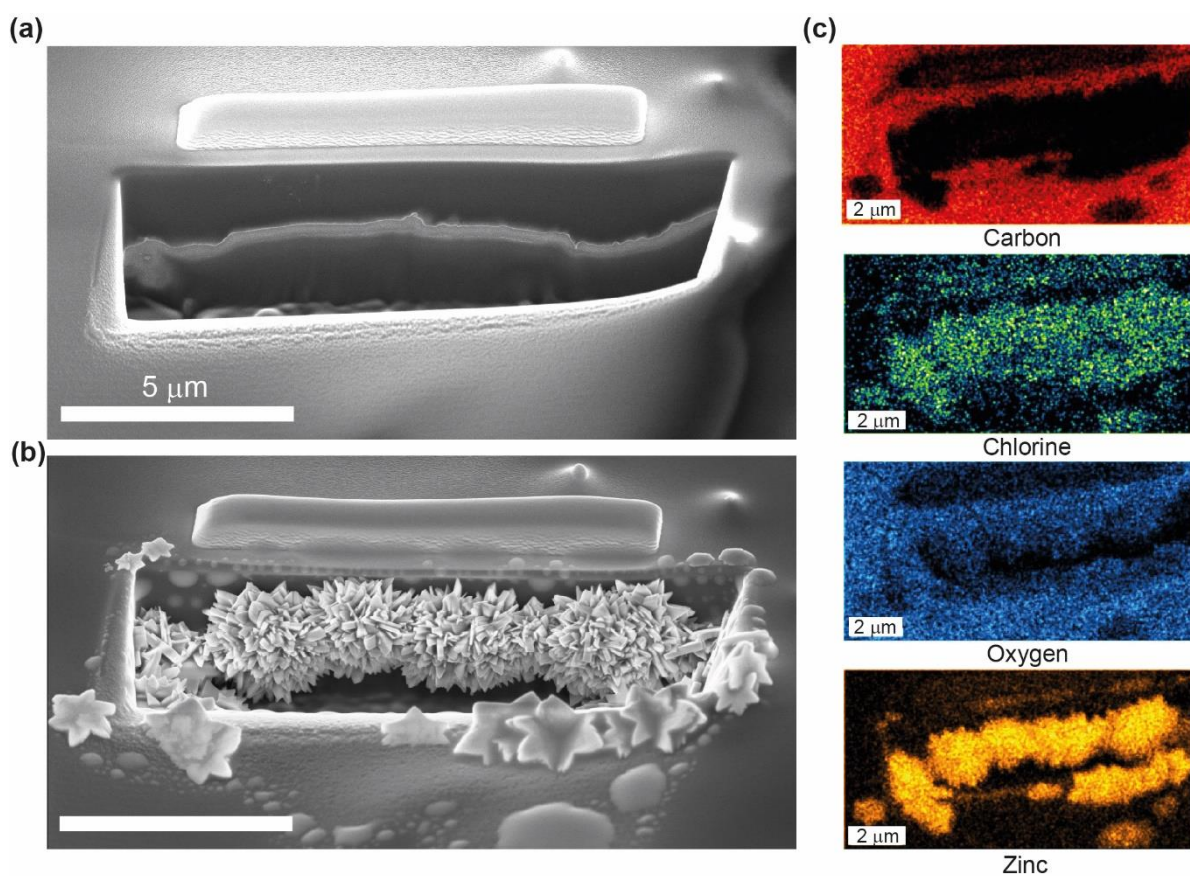
Figure 5.10 SEM images of a cross-sectioned ParyleneC/ZnO sample (a) before and (b) after exposure to air, and (c) EDX elemental maps of zinc, oxygen, carbon, and chlorine in (b).

5.4 Restoring the electronic functionality

Healing of a material implies restoring its functionality, i.e., for conducting materials mending of a scratch should rebuild conduction pathways. However, dispersed NPs inside the polymer also contain metal chloride inclusions which potentially can inhibit the electronic conductivity. [245] A simple comparison of indium oxide films with and without a hybrid layer, bent over radius of 1 mm, visually shows that the hybrid structure is able to maintain the conduction pathways (Figure 5.11 a), while they were interrupted in the In_xO_y film without a hybrid interlayer (Figure 5.11 b).

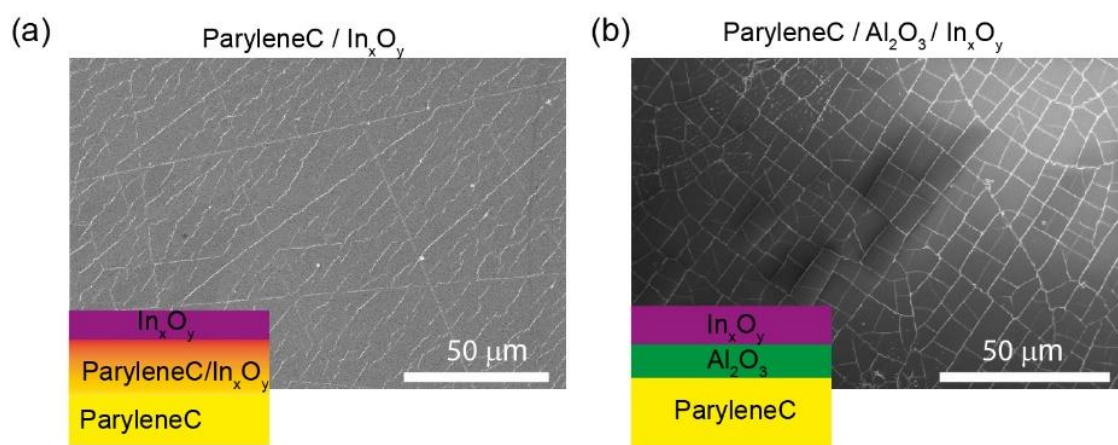Figure 5.11 Surface of (a) ParyleneC/In_xO_y hybrid and (b) nanolaminate ParyleneC/Al_2O_3/In_xO_y after being bent over a curvature with 1 mm radius.

For the further evaluation of the electronic functionality, we used the most common TCOs: IZO and ITO for their technological relevance. Multiple bending of an IZO-infiltrated ParyleneC sample over a radius of 5.5 mm showed a surprising decrease in sheet resistance from 9.5 kOhm/□ to 3.1 kOhm/□ (Figure 5.12 a), which can be explained with the migration and agglomeration of the inorganic NPs near the interface, resulting in new conduction pathways. We performed the same experiment with an IZO-coated ParyleneC, but without infiltration. To eliminate infiltration, 10-nm aluminum oxide was pre-deposited on the polymer to prevent in-diffusion of TMIn. The sheet resistance of the coated structure was ca. 0.55 kOhm/□ (Figure 5.12 b), which is one order of magnitude less than that of the infiltrated ParyleneC/IZO hybrid. The difference may lie in the fact that, in contrast to the nanolaminate, the ParyleneC/IZO sample had no well-defined film on the surface, but rather the indium oxide intermixed with the polymer (Figure 3.9 b). Interestingly, in contrast to the hybrid ParyleneC/IZO sample, the ParyleneC/Al_2O_3/In_xO_y nanolaminate didn't show significant changes in the sheet resistance upon multiple bending and no resistance changes were observed upon initial bending events, which agrees with the hypothesis of redistribution of NPs within the polymer.
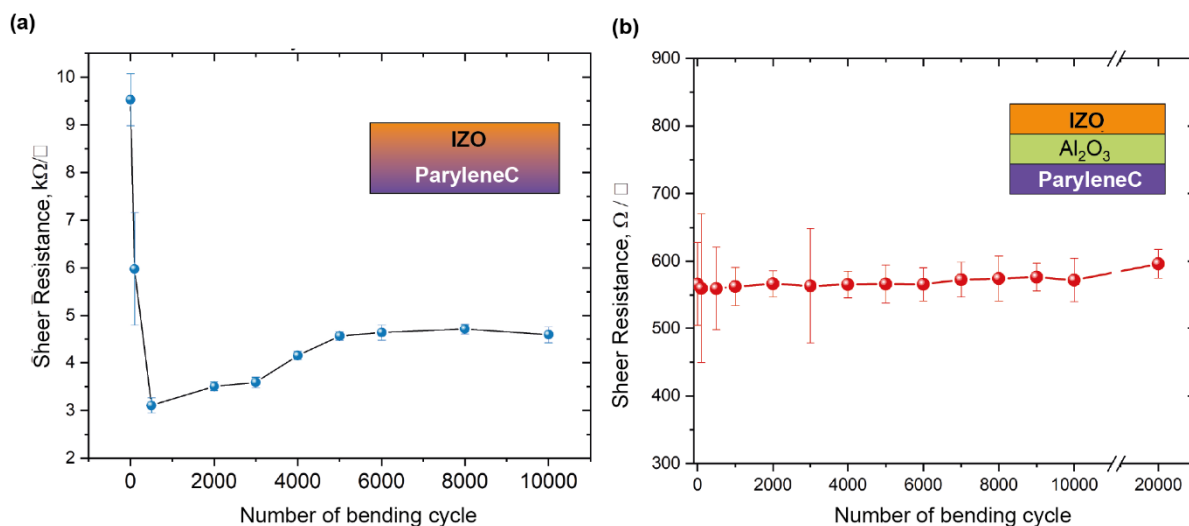
Figure 5.12 Evolution of the sheet resistance as a function of bending events of the (a) ParyleneC/IZO hybrid; (b) ParyleneC/Al$_2$O$_3$/In$_x$O$_y$ nanolaminate.

To verify whether the conductivity of a healed micro-defect can be restored, we fabricated an ITO based hybrid and FIB-etched a rectangular strip to obtain a 190 µm-long and 35 µm-wide conductive area (Figure 5.13 a) with an electrical resistance of 4.5 kOhm (Figure 5.13 b). We measured the resistance while cutting the strip in two halves by FIB, which made the resistance rise towards GOhm values. Sectioning of the strip opened the circuit and lead to the buildup of different potentials on the two separated halves. Opposite charges at the two probes and halves of the stripe resulted in the attraction or repulsion of the electron beam, which results in the contrast differences observed in the micrograph (Figure 5.13(2)). The etching and the measurements were conducted in high vacuum inside the chamber of our electron microscope where no healing was observed. Upon flooding the chamber with air, the resistance initially halved and after a steady state during 8 seconds in air a rapid drop by almost 5 orders of magnitude to 46 kOhm occurred within 1 second (Figure 5.13 c). The post-examination of the FIB-patterned area showed mending of the thin ITO film and formation of some bridges between the two separated parts of the conductive strip (Figure 5.13 a(3)). Thus, the healing process not only closed the gap in the material, but also restored the electronic functionality.
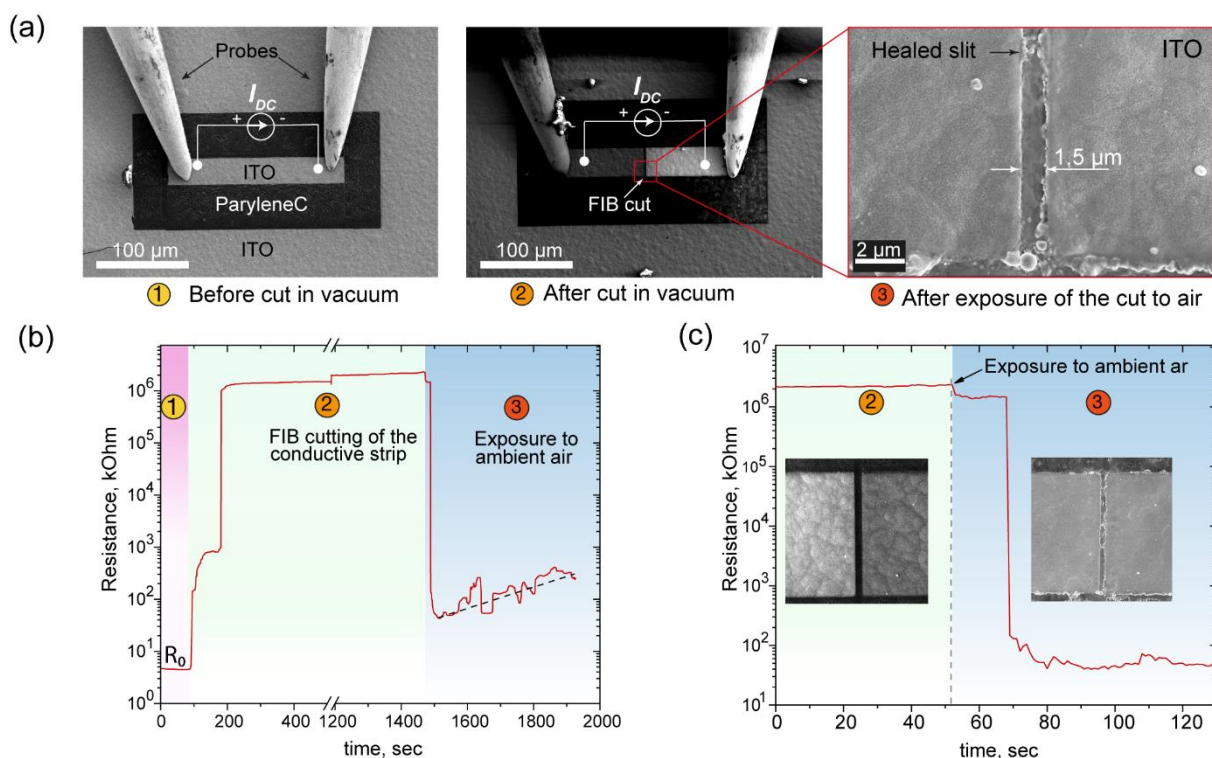
Figure 5.13 Restoring of the electrical conductivity (a) SEM images of the FIB etched area on the surface of ParyleneC/ITO and two probes placed on a conductive stripe: (1) Before cutting into two halves; (2) after cutting the stripe into two halves; (3) After exposure of the cut to air. (b) Evolution of the resistance of the conductive ITO stripe during the stages 1-3 of cutting and exposure to air. (c) Magnified boundary section of stage 2 and 3 in Figure 5.13b, revealing the evolution of the resistance of the conductive ITO stripe at the stages 2-3 during exposure to air. The insets show SEM images of the sectioned stripe before and after self-formation of electronic contacts.

5.5 Depletion attraction forces

The ability of the obtained polymer/MeO systems to self-heal can be explained by entropic interactions. [58], [93], [246], [247] The depletion attraction forces between the NPs and confining surfaces are entropic in nature and lead to a surface segregation of the NPs. [115], [119] These forces are caused by excluded-volume interaction and arise in an athermal blend of NPs and polymers. In particular, the system gains conformational entropy if the NPs migrate to the surface and consequently the polymer chains do not have to embrace the NPs inside the polymer. [248] This mechanism explains the mobility especially of larger particles. Smaller particles do not perturb the conformation of polymer chains, but, as a consequence of depletion attraction, they will aggregate to larger assemblies. [249] When two NPs get close enough to each other, a part of the previously

excluded volume overlaps, liberating some volume elsewhere in the system for occupation by the polymer. In this way, an anisotropic pressure is exerted, leading to a strong attractive force between nanoparticles. Such bulk segregated particles can become large enough to perturb the polymer chains and become expelled towards newly formed surface, i.e., cracks. [119]
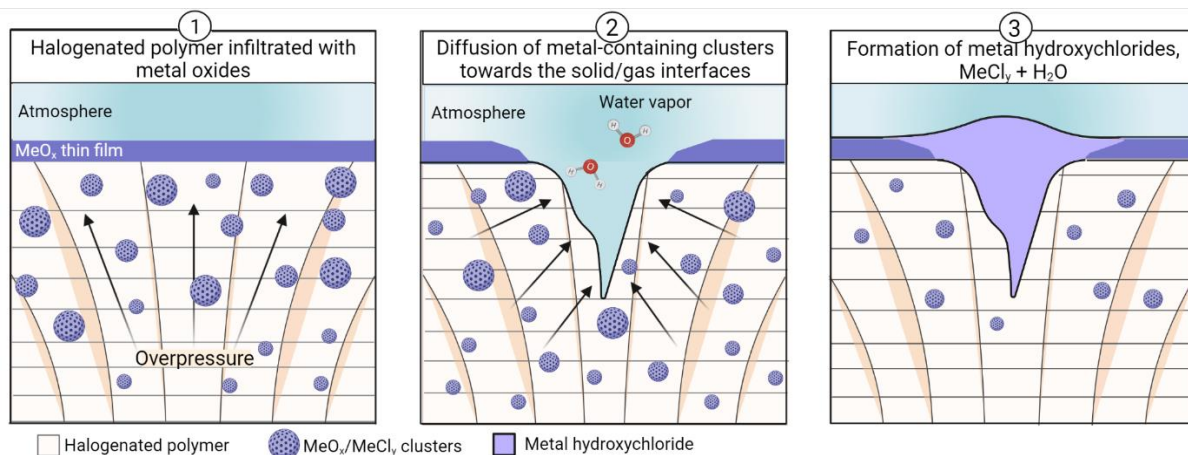

Figure 5.14 Healing scheme of the VPI-grown hybrid structure. The osmotic pressure is indicated with black arrows in image 1. Once the coating on the surface has a defect (image 2), the particles move to the defect side and form a capping of the defect (image 3).

This concept can be applied to our hybrid polymer/MeO systems. VPI was performed at elevated temperatures, which led to the expansion of the polymer and consequently to an increase of its free volume, making it accessible for the sorption of small molecules. [10] After the infiltration process the system was cooled down to ambient temperatures and the volume of the polymer consequently compressed again. However, the polymer was already infiltrated with MeO particles, which imparted an increase in osmotic pressure (Figure 5.14). [249] Yet, the immediate diffusion of the NPs towards the surface was limited due to the MeO capping layer which acted as a diffusional barrier. Once the surface integrity was disturbed through the defect induced by the FIB, metal oxide NPs diffused towards the freshly formed air-solid interface (Figure 5.15, Figure 5.16). Evidence for such diffusion is the depleted surrounding of the letter N in Figure 5.7 b, c.

The sizes of the overgrown features observed at the interfaces depend on the amount of the infiltrated healing material within the polymer matrix. As shown in Chapter 4, the infiltration depth and, consequently, the amount of infiltrated zinc oxide can be tuned by the infiltration temperature. With larger amounts of incorporated zinc oxide NPs, i.e., at higher processing temperatures, neoformations of higher surface area formed (Figure 5.15). After 5-minutes of exposure of the FIB cuts to air, the surface areas of the neoformations reached 5.3 μm^2, 13.8 μm^2, and 14.1 μm^2 for hybrids fabricated at 100°C, 150°C, and 210°C, respectively.
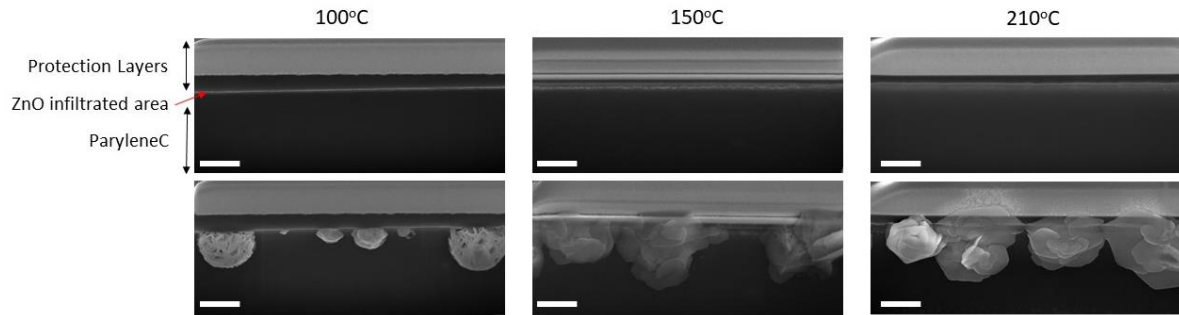
Figure 5.15 FIB cross-section of the ParyleneC/ZnO hybrid before (top) and after (bottom) exposure to air. Scale bars: 1 μm.
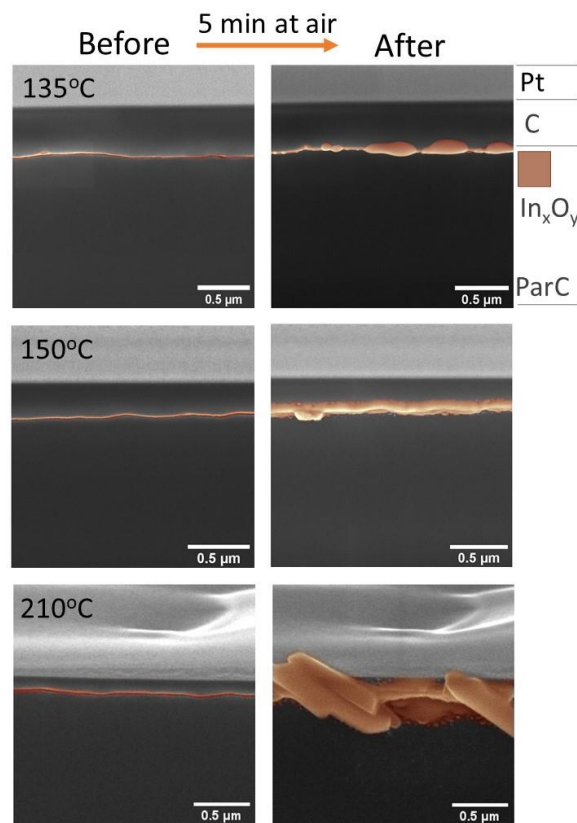
Figure 5.16 FIB cross-section of a ParyleneC/In$_x$O$_y$ hybrid obtained after VPI of TMIn/H$_2$O$_2$ at temperatures of 135°C, 150°C, and 210°C, as indicated, before (left column) and after (right column) exposure to air.

A similar effect is seen from the ParyleneC/In$_x$O$_y$ hybrids (Figure 5.16). Indium oxide VPI results in a much shallower infiltration depth when compared to ZnO infiltration, as discussed in Chapter 3, but it similarly depends on the VPI process temperature. Comparison of the FIB cross-sections of the ParyleneC/In$_x$O$_y$ hybrids fabricated at different infiltration temperatures shows that the surface area of the neoformations increases with the processing temperature, reaching 0.2 μm^2, 0.4 μm^2, and

1.1 μm^2 for 135 °C, 150 °C, and 210ºC, respectively (Figure 5.16). Thus, the polymer matrix serves as reservoir for the metal oxides, and the amount of stored NPs defines the possibility of a formation of a self-healed metal oxide film and the resulting feature dimensions.

To prove that the concept is applicable to further metal oxides, we tested the self-healing ability with nickel oxide-based hybrids. Those were obtained by applying 400 VPI cycles of $NiCp_2/O_3$ to ParyleneC. The SEM images of the cross-sections revealed that under the applied conditions a nickel oxide film of 80 nm thickness formed (Figure 5.17 a). Despite the infiltration process, a hybrid layer was not distinguishable by SEM. However, exposure of the sample to air led to the appearance of neoformations with spherical shapes on the ParyleneC/Ni_xO_y interface (Figure 5.17 b). The chemical composition analysis by EDX proved that the newly formed spheres consist of nickel, oxygen, and chlorine (Figure 5.17 c). Nickel oxide is a semiconductor material with great applicability in photocatalysis, lithium-ion batteries, chemical sensing, and electrochromic materials. Therefore, achieving self-healing of nickel oxide films can have a considerable technological and industrial impact.
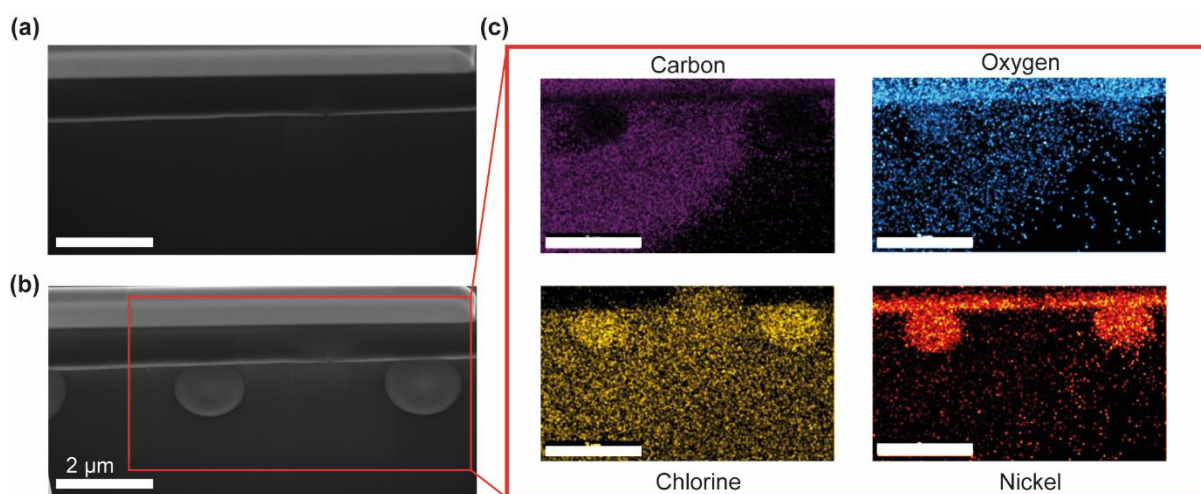
Figure 5.17 FIB cross-section of a ParyleneC/Ni_xO_y hybrid obtained after VPI of $NiCp_2/O_3$ at 220 ºC (a) before and (b) after exposure to air. (c) EDX elemental maps of the neoformations on the ParyleneC/Ni_xO_y cross-section after exposure to air. Scale bars: 2 µm.

5.6 Hybrid structures based on non-chlorinated polymers

The entropic penalty alone was not the only effect imparting the self-healing response to the MeO nanoparticles. To test if the same healing effect can be achieved in non-chlorinated polymers, several polymeric substrates were subjected to infiltration of DEZ and water vapors. The infiltration

temperature was 80°C for all polymers and the pulse/purge/exposure sequence was 0.4/30/60 seconds, respectively. After 100 VPI cycles, cross-sections were prepared as before to investigate the success of infiltration (Table 6). As described in the experimental part, a typical cross-section consists of platinum and carbon protective layers, a metal oxide thin film, a hybrid organic-inorganic layer, and a polymer. In some cases, the hybrid layer can be absent or too thin to be resolved by scanning electron microscopy.

Table 6. Cross-sections of the polymers, their names, chemical formulas, and glass transition temperatures. The scale bar of each cross-section corresponds to 2 μm.

SEM cross-section	Polymer	Formula	Tg, °C
2 μm	Polypropylene		-25 [250]
	Polyurethane (PU)		-53 [251]
	Polydimethyl-siloxane (PDMS)		-123 [252]
	Natural rubber		-73 [253]
	Acrylonitrile butadiene styrene (ABS)		101 [254]
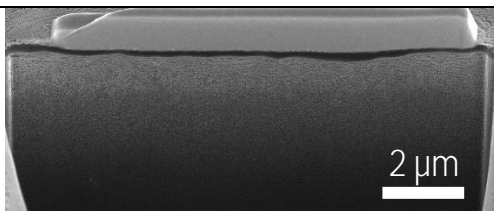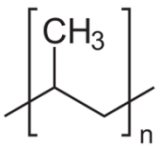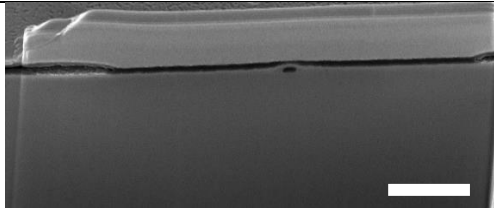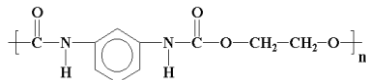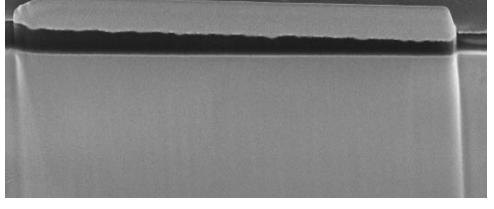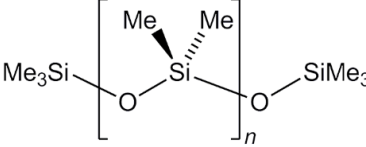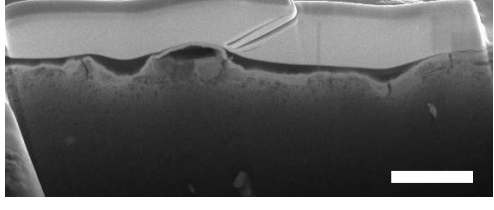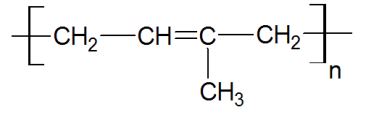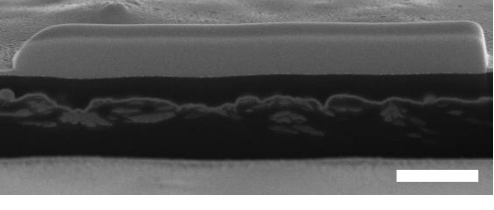
	Polytetrafluoro ethylene (PTFE, Teflon)		-65-(-35) [255]
	Polystyrene (PS)		95 [250]
	Polyethylene terephthalate (PET)		67-81 [256]
	Polyethylene naphtalate (PEN)		120-135 [257]
	Polycarbonate (PC)		149 [250]
	Polyamide 6 (Nylon)		49 [250]
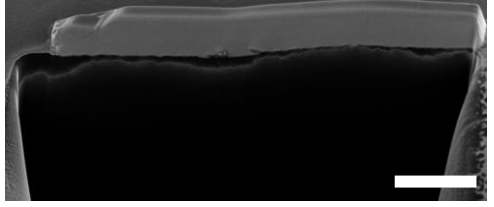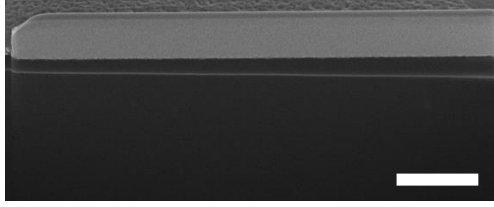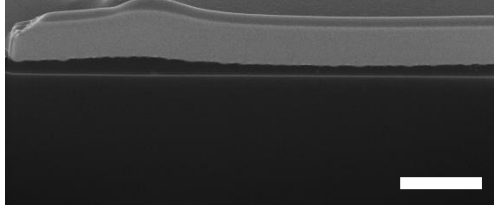
The cross-sections of the infiltrated polymers which are shown in the table were recorded before the exposure of the samples to air. However, exposure to ambience did not induce any changes in their structures and morphologies and, therefore, the images recorded after the exposure to air are not shown. This indicates that the polymeric substrate is not only a host matrix for NPs, but also a functional part of the hybrid system. The non-halogenated and metal oxide-infiltrated polymers remained stable even after irradiation with a high-voltage electron beam or thermal treatment. The absence of healing behavior in those cases can be explained with strong attractive interactions or chemical bonding between the polymers and the infiltrated metal oxide NPs, which counteract the gain in conformational entropy in the system and therefore limit the migration of the NPs.

The appearance of the samples after infiltration was also very different among the polymers in Table 6. Cross-sectional images of VPI-modified nylon, PET, PEN, and polycarbonate reveal sharp interfaces between the ZnO thin film and the polymer surface. This indicates the absence of a hybrid layer or a at least a very shallow infiltration which is not resolved by SEM. The reason for this is most likely the high density of the used commercial polymer foils and the resulting limited free volume and their high glass transition temperatures. In contrast, ABS, PP, PU, rubber, PDMS, and PTFE showed a high loading of zinc oxide inside the polymeric matrixes. Most of those polymers have negative glass transition temperatures, therefore the VPI processes in all those cases have been performed above glass transition.

5.7 Polyvinyl chloride-based hybrids

To confirm the vital impact of the halogens on the self-healing properties, besides ParyleneC another halogen-containing substrate was tested: PVC. Despite the high glass transition temperature of 87°C, [258] 100 VPI cycles of DEZ/H_2O at 120°C and the pulse/exposure/purging sequence of 0.4/30/60 seconds resulted in a 2 μm thick PVC/zinc-containing hybrid (Figure 5.18). The near-surface layer of higher density with inorganic NPs had a thickness of 130 nm and can be easily distinguished.
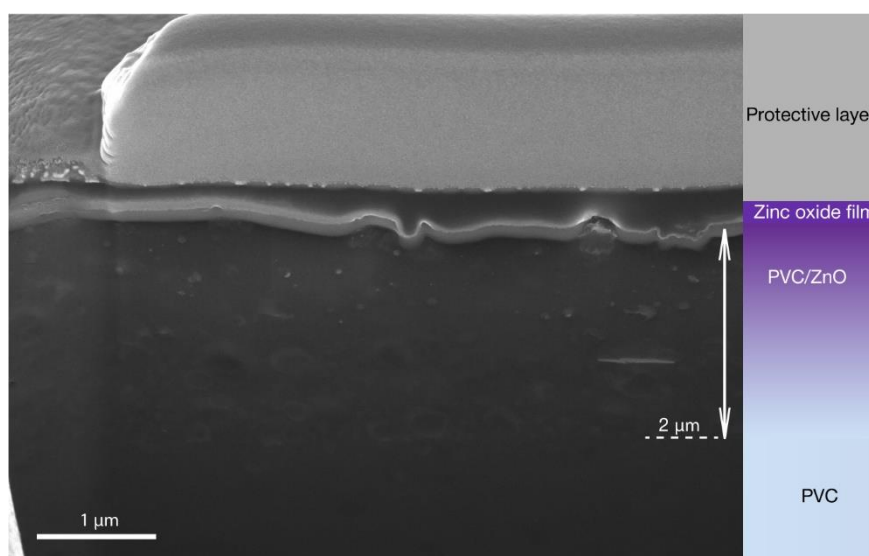
Figure 5.18 FIB cross-section of a VPI-infiltrated PVC/ZnO hybrid.

The chemical analysis by XPS, performed after 20 minutes of Ar$^+$ etching revealed the simultaneous presence of carbon, chlorine, zinc, and oxygen, proving the hybrid nature of the infiltrated part. We measured the characteristic Cl 2p peak and compared it to the Cl peak of the untreated polymer

(Figure 5.19). Despite the main contribution at 200 eV arising from chlorine bound to organic carbon, additional Zn-Cl compounds were formed, as seen from the increased width of the peak at lower binding energies (Figure 5.19). [184]
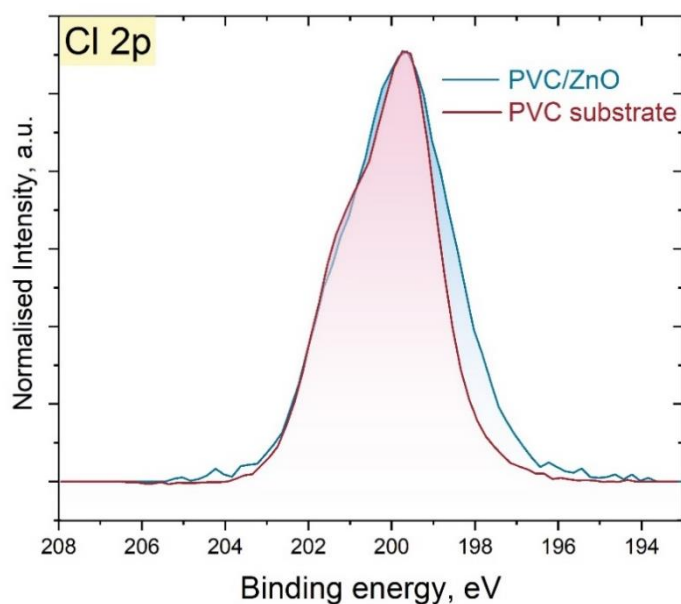
Figure 5.19 Comparison of the XPS Cl 2p doublets in the PVC/ZnO hybrid (blue) and the PVC substrate (red). The broadening of the Cl 2p peak of the PVC/ZnO hybrid results from the contribution of Zn-Cl.

Repeating the same procedure of FIB etching followed by exposure to air resulted in the mending of induced defects. The agglomeration of the NPs at the hybrid/air interface of the FIB-etched pattern was already apparent after five minutes of exposure to air and continued until complete closure of the rupture. (Figure 5.20).
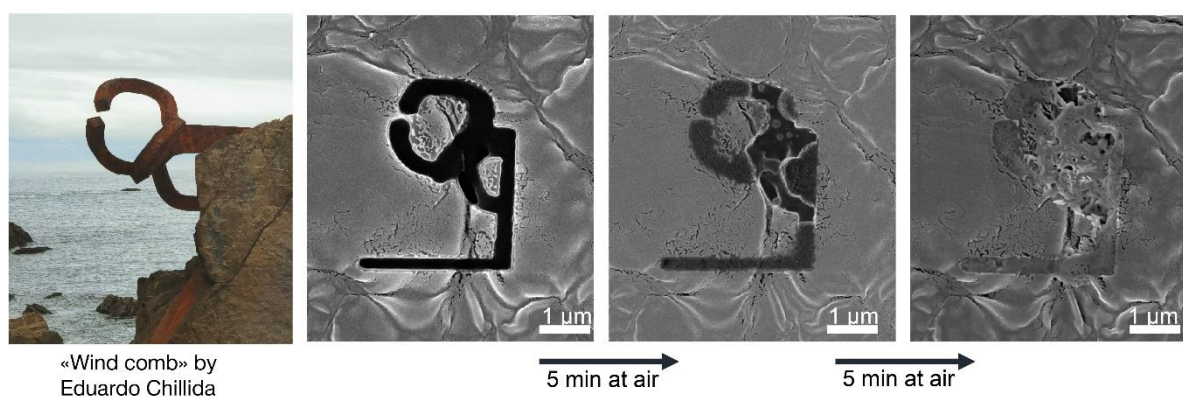
Figure 5.20 Healing of a selectively FIB-etched pattern on the PVC/ZnO surface over time. The left image is a photo of the sculpture "Wind comb", created by Eduardo Chillida.

The discriminating element between the various systems is the chlorine functionality present in ParyleneC and PVC, but not in the other studied polymers. In the ParyleneC/In$_x$O$_y$ system, the crystal structure of the NPs matches cubic indium oxide, but no electron diffraction reflections from crystalline indium chloride were observed (Figure 5.3a). At the same time, XPS clearly identified the chemical states of indium bound to chlorine (Figure 5.2 b). TMIn has 3 methyl groups that can abstract nucleophile methylene groups. Due to having chlorine bound to the aromatic rings in ParyleneC, it is likely that upon infiltration some fraction of the polymer undergoes a nucleophilic aromatic substitution of chloride with methylene groups and in turn the substituted chloride binds to indium to form indium chloride. Given the fact that TMIn can likely react with only one chlorine at a time due to steric reasons, indium chloride might be neither stoichiometric nor crystalline. But it would be an indium chloride – indium oxide mixed compound. With an external stimulus, such as UV radiation, thermal treatment, or electron beam irradiation, the energy of the system reaches a critical value required for the depletion attraction-driven NP diffusion towards the damaged sites. The halogen in/on the NPs enhances the mobility of the NPs by reducing the interaction of the particle with the polymer backbone.

It is important to note, that PTFE also didn't show healing ability despite being halogenated. Although PTFE is very inert, it was successfully homogeneously infiltrated to a depth of more than 6 µm. The used PTFE had a highly porous structure that facilitated easier diffusion of the precursors and, therefore, a profound infiltrated layer. Since XPS measurements on PTFE/ZnO structures were not performed, there are no data about the possible formation of zinc fluorides.

5.8 Chlorination of polymers

The strategy of particle chlorination for enhancing their mobility has been earlier applied to gold [259] and silver [260] metal NPs and appears to be applicable for our system as well. Moreover, one may extend our approach also to non-halogenated polymers by using a third, Cl-containing precursor during VPI processing. We performed such an experiment by introducing a chlorination agent, thionyl chloride (SOCl$_2$), into the system. The processing conditions are indicated in Table 7. The repetition of one pulse of SOCl$_2$ and 7 cycles of DEZ/H$_2$O constituted 1 Supercycle.

Table 7. Conditions of one VPI supercycle for simultaneous chlorination and ZnO infiltration.

Precursors	Pulse, sec	Exposure, sec	Purge, sec	Number of cycles
SOCl$_2$	0.4	30	20	1
DEZ	0.4	30	60	7
H$_2$O	0.4	30	60	

We applied 15 such supercycles to non-halogenated PDMS at 120°C (Figure 5.21 a). Mobility of the infiltrated ZnO clusters was observed in the SOCl$_2$-treated samples (Figure 5.21 b, c), but not in those without SOCl$_2$ treatment, further confirming the important role of the halogen for the migration of the clusters. The chlorination facilitated the mobility and once the chlorine-containing NPs reach an open surface, for example the FIB-etched or mechanically damaged area, the contained metal chloride reacts with ambient air to form a metal oxychloride or metal oxide.
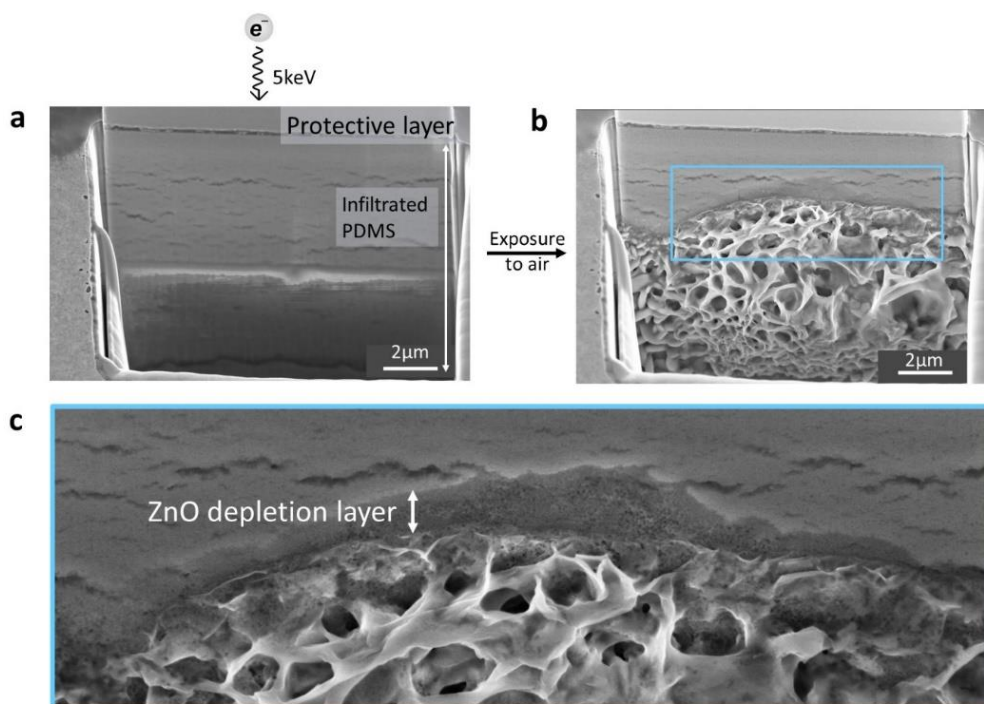
Figure 5.21 FIB cross-section of SOCl$_2$ and DEZ/H$_2$O VPI-treated PDMS before (a) and after (b) exposure to air. (c) Magnification of the marked area in (b). During the VPI process, one SOCl$_2$ pulse was performed after every 7th cycle of DEZ/H$_2$O.

Application of this three-precursor process to PA-6 didn't induce such a significant mobility of the NPs, however, we observed few neoformations at the interface of the polymer and the hybrid layer (Figure 5.22). Most likely the density of the inorganic NPs was too high for an efficient mobility, but in regions where the density of the particles is lower due to the infiltration gradient formation, the mobility was enabled.
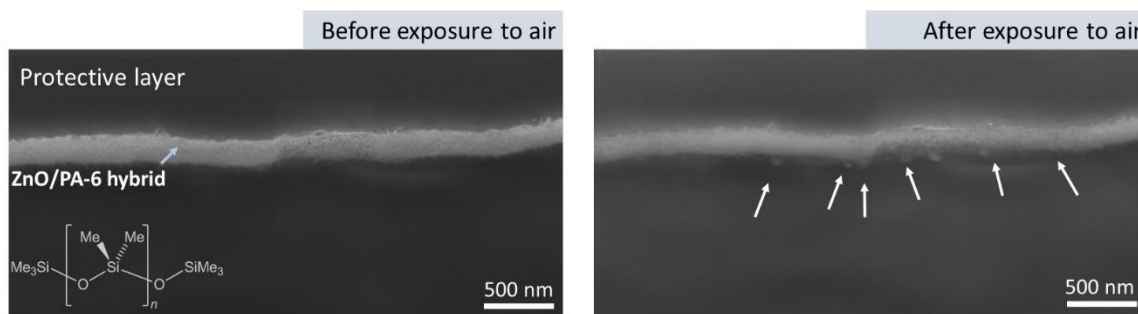
Figure 5.22 FIB cross-sections of nylon-6 before and after exposure to ambient air.

The polymer-inorganic hybrid systems are very complex in their composition and have numerous degrees of freedom for their design. Therefore, besides preventing Van-der-Walls attraction between the NPs and polymers, also other factors should be considered for fabricating hybrid self-healing systems. The polymer crystallinity, density, and molecular weight affect the infiltration depth, [10] which will considerably change the total amount of NPs stored in the bulk of the polymer and available for self-healing. Those factors also will affect the free volume of a polymer and hence the size of the NPs and their distribution. Smaller NPs possess higher diffusion rates, [261] however, larger NPs cause a gain in conformational entropy upon migration to a newly formed surface (e.g., defect), [248] thus larger particles may be preferred. The concentration of NPs in a blend also plays a crucial role, since too high concentrations will lead to bulk segregation [119] and likely have a negative impact on the material healing process

5.9 Conclusions

The present work demonstrates a methodology for the self-healing of metal oxide coatings. This was done without the use of liquid and reactive healing agents, but through the growth of well-dispersed metal oxide NPs inside chlorinated polymers and enabling their diffusion and aggregation. Artificially induced defects in the coatings became sealed after exposure of the system to air. This self-healing is likely driven by an entropic penalty, which arises in the metal oxide/polymer hybrid system and drives the migration of NPs to the damaged sites and microcracks. Furthermore, our studies reveal that the presence of metal halides, here chlorides, is of crucial importance for enhancing the mobility of the MeO nanoparticles inside the host polymeric matrix and thereby the ability of the system to self-heal in general.

The investigated oxides of zinc and indium in this study are constituent materials of the common TCOs. IZO or aluminum-doped zinc oxide are often considered to be possible substitutes for the most widely used TCO, namely ITO. Therefore, our methodology can support the longevity of current transparent conductive materials as cracks that occur upon bending could recover up to a certain degree. Moreover, this discovery forms a cornerstone for the development of further

inorganic self-healing materials by infiltrating alternative metal oxides into halogenated polymers or speculatively also growing halogenated MeO particles inside a broader variety of non-halogenated polymers. Consequently, this development might benefit numerous technological areas: flexible electronics, wearable sensors, photovoltaics, displays, and energy by potentially enhancing the durability and longevity of the materials.

Summary and outlook

Our society undergoes constant transformation, relying more and more on electronic devices with progressing time. The design of those devices is becoming increasingly sophisticated and in the current state-of-the-art includes also flexible or foldable electronics and personal medical devices. Such highly complex products cannot anymore rely only on conventional materials, but they require additional engineering and research efforts. Hybrid materials promise an added value to the final devices through a merger of the functionality of their constituents or even additional properties emerging from synergies between the constituents. For example, simultaneous presence of mechanical flexibility and robustness towards mechanical damage are promising concepts in the battle for a device's longevity. A respectful attitude to all the constituent elements to avoid single-use devices is a necessary step forward to a sustainable future.

The hybridization of conductive metal oxides with polymers via VPI is a promising pathway for obtaining conductive and simultaneously flexible materials. The constraints arising from the thermal stability of a polymer or reactivity and the size of precursors can be tackled through a careful choice of materials. In this aspect, the use of less reactive precursors and polymeric matrixes without available chemical functionalities can be beneficial. In Chapter 3, we discussed the formation of a hybrid material combination between ParyleneC/In_xO_y. Indium oxide nanocrystals grew within the polymeric matrix even at low processing temperatures of 120-170°C, which depended on the oxygen source used. They yield electrical conductivities of about 10 kOhm/□ even without the otherwise typical annealing procedures. Nevertheless, those values are lower than those of nanolaminates composed of the same materials with well-determined interfaces between the organic and inorganic counterparts. Most likely the reason can be found in the large number of boundaries between the crystallites that scatter and trap electrons. The hybrid nature allowed bending of the resulting hybrid sheets over a small radius of 1 mm, suppressing crack propagation, and preserving the conductive pathways. Additionally, the ParyleneC/In_xO_y hybrid showed persistent photoconductivity that remained over days.

Zinc oxide is also of technological importance as a constituent of various transparent conductive oxides. Infiltration of ZnO into ParyleneC resulted in the formation of a more profound hybrid layer than that of indium oxide, as shown in Chapter 4. Despite DEZ being more reactive than TMIn, the ZnO VPI didn't lead to the formation of metal chlorides as observed in the case of TMIn, which could be beneficial for electronic applications. The formed embedded ZnO nanoparticles had a cubic structure and the use of hydrogen peroxide as second precursor instead of water increased the degree of crystallinity. Such loading of ParyleneC with a metal oxide led to an enhancement of the thermal stability.

Chapter 5 investigates the ability of these hybrid structures to self-heal. All studied metal oxides: indium, zinc, IZO, ITO, and nickel oxides showed a self-healing functionality. The use of the vapor phase approach instead of solution-based methods is beneficial for this target. Namely, VPI leads to

the formation of NPs only within the accessible free volume of a polymer, leaving the NPs surrounded by polymer chains. Since the free volume of a polymer expands with heating above its glass transition temperature, and VPI is performed at elevated temperatures, cooling of the system after the process leads to the shrinkage of the polymeric matrix and, consequently, to an increased osmotic pressure on the NPs, which eventually induces a mobility of the NPs. We found that the crucial trigger for the mass mobility is the halogen contained in the polymer matrix of ParyleneC and PVC that prevents strong binding of the infiltrate to the polymer backbone, allowing easier mobility within the matrix. This was further confirmed with the use of thionyl chloride as non-intrinsic halogen source during the infiltration process and a non-halogenated polymer, which also allowed the material to migrate upon creation of a damage in the surface. Besides the halogen, the density of the inorganic NPs and the contact with air are confirmed to be further important factors for the diffusion and, consequently, self-healing processes. Summarizing our experimental results, an interplay of entropic and enthalpic interactions in the system makes the self-healing of semiconductors possible and with the choice of substrate, infiltrate and, where needed, halogen source, the capability of the material system to self-heal can be controlled.

This thesis offers a first endeavor for the formation of self-healing semiconducting materials, which was not available up-to date. Being an indispensable part of electrical devices, the research works conducted in this field remain scarce due to the opposite nature of rigid semiconductors and the flexibility of a material which is required for self-healing. The entropy-driven aggregation of the NPs at the interfaces aims to answer this challenge, avoiding liquid healing agents but employing mobile NPs with diameters of 3-5 nm instead. The use of gas-phase approaches brings the possibility of post-processing of nanostructured materials and makes their up-scaling feasible, while simultaneously avoiding the use of solvents and their rather expensive removal from the material and regeneration. With the choice of dielectric polymeric substrates, the introduced hybrid structures can serve as electrodes which are already sealed with a dielectric shell.

Further research on other polymer-inorganic material combinations is likely to result in even more inspiring outcomes. Since the overall response of a system is a convergence between its components, a profound investigation of the impact of various parameters is still needed. Among those are the polymer molar mass, porosity and tortuosity of the free volume, density and size of inorganic NPs, lateral and depth dimensions of defects, energetic inputs on the system, including thermal, electrical, or optical, and the impact of the ambience. A careful investigation of the mechanisms of healing can bring more control over the process, anticipating future prosperous applications

Bibliography

[1]   M. Faustini, L. Nicole, E. Ruiz-Hitzky, and C. Sanchez, "History of Organic–Inorganic Hybrid Materials: Prehistory, Art, Science, and Advanced Applications," *Adv Funct Mater*, vol. 28, no. 27, pp. 1–30, 2018, doi: 10.1002/adfm.201704158.

[2]   Y. Liu, K. He, G. Chen, W. R. Leow, and X. Chen, "Nature-Inspired Structural Materials for Flexible Electronic Devices," *Chem Rev*, vol. 117, no. 20, pp. 12893–12941, Oct. 2017, doi: 10.1021/acs.chemrev.7b00291.

[3]   A. Kaushik, R. Kumar, S. K. Arya, M. Nair, B. D. Malhotra, and S. Bhansali, "Organic-Inorganic Hybrid Nanocomposite-Based Gas Sensors for Environmental Monitoring," *Chemical Reviews*, vol. 115, no. 11. American Chemical Society, pp. 4571–4606, Jun. 10, 2015. doi: 10.1021/cr400659h.

[4]   A. Li *et al.*, "Mineral Enhanced Polyacrylic Acid Hydrogel as Oyster-Inspired Organic-Inorganic Hybrid Adhesive," 2018.

[5]   V. K. Perla, S. K. Ghosh, and K. Mallick, "Nonvolatile switchable resistive behaviour via organic–inorganic hybrid interactions," *J Mater Sci*, vol. 54, no. 3, pp. 2324–2332, Feb. 2019, doi: 10.1007/s10853-018-2969-x.

[6]   Y. Zhang *et al.*, "Ambient Fabrication of Organic–Inorganic Hybrid Perovskite Solar Cells," *Small Methods*, vol. 5, no. 1. John Wiley and Sons Inc, Jan. 01, 2021. doi: 10.1002/smtd.202000744.

[7]   N. Nashrah *et al.*, "metals Hybrid Organic-Inorganic Materials on Metallic Surfaces: Fabrication and Electrochemical Performance Citation: Nashrah, N Hybrid Organic-Inorganic Materials on Metallic Surfaces: Fabrication and Electrochemical Performance. Metals," 2021, doi: 10.3390/met11071043.

[8]   K. Ashurbekova, K. Ashurbekova, G. Botta, O. Yurkevich, and M. Knez, "Vapor phase processing: A novel approach for fabricating functional hybrid materials," *Nanotechnology*, vol. 31, no. 34, Aug. 2020, doi: 10.1088/1361-6528/ab8edb.

[9]   K. Gregorczyk and M. Knez, "Hybrid nanomaterials through molecular and atomic layer deposition: Top down, bottom up, and in-between approaches to new materials," *Prog Mater Sci*, vol. 75, pp. 1–37, Jan. 2016, doi: 10.1016/j.pmatsci.2015.06.004.

[10]   C. Z. Leng and M. D. Losego, "Vapor phase infiltration (VPI) for transforming polymers into organic-inorganic hybrid materials: A critical review of current progress and future challenges," *Materials Horizons*, vol. 4, no. 5. Royal Society of Chemistry, pp. 747–771, Sep. 01, 2017. doi: 10.1039/c7mh00196g.

[11]   P. Sundberg and M. Karppinen, "Organic and inorganic–organic thin film structures by molecular layer deposition: A review," *Beilstein Journal of Nanotechnology 5:123*, vol. 5, no. 1, pp. 1104–1136, Jul. 2014, doi: 10.3762/bjnano.5.123.

[12]   R. L. Puurunen, Surface chemistry of atomic layer deposition: a case study for the trimethylaluminum/*water process*, vol. 97, no. 12. 2005. doi: 10.1063/1.1940727.

[13]   R. W. Johnson, A. Hultqvist, and S. F. Bent, "A brief review of atomic layer deposition: From fundamentals to applications," *Materials Today*, vol. 17, no. 5, pp. 236–246, 2014, doi: 10.1016/j.mattod.2014.04.026.

[14]   S. M. George, "Atomic layer deposition: An overview," *Chem Rev*, vol. 110, no. 1, pp. 111–131, 2010, doi: 10.1021/cr900056b.

[15]   A. A. Dameron *et al.*, "Molecular layer deposition of alucone polymer films using trimethylaluminum and ethylene glycol," *Chemistry of Materials*, vol. 20, no. 10, pp. 3315–3326, 2008, doi: 10.1021/cm7032977.

[16]   B. Yoon, B. H. Lee, and S. M. George, "Molecular layer deposition of flexible, transparent and conductive hybrid organic-inorganic thin films," *ECS Trans*, vol. 41, no. 2, pp. 271–277, 2011, doi: 10.1149/1.3633677.

[17]   B. H. Lee, V. R. Anderson, and S. M. George, "Molecular layer deposition of zircone and ZrO2/zircone alloy films: Growth and properties," *Chemical Vapor Deposition*, vol. 19, no. 4–6, pp. 204–212, 2013, doi: 10.1002/cvde.201207045.

[18]   B. H. Lee, V. R. Anderson, and S. M. George, "Growth and properties of hafnicone and HfO2/Hafnicone nanolaminate and alloy films using molecular layer deposition techniques," *ACS Appl Mater Interfaces*, vol. 6, no. 19, pp. 16880–16887, 2014, doi: 10.1021/am504341r.

[19]   K. Van de Kerckhove, F. Mattelaer, J. Dendooven, and C. Detavernier, "Molecular layer deposition of 'vanadicone', a vanadium-based hybrid material, as an electrode for lithium-ion batteries," *Dalton Transactions*, vol. 46, no. 14, pp. 4542–4553, 2017, doi: 10.1039/c7dt00374a.

[20]   S. Lee *et al.*, "Molecular layer deposition of indicone and organic-inorganic hybrid thin films as flexible transparent conductor," *Appl Surf Sci*, vol. 525, Sep. 2020, doi: 10.1016/j.apsusc.2020.146383.

[21]   J. J. Eldridge *et al.*, "Greatly Increased Toughness of Infiltrated Spider Silk," *Science (1979)*, vol. 324, no. APRIL 2009, pp. 488–492, 2009.

[22]   S. Choy, D. Van Lam, S. M. Lee, and D. S. Hwang, "Prolonged Biodegradation and Improved Mechanical Stability of Collagen via Vapor-Phase Ti Stitching for Long-Term Tissue Regeneration," *ACS Appl Mater Interfaces*, vol. 11, no. 42, pp. 38440–38447, Oct. 2019, doi: 10.1021/acsami.9b12196.

[23] S. Choy *et al.*, "Tough and Immunosuppressive Titanium-Infiltrated Exoskeleton Matrices for Long-Term Endoskeleton Repair," *ACS Appl Mater Interfaces*, vol. 11, no. 10, pp. 9786–9793, Mar. 2019, doi: 10.1021/acsami.8b21569.

[24] K. E. Gregorczyk, D. F. Pickup, M. G. Sanz, I. A. Irakulis, C. Rogero, and M. Knez, "Tuning the tensile strength of cellulose through vapor-phase metalation," *Chemistry of Materials*, vol. 27, no. 1, pp. 181–188, Jan. 2015, doi: 10.1021/cm503724c.

[25] K. Pyronneau *et al.*, "Wash Fastness of Hybrid AlOx-PET Fabrics Created via Vapor-Phase Infiltration," *ACS Appl Polym Mater*, 2021, doi: 10.1021/acsapm.1c01851.

[26] H. I. Akyildiz, M. Lo, E. Dillon, A. T. Roberts, H. O. Everitt, and J. S. Jur, "Formation of novel photoluminescent hybrid materials by sequential vapor infiltration into polyethylene terephthalate fibers," *J Mater Res*, vol. 29, no. 23, pp. 2817–2826, Nov. 2014, doi: 10.1557/jmr.2014.333.

[27] Y. Yu, Z. Li, Y. Wang, S. Gong, and X. Wang, "Sequential Infiltration Synthesis of Doped Polymer Films with Tunable Electrical Properties for Efficient Triboelectric Nanogenerator Development," *Advanced Materials*, vol. 27, no. 33, pp. 4938–4944, 2015, doi: 10.1002/adma.201502546.

[28] X. He *et al.*, "Resolving the atomic structure of sequential infiltration synthesis derived inorganic clusters," *ACS Nano*, vol. 14, no. 11, pp. 14846–14860, 2020, doi: 10.1021/acsnano.0c03848.

[29] C. D. McClure, C. J. Oldham, and G. N. Parsons, "Effect of Al2O3 ALD coating and vapor infusion on the bulk mechanical response of elastic and viscoelastic polymers," *Surf Coat Technol*, vol. 261, pp. 411–417, Jan. 2015, doi: 10.1016/j.surfcoat.2014.10.029.

[30] Y. Li *et al.*, "Highly-stable PEN as a gas-barrier substrate for flexible displays via atomic layer infiltration," *Dalton Transactions*, vol. 50, no. 44, pp. 16166–16175, Nov. 2021, doi: 10.1039/d1dt02764f.

[31] I. Azpitarte *et al.*, "Suppressing the Thermal and Ultraviolet Sensitivity of Kevlar by Infiltration and Hybridization with ZnO," *Chemistry of Materials*, vol. 29, no. 23, pp. 10068–10074, 2017, doi: 10.1021/acs.chemmater.7b03747.

[32] S. M. Lee *et al.*, "An Alternative Route Towards Metal–Polymer Hybrid Materials Prepared by Vapor-Phase Processing," *Adv Funct Mater*, vol. 21, no. 16, pp. 3047–3055, Aug. 2011, doi: 10.1002/adfm.201100384.

[33] X. Ye *et al.*, "Effects of Residual Solvent Molecules Facilitating the Infiltration Synthesis of ZnO in a Nonreactive Polymer," *Chemistry of Materials*, vol. 29, no. 10, pp. 4535–4545, 2017, doi: 10.1021/acs.chemmater.7b01222.

[34] E. Barry, A. U. Mane, J. A. Libera, J. W. Elam, and S. B. Darling, "Advanced oil sorbents using sequential infiltration synthesis," *J Mater Chem A Mater*, vol. 5, no. 6, pp. 2929–2935, 2017, doi: 10.1039/c6ta09014a.

[35] W. Wang *et al.*, "Conductive Polymer-Inorganic Hybrid Materials through Synergistic Mutual Doping of the Constituents," *ACS Appl Mater Interfaces*, vol. 9, no. 33, pp. 27964–27971, 2017, doi: 10.1021/acsami.7b09270.

[36] C. Y. Nam and A. Stein, "Extreme Carrier Depletion and Superlinear Photoconductivity in Ultrathin Parallel-Aligned ZnO Nanowire Array Photodetectors Fabricated by Infiltration Synthesis," *Adv Opt Mater*, vol. 5, no. 24, p. 1700807, Dec. 2017, doi: 10.1002/ADOM.201700807.

[37] Y. Sun, R. P. Padbury, H. I. Akyildiz, M. P. Goertz, J. A. Palmer, and J. S. Jur, "Influence of Subsurface Hybrid Material Growth on the Mechanical Properties of Atomic Layer Deposited Thin Films on Polymers," *Chemical Vapor Deposition*, vol. 19, no. 4–6, pp. 134–141, Jun. 2013, doi: 10.1002/cvde.201207042.

[38] K. J. Dusoe, X. Ye, K. Kisslinger, A. Stein, S. W. Lee, and C. Y. Nam, "Ultrahigh Elastic Strain Energy Storage in Metal-Oxide-Infiltrated Patterned Hybrid Polymer Nanocomposites," *Nano Lett*, vol. 17, no. 12, pp. 7416–7423, Dec. 2017, doi: 10.1021/acs.nanolett.7b03238.

[39] L. Cheng *et al.*, "Sub-10 nm Tunable Hybrid Dielectric Engineering on MoS2 for Two-Dimensional Material-Based Devices," *ACS Nano*, vol. 11, no. 10, pp. 10243–10252, 2017, doi: 10.1021/acsnano.7b04813.

[40] B. Yoon, B. H. Lee, and S. M. George, "Highly conductive and transparent hybrid organic-inorganic zincone thin films using atomic and molecular layer deposition," *Journal of Physical Chemistry C*, vol. 116, no. 46, pp. 24784–24791, 2012, doi: 10.1021/jp3057477.

[41] W. Ren *et al.*, "High-performance wearable thermoelectric generator with self-healing, recycling, and Lego-like reconfiguring capabilities," *Sci Adv*, vol. 7, no. 7, p. eabe0586, 2021, doi: 10.1126/sciadv.abe0586.

[42] M. D. Hager, "Self-healing Materials," pp. 201–226, 2017.

[43] R. Han and K. P. Campbell, "Dysferlin and muscle membrane repair," *Curr Opin Cell Biol*, vol. 19, no. 4, pp. 409–416, Aug. 2007, doi: 10.1016/j.ceb.2007.07.001.

[44] R. París, L. Lamattina, and C. A. Casalongué, "Nitric oxide promotes the wound-healing response of potato leaflets," *Plant Physiology and Biochemistry*, vol. 45, no. 1, pp. 80–86, Jan. 2007, doi: 10.1016/j.plaphy.2006.12.001.

[45] C. N. Z. Schmitt, Y. Politi, A. Reinecke, and M. J. Harrington, "Role of sacrificial protein-metal bond exchange in mussel byssal thread self-healing," *Biomacromolecules*, vol. 16, no. 9, pp. 2852–2861, Sep. 2015, doi: 10.1021/acs.biomac.5b00803.

[46] M. Khatib, O. Zohar, and H. Haick, "Self-Healing Soft Sensors: From Material Design to Implementation," *Advanced Materials*, vol. 33, no. 11, pp. 1–32, 2021, doi: 10.1002/adma.202004190.

[47] K. A. Williams, A. J. Boydston, and C. W. Bielawski, "Towards electrically conductive, self-healing materials," *J R Soc Interface*, vol. 4, no. 13, pp. 359–362, Apr. 2007, doi: 10.1098/rsif.2006.0202.

[48] J. Y. Oh *et al.*, "Intrinsically stretchable and healable semiconducting polymer for organic transistors," *Nature*, vol. 539, no. 7629, pp. 411–415, 2016, doi: 10.1038/nature20102.

[49] B. J. Blaiszik, S. L. B. Kramer, S. C. Olugebefola, J. S. Moore, N. R. Sottos, and S. R. White, "Self-healing polymers and composites," *Annu Rev Mater Res*, vol. 40, pp. 179–211, 2010, doi: 10.1146/annurev-matsci-070909-104532.

[50] S. Wang and M. W. Urban, "Self-healing polymers," *Nat Rev Mater*, vol. 5, no. 8, pp. 562–583, 2020, doi: 10.1038/s41578-020-0202-4.

[51] V. K. Thakur and M. R. Kessler, "Self-healing polymer nanocomposite materials: A review," *Polymer (Guildf)*, vol. 69, pp. 369–383, Jul. 2015, doi: 10.1016/j.polymer.2015.04.086.

[52] Y. Yang, D. Davydovich, C. C. Hornat, X. Liu, and M. W. Urban, "Leaf-Inspired Self-Healing Polymers," *Chem*, vol. 4, no. 8, pp. 1928–1936, Aug. 2018, doi: 10.1016/j.chempr.2018.06.001.

[53] S. Terryn *et al.*, "A review on self-healing polymers for soft robotics," *Materials Today*, vol. 47, pp. 187–205, Jul. 2021, doi: 10.1016/j.mattod.2021.01.009.

[54] R. P. Wool and K. M. O'Connor, "A theory crack healing in polymers," *J Appl Phys*, vol. 52, no. 10, p. 5953, Jun. 1998, doi: 10.1063/1.328526.

[55] J. Nji and G. Li, "A biomimic shape memory polymer based self-healing particulate composite," *Polymer (Guildf)*, vol. 51, no. 25, pp. 6021–6029, Nov. 2010, doi: 10.1016/j.polymer.2010.10.021.

[56] Y. Chen, A. M. Kushner, G. A. Williams, and Z. Guan, "Multiphase design of autonomic self-healing thermoplastic elastomers," *Nature Chemistry 2012 4:6*, vol. 4, no. 6, pp. 467–472, Apr. 2012, doi: 10.1038/nchem.1314.

[57] C. C. Corten, M. W. Urban, and F. Shelby, "Repairing Polymers Using Oscillating Magnetic Field," *Advanced Materials*, vol. 21, no. 48, pp. 5011–5015, Dec. 2009, doi: 10.1002/adma.200901940.

[58] S. Gupta, Q. Zhang, T. Emrick, A. C. Balazs, and T. P. Russell, "Entropy-driven segregation of nanoparticles to cracks in multilayered composite polymer structures," *Nat Mater*, vol. 5, no. 3, pp. 229–233, 2006, doi: 10.1038/nmat1582.

[59] J. Dahlke, S. Zechel, M. D. Hager, and U. S. Schubert, "How to Design a Self-Healing Polymer: General Concepts of Dynamic Covalent Bonds and Their Application for Intrinsic Healable Materials," *Adv Mater Interfaces*, vol. 5, no. 17, p. 1800051, Sep. 2018, doi: 10.1002/admi.201800051.

[60] M. M. Perera and N. Ayres, "Dynamic covalent bonds in self-healing, shape memory, and controllable stiffness hydrogels," *Polym Chem*, vol. 11, no. 8, pp. 1410–1423, Feb. 2020, doi: 10.1039/c9py01694e.

[61] B. Ghosh and M. W. Urban, "Self-repairing oxetane-substituted chitosan polyurethane networks," *Science (1979)*, vol. 323, no. 5920, pp. 1458–1460, Mar. 2009, doi: 10.1126/science.1167391.

[62] A. Campanella, D. Döhler, W. H. Binder, A. Campanella, D. Döhler, and H. Binder, "Self-Healing in Supramolecular Polymers," *Macromol Rapid Commun*, vol. 39, no. 17, p. 1700739, Sep. 2018, doi: 10.1002/marc.201700739.

[63] Y. Yang, M. W. Urban, Y. Yang, and M. W. Urban, "Self-Healing of Polymers via Supramolecular Chemistry," *Adv Mater Interfaces*, vol. 5, no. 17, p. 1800384, Sep. 2018, doi: 10.1002/admi.201800384.

[64] W. Zhang *et al.*, "Recent achievements in self-healing materials based on ionic liquids: a review," *J Mater Sci*, vol. 55, no. 28, pp. 13543–13558, Oct. 2020, doi: 10.1007/S10853-020-04981-0.

[65] C. H. Li and J. L. Zuo, "Self-Healing Polymers Based on Coordination Bonds," *Advanced Materials*, vol. 32, no. 27, pp. 1–29, 2020, doi: 10.1002/adma.201903762.

[66] M. R. Kessler, N. R. Sottos, and S. R. White, "Self-healing structural composite materials," *Compos Part A Appl Sci Manuf*, vol. 34, no. 8, pp. 743–753, Aug. 2003, doi: 10.1016/S1359-835X(03)00138-6.

[67] S. M. Aouadi, J. Gu, and D. Berman, "Self-healing ceramic coatings that operate in extreme environments: A review," *Journal of Vacuum Science & Technology A*, vol. 38, no. 5, p. 050802, 2020, doi: 10.1116/6.0000350.

[68] D. Mohanty, A. Sil, and K. Maiti, "Development of input output relationships for self-healing Al2O3/SiC ceramic composites with Y2O3 additive using design of experiments," *Ceram Int*, vol. 37, no. 6, pp. 1985–1992, Aug. 2011, doi: 10.1016/j.ceramint.2011.03.046.

[69] F. Tavangarian and G. Li, "Bio-inspired crack self-healing of SiC/spinel nanocomposite," *Ceram Int*, vol. 41, no. 2, pp. 2828–2835, Mar. 2015, doi: 10.1016/j.ceramint.2014.10.103.

[70] L. Y. Wang, R. Y. Luo, G. yuan Cui, and Z. feng Chen, "Oxidation resistance of SiCf/SiC composites with a PyC/SiC multilayer interface at 500 °C to 1100°C," *Corros Sci*, vol. 167, p. 108522, May 2020, doi: 10.1016/j.corsci.2020.108522.

[71] Z. H. Yang, D. C. Jia, Y. Zhou, P. Y. Shi, C. Bin Song, and L. Lin, "Oxidation resistance of hot-pressed SiC–BN composites," *Ceram Int*, vol. 34, no. 2, pp. 317–321, Mar. 2008, doi: 10.1016/j.ceramint.2006.10.010.

[72] K. Houjou, K. Ando, and K. Takahashi, "Crack-healing behaviour of ZrO2/SiC composite ceramics," *International Journal of Structural Integrity*, vol. 1, no. 1, pp. 73–84, 2010, doi: 10.1108/17579861011023810.

[73] A. S. Farle, C. Kwakernaak, S. van der Zwaag, and W. G. Sloof, "A conceptual study into the potential of Mn+1AXn-phase ceramics for self-healing of crack damage," *J Eur Ceram Soc*, vol. 35, no. 1, pp. 37–45, Jan. 2015, doi: 10.1016/j.jeurceramsoc.2014.08.046.

[74] H. J. Yang, Y. T. Pei, J. C. Rao, and J. T. M. De Hosson, "Self-healing performance of Ti2AlC ceramic," *J Mater Chem*, vol. 22, no. 17, pp. 8304–8313, Apr. 2012, doi: 10.1039/c2jm16123k.

[75] O. Berger and R. Boucher, "Crack healing in Y-doped Cr2AlC-MAX phase coatings," vol. 33, no. 3, pp. 192–203, Mar. 2016, doi: 10.1080/02670844.2016.1201366.

[76] J. J. Gu, D. Steiner, J. E. Mogonye, and S. M. Aouadi, "Precipitation-induced healing of Nb2O5," *J Eur Ceram Soc*, vol. 37, no. 13, pp. 4141–4146, Oct. 2017, doi: 10.1016/j.jeurceramsoc.2017.04.054.

[77] L. Jun, Z. X. Zheng, H. F. Ding, and Z. H. Jin, "Preliminary study of the crack healing and strength recovery of Al2O3-matrix composites," *Fatigue Fract Eng Mater Struct*, vol. 27, no. 2, pp. 89–97, Feb. 2004, doi: 10.1111/j.1460-2695.2004.00725.x.

[78] Guangyong Li, Xuan Wu, and Dong-Weon Lee, "A galinstan-based inkjet printing system for highly stretchable electronics with self-healing capability," *Lab Chip*, vol. 16, no. 8, pp. 1366–1373, Apr. 2016, doi: 10.1039/c6lc00046k.

[79] J. William Boley, E. L. White, R. K. Kramer, J. W. Boley, E. L. White, and R. K. Kramer, "Mechanically Sintered Gallium–Indium Nanoparticles," *Advanced Materials*, vol. 27, no. 14, pp. 2355–2360, Apr. 2015, doi: 10.1002/adma.201404790.

[80] E. Palleau, S. Reece, S. C. Desai, M. E. Smith, and M. D. Dickey, "Self-Healing Stretchable Wires for Reconfigurable Circuit Wiring and 3D Microfluidics," *Advanced Materials*, vol. 25, no. 11, pp. 1589–1592, Mar. 2013, doi: 10.1002/adma.201203921.

[81] R. Tutika, A. B. M. T. Haque, and M. D. Bartlett, "Self-healing liquid metal composite for reconfigurable and recyclable soft electronics," *Communications Materials 2021 2:1*, vol. 2, no. 1, pp. 1–8, Jun. 2021, doi: 10.1038/s43246-021-00169-4.

[82] E. J. Markvicka, M. D. Bartlett, X. Huang, and C. Majidi, "An autonomously electrically self-healing liquid metal-elastomer composite for robust soft-matter robotics and electronics," *Nat Mater*, vol. 17, no. 7, pp. 618–624, Jul. 2018, doi: 10.1038/s41563-018-0084-7.

[83] H. A. Liu, B. E. Gnade, and K. J. Balkus, "A delivery system for self-healing inorganic films," *Adv Funct Mater*, vol. 18, no. 22, pp. 3620–3629, 2008, doi: 10.1002/adfm.200701470.

[84] H. Yue, Z. Wang, and Y. Zhen, "Recent Advances of Self-Healing Electronic Materials Applied in Organic Field-Effect Transistors," *ACS Omega*, vol. 7, no. 22, pp. 18197–18205, Jun. 2022, doi: 10.1021/acsomega.2c00580.

[85] M. Shin *et al.*, "Polythiophene Nanofibril Bundles Surface-Embedded in Elastomer: A Route to a Highly Stretchable Active Channel Layer," *Advanced Materials*, vol. 27, no. 7, pp. 1255–1261, Feb. 2015, doi: 10.1002/adma.201404602.

[86] M. Kaltenbrunner *et al.*, "Ultrathin and lightweight organic solar cells with high flexibility," *Nature Communications 2012 3:1*, vol. 3, no. 1, pp. 1–7, Apr. 2012, doi: 10.1038/ncomms1772.

[87] M. Khatib *et al.*, "A Freestanding Stretchable and Multifunctional Transistor with Intrinsic Self-Healing Properties of all Device Components," *Small*, vol. 15, no. 2, pp. 1–8, 2019, doi: 10.1002/smll.201803939.

[88] D. Choi *et al.*, "Elastomer-Polymer Semiconductor Blends for High-Performance Stretchable Charge Transport Networks," *Chemistry of Materials*, vol. 28, no. 4, pp. 1196–1204, 2016, doi: 10.1021/acs.chemmater.5b04804.

[89] J. Xu *et al.*, "Highly stretchable polymer semiconductor films through the nanoconfinement effect," *Science (1979)*, vol. 355, no. 6320, Jan. 2017, doi: 10.1126/science.aah4496.

[90] S. Zhang *et al.*, "Tacky Elastomers to Enable Tear-Resistant and Autonomous Self-Healing Semiconductor Composites," *Adv Funct Mater*, vol. 30, no. 27, p. 2000663, Jul. 2020, doi: 10.1002/adfm.202000663.

[91] E. Roduner, "Size matters: why nanomaterials are different," *Chem Soc Rev*, vol. 35, no. 7, pp. 583–592, Jun. 2006, doi: 10.1039/B502142C.

[92] R. S. Berry, "Phases and Phase Changes of Small Systems," pp. 1–26, 1999, doi: 10.1007/978-3-642-58389-6_1.

[93] G. Zhu, Z. Huang, Z. Xu, and L. T. Yan, "Tailoring Interfacial Nanoparticle Organization through Entropy," *Acc Chem Res*, vol. 51, no. 4, pp. 900–909, 2018, doi: 10.1021/acs.accounts.8b00001.

[94] K. Das, L. Gabrielli, and L. J. Prins, "Chemically Fueled Self-Assembly in Biology and Chemistry," *Angewandte Chemie International Edition*, vol. 60, no. 37, pp. 20120–20143, Sep. 2021, doi: 10.1002/anie.202100274.

[95] Z. Li, Q. Fan, and Y. Yin, "Colloidal Self-Assembly Approaches to Smart Nanostructured Materials," *Chem Rev*, vol. 122, no. 5, pp. 4976–5067, Mar. 2022, doi: 10.1021/acs.chemrev.1c00482.

[96]   B. J. Alder and T. E. Wainwright, "Phase transition for a hard sphere system," *J Chem Phys*, vol. 27, no. 5, pp. 1208–1209, 1957, doi: 10.1063/1.1743956.

[97]   D. Frenkel, H. N. W. Lekkerkerker, and A. Stroobants, "Thermodynamic stability of a smectic phase in a system of hard rods," *Nature 1988 332:6167*, vol. 332, no. 6167, pp. 822–823, 1988, doi: 10.1038/332822a0.

[98]   S. Dussi and M. Dijkstra, "Entropy-driven formation of chiral nematic phases by computer simulations," *Nature Communications 2016 7:1*, vol. 7, no. 1, pp. 1–10, Apr. 2016, doi: 10.1038/ncomms11175.

[99]   P. F. Damasceno, M. Engel, and S. C. Glotzer, "Predictive self-assembly of polyhedra into complex structures," *Science (1979)*, vol. 337, no. 6093, pp. 453–457, Jul. 2012, doi: 10.1126.

[100]   J. S. Martin, N. A. Smith, and C. D. Francis, "Removing the entropy from the definition of entropy: Clarifying the relationship between evolution, entropy, and the second law of thermodynamics," *Evolution: Education and Outreach*, vol. 6, no. 1, pp. 1–9, Oct. 2013, doi: 10.1186/1936-6434-6-30.

[101]   R. Clausius, "X. On a modified form of the second fundamental theorem in the mechanical theory of heat," *The London, Edinburgh, and Dublin Philosophical Magazine and Journal of Science*, vol. 12, no. 77, pp. 81–98, Aug. 1856, doi: 10.1080/14786445608642141.

[102]   M. Planck, "On the Law of Distribution of Energy in the Normal Spectrum," *Ann Phys*, vol. 4, p. 553, 1901.

[103]   D. Frenkel, "Order through entropy," *Nat Mater*, vol. 14, no. 1, pp. 9–12, 2015, doi: 10.1038/nmat4178.

[104]   L. Onsager, "The effects of shape on the interaction of colloidal particles," *Ann N Y Acad Sci*, vol. 51, no. 4, pp. 627–659, May 1949, doi: 10.1111/j.1749-6632.1949.tb27296.x.

[105]   W. W. Wood and J. D. Jacobson, "Preliminary Results from a Recalculation of the Monte Carlo Equation of State of Hard Spheres," *J Chem Phys*, vol. 27, no. 5, p. 1207, Aug. 1957, doi: 10.1063/1.1743956.

[106]   L. M. Prince, D. J. Microemulsion ; 6. Cebula, L. Harding, R. H. Ottewill, and P. N. Pusey, "Phase behaviour of concentrated suspensions of nearly hard colloidal spheres," *Nature 1986 320:6060*, vol. 320, no. 6060, pp. 340–342, 1986, doi: 10.1038/320340a0.

[107]   J. De Graaf, R. Van Roij, and M. Dijkstra, "Dense regular packings of irregular nonconvex particles," *Phys Rev Lett*, vol. 107, no. 15, p. 155501, Oct. 2011, doi: 10.1103/physrevlett.107.155501.

[108]   P. F. Damasceno, M. Engel, and S. C. Glotzer, "Crystalline assemblies and densest packings of a family of truncated tetrahedra and the role of directional entropic forces," *ACS Nano*, vol. 6, no. 1, pp. 609–614, Jan. 2012, doi: 10.1021/nn204012y.

[109] R. D. Kamien, "Entropic Attraction and Ordering," *Soft Matter*, pp. 1–40, Mar. 2014, doi: 10.1002/9783527682300.ch1.

[110] Q. Chen, S. C. Bae, and S. Granick, "Directed self-assembly of a colloidal kagome lattice," *Nature 2011 469:7330*, vol. 469, no. 7330, pp. 381–384, Jan. 2011, doi: 10.1038/nature09713.

[111] X. Mao, Q. Chen, and S. Granick, "Entropy favours open colloidal lattices," *Nature Materials 2012 12:3*, vol. 12, no. 3, pp. 217–222, Jan. 2013, doi: 10.1038/nmat3496.

[112] K. K. Frederick, M. S. Marlow, K. G. Valentine, and A. J. Wand, "Conformational entropy in molecular recognition by proteins," *Nature 2007 448:7151*, vol. 448, no. 7151, pp. 325–329, Jul. 2007, doi: 10.1038/nature05959.

[113] S. J. Chen, "RNA Folding: Conformational Statistics, Folding Kinetics, and Ion Electrostatics," *Annu Rev Biophys*, vol. 37, p. 197, 2008, doi: 10.1146/annurev.biophys.37.032807.125957.

[114] S. K. Kumar, N. Jouault, B. Benicewicz, and T. Neely, "Nanocomposites with polymer grafted nanoparticles," *Macromolecules*, vol. 46, no. 9, pp. 3199–3214, May 2013, doi: 10.1021/MA4001385.

[115] S. Asakura and F. Oosawa, "On Interaction between Two Bodies Immersed in a Solution of Macromolecules," *J Chem Phys*, vol. 22, no. 7, p. 1255, Dec. 1954, doi: 10.1063/1.1740347.

[116] A. VRIJ, "polymers at interfaces and the interactions in colloidal dispersions," *Colloid and Surface Science*, pp. 471–483, Jan. 1977, doi: 10.1016/b978-0-08-021570-9.50016-4.

[117] M. J. A. Hore and R. J. Composto, "Using miscible polymer blends to control depletion-attraction forces between Au nanorods in nanocomposite films," *Macromolecules*, vol. 45, no. 15, pp. 6078–6086, Aug. 2012, doi: 10.1021/ma300992e.

[118] O. Yurkevich, E. Modin, I. Šarić, M. Petravić, and M. Knez, "Entropy-driven Self-healing of Metal Oxides Assisted By Polymer-inorganic Hybrid Materials," *Advanced Materials*, p. 2202989, May 2022, doi: 10.1002/adma.202202989.

[119] C. Y. Teng, Y. J. Sheng, and H. K. Tsao, "Surface Segregation and Bulk Aggregation in an Athermal Thin Film of Polymer-Nanoparticle Blends: Strategies of Controlling Phase Behavior," *Langmuir*, vol. 33, no. 10, pp. 2639–2645, Mar. 2017, doi: 10.1021/acs.langmuir.6b04681.

[120] R. S. Krishnan, M. E. Mackay, C. J. Hawker, and B. van Horn, "Influence of molecular architecture on the dewetting of thin polystyrene films," *Langmuir*, vol. 21, no. 13, pp. 5770–5776, Jun. 2005, doi: 10.1021/LA0474060.

[121] R. S. Krishnan *et al.*, "Improved polymer thin-film wetting behavior through nanoparticle segregation to interfaces," *Journal of Physics: Condensed Matter*, vol. 19, no. 35, p. 356003, Aug. 2007, doi: 10.1088/0953-8984/19/35/356003.

[122] E. S. Mcgarrity, A. L. Frischknecht, L. J. D. Frink, and M. E. Mackay, "Surface-Induced First-Order Transition in Athermal Polymer-Nanoparticle Blends," 2007, doi: 10.1103/PhysRevLett.99.238302.

[123] J. Y. Lee, G. A. Buxton, and A. C. Balazs, "Using nanoparticles to create self-healing composites," *Journal of Chemical Physics*, vol. 121, no. 11, pp. 5531–5540, Sep. 2004, doi: 10.1063/1.1784432.

[124] R. R. Petit, J. Li, B. van de Voorde, S. van Vlierberghe, P. F. Smet, and C. Detavernier, "Atomic Layer Deposition on Polymer Thin Films: On the Role of Precursor Infiltration and Reactivity," *ACS Appl Mater Interfaces*, vol. 13, no. 38, pp. 46151–46163, Sep. 2021, doi: 10.1021/acsami.1c12933.

[125] V. Chawla *et al.*, "Fracture Mechanics and Oxygen Gas Barrier Properties of Al2O3/ZnO Nanolaminates on PET Deposited by Atomic Layer Deposition," *Nanomaterials 2019, Vol. 9, Page 88*, vol. 9, no. 1, p. 88, Jan. 2019, doi: 10.3390/nano9010088.

[126] L. Lee *et al.*, "Ultra Gas-Proof Polymer Hybrid Thin Layer," *Nano Lett*, vol. 18, no. 9, pp. 5461–5466, 2018, doi: 10.1021/acs.nanolett.8b01855.

[127] Y. C. Tseng, Q. Peng, L. E. Ocola, D. A. Czaplewski, J. W. Elam, and S. B. Darling, "Enhanced polymeric lithography resists via sequential infiltration synthesis," *J Mater Chem*, vol. 21, no. 32, pp. 11722–11725, Aug. 2011, doi: 10.1039/c1jm12461g.

[128] S. A. Gregory, Y. Li, T. D. Monroe, J. Li, S. K. Yee, and M. D. Losego, "Vapor Phase Infiltration Doping of the Semiconducting Polymer Poly(aniline) with TiCl4+ H2O: Mechanisms, Reaction Kinetics, and Electrical and Optical Properties," *ACS Appl Polym Mater*, vol. 3, no. 2, pp. 720–729, Feb. 2021, doi: 10.1021/acsapm.0c01014.

[129] W. Wang, F. Yang, C. Chen, L. Zhang, Y. Qin, and M. Knez, "Tuning the Conductivity of Polyaniline through Doping by Means of Single Precursor Vapor Phase Infiltration," *Adv Mater Interfaces*, vol. 4, no. 4, pp. 1–8, 2017, doi: 10.1002/admi.201600806.

[130] I. Azpitarte and M. Knez, "Vapor phase infiltration: from a bioinspired process to technologic application , a prospective review," *MRS Commun*, vol. 8, no. 3, pp. 727–741, 2018, doi: 10.1557/mrc.2018.126.

[131] R. Z. Waldman, N. Jeon, D. J. Mandia, O. Heinonen, S. B. Darling, and A. B. F. Martinson, "Sequential Infiltration Synthesis of Electronic Materials: Group 13 Oxides via Metal Alkyl Precursors," *Chemistry of Materials*, vol. 31, no. 14, pp. 5274–5285, Jul. 2019, doi: 10.1021/acs.chemmater.9b01714.

[132] E. K. McGuinness, F. Zhang, Y. Ma, R. P. Lively, and M. D. Losego, "Vapor Phase Infiltration of Metal Oxides into Nanoporous Polymers for Organic Solvent Separation Membranes," *Chemistry of Materials*, vol. 31, no. 15, pp. 5509–5518, 2019, doi: 10.1021/acs.chemmater.9b01141.

[133] R. Z. Waldman, N. Jeon, D. J. Mandia, O. Heinonen, S. B. Darling, and A. B. F. Martinson, "Sequential Infiltration Synthesis of Electronic Materials: Group 13 Oxides via Metal Alkyl Precursors," *Chemistry of Materials*, vol. 31, no. 14, pp. 5274–5285, 2019, doi: 10.1021/acs.chemmater.9b01714.

[134] B. J. Inkson, *Scanning Electron Microscopy (SEM) and Transmission Electron Microscopy (TEM) for Materials Characterization*. Elsevier Ltd, 2016. doi: 10.1016/B978-0-08-100040-3.00002-X.

[135] L. J. van der Pauw, "A Method of Measuring Specific Resistivity and Hall Effect of Discs of Arbitrary Shape," *Philips Research Reports*, vol. 13, no. 1, pp. 1–9, 1958.

[136] G. González-Díaz *et al.*, "A robust method to determine the contact resistance using the van der Pauw set up," *Measurement (Lond)*, vol. 98, pp. 151–158, Feb. 2017, doi: 10.1016/j.measurement.2016.11.040.

[137] W. L. V. Price, "Electric potential and current distribution in a rectangular sample of anisotropic material with application to the measurement of the principal resistivities by an extension of van der Pauw's method," *Solid State Electronics*, vol. 16, no. 7, pp. 753–762, 1973, doi: 10.1016/0038-1101(73)90171-8.

[138] P. Makuła, M. Pacia, and W. Macyk, "How To Correctly Determine the Band Gap Energy of Modified Semiconductor Photocatalysts Based on UV-Vis Spectra," *Journal of Physical Chemistry Letters*, vol. 9, no. 23, pp. 6814–6817, 2018, doi: 10.1021/acs.jpclett.8b02892.

[139] H. Salami, A. Uy, A. Vadapalli, C. Grob, V. Dwivedi, and R. A. Adomaitis, "Atomic layer deposition of ultrathin indium oxide and indium tin oxide films using a trimethylindium, tetrakis(dimethylamino)tin, and ozone precursor system," *Journal of Vacuum Science & Technology A*, vol. 37, no. 1, p. 010905, Jan. 2019, doi: 10.1116/1.5058171.

[140] G. Kresse and J. Furthmüller, "Efficient iterative schemes for ab initio total-energy calculations using a plane-wave basis set," *Phys Rev B*, vol. 54, no. 16, p. 11169, Oct. 1996, doi: 10.1103/PhysRevB.54.11169.

[141] J. P. Perdew, K. Burke, and M. Ernzerhof, "Generalized Gradient Approximation Made Simple," *Phys Rev Lett*, vol. 77, no. 18, p. 3865, Oct. 1996, doi: 10.1103/PhysRevLett.77.3865.

[142] P. E. Blöchl, "Projector augmented-wave method," *Phys Rev B*, vol. 50, no. 24, p. 17953, Dec. 1994, doi: 10.1103/PhysRevB.50.17953.

[143] S. Grimme, J. Antony, S. Ehrlich, and H. Krieg, "A consistent and accurate ab initio parametrization of density functional dispersion correction (DFT-D) for the 94 elements H-Pu," *J Chem Phys*, vol. 132, no. 15, p. 154104, Apr. 2010, doi: 10.1063/1.3382344.

[144] R. Z. Waldman, D. J. Mandia, A. Yanguas-Gil, A. B. F. Martinson, J. W. Elam, and S. B. Darling, "The chemical physics of sequential infiltration synthesis - A thermodynamic and

kinetic perspective," *Journal of Chemical Physics*, vol. 151, no. 19, 2019, doi: 10.1063/1.5128108.

[145] E. K. Mcguinness, C. Z. Leng, and M. D. Losego, "Increased Chemical Stability of Vapor-Phase Infiltrated AlOx-Poly(methyl methacrylate) Hybrid Materials," *ACS Appl Polym Mater*, vol. 2, no. 3, pp. 1335–1344, 2020, doi: 10.1021/acsapm.9b01207.

[146] I. Azpitarte, G. Botta, C. Tollan, and M. Knez, "SCIP: a new simultaneous vapor phase coating and infiltration process for tougher and UV-resistant polymer fibers," *RSC Adv*, vol. 10, no. 27, pp. 15976–15982, Apr. 2020, doi: 10.1039/d0ra02073g.

[147] B. K. Barick, A. Simon, I. Weisbord, N. Shomrat, and T. Segal-Peretz, "Tin oxide nanostructure fabrication via sequential infiltration synthesis in block copolymer thin films," *J Colloid Interface Sci*, vol. 557, pp. 537–545, 2019, doi: 10.1016/j.jcis.2019.09.044.

[148] J. J. Kim *et al.*, "Mechanistic understanding of tungsten oxide in-plane nanostructure growth: Via sequential infiltration synthesis," *Nanoscale*, vol. 10, no. 7, pp. 3469–3479, 2018, doi: 10.1039/c7nr07642h.

[149] D. H. Yi, C. Y. Nam, G. Doerk, C. T. Black, and R. B. Grubbs, "Infiltration Synthesis of Diverse Metal Oxide Nanostructures from Epoxidized Diene-Styrene Block Copolymer Templates," *ACS Appl Polym Mater*, vol. 1, no. 4, pp. 672–683, Apr. 2019, doi: 10.1021/acsapm.8b00138.

[150] G. Huseynova, J. H. Lee, Y. H. Kim, and J. Lee, "Transparent Organic Light-Emitting Diodes: Advances, Prospects, and Challenges," *Adv Opt Mater*, vol. 9, no. 14, p. 2002040, Jul. 2021, doi: 10.1002/adom.202002040.

[151] R. S. Datta *et al.*, "Flexible two-dimensional indium tin oxide fabricated using a liquid metal printing technique," *Nature Electronics 2020 3:1*, vol. 3, no. 1, pp. 51–58, Jan. 2020, doi: 10.1038/s41928-019-0353-8.

[152] S. K. Hyun, P. D. Byrne, A. Facchetti, and T. J. Marks, "High performance solution-processed indium oxide thin-film transistors," *J Am Chem Soc*, vol. 130, no. 38, pp. 12580–12581, Sep. 2008, doi: 10.1021/ja804262z.

[153] P. Chen, X. Yin, M. Que, X. Liu, and W. Que, "Low temperature solution processed indium oxide thin films with reliable photoelectrochemical stability for efficient and stable planar perovskite solar cells," *J Mater Chem A Mater*, vol. 5, no. 20, pp. 9641–9648, May 2017, doi: 10.1039/c7ta00183e.

[154] C. G. Granqvist, İ. Bayrak Pehlivan, and G. A. Niklasson, "Electrochromics on a roll: Web-coating and lamination for smart windows," *Surf Coat Technol*, vol. 336, pp. 133–138, Feb. 2018, doi: 10.1016/j.surfcoat.2017.08.006.

[155] E. B. Aydın and M. K. Sezgintürk, "Indium tin oxide (ITO): A promising material in biosensing technology," *TrAC Trends in Analytical Chemistry*, vol. 97, pp. 309–315, Dec. 2017, doi: 10.1016/j.trac.2017.09.021.

[156] A. U. Mane, A. J. Allen, R. K. Kanjolia, and J. W. Elam, "Indium Oxide Thin Films by Atomic Layer Deposition Using Trimethylindium and Ozone," *Journal of Physical Chemistry C*, vol. 120, no. 18, pp. 9874–9883, May 2016, doi: 10.1021/acs.jpcc.6b02657.

[157] A. D. Taggart *et al.*, "Electronic Conductivity of Nanoporous Indium Oxide Derived from Sequential Infiltration Synthesis," *The Journal of Physical Chemistry C*, 2021, doi: 10.1021/acs.jpcc.1c06103.

[158] I. H. Khawaji, C. Chindam, O. O. Awadelkarim, and A. Lakhtakia, "Selectablity of mechanical and dielectric properties of Parylene-C columnar microfibrous thin films by varying deposition angle," *Flexible and Printed Electronics*, vol. 2, no. 4, 2017, doi: 10.1088/2058-8585/aa9f33.

[159] C. Chindam, N. R. Brown, A. Lakhtakia, O. O. Awadelkarim, and W. Orfali, "Temperature-dependent dynamic moduli of Parylene-C columnar microfibrous thin films," *Polym Test*, vol. 53, pp. 89–97, 2016, doi: 10.1016/j.polymertesting.2016.05.010.

[160] A. Kahouli, A. Sylvestre, F. Jomni, B. Yangui, and J. Legrand, "Ac-conductivity and dielectric relaxations above glass transition temperature for parylene-C thin films," *Appl Phys A Mater Sci Process*, vol. 106, no. 4, pp. 909–913, Mar. 2012, doi: 10.1007/S00339-011-6706-4.

[161] K. Alexandrou, N. Petrone, J. Hone, and I. Kymissis, "Encapsulated graphene field-effect transistors for air stable operation," *Appl Phys Lett*, vol. 106, no. 11, p. 113104, Mar. 2015, doi: 10.1063/1.4915513.

[162] E. Y. Shin, E. Y. Choi, and Y. Y. Noh, "Parylene based bilayer flexible gate dielectric layer for top-gated organic field-effect transistors," *Org Electron*, vol. 46, pp. 14–21, Jul. 2017, doi: 10.1016/j.orgel.2017.04.005.

[163] H. Park, H. Ahn, J. Kwon, S. Kim, and S. Jung, "Parylene-Based Double-Layer Gate Dielectrics for Organic Field-Effect Transistors," *ACS Appl Mater Interfaces*, vol. 10, no. 44, pp. 37767–37772, Nov. 2018, doi: 10.1021/acsami.8b12663.

[164] S. Yin *et al.*, "Nonvolatile Memory Action Due to Hot-Carrier Charge Injection in Graphene-on-Parylene Transistors," *ACS Appl Electron Mater*, vol. 1, no. 11, pp. 2260–2267, Nov. 2019, doi: 10.1021/acsaelm.9b00467.

[165] A. Petritz *et al.*, "Imperceptible energy harvesting device and biomedical sensor based on ultraflexible ferroelectric transducers and organic diodes," *Nature Communications 2021 12:1*, vol. 12, no. 1, pp. 1–14, Apr. 2021, doi: 10.1038/s41467-021-22663-6.

[166] T. Asikainen, "Growth of In2O3 Thin Films by Atomic Layer Epitaxy," *J Electrochem Soc*, vol. 141, no. 11, p. 3210, Dec. 1994, doi: 10.1149/1.2059303.

[167] M. Ritala, T. Asikainen, and M. Leskelä, "Enhanced growth rate in atomic layer epitaxy of indium oxide and indium-tin oxide thin films," *Electrochemical and Solid-State Letters*, vol. 1, no. 3, pp. 156–157, Jul. 1998, doi: 10.1149/1.1390669.

[168] A. R. Berens and H. B. Hopfenberg, "Diffusion of organic vapors at low concentrations in glassy PVC, polystyrene, and PMMA," *J Memb Sci*, vol. 10, no. 2–3, pp. 283–303, Apr. 1982, doi: 10.1016/S0376-7388(00)81415-5.

[169] J. A. Libera, J. N. Hryn, and J. W. Elam, "Indium Oxide Atomic Layer Deposition Facilitated by the Synergy between Oxygen and Water," *Chem. Mater*, vol. 23, pp. 2150–2158, 2011, doi: 10.1021/cm103637t.

[170] W. J. Maeng, D. W. Choi, J. Park, and J. S. Park, "Indium oxide thin film prepared by low temperature atomic layer deposition using liquid precursors and ozone oxidant," *J Alloys Compd*, vol. 649, pp. 216–221, Jul. 2015, doi: 10.1016/j.jallcom.2015.07.150.

[171] J. Sheng, D. W. Choi, S. H. Lee, J. Park, and J. S. Park, "Performance modulation of transparent ALD indium oxide films on flexible substrates: Transition between metal-like conductor and high performance semiconductor states," *J Mater Chem C Mater*, vol. 4, no. 32, pp. 7571–7576, Aug. 2016, doi: 10.1039/c6tc01199c.

[172] J. H. Han *et al.*, "Atomic layer deposition of indium oxide thin film from a liquid indium complex containing 1-dimethylamino-2-methyl-2-propoxy ligands," *Appl Surf Sci*, vol. 383, pp. 1–8, 2016, doi: 10.1016/j.apsusc.2016.04.120.

[173] D. J. Lee, J. Y. Kwon, J. Il Lee, and K. B. Kim, "Self-limiting film growth of transparent conducting In2O3 by atomic layer deposition using trimethylindium and water vapor," *Journal of Physical Chemistry C*, vol. 115, no. 31, pp. 15384–15389, Aug. 2011, doi: 10.1021/jp2024389.

[174] A. W. Ott, J. M. Johnson, J. W. Klaus, and S. M. George, "Surface chemistry of In2O3 deposition using In(CH3)3 and H2O in a binary reaction sequence," *Appl Surf Sci*, vol. 112, pp. 205–215, Mar. 1997, doi: 10.1016/S0169-4332(96)00977-4.

[175] A. H. McDaniel and M. D. Allendorf, "Autocatalytic behavior of trimethylindium during thermal decomposition," *Chemistry of Materials*, vol. 12, no. 2, pp. 450–460, 2000, doi: 10.1021/cm990497f.

[176] A. W. Ott, J. W. Klaus, J. M. Johnson, and S. M. George, "Al2O3 thin film growth on Si(100) using binary reaction sequence chemistry," *Thin Solid Films*, vol. 292, no. 1–2, pp. 135–144, Jan. 1997, doi: 10.1016/S0040-6090(96)08934-1.

[177] A. C. Dillon, A. W. Ott, J. D. Way, and S. M. George, "Surface chemistry of Al2O3 deposition using Al(CH3)3 and H2O in a binary reaction sequence," *Surf Sci*, vol. 322, no. 1–3, pp. 230–242, Jan. 1995, doi: 10.1016/0039-6028(95)90033-0.

[178] J. R. Schneider, J. G. Baker, and S. F. Bent, "The Influence of Ozone: Superstoichiometric Oxygen in Atomic Layer Deposition of Fe2O3 Using tert-Butylferrocene and O3," *Adv Mater Interfaces*, vol. 7, no. 11, pp. 1–10, 2020, doi: 10.1002/admi.202000318.

[179] J. R. Schneider, C. De Paula, N. E. Richey, J. G. Baker, T. Solomon, and S. F. Bent, "Understanding and Utilizing Reactive Oxygen Reservoirs in Atomic Layer Deposition of Metal Oxides with Ozone," *ChemRxiv. Cambridge: Cambridge Open Engage.*, 2022.

[180] J. W. Elam, D. A. Baker, A. J. Hryn, A. B. F. Martinson, M. J. Pellin, and J. T. Hupp, "Atomic layer deposition of tin oxide films using tetrakis(dimethylamino) tin," *Journal of Vacuum Science & Technology A: Vacuum, Surfaces, and Films*, vol. 26, no. 2, p. 244, Jan. 2008, doi: 10.1116/1.2835087.

[181] W. J. Lee *et al.*, "Comparative study of the electrical characteristics of ALD-ZnO thin films using H2O and H2O2 as the oxidants," *Journal of the American Ceramic Society*, vol. 102, no. 10, pp. 5881–5889, 2019, doi: 10.1111/jace.16429.

[182] C. M. Lousada, M. Yang, K. Nilsson, and M. Jonsson, "Catalytic decomposition of hydrogen peroxide on transition metal and lanthanide oxides," *J Mol Catal A Chem*, vol. 379, pp. 178–184, Nov. 2013, doi: 10.1016/j.molcata.2013.08.017.

[183] J. Njeim *et al.*, "Effect of the Al2O3 Deposition Method on Parylene C: Highlights on a Nanopillar-Shaped Surface," *ACS Omega*, vol. 5, no. 26, pp. 15828–15834, 2020, doi: 10.1021/acsomega.0c00735.

[184] I. Bello, W. H. Chang, and W. M. Lau, "Mechanism of cleaning and etching Si surfaces with low energy chlorine ion bombardment," *J Appl Phys*, vol. 75, no. 6, pp. 3092–3097, 1994, doi: 10.1063/1.356160.

[185] R. Narain, Ed., *Polymer Science and Nanotechnology: Fundamentals and Applications*, 1st ed. Elsevier, 2020. doi: 10.1016/b978-0-12-816806-6.09991-x.

[186] S. Lin and D. Xie, "Initial Decomposition of Methanol and Water on In2O3(110): A Periodic DFT Study," *Chin J Chem*, vol. 30, no. 9, pp. 2036–2040, Sep. 2012, doi: 10.1002/cjoc.201200714.

[187] T. Asikainen, M. Ritala, and M. Leskelä, "Growth of In2O3 thin films by atomic layer epitaxy," *Appl Surf Sci*, vol. 82–83, no. C, pp. 122–125, 1994, doi: 10.1016/0169-4332(94)90206-2.

[188] R. Caldwell, M. G. Street, R. Sharma, P. Takmakov, B. Baker, and L. Rieth, "Characterization of Parylene-C degradation mechanisms: In vitro reactive accelerated aging model compared to multiyear in vivo implantation," *Biomaterials*, vol. 232, no. December 2019, p. 119731, 2020, doi: 10.1016/j.biomaterials.2019.119731.

[189] D. W. Grattan and M. Bilz, "the Thermal Aging Ofparylene Antioxidant," vol. 36, pp. 44–52, 1991.

[190] Z. Song *et al.*, "Carbon electrode obtained via pyrolysis of plasma-deposited parylene-C for electrochemical immunoassays," vol. 1, 2022, doi: 10.1039/d2an00854h.

[191] M. J. Herman and M. W. Blair, "Determination of chemical decay mechanisms of Parylene-C during X-ray irradiation using two-dimensional correlation FTIR," *Polym Degrad Stab*, vol. 171, p. 109024, 2020, doi: 10.1016/j.polymdegradstab.2019.109024.

[192] A. A. Nesmelov *et al.*, "Poly(p-Xylylene) and Poly(chloro-p-Xylylene) Protective Coatings Prepared by Deposition in a Nitrogen Flow," *Nanotechnol Russ*, vol. 15, no. 9–10, pp. 647–654, 2020, doi: 10.1134/s1995078020050092.

[193] M. Bera, A. Rivaton, C. Gandon, and J. L. Gardette, "Photooxidation of poly(para-xylylene)," *Eur Polym J*, vol. 36, no. 9, pp. 1753–1764, 2000, doi: 10.1016/S0014-3057(99)00258-x.

[194] C. Satheeshkumar, B.-J. Jung, H. Jang, W. Lee, and M. Seo, "Surface Modification of Parylene C via Buchwald-Hartwig Amination for Organic-Solvent compatible and Flexible Microfluidic Channel Bonding," *Macromol Rapid Commun*, vol. 42, p. 2000520, 2021, doi: 10.1002/marc.202000520.

[195] G. Xiong, U. Pal, J. G. Serrano, K. B. Ucer, and R. T. Williams, "Photoluminescence and FTIR study of ZnO nanoparticles: The impurity and defect perspective," *Physica Status Solidi (C) Current Topics in Solid State Physics*, vol. 3, no. 10, pp. 3577–3581, 2006, doi: 10.1002/pssc.200672164.

[196] E. M. Davis, N. M. Benetatos, W. F. Regnault, K. I. Winey, and Y. A. Elabd, "The influence of thermal history on structure and water transport in Parylene C coatings," *Polymer (Guildf)*, vol. 52, no. 23, pp. 5378–5386, Oct. 2011, doi: 10.1016/j.polymer.2011.08.010.

[197] J. Kane, H. P. Schweizer, and W. Kern, "Chemical vapor deposition of transparent electrically conducting layers of indium oxide doped with tin," *Thin Solid Films*, vol. 29, no. 1, pp. 155–163, Sep. 1975, doi: 10.1016/0040-6090(75)90224-2.

[198] H. I. Yeom, J. B. Ko, G. Mun, and S. H. K. Park, "High mobility polycrystalline indium oxide thin-film transistors by means of plasma-enhanced atomic layer deposition," *J Mater Chem C Mater*, vol. 4, no. 28, pp. 6873–6880, 2016, doi: 10.1039/c6tc00580b.

[199] O. Bierwagen, "Indium oxide - A transparent, wide-band gap semiconductor for (opto)electronic applications," *Semicond Sci Technol*, vol. 30, no. 2, p. 24001, 2015, doi: 10.1088/0268-1242/30/2/024001.

[200] H. I. Yeom, J. B. Ko, G. Mun, and S. H. K. Park, "High mobility polycrystalline indium oxide thin-film transistors by means of plasma-enhanced atomic layer deposition," *J Mater Chem C Mater*, vol. 4, no. 28, pp. 6873–6880, 2016, doi: 10.1039/c6tc00580b.

[201] J. Buckeridge *et al.*, "Deep vs shallow nature of oxygen vacancies and consequent n-type carrier concentrations in transparent conducting oxides," *Phys Rev Mater*, vol. 2, p. 54604, 2018, doi: 10.1103/PhysRevMaterials.2.054604.

[202] L. T. Duy, H. Kang, H. Shin, S. Han, R. Singh, and H. Seo, "Multifunctional Nanohybrid of Alumina and Indium Oxide Prepared Using the Atomic Layer Deposition Technique," 2021, doi: 10.1021/acsami.1c18623.

[203] B. Macco, H. C. M. Knoops, and W. M. M. Kessels, "Electron Scattering and Doping Mechanisms in Solid-Phase-Crystallized In2O3:H Prepared by Atomic Layer Deposition," *ACS Appl Mater Interfaces*, vol. 7, no. 30, pp. 16723–16729, 2015, doi: 10.1021/acsami.5b04420.

[204] T. Tohsophon, A. Dabirian, S. De Wolf, M. Morales-Masis, and C. Ballif, "Environmental stability of high-mobility indium-oxide based transparent electrodes," *APL Mater*, vol. 3, no. 11, 2015, doi: 10.1063/1.4935125.

[205] H. Wu *et al.*, "A transparent electrode based on a metal nanotrough network," *Nature Nanotechnology 2013 8:6*, vol. 8, no. 6, pp. 421–425, May 2013, doi: 10.1038/nnano.2013.84.

[206] S.-K. Lu, J.-T. Huang, T.-H. Lee, J.-J. Wang, and D.-S. Liu, "Flexibility of the Indium Tin Oxide Transparent Conductive Film Deposited Onto the Plastic Substrate," *Smart Science*, vol. 2, no. 1, pp. 7–12, Jan. 2016, doi: 10.1080/23080477.2014.11665597.

[207] H. J. Queisser, "Persistent Photoconductivity in Semiconductors.," pp. 1303–1308, 1985.

[208] J. Bao *et al.*, "Photoinduced oxygen release and persistent photoconductivity in ZnO nanowires," *Nanoscale Res Lett*, vol. 6, no. 1, pp. 1–7, May 2011, doi: 10.1186/1556-276x-6-404.

[209] A. Dixit *et al.*, "Robust room temperature persistent photoconductivity in polycrystalline indium oxide films," *Appl Phys Lett*, vol. 94, no. 25, pp. 1–4, 2009, doi: 10.1063/1.3159623.

[210] A. Sumanth, K. Lakshmi Ganapathi, M. S. Ramachandra Rao, and T. Dixit, "A review on realizing the modern optoelectronic applications through persistent photoconductivity," *J Phys D Appl Phys*, vol. 55, no. 39, 2022, doi: 10.1088/1361-6463/ac7f66.

[211] B. Pashmakov, B. Claflin, and H. Fritzsche, "Photoreduction and oxidation of amorphous indium oxide," *Solid State Commun*, vol. 86, no. 10, pp. 619–622, Jun. 1993, doi: 10.1016/0038-1098(93)90826-9.

[212] M. Lee *et al.*, "Brain-Inspired Photonic Neuromorphic Devices using Photodynamic Amorphous Oxide Semiconductors and their Persistent Photoconductivity," *Advanced Materials*, vol. 29, no. 28, pp. 1–8, 2017, doi: 10.1002/adma.201700951.

[213] A. di Mauro, M. Cantarella, G. Nicotra, V. Privitera, and G. Impellizzeri, "Low temperature atomic layer deposition of ZnO: Applications in photocatalysis," *Appl Catal B*, vol. 196, pp. 68–76, 2016, doi: 10.1016/j.apcatb.2016.05.015.

[214] T. Tynell and M. Karppinen, "Atomic layer deposition of ZnO: a review," *Semicond Sci Technol*, vol. 29, no. 4, p. 043001, Apr. 2014, doi: 10.1088/0268-1242/29/4/043001.

[215] A. Das and D. Basak, "Efficacy of Ion Implantation in Zinc Oxide for Optoelectronic Applications: A Review," *ACS Appl Electron Mater*, 2021, doi: 10.1021/acsaelm.1c00393.

[216] T. Khalafi, F. Buazar, and K. Ghanemi, "Phycosynthesis and Enhanced Photocatalytic Activity of Zinc Oxide Nanoparticles Toward Organosulfur Pollutants," *Sci Rep*, vol. 9, no. 1, pp. 1–10, 2019, doi: 10.1038/s41598-019-43368-3.

[217] Z. Gao and P. Banerjee, "Review Article: Atomic layer deposition of doped ZnO films," *Citation: Journal of Vacuum Science & Technology A*, vol. 37, p. 50802, 2019, doi: 10.1116/1.5112777.

[218] W. Wang, F. Yang, C. Chen, L. Zhang, Y. Qin, and M. Knez, "Tuning the Conductivity of Polyaniline through Doping by Means of Single Precursor Vapor Phase Infiltration," *Adv Mater Interfaces*, vol. 4, no. 4, p. 1600806, 2017, doi: 10.1002/admi.201600806.

[219] J. Pilz, A. M. Coclite, and M. D. Losego, "Vapor phase infiltration of zinc oxide into thin films of cis -polyisoprene rubber," *Mater Adv*, vol. 1, no. 6, pp. 1695–1704, Sep. 2020, doi: 10.1039/d0ma00304b.

[220] L. E. Ocola, A. Connolly, D. J. Gosztola, R. D. Schaller, and A. Yanguas-Gil, "Infiltrated zinc oxide in poly(methyl methacrylate): An atomic cycle growth study," *Journal of Physical Chemistry C*, vol. 121, no. 3, pp. 1893–1903, Jan. 2017, doi: 10.1021/acs.jpcc.6b08007.

[221] S. Obuchovsky, H. Frankenstein, J. Vinokur, A. K. Hailey, Y. L. Loo, and G. L. Frey, "Mechanism of Metal Oxide Deposition from Atomic Layer Deposition inside Nonreactive Polymer Matrices: Effects of Polymer Crystallinity and Temperature," *Chemistry of Materials*, vol. 28, no. 8, pp. 2668–2676, May 2016, doi: 10.1021.

[222] J. Cai *et al.*, "A revisit to atomic layer deposition of zinc oxide using diethylzinc and water as precursors," *J Mater Sci*, vol. 54, no. 7, pp. 5236–5248, Apr. 2019, doi: 10.1007/s10853-018-03260-3.

[223] Y. Wang, K. M. Kang, M. Kim, and H. H. Park, "Effective oxygen-defect passivation in zno thin films prepared by atomic layer deposition using hydrogen peroxide," *Journal of the Korean Ceramic Society*, vol. 56, no. 3, pp. 302–307, 2019, doi: 10.4191/kcers.2019.56.3.11.

[224] Y. J. Choi, K. M. Kang, H. S. Lee, and H. H. Park, "Non-laminated growth of chlorine-doped zinc oxide films by atomic layer deposition at low temperatures," *J Mater Chem C Mater*, vol. 3, no. 32, pp. 8336–8343, 2015, doi: 10.1039/c5tc01763g.

[225] N. Asakuma *et al.*, "Photocrystallization of amorphous ZnO," *J Appl Phys*, vol. 92, no. 10, pp. 5707–5710, 2002, doi: 10.1063/1.1513197.

[226] N. Y. Yuan, S. Y. Wang, C. B. Tan, X. Q. Wang, G. G. Chen, and J. N. Ding, "The influence of deposition temperature on growth mode, optical and mechanical properties of ZnO films prepared by the ALD method," *J Cryst Growth*, vol. 366, pp. 43–46, Mar. 2013, doi: 10.1016/j.jcrysgro.2012.12.024.

[227] H. Y. Lee, B. K. Wu, and M. Y. Chern, "Study on the formation of zinc peroxide on zinc oxide with hydrogen peroxide treatment using x-ray photoelectron spectroscopy (XPS)," *Electronic Materials Letters*, vol. 10, no. 1, pp. 51–55, 2014, doi: 10.1007/s13391-013-2244-x.

[228] K. Persson, "Materials Project, mp-2133: ZnO (hexagonal, P6_3mc, 186)," *Materials Data on ZnO (SG:186) by Materials Project*, 2014. https://materialsproject.org/materials/mp-2133/ (accessed Aug. 09, 2022).

[229] J. Park, T. H. Jung, J. H. Lee, H. S. Kim, and J. S. Park, "The growth behavior and properties of atomic layer deposited zinc oxide films using hydrogen peroxide (H2O2) and ozone (O3) oxidants," *Ceram Int*, vol. 41, no. 1, pp. 1839–1845, 2015, doi: 10.1016/j.ceramint.2014.09.133.

[230] S. Alamdari *et al.*, "Preparation and characterization of zinc oxide nanoparticles using leaf extract of sambucus ebulus," *Applied Sciences (Switzerland)*, vol. 10, no. 10, pp. 1–19, 2020, doi: 10.3390/app10103620.

[231] L. Keskiväli *et al.*, "Comparison of the Growth and Thermal Properties of Nonwoven Polymers after Atomic Layer Deposition and Vapor Phase Infiltration," *Coatings 2021, Vol. 11, Page 1028*, vol. 11, no. 9, p. 1028, Aug. 2021, doi: 10.3390/coatings11091028.

[232] Q. Ma *et al.*, "Atomic-Layer-Deposition of Indium Oxide Nano-films for Thin-Film Transistors," *Nanoscale Res Lett*, vol. 13, no. 1, pp. 2–9, 2018, doi: 10.1186/s11671-017-2414-0.

[233] C. Laschi, B. Mazzolai, and M. Cianchetti, "Soft robotics: Technologies and systems pushing the boundaries of robot abilities," *Sci Robot*, vol. 1, no. 1, Dec. 2016, doi: 10.1126/scirobotics.aah3690.

[234] Y. J. Tan, J. Wu, H. Li, and B. C. K. Tee, "Self-Healing Electronic Materials for a Smart and Sustainable Future," *ACS Appl Mater Interfaces*, vol. 10, no. 18, pp. 15331–15345, 2018, doi: 10.1021/acsami.7b19511.

[235] S. Zhang and F. Cicoira, "Water-Enabled Healing of Conducting Polymer Films," *Advanced Materials*, vol. 29, no. 40, p. 1703098, Oct. 2017, doi: 10.1002/adma.201703098.

[236] Y. Cao *et al.*, "A Transparent, Self-Healing, Highly Stretchable Ionic Conductor," *Advanced Materials*, vol. 29, no. 10, p. 1605099, Mar. 2017, doi: 10.1002/adma.201605099.

[237] J. Huang *et al.*, "Electrically programmable adhesive hydrogels for climbing robots," *Sci Robot*, vol. 6, no. 53, p. 1858, Apr. 2021, doi: 10.1126/scirobotics.abe1858.

[238] G. Xu *et al.*, "Optimal Reactivity and Improved Self-Healing Capability of Structurally Dynamic Polymers Grafted on Janus Nanoparticles Governed by Chain Stiffness and Spatial Organization," *Small*, vol. 13, no. 13, p. 1603155, Apr. 2017, doi: 10.1002/smll.201603155.

[239] J. Y. Oh *et al.*, "Stretchable self-healable semiconducting polymer film for active-matrix strain-sensing array," *Sci Adv*, vol. 5, no. 11, 2019, doi: 10.1126/sciadv.aav3097.

[240] X. Li *et al.*, "Effect of mesoscale phase contrast on fatigue-delaying behavior of self-healing hydrogels," *Sci Adv*, vol. 7, no. 16, pp. 8210–8224, Apr. 2021, doi: 10.1126/sciadv.abe8210.

[241] M. D. Losego and Q. Peng, "Atomic Layer Deposition and Vapor Phase Infiltration," in *Surface Modification of Polymers*, Weinheim: Wiley-VCH Verlag GmbH &Co. KGaA, 2019, p. Ch. 5.

[242] I. Sanzari, M. Callisti, A. De Grazia, D. J. Evans, T. Polcar, and T. Prodromakis, "Parylene C topographic micropattern as a template for patterning PDMS and Polyacrylamide hydrogel," *Scientific Reports 2017 7:1*, vol. 7, no. 1, pp. 1–11, Jul. 2017, doi: 10.1038/s41598-017-05434-6.

[243] Md. A. Hossain *et al.*, "Atomic layer deposition enabling higher efficiency solar cells: A review," *Nano Materials Science*, vol. 2, no. 3, pp. 204–226, Oct. 2019, doi: 10.1016/j.nanoms.2019.10.001.

[244] M. G. Helander *et al.*, "Chlorinated indium tin oxide electrodes with high work function for organic device compatibility," *Science (1979)*, vol. 332, no. 6032, pp. 944–947, May 2011, doi: 10.1126/science.1202992.

[245] C. Ruan, Q. Sun, D. Xiao, H. Li, G. Xia, and S. Wang, "Lightwave irradiation-assisted low-temperature solution synthesis of indium-tin-oxide transparent conductive films," *Ceram Int*, Jan. 2022, doi: 10.1016/j.ceramint.2022.01.094.

[246] Y. Yang *et al.*, "Defect-targeted self-healing of multiscale damage in polymers," *Nanoscale*, vol. 12, no. 6, pp. 3605–3613, 2020, doi: 10.1039/c9nr09438e.

[247] R. Zhang *et al.*, "Entropy-driven segregation of polymer-grafted nanoparticles under confinement," *Proc Natl Acad Sci U S A*, vol. 114, no. 10, pp. 2462–2467, Mar. 2017, doi: 10.1073/pnas.1613828114.

[248] J. Y. Lee, G. A. Buxton, and A. C. Balazs, "Using nanoparticles to create self-healing composites," *Journal of Chemical Physics*, vol. 121, no. 11, pp. 5531–5540, 2004, doi: 10.1063/1.1784432.

[249] T. Biben, P. Bladon, and D. Frenkel, "Depletion effects in binary hard-sphere fluids," *Journal of Physics: Condensed Matter*, vol. 8, no. 50, p. 10799, Dec. 1996, doi: 10.1088/0953-8984/8/50/008.

[250] J. P. Greene, "Microstructures of Polymers," *Automotive Plastics and Composites*, pp. 27–37, Jan. 2021, doi: 10.1016/B978-0-12-818008-2.00009-X.

[251] H. Hatakeyama, H. Matsumura, and T. Hatakeyama, "Glass transition and thermal degradation of rigid polyurethane foams derived from castor oil-molasses polyols," *J Therm Anal Calorim*, vol. 111, no. 2, pp. 1545–1552, Feb. 2013, doi: 10.1007/S10973

[252] K. Zalewski, Z. Chyłek, and W. A. Trzciński, "A Review of Polysiloxanes in Terms of Their Application in Explosives," *Polymers 2021, Vol. 13, Page 1080*, vol. 13, no. 7, p. 1080, Mar. 2021, doi: 10.3390/polym13071080.

[253] M. J. R. Loadman, "The glass transition temperature of natural rubber," *J Therm Anal Calorim*, vol. 30, no. 4, pp. 929–941, Jul. 2005, doi: 10.1007/bf01913321.

[254] S. Yang, J. R. Castilleja, E. v. Barrera, and K. Lozano, "Thermal analysis of an acrylonitrile–butadiene–styrene/SWNT composite," *Polym Degrad Stab*, vol. 83, no. 3, pp. 383–388, Mar. 2004, doi: 10.1016/j.polymdegradstab.2003.08.002.

[255] X. Zhao, W. Liu, X. Jiang, al -, D. Golodnitsky, and E. Strauss, "Mechanical Relaxations and Transitions in Polytetrafluoroethylene," *Jpn J Appl Phys*, vol. 3, no. 8, p. 436, Aug. 1964, doi: 10.1143/jjap.3.436.

[256] J. Park, H. R. Yoon, M. A. Khan, S. Cho, and M. M. Sung, "Selective Infiltration in Polymer Hybrid Thin Films as a Gas-Encapsulation Layer for Stretchable Electronics," *ACS Appl Mater Interfaces*, vol. 12, no. 7, pp. 8817–8825, 2020, doi: 10.1021/acsami.9b19269.

[257] P. J. Hine, A. Astruc, and I. M. Ward, "Hot compaction of polyethylene naphthalate," *J Appl Polym Sci*, vol. 93, no. 2, pp. 796–802, Jul. 2004, doi: 10.1002/app.20517.

[258] M. Kosaki, K. Sugiyama, and M. Ieda, "Ionic Jump Distance and Glass Transition of Polyvinyl Chloride," *J Appl Phys*, vol. 42, no. 9, p. 3388, Dec. 2003, doi: 10.1063/1.1660742.

[259] M. Mesgar *et al.*, "Chlorine-enhanced surface mobility of Au(100)," *ChemPhysChem*, vol. 14, no. 1, pp. 233–236, 2013, doi: 10.1002/cphc.201200621.

[260] A. J. F. van Hoof, R. C. J. van der Poll, H. Friedrich, and E. J. M. Hensen, "Dynamics of silver particles during ethylene epoxidation," *Appl Catal B*, vol. 272, no. February, p. 118983, 2020, doi: 10.1016/j.apcatb.2020.118983.

[261] C. A. Grabowski and A. Mukhopadhyay, "Size effect of nanoparticle diffusion in a polymer melt," *Macromolecules*, vol. 47, no. 20, pp. 7238–7242, 2014, doi: 10.1021/ma501670u.

List of Publications

This thesis is based on the following publications and patent:

[1] O. Yurkevich, E. Modin, I. Šarić, M. Petravić, and M. Knez, "Entropy-Driven Self-Healing of Metal Oxides Assisted by Polymer–Inorganic Hybrid Materials," Adv. Mater., p. 2202989, Jun. 2022, doi: 10.1002/adma.202202989.

[2] K. Ashurbekova, K. Ashurbekova, G. Botta, O. Yurkevich, and M. Knez, "Vapor phase processing: A novel approach for fabricating functional hybrid materials," Nanotechnology, vol. 31, no. 34, 2020, doi: 10.1088/1361-6528/ab8edb.

[3] O. Yurkevich, E. Modin, I. Šarić Janković, R. Peter, M. Petravić, and M. Knez, "Introducing a Flexible Conductive Hybrid: Indium Oxide-ParyleneC obtained by Vapor Phase Infiltration", manuscript submitted.

[4] European patent application: O. Yurkevich & M. Knez, "Method for producing self-healing organic-inorganic materials", Patent number: P21250EP00

Beyond the scope of this thesis, the author contributed to the following publication:

[5] Martina Rihova, Oksana Yurkevich, Martin Motola, Ludek Hromadko, Zdenek Spotz, Raul Zazpe, Mato Knez, and Jan M. Macak, "ALD coating of centrifugally spun polymeric fibers and postannealing: case study for nanotubular TiO_2 photocatalyst," Nanoscale Adv., vol. 3, no. 15, pp. 4589–4596, 2021, doi: 10.1039/d1na00288k.

List of Abbreviations

ABS	Acrylonitrile butadiene styrene
ALD	Atomic Layer Deposition
ATR-FTIR	Attenuated Total Reflection FTIR
BSE	Backscattered Electrons
CVD	Chemical Vapor Deposition
DEZ	Diethyl Zinc
DFT	Density Functional Theory
DTA	Derivative Thermogravimetric Analysis
EDX	Energy-Dispersive X-Ray Spectroscopy
FFT	Fast Fourier Transformation
FIB	Focused Ion Beam
FTIR	Fourier Transform Infrared Spectroscopy
GPC	Growth per Cycle
HRTEM	High Resolution Transmission Electron Microscopy
IR	Infrared
ITO	Indium Tin Oxide
IZO	Indium Zinc Oxide
LM	Liquid Metal
MeO	Metal Oxide
MLD	Molecular Layer Deposition
$NiCp_2$	Nickelocene
NP	Nanoparticle
OTFT	Organic Thin Film Transistor
PA-6	Polyamide 6
PDMS	Polydimethylsiloxane
PET	Polyethylene Terephthalate
PMMA	Polymethylmetacrylate
PP	Polypropylene

133

PPC	Persistent Photoconductivity
PS	Polystyrene
PTFE	Polytetrafluoroethylene
PU	Polyurethane
PVC	Polyvinyl Chloride
RT	Room Temperature
SE	Secondary Electrons
SEM	Scanning Electron Microscopy
SIMS	Secondary Ion Mass Spectrometry
SHM	Self-Healing Material
SIS	Sequential Infiltration Synthesis
TCO	Transparent Conductive Oxide
TEM	Transmission Electron Microscopy
Tg	Glass Transition Temperature
TGA	Thermogravimetric Analysis
TMA	Trimethylaluminum
TMIn	Trimethylindium
TDMA-Sn	Tetrakis(dimethylamino)tin
UV-VIS	Ultraviolet – Visible Spectroscopy
XPS	X-ray Photoelectron Spectroscopy
XRR	X-ray reflectivity
XRD	X-ray Diffraction
VPI	Vapor Phase Infiltration

Acknowledgments

I am deeply grateful to my professor Mato Knez for making this exciting journey possible. For all your support, which started a long time before I joined your group. For encouraging me to keep my eyes open for unexpected discoveries, welcoming all the ideas, and sharing yours. For being truly motivational and positive through these years. It was an unforgettable experience to be a part of your team, and I hope to continue being lucky to have you as a mentor even after my leave from the group.

I want to thank all the past and present members of the Nanomaterials group, for a constantly friendly atmosphere and all the great time we spent together in the lab. Our language exchanges, diversified playlists, and group meetings were really enjoyable and cheerful. Without the help of our great technicians (Mikel Beltran and Raydel Pérez) and all the chemists in my group, my life would be way more complicated. Additional gratitude to Gabriele who tried out a few lithography processes for me and Natalia for taking care of my gramma in Spanish.

My research contains a bunch of electron images and FIB preparation, which couldn't be possible without the guidance of Andrey Chuvilin, Evgeny Modin, and Christopher Tollan from the Electron Microscopy group. You taught me how to deal with EM on my own and in this way gifted me with such a large playground. Thanks for sharing your knowledge and for tolerating me occupying the microscopes for so long.

Many thanks to Roger Llopis for teaching me how to conduct the electrical investigations and helping with non-routine measurements. I am grateful to the neighboring Ctech lab for sharing its facilities and to Daniel Simo for life-affirming discussions. Further, I want to express additional gratitude to Nanogune's management for helping my smooth integration in Spain.

I want to additionally thank colleagues from the University of Rijeka in Croatia: Iva Šarić, Robert Peter, Mladen Petravić, Maria Kolympadi and Gabriela Ambrožić for making my secondment in Rijeka not only scientifically fruitful but also enjoyable and comfortable.

I was lucky to be a member of the HYCOAT project, where I met all the great people from the warm and open ALD community. I am very grateful for Christophe Detavernier and Jolien Dendooven for the great organization of our consortium and constant support of the ESRs. Unquestionably, it was precious for us, fresh ALD people, to meet on our PhD way. It is my hope to see you soon, and

Acknowledgments

I wish you all the best in your future careers and life. I truly appreciate Michael Nolan and Arbresha Muriqi from the consortium for our collaboration which was vital for a deeper understanding of my research results.

I also want to express gratitude to my former group, Research and Educational Centre "Functional Nanomaterials" in I. Kant Baltic Federal University for cultivating my interest in nanoscience and for the undoubtful impact on my future. You have provided me with exciting possibilities, opened many doors on this path, and shared the passion for science.

My friends made this journey even more enjoyable. I am glad I met such great people who faced my doubts and down moments together with me. But also accompanied me on our travels around the Iberian Penisula, discovered mountains together, cultivated my abilities in skiing, joining our music sessions, climbing, dancing, or biking.

Let me express my immense gratitude towards my family. Even though life turned out to be somewhat complicated for travels during these years, you surrounded me with absolute love and support in all possible ways.

<div align="right">

O.Ю.
October 2022

</div>